Author:
Psyrras, Nick

Title:
The Seismic Response Of Buried Gas Pipelines In Inhomogeneous Soil

The Seismic Response Of Buried Gas Pipelines In Inhomogeneous Soil

by

Nikolaos Psyrras, M.Eng.

A Dissertation Submitted to the University of Bristol in Accordance with the Requirements for Award of the Degree of

DOCTOR OF PHILOSOPHY

in the Faculty of Engineering, Department of Civil Engineering

November, 2019

Word Count: 62,975

Abstract

Buried gas pipelines constitute lifeline systems whose uninterrupted operation is critical to the well-being of the community. Given that these systems are spatially extended, their unavoidable exposure to seismic hazards such as wave propagation is an issue of concern requiring better understanding. This thesis is concerned with the performance of gas transmission pipes buried in laterally inhomogeneous soil during earthquake ground shaking. The broad goal is to identify which conditions can lead to failure, particularly buckling, and characterize those failure mechanisms.

The dynamic soil-pipe interaction problem was approached numerically and experimentally. A rigorous yet efficient two-step numerical methodology involving a global and a local model was developed to capture the response at site, soil-pipe interaction, and pipeline levels. Critical states of ground deformation for the pipe were identified by considering a range of case studies and generic site scenarios. The worst-case ground deformations were obtained for a combination of high site impedance contrast, soft soil and long-period input excitations. Under strong excitations, the soil response was nonlinear with sharp horizontal and vertical differential movements. When subjected to such soil load profiles, it was found that a pipeline with relatively high radius-to-thickness ratios, low internal pressure, and high surface roughness can experience plastic buckling. The instability was governed by interaction between axial load and bending moment, while the critical loads and strains were found to be much lower than those under pure axial compression.

Shaking table tests of a scale model of a long pipeline laid through a three-block configuration of sands were also performed. The results overall confirmed the significant pipe strain concentrations at soil interfaces predicted by the numerical models. Strains were maximized at resonant frequencies and also increased notably with surface acceleration. Models more advanced than the commonly used beam on springs are necessary to capture this complex localised response pattern.

Acknowledgements

I express my sincere gratitude to my main supervisor, Prof. Anastasios Sextos, for his continuous guidance and support during the period of my research. Acting constantly as a close mentor, he shared his experience, encouraged me to shape an independent path, and offered moral uplifting during difficult times. Without his help, this work would not have been possible. Special thanks is owed to my second supervisor, Assoc. Prof. Adam Crewe, for his advisory role on the experimental aspect of this research.

Moreover, I wish to thank project partner Prof. Oh-Sung Kwon for hosting me as a visiting graduate student at the University of Toronto for twelve months; his support and insightful discussions were key in progressing my study and are greatly appreciated. Equally, I would like to acknowledge the assistance of Prof. George Mylonakis, whose useful feedback and extensive knowledge helped improve the quality of this work. I am also indebted to all technical staff of the Earthquake and Geomechanics Laboratories at University of Bristol who assisted in the experiments, in particular Mr Mictroy Mitchell and Mr Lawrence de Leeuw.

This doctoral research was carried out with the financial support of the EPSRC (grant no.: EP/M507994/1). My time as a visiting scholar at the University of Toronto was sponsored by the Horizon 2020 Programme of the European Commission through grant MSCA-RISE-2015-691213-EXCHANGE-Risk. Both sources of funding are hereby acknowledged.

Finally, I am grateful for the unconditional support from my family and Chrysa; their encouragement was critical to cross the finish line.

Nikolaos Psyrras

Author's Declaration

I declare that the work in this dissertation was carried out in accordance with the requirements of the University's *Regulations and Code of Practice for Research Degree Programmes* and that it has not been submitted for any other academic award. Except where indicated by specific reference in the text, the work is the candidate's own work. Work done in collaboration with, or with the assistance of, others, is indicated as such. Any views expressed in the dissertation are those of the author.

SIGNED:  ..... DATE: 08/06/2020 .....

Table of Contents

List of Tables

List of Figures

Chapter 1

Introduction

1.1 Background and motivation

Natural gas is nowadays a cornerstone in fulfilling the energy needs of households, the industry and transportation. The growing reliance of the global energy market on natural gas is reflected in statistics: 29% of the total energy mix in the US and 25% in the European Union is currently due to natural gas (The European Union, 2010; The U.S. Energy Information Administration (EIA), 2017), while it is projected that by 2040 nearly 1/4 of global electricity will be generated from natural gas (International Energy Agency, 2015).

Extensive interconnected grids of buried pipelines have come to be the safest and most efficient means of onshore transportation of natural gas from wells to regions of demand, with steel being the exclusive material for the pipeline. However, of the heaviest dependents on natural gas are seismically active regions, such as California in the U.S., parts of south-eastern Europe (Italy, Greece, Turkey and the Balkans), Japan and New Zealand, all exposed to significant seismic hazard as demonstrated in **Figure 1-1**.

Earthquake effects on buried pipelines are typically divided in two types of 'geohazards' based on the temporal nature of the damage cause:

a. transient ground deformation due to seismic wave propagation, and

b. permanent ground deformation (PGD), in the form of active fault movements, landslides, liquefaction-induced settlement or lateral spreading.

PGD hazards have attracted major interest by a great many researchers in recent years and the relevant body of work is quite mature. This study will only consider the effects of transient ground deformation.

Due to their geographical extent, gas transmission pipelines cross terrain of variable morphology and are thus prone to spatially non-uniform earthquake excitation. The vulnerability of such long-span structures to differential ground motions is a long-standing topic in research, now being especially relevant with the global transition towards cleaner and more reliable energy sources and the associated need to protect these high-value energy infrastructure assets against earthquakes.

Buried pipelines are subjected to transient ground motions induced by various types of seismic waves, most commonly shear waves (S-waves), compressional waves (P-waves) and Rayleigh waves (R-waves). As shown in **Figure 1-2**, different ground displacement components act on the pipeline due to each type of wave; in the general case, all these components will superpose. Depending on the dominant type of wave striking the pipeline, the angle of wave incidence θ with respect to the horizontal, and the pipeline alignment with respect to the horizontal projection of the ray path (i.e., yaw), the primary modes of deformation of the pipeline consist of axial tension-compression, longitudinal bending in the vertical or horizontal plane, or a combination of them. Racking deformations, although prevalent in larger liners such as tunnels, are not relevant in pipelines.

Evidence from past earthquakes shows that damage inflicted to the gas transmission network can cause long service disruption and severe, difficult-to-predict socioeconomic loss. While most of the pipeline damage reported to date is attributed to PGD, there exists sufficient field evidence to say that travelling seismic waves can also be a source of damage. For instance, occurrences of local buckling in steel pipelines have been observed, where localized curvatures and strains have become large enough to lead to collapse of the pipe section or even wall cracking and gas leakage. Such localised damage is likely to cause disproportionately large disruption in the network affecting a community in a wider sense.

This work forms part of a wider research project, 'Experimental and Computational Hybrid Assessment of Natural Gas Pipelines Exposed to Seismic Risk' (EXCHANGE-Risk). EXCHANGE-Risk is an international, intersectoral research and innovation transfer scheme led by the University of Bristol focusing on seismic risk mitigation of buried gas pipeline networks. Its aims are to enhance the knowledge on the seismic vulnerability of such systems by utilising the concept of hybrid experimentation (combination of physical and numerical computational models), to develop innovative methods for pre- and post-earthquake pipeline inspection, system monitoring and network resilience, and to promote collaboration between the participating academic and industrial partners in Europe and North America.

1.2 Objectives

Understanding the ways that buried gas pipelines behave under seismic loads and the circumstances under which these loads can cause damage is key to taking appropriate safety measures to safeguard the network serviceability. This thesis pursues to advance the current state of knowledge on the response of buried gas transmission pipelines in laterally variable soil to earthquake ground shaking. In this spirit, specific objectives are as follows:

a. to parametrically establish when and how transient seismic loads can lead to pipeline damage, and identify and characterise those damage mechanisms;

b. to develop a computationally efficient methodology able to reliably predict the seismic pipe response and capture potential failure modes by considering essential aspects of the system mechanics, including the soil and soil-pipe contact response;

c. to capture the effect of key geotechnical and structural parameters on the the pipeline performance;

d. to establish a valid connection between a suitable intensity measure of ground motion and pipeline damage;

e. to experimentally observe the key response mechanisms of a typical buried gas pipeline under strong ground shaking, measure the magnitude of the induced deformation in the pipe and determine the parameters that govern it;

f. to assess the applicability of current soil-pipe interaction models on problems of seismic response of pipelines buried in inhomogeneous soil.

1.3 Scope of research

In achieving the above objectives, the research programme described in this thesis has been designed to embrace both numerical and physical modelling. In more detail, the scope of work includes:

- Thorough revision and analysis of the existing body of knowledge on the seismic response of buried gas pipelines to identify key areas that need reconsideration or further scrutiny;

- Development of a rigorous numerical analysis methodology to predict the seismic response of the soil-pipe system and detect buckling failure in the pipe, accounting for important details of the behavior of the system, such as material and geometric nonlinearity;

- Application of the above methodology in a parametric context to determine which ground and loading conditions can be critical for the pipeline integrity;

- Identification and characterization of the failure modes occurring in the pipe, including establishing critical loads and deformation measures;

- Further application of advanced soil-pipe numerical models to explore the effect of various system parameters on the critical failure loads and deformations;

- Design and execution of a seismic testing programme to physically model the problem at hand, including development of a novel soil-pipe test setup on a shaking table and of a suitable instrumentation array to monitor the response of both the pipe and the soil.

1.4 Thesis organisation and content

This dissertation is organised into six chapters and three appendices.

- Chapter 1 is the general introduction (this chapter).

- Chapter 2 provides a survey of the literature on fundamental topics related to the response of buried gas pipelines to seismic excitations, including field evidence for the dominant failure modes, soil-pipe interaction models, spatially variable earthquake ground motions, methods of pipeline response analysis, and code provisions for the seismic design of buried pipelines.

- Chapters 3 and 4 present the development and application of a numerical methodology for the performance assessment of gas pipelines buried in laterally inhomogeneous ground under seismic wave loads. Chapter 3 outlines the proposed methodology and then progresses to present the first analysis stage concerning the seismic response of the soil. Chapter 4 addresses the analysis of the structural response of the pipeline subjected to the free-field seismic motions determined in Chapter 3.

- Chapter 5 describes the experimental approach of this research. The equipment used, test setup, scaling considerations, measurements obtained and limitations are discussed in detail. Results are juxtaposed to numerical findings of Chapters 3 and 4 and validated with simple numerical models. The adequacy of standard analytical models used in practice is evaluated in those cases.

- Chapter 6 contains a summary of the research and the overall conclusions drawn from it. Suggestions for future research on unresolved issues are also provided.

- Appendix A presents a short study on the quantification of the effect of kinematic soil-pipe interaction on the seismic response of a buried gas pipelines, which is a central assumption in the research methodology. Appendix B lists a series of programming scripts and code snippets that have facilitated the generation of the numerical results, and are required to reproduce them. Appendix C presents some key theoretical aspects related to buckling of pipe shells for completeness. Appendix D contains supplementary information about an exploratory numerical study performed during the design phase of the experiments.

1.5 Relevant publications

In the course of this PhD programme, the following publications have been produced:

(1) Psyrras, N. K., and Sextos, A. G. (2017). "Safety of buried steel natural gas pipelines under earthquake-induced ground shaking : a review." *Soil Dynamics and Earthquake Engineering*, Elsevier Ltd, 106(March), 254–277.

(2) Psyrras, N., Sextos, A. G., Kwon, O.-S., and Gerasimidis, S. (2018). "Safety factors of buried steel natural gas pipelines under spatially variable earthquake ground motion." *11th National Conference on Earthquake Engineering*, Earthquake Engineering Research Institute, Los Angeles, California.

(3) Psyrras, N., Kwon, O., Gerasimidis, S., and Sextos, A. (2019). "Can a buried gas pipeline experience local buckling during earthquake ground shaking?" *Soil Dynamics and Earthquake Engineering*, Elsevier Ltd, 116, 511–529.

(4) Tsinidis, G., Di Sarno, L., Sextos, A., Psyrras, N., and Furtner, P. (2018). "On the numerical simulation of the response of gas pipelines under compression." *Ninth International Conference on Advances in Steel Structures (ICASS)*.

(5) Psyrras N., Sextos A., Crewe A., Dietz M.. "Physical modelling of the seismic response of gas pipelines in laterally layered inhomogeneous soils." *Journal of*

Geotechnical and Geoenvironmental Engineering. DOI: 10.1061/(ASCE)GT.1943-5606.0002242.

(6) Psyrras N., Sextos A., Crewe A., Dietz M., de Leeuw L. W. (2019). "Shaking table tests of the seismic response of transmission gas pipelines in non-homogeneous soil." *Second International Conference on Natural Hazards and Infrastructure (ICONHIC)*, Chania, Greece.

(7) Psyrras N., and Sextos A. (2019). "Analysis of the effect of kinematic soil-pipe interaction on the response of buried gas pipelines to seismic excitation". *4th Hellenic National Conference on Earthquake Engineering and Seismology*, Hellenic Association for Earthquake Engineering/Technical Chamber of Greece, Athens, Greece.

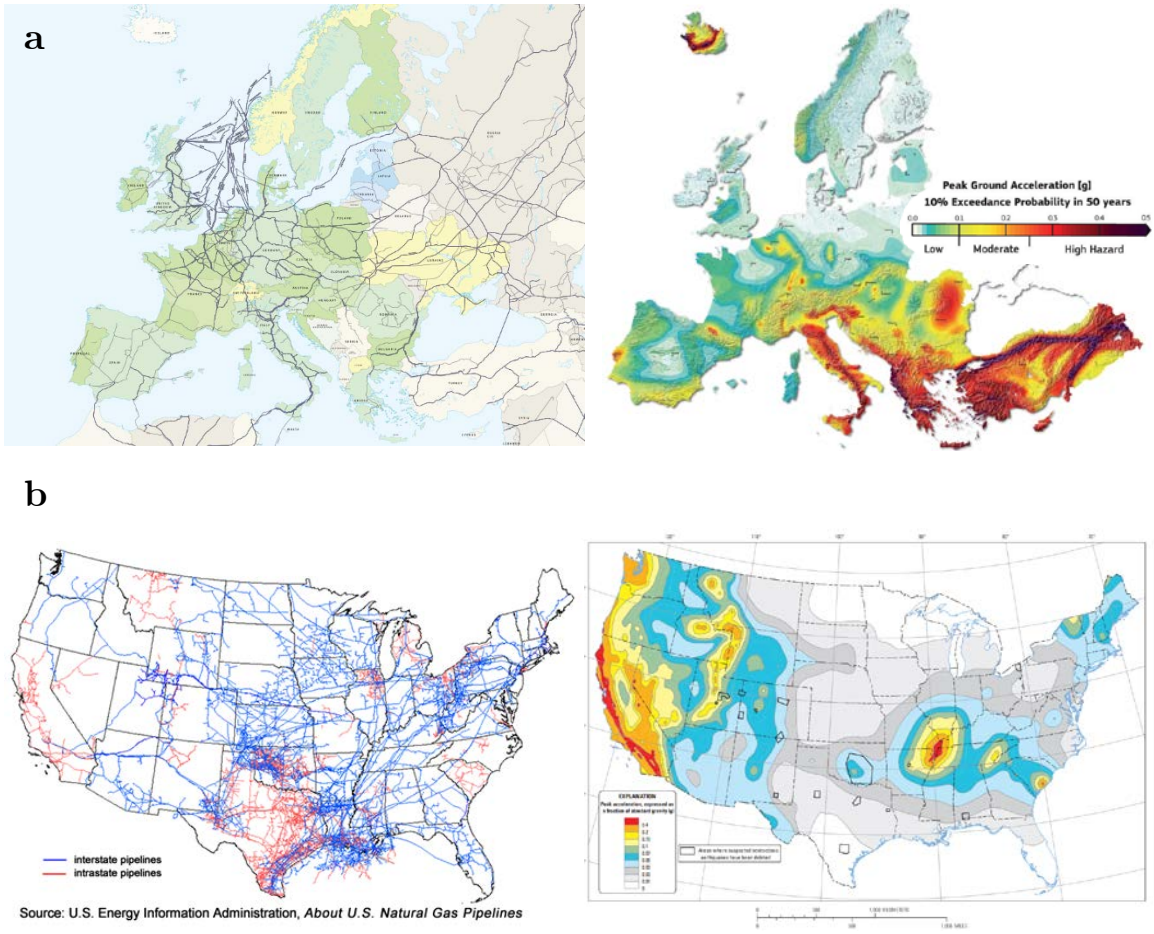

Figure 1-1. Gas transmission grid maps and seismic hazard maps (10% probability of exceedance in 50 years for PGA) side-by-side for (a) Europe and (b) the US

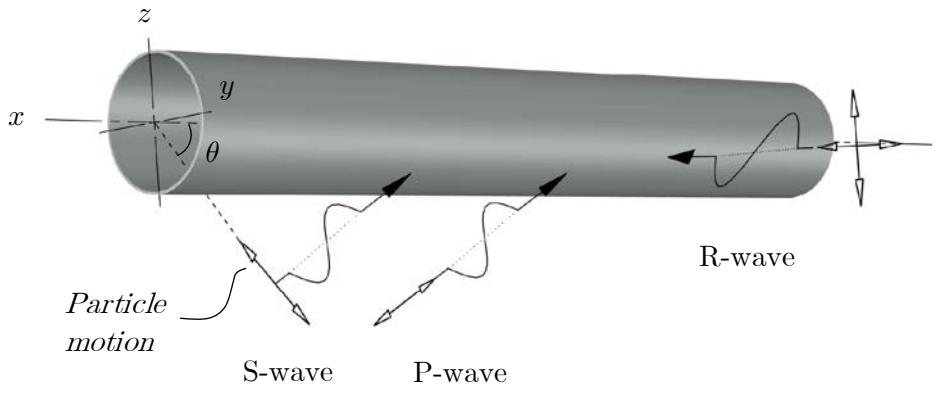

Figure 1-2. A buried pipeline struck by trains of S-waves and P-waves propagating under angle θ with respect to the pipe centreline and R-waves propagating along the pipe

Chapter 2

Literature Review

In this chapter, the literature on fundamental topics relating to the response of buried gas pipelines to seismic excitations is surveyed. These topics include the identification and field evidence for the dominant failure modes; soil-pipe interaction models; multi-support earthquake loading; methods of pipeline response analysis; and seismic design requirements for buried pipelines set by codes of practice. Besides collating previous developments that have shaped our current understanding of the seismic behaviour of these structures, this chapter identifies critical domains that require further research and highlights the challenges involved in them.

2.1 Pipeline technology and typologies

A gas transportation system comprises smaller networks of pipes that may fall under one of three categories, gathering lines, transmission lines, and distribution lines. The purpose of transmission lines is to act as the link between gathering and distribution lines, and to this end, they need to traverse large territories of diverse geomorphology. Typically, mainline transmission pipes have large diameters D in excess of 400 mm, accommodate high operating pressures P in the range 3~15 MPa, and are made from carbon-rich steel of API X grades with minimum specified yield strength σ_y greater than 350 MPa. A minimum wall thickness $t_{w,min}$ for pressure containment is calculated by limiting the hoop stress σ_θ to an allowable stress equal to the factored-down yield stress of steel:

$$\sigma_\theta = \frac{PD}{2t_{w,min}} \leq f\sigma_y \Rightarrow t_{w,min} \geq \frac{PD}{f\sigma_y} \tag{2.1}$$

The design factor f is a safety factor varying from 0.66 to 0.8, depending on which design standard is used. Section design based on pressure containment usually leads to radius-to-thickness ratios R/t_w of less than 50. As will be discussed in the following, this ratio largely controls the type and characteristics of buckling failures in shells of revolution. The individual pipe segments are joined together by stringent welding procedures to form a continuous system. Burial depths d measured from ground surface to pipe crown usually vary from 0.6 m to 1.5 m, depending on local ground conditions. Most often, it is the native soil excavated to create the trench that is used for backfilling. For further details on gas pipeline technology and especially construction techniques, the interested reader is referred to Folga (2007).

To organise our knowledge on the current stock of gas pipelines, a database has been compiled containing technical, operational and geographical information about major national and transnational gas piping systems in Europe. The data are presented in **Table 2-1**; they consist of 50 entries with 15 data fields each. Frequency distributions of two parameters of particular interest—diameter and maximum operating pressure—are shown in **Figure 2-1**. It is seen that the majority of pipelines have diameters that lie in the $[900, 1100]$ mm range. Maximum operating pressures are skewed to the lowest bin $[5, 9]$ MPa. Even though some data could not be retrieved on confidentiality grounds (notably, operating pressures and wall thicknesses), the database provides a perspective of the main pipeline typologies encountered in practice; additionally, it allows selection of representative prototypes for research purposes.

2.2 Failure mechanisms and field evidence

Identifying the principal mechanisms leading to pipeline failure is a key first step in selecting effective response analysis procedures and establishing appropriate design

criteria. Previous field surveys classify the most frequently occurring failure modes into two main groups, those common in *continuous* pipelines and those observed in *segmented* pipelines. The first group includes line pipes assembled with welding techniques, the welds being equally strong or stronger than the pipe barrels themselves. The second group includes pipelines in which connections between pipe barrels are achieved by mechanical joints, which are normally the weak link of the chain due to their lower strength. Herein, discussion is limited to continuous pipelines, because they are overwhelmingly preferred for gas networks. One can distinguish between the following earthquake-triggered damage mechanisms in continuous steel-welded pipelines (O'Rourke and Liu, 1999):

a. shell-mode buckling

b. beam-mode buckling

c. tensile rupture

d. section ovalisation

These mechanisms are illustrated in **Figure 2-2** and described in detail below. In addition, **Figure 2-3** depicts photographic evidence of failures on buried gas pipelines caused by some of these mechanisms.

2.2.1 Shell-mode buckling

Shell-mode (also referred to as *local* or simply *shell*) buckling is an instability failure of thin-walled bodies loaded in compression, resulting from a sudden transition from a stable to an unstable state of equilibrium. Typical R/t_w ratios and steel grades used in gas applications dictate that such instabilities are expected in the post-elastic range of response both in uniform compression and in bending (Kyriakides and Corona, 2007). In a pipeline shell with ideally perfect geometry, shell buckling involves two types of behaviour: *bifurcation buckling*, which marks the transition from one mode of deformation to another (e.g., from axisymmetric to non-axisymmetric), and *nonlinear*

collapse at a limit point ('limit point' or 'snap-through' buckling). In a real, imperfect pipeline shell, only the latter behaviour is possible (Bushnell, 1982).

These two behaviours are exposed in **Figure 2-4**, which shows characteristic load-deflection curves of perfect and imperfect shells. For a perfect shell, the most prevalent situation is when the bifurcation point B precedes the limit point A (the reverse is also possible though). Path OAC is called the fundamental path, corresponding to axisymmetric deformation; path BD is the post-bifurcation path and is associated with extreme non-axisymmetric deformations, if OB is axisymmetric. For an imperfect shell, only the fundamental nonlinear path OEF is valid, with failure expected at the limit load at E. A more detailed description of the evolution of a typical load-deformation curve in plastic buckling and its sensitivity to various parameters will follow in Chapter 4.

Shell buckling is common in steel pipelines as records show from past earthquakes (Housner and Jennings, 1972; O'Rourke and Liu, 1999). Specifically, a water pipe failed in buckling during the 1985 Michoacan earthquake in Mexico City, whilst liquid fuel, water and gas pipelines suffered similar damage in the 1991 Costa Rica and 1994 Northridge earthquakes. Shell buckling was also observed in pipelines at normal and reverse fault crossings in the 1971 San Fernando earthquake. Ultimately, the highly localized deformations due to buckling initiation may either cause wall fracture directly or lead to fatigue cracks in the long run, and possibly content leakage.

Elastic and plastic buckling of standalone circular cylindrical shells are well-established topics in literature pertaining to aerospace engineering and pressure vessel technology. On the other hand, the problem of buckling of shallow-buried cylindrical shells, that is, buckling under external constraints (soil confinement), is not yet as mature. Yun & Kyriakides (1990) studied the parameters influencing the occurrence of shell-buckling in buried pipelines under seismically-induced axial compression. They showed that combination of conditions such as large D, large R/t_w and large h favours emergence of shell-mode buckling. Pipelines embedded in stiffer soils display a slight

increase in buckling stress and strain, but what exerts greater influence on the pipe response is the amplitude of the initial imperfections.

Hall & Newmark (1977), based on previous experiments, recommended a strain-based criterion for the onset of shell buckling in buried pipelines as a function of t_w/R, also adopted in the guidelines by the ASCE Technical Council on Lifeline Earthquake Engineering (1984):

$$0.15(t_w/R) \leq \varepsilon_{cr} \leq 0.2(t/R) \tag{2.1}$$

where ε_{cr} is a critical wrinkling strain. O'Rourke & Liu (1999) note that the above criterion finds better applicability on thin-walled pipes, while it appears conservative for thick-walled ones; most gas transmission pipelines rather lie in the moderately low to low R/t_w range. Vazouras et al. (2010) established the following no-buckling condition for buried pipelines subjected to strike-slip fault movement

$$R/t_w \leq 0.05a(L/R)^2 \tag{2.2}$$

where L is the length of the deformed segment of the pipeline and a is a parameter that depends on the pipe material and initial wall imperfections.

2.2.2 Beam-mode buckling

Shallow-buried gas pipelines subject to compressive ground forces are likely to suffer from beam-mode buckling—sometimes referred to as *upheaval* buckling, though this term is not preferred here. In this failure mode, an axially loaded pipeline is forced to bend upwards, where soil resistance is lower, due to 2nd order effects—much like a slender column will buckle laterally under axial load; the pipeline may even reveal itself out of the ground as witnessed in certain cases. Because localization of deformation is not as severe as in shell-mode buckling, pipe breaks are rare in this case; for this reason, beam-mode buckling is seen as a less catastrophic failure. A limit state criterion for beam-mode buckling should depend on a number of parameters, including the flexural rigidity EI of the pipe section, potential imperfections, and the burial depth d.

Field studies from past earthquakes verify the occurrence of beam-mode buckling in some cases. In 1959, oil pipelines embedded in a shallow trench with a depth ranging between 0.15 and 0.30m and traversing the Buena Vista reverse fault lifted out of the ground because of excessive compressive loads. In another interesting case during the 1979 Imperial Valley event, there was no evidence of upheaval buckling until inspections by means of backfill excavation forced the pipelines to buckle upwards (McNorgan, 1989). This also an indication that beam-mode buckling does not necessarily cause interruption of content flow. Beam-mode buckling was also reported after the Niigataken Chuetsu-oki earthquake in Japan.

Yun & Kyriakides (1990) analysed the factors that contribute to beam-mode buckling. Pipelines with smaller D, smaller R/t_w and smaller h were found to be more susceptible to beam-mode buckling. However, under real-life conditions, shell- and beam-mode buckling essentially interact; in fact, this type of response is associated with buckling loads lower than those predicted for either shell- or beam-buckling alone. Meyersohn & O'Rourke (1991) noticed that pipelines covered with soft backfill are more likely to fail by means of beam-mode buckling. They pointed out that a cover depth to crown of 0.5 to 1 m is sufficient to ensure the pipeline will not suffer beam-mode buckling.

More recently, Matheson et al. (2008) carried out a parametric numerical study of an idealized buried pipeline model with hill-crest overbend imperfection under service loads, in order to establish an empirical formula and limit state for the critical upheaval buckling load. Wang et al. (2011) set to determine the pipe uplift required to mobilise the upheaval buckling load by full-scale laboratory testing of a plane strain soil-pipe system. It was found that mobilisation uplift relates linearly to the ratio h/D.

Mitsuya et al. (2013) reproduced the beam-mode buckling failure that occurred in buried pipelines during the Niigataken Chuetsu-oki earthquake by developing a limit state expression that relies on elastic stability theory and tangent modulus theory. The critical strain is given as

$$\varepsilon_{cr} = \left(\frac{4k_\ell I}{A^2}\frac{\varepsilon_{0.2}^n}{\sigma_{0.2}}n\right)^{\frac{1}{n+1}} \tag{2.2}$$

where A is the area of the pipe cross-section, I its second moment of inertia, k_ℓ the lateral soil spring constant, $\sigma_{0.2}$ and $\varepsilon_{0.2}$ the 0.2% steel proof stress and the corresponding strain, n is a material work-hardening exponent.

2.2.3 Tensile rupture

When a pipeline is subjected to tensile loads beyond yield, rupture is anticipated as plastic longitudinal strains become unacceptably large. This type of failure is rarely seen in arc-welded steel pipelines with butt connections due to their high ductility. On the other hand, steel pipelines assembled with gas-welded slip joints are more vulnerable because these joints cannot withstand substantial yielding before rupture. Generally speaking, records from fairly recent earthquakes reveal that most steel pipelines performed well against tensile loads, since modern manufacturing techniques are able to guarantee the minimum ductility requirements.

While the ultimate strain of X-grade carbon steel may well reach 21% according to manufacturers' specifications, usually more conservative limits of 2%~4% are adopted in design standards and research. However, it is debatable how representative these limits are of the real ductility capacity of steel at the weakest spots of a welded pipeline, namely girth welds, potential wall defects and corroded segments. Girth welds, although designed with higher strength provisions than pipe barrels, may exhibit lower ductility than the nominal value owing to metallurgical alterations induced by the welding process. Steel corrosion is known to correlate with a reduction in ductility and an increase of brittleness. With these considerations, it becomes clear that even the most conservative of the proposed tensile strain limits involves a degree of uncertainty. In practice, a way to determine a lower bound ultimate strain during the design process is to perform tensile tests using samples containing welds or induced corrosion.

2.2.4 Section ovalisation

Under bending action, an unpressurised pipe will experience ring ovalisation, also known as flattening or Brazier effect, after L. Brazier who first studied this behavior (Brazier, 1927). This type of instability can be thought to arise from the radial components of the bending stresses induced in the beam-pipe due to applied curvature. These radial 'ovalising' forces make the initially circular section flatten into an oval-like shape, an effect that causes loss of bending stiffness and produces nonlinear softening in the moment-curvature path.

Though not an ultimate limit state, ovalisation can pose a serviceability risk to the gas-carrying capacity of the pipeline. A limit state for ovalisation is recommended by Gresnigt (1986) in Eq. (2.3) as the ratio of the critical change in diameter ΔD_{cr} in the plane of bending to the original D

$$\Delta D_{cr}/D = 0.15 \tag{2.3}$$

In a pressurized pipeline, internal pressure exerts on the diameter an action opposite to the ovalising forces; under these circumstances, the net change of diameter can be negative or positive, depending on the pressure level and on whether plasticity occurs.

2.3 Soil-pipe interaction

What sets apart buried infrastructure like pipelines from aboveground structures in terms of earthquake response is the continuous restraint supplied by the surrounding soil, and the emergence or not of interaction effects. When an earthquake hits and travelling stress waves arrive at points along a pipeline, in-phase or out-of-phase, relative motion between the soil and the pipe is a mechanism that can generate stress in the pipe. This type of load is displacement-controlled because pipeline deformation results directly from the imposed ground motions rather than by inertial loads.

In contrast to the well-understood, inertia-driven dynamic response of aboveground structures to ground excitation, buried pipelines are minimally affected

by inertial loads (Kubo, 1975; Shinozuka and Koike, 1979; Shinozuka, Kameda and Koike, 1983). The generated inertia in a seismically excited pipeline is small owing to the low pipe mass relative to the replaced soil mass. As a consequence, inertial soil-structure interaction effects in the form they manifest in super-structures are practically negligible. Further, kinematic interaction, which refers to the ground motion modification at foundation level due to the soil-structure stiffness contrast, is intuitively expected to be also negligible for pipelines – this is demonstrated by parametric finite-element analysis in Appendix A. It follows that soil-pipe interaction (*SPI* hereinafter) can be sufficiently described in the quasi-static regime, provided that major forms of energy dissipation are somehow accounted for. It can be argued then that, in terms of mechanics, this class of problems bears essential similarity to that of a buried pipeline under PGD.

Under seismic excitation, the pipeline interacts with the ground fundamentally in two modes, laterally (longitudinal bending) and axially. The level of interaction in the system in either mode depends on geometric and material parameters. For the lateral mode, the following *pipe-to-soil* flexibility ratio F_ℓ encapsulates the degree of interaction

$$F_\ell = \frac{2E(1-\nu_p^2)R^3}{E_p(1+\nu)t_w^3} \tag{2.4}$$

where the subscripted symbols refer to pipe variables. A few studies (e.g., Peck et al. 1972) have concluded that as long as $F_\ell > 20$, the pipe will not interact with the ground; otherwise, SPI should be considered in analysis.

A similar dimensionless ratio can be constructed for the axial mode of response. Consider a cantilever beam constrained to move only axially — a uniaxial strain state (**Figure 2-5**). For a hollow circular section of radius R and thickness t_w, it is elementary to express the axial flexibility of the pipe $f_p = \Delta l/P$ by applying a unit axial force at the free end and calculating the respective change of length. By doing

the same for a solid soil bar of the same radius, the relative axial pipe-to-soil flexibility can be expressed as

$$F_a = \frac{f_p}{f_s} = \frac{E(1-\nu)(1+\nu_p)(1-2\nu_p)R}{2E_p(1-\nu_p)(1+\nu)(1-2\nu)t} \tag{2.5}$$

It is obvious from Eqs. (2.4) and (2.5) that, given $\nu \approx \nu_p$, the ratio F_ℓ/F_a varies with $(R/t)^2$. This means that for common ratios R/t_w encountered in practice, a pipeline buried in ground is 3 to 4 orders of magnitude stiffer axially than laterally with respect to the ground.

Under conditions of laterally homogeneous ground, it is easy to understand that certain types of seismic waves will only excite rigid-body modes, thus resulting in zero stress and strain. For instance, this is the case for an infinitely long pipeline with assumed free ends, swept by vertically propagating P- or SH-waves. However, even in the absence of relative soil-pipe motion, a buried pipeline may deform. For example, a pipeline subjected to asynchronous ground motions triggered by seismic waves travelling along its path will also develop strains; the same applies for a pipeline embedded in soil strata with stiffness varying along its route. These cases of *spatially variable ground motion* are of major interest and constitute the main topic of research of this thesis; a background on the spatial variation of ground motion is provided in Section 2.4.

Various mathematical models of SPI from the state-of-the-art are discussed in the following.

2.3.1 The zero soil-pipe interaction model

The most basic model of a pipeline buried in soil is conceived by assuming that the supporting soil possesses much greater stiffness than the pipeline itself in all response modes, therefore the pipeline is flexible enough to conform to ground motions; this is a result observed in field tests (Sakurai and Takanashi, 1969). From this assumption it follows that the pipe will distort—by experiencing axial straining and

curvature—as much as the ground in direct contact with it. This means that solutions for the ground deformation suffice to describe pipe deformation too.

Closed-form solutions for the ground deformation due to travelling waves assuming zero interaction can be derived by resorting to the theory of plane wave propagation in an infinite, homogeneous, isotropic medium. Without loss of generality, consider a plane wave front travelling in the x direction with apparent wave speed c; Newmark (1968) proposed that the free-field axial strain and curvature given by

$$\frac{\partial u_g}{\partial x} = -\frac{1}{c}\frac{\partial u_g}{\partial t} \tag{2.6}$$

$$\frac{\partial^2 v_g}{\partial x^2} = \frac{1}{c^2}\frac{\partial v_g}{\partial t} \tag{2.7}$$

where u_g and v_g represent the soil particle displacement components parallel and perpendicular, respectively, to the wave propagation vector and t = time, are used to also express the axial strain and curvature of the pipe. These expressions were generalised (St John and Zahrah, 1987) for the case of P-waves, S-waves and R-waves incident under arbitrary angle θ and are summarized in **Table 2-2** along with the critical angles that produce the maximum values. Kuesel (1969) had earlier applied this method for the seismic design of the San Francisco Trans-Bay Tube. Further, Kouretzis et al (2006) and Kouretzis et al (2011), employing 3-D thin shell theory, provided a more comprehensive set of analytical descriptions for the axial, hoop, shear and principal pipeline strain in the general case of impinging S- and R-waves, respectively.

The zero-interaction approach provides a practical tool for preliminary evaluation of pipeline strains and curvatures; its shortcoming of course is that it is always conservative (for linearly elastic ground response) in that it leads to design strains larger than would be if the pipe was able to resist any imposed soil motions (i.e. a system described by a finite soil-pipe stiffness ratio). The method can be highly

accurate only for laterally flexible pipes, that means, soil-pipe systems with high F_ℓ ratios. Typical gas transmission pipelines have stiffness that prevent them from exactly following soil motions—this is particularly true for the axial mode. Therefore, applying this approach to analyse these structures is not justified for all cases.

2.3.2 Models for soil-pipe interaction

Winkler foundation

When a buried pipeline offers appreciable resistance to ground motion, the pipeline response will deviate from the ground response and SPI effects are likely to play a role. The most widely used model able to capture this behaviour is based on the theory of an elastic beam on elastic (Winkler) foundation. The pipeline is treated as an Euler-Bernoulli beam resting on a continuous bed of lateral or axial springs representing SPI; the soil foundation is characterised by an elastic modulus (spring constant) per unit length of the pipe. In the dynamic analogue, a bed of linear dashpots acting in the corresponding direction is introduced to model seismic energy dissipation. With reference to **Figure 2-6**, the governing equation of motion of such a model subject to a ground excitation time-history in a transverse direction is

$$m\frac{\partial^2 v}{\partial t^2} + C_\ell \frac{\partial v}{\partial t} + K_\ell v + E_p I \frac{\partial^4 v}{\partial x^4} = C_\ell \frac{\partial v_g}{\partial t} + K_\ell v_g \tag{2.8}$$

where $v = v(x,t)$ and $v_g = v_g(t)$ denote the transverse pipe and ground displacement respectively; m = mass per unit length of the pipe; I = the second moment of area of the pipe section; K_ℓ = the elastic constant of the distributed transverse spring; C_ℓ = the coefficient of the distributed transverse dashpot. Similarly, the response of the corresponding model subject to horizontal ground excitation is described by

$$m\frac{\partial^2 u}{\partial t^2} + C_a \frac{\partial u}{\partial t} + K_a u - E_p A \frac{\partial^2 u}{\partial x^2} = C_a \frac{\partial u_g}{\partial t} + K_a u_g \tag{2.9}$$

where $u = u(x,t)$ and $u_g = u_g(t)$ stand for the time-varying axial pipe and ground displacement respectively, A = the area of the pipe section, K_a = the elastic constant

of the distributed axial spring, C_a = the coefficient of the distributed axial dashpot. Coefficients C_ℓ and C_a are usually assumed to represent damping action due to the soil only; internal damping of the pipe itself is comparably small. If the dynamic terms are ignored, the response is quasi-static and Eqs. (2.12) and (2.9) become respectively

$$E_p I \frac{\partial^4 v}{\partial x^4} + K_\ell v_{rel} = 0 \tag{2.10}$$

$$E_p A \frac{\partial^2 u}{\partial x^2} - K_a u_{rel} = 0 \tag{2.11}$$

where $v_{rel} = v - v_g$ and $u_{rel} = u - u_g$ are the relative pipe-soil displacements. Eqs. (2.12) and (2.9) or their quasi-static equivalents (2.10) and (2.11) can be modified to model nonlinear interactions by substituting $K_\ell v_{rel}$ for $F_\ell(v_{rel})$ and $K_a u_{rel}$ for $t(u_{rel})$. Closed-form solutions of the equations of motion can be obtained only for simple idealised input excitations, e.g., of sinusoidal form, and under certain assumptions in the case of nonlinear interaction. For more complex cases, the spatially continuous model is discretised and solved by numerical methods.

Central in a dynamic Winkler model is the determination of the spring and dashpot coefficients (or the relationship between soil restraint and relative soil-pipe displacement in the case of nonlinear interaction) to reflect the actual interaction at the soil-pipe interface. A number of such models have been proposed to date and have been paired with the beam-on-dynamic-Winkler-foundation (BDWF hereinafter) model presented above or its matrix version to investigate SPI effects.

Parmelee & Ludtke (1975) considered a plane-strain lateral vibration model of a pipe in linearly elastic half-space; Mindlin's static solution (Mindlin, 1936) for incompressible soil was used to modify Eq. (2.12) and a nonlinear lateral spring coefficient was calculated as $K_\ell = \beta(H/R)E$, where $\beta(H/R)$ is a monotonically increasing function. Their analysis concluded that lateral SPI effects are small.

One of the first known experiments to investigate SPI effects is due to Audibert & Nyman (1977) who explored the lateral horizontal response of steel pipelines with

diameters up to 114 mm buried in sand, under a wide range of h/D ratios ($h = d + R$ being the burial depth measured from ground surface to pipe centreline). A rectangular hyberbola was fitted to test data representing lateral soil resistance as a function of the lateral relative movement, with an ultimate value

$$R_\ell = \gamma' D H N_q \tag{2.12}$$

in which γ' is the effective unit weight of the soil and N_q the bearing capacity factor estimated from relevant charts. O'Rourke & Wang (1978) proposed that the SPI stiffness be given by the following linear functions of the soil shear modulus G

$$K_\ell = 3G; \qquad K_a = 2G \tag{2.13}$$

Hindy & Novak (1979) constructed a stiffness matrix containing soil reactions to unit axial and lateral pipe movements. To achieve this, plane-strain solutions for the complex dynamic soil stiffness describing the soil reaction per unit length to harmonic vibration of a rigid cylinder embedded in an infinite, linearly viscoelastic soil with hysteretic damping were considered; for example, Eq. (2.14) gives the complex form of dynamic stiffness for lateral vibrations

$$k_\ell = G[S_{a1}(a_0, \nu, \tan\delta) + iS_{a2}(a_0, \nu, \tan\delta)] \tag{2.14}$$

where $a_0 = R\omega/V_s$ is the dimensionless frequency, ω the vibration frequency, V_s the soil shear wave velocity, $i = \sqrt{1}$, δ is the soil loss angle, and S_a are dimensionless quantities. The real part of Eq. (2.14) expresses the stiffness of the soil, whereas the imaginary part represents geometric damping. Then, the complex stiffness solutions were compared to static solutions of the plane-strain problem after Mindlin, calculated over a range of geometric parameters. Where the static solution coincided with the dynamic one, those static stiffness coefficients were used to assemble the soil stiffness matrix.

To validate the available analytical models against experimental data, Trautmann & O'Rourke (1985) performed multi-parametric pseudo-static tests to

measure the response of typical buried pipelines to lateral soil motion. A best-fit hyperbolic expression was proposed to describe the lateral force-displacement curves $F_\ell - v_{rel}$ obtained from the tests, given in dimensionless form as

$$\frac{F_\ell}{F_{U,\ell}} = \frac{v_{rel}/v_{y,rel}}{0.17 + 0.83\, v_{rel}/v_{y,rel}} \tag{2.15}$$

in which $F_{U,\ell} = \gamma DHLN_q$ is the ultimate force (L: 'length factor'; $N_q = N_q(H/D\,, \varphi)$: 'force factor') and $v_{y,rel}$ denotes the yield relative displacement. Test results indicated a strong variation for $v_{y,rel}$ with soil density, ranging from $0.13H$ for loose, to $0.08H$ for medium-dense and $0.03H$ for dense soil.

Selvadurai (1985) calculated the transverse vertical elastic SPI stiffness as $K_v = 1.3G/(1-\nu)$. St John & Zahrah (1987) determined an elastic foundation modulus for axial SPI by approximately solving Kelvin's problem for a sinusoidal load with wavelength λ as

$$K_a = \frac{16\pi}{\lambda}\frac{(1-\nu)}{(3-4\nu)}GD \tag{2.16}$$

The same expression is applicable to the transverse horizontal direction. In the same fashion, but this time manipulating the solution to Flamant's problem, they arrived at an estimate for the elastic transverse vertical foundation modulus

$$K_v = \frac{2\pi}{\lambda}\frac{GD}{(1-\nu)} \tag{2.17}$$

To determine an appropriate axial spring constant, El Hmadi & O'Rourke (1988) combined theoretical considerations with previous experimental data and calculated upper and lower bounds as

$$1.57G \leq K_a \leq 1.70G \tag{2.18}$$

This range incorporates the effect of strain-dependent soil shear moduli. Another interesting finding of this study was that the inertial axial force developed in the

pipeline was over two orders of magnitude smaller than the soil resistance. O'Rourke & Hmadi (1988) considered the classical Coulomb friction law to calculate an averaged measure of peak resistance per unit length that develops due to friction at the soil-pipe interface under relative axial motion as the product of the hydrostatic pressure of the soil at the pipe centreline and μ

$$R_a = \mu\gamma' H \left(\frac{1+k_0}{2}\right)\pi D \tag{2.19}$$

where k_0 is the coefficient of lateral earth pressure. This solution applies to uniform soil conditions and is approximate in a theoretical sense. Moreover, some experiments have shown that it generally underpredicts the actual axial resistance (Karimian, 2006; Sheil *et al.*, 2018). Further, Matsubara & Masaru (2000) derived the axial elastic SPI stiffness using the theory of elasticity as $K_a = 2\pi G/\log r$, where r is defined as the ratio of an imaginary outer radius, at which displacements vanish, to R.

In an experimental study, Hsu et al. (2001) investigated the response of pipes in loose sand subjected to oblique-horizontal displacements. A large-scale test was carried out involving various pipe specimens and cover depths, wherein the pipe axis was successively rotated in the horizontal plane. Results showed that the peak soil restraints in the oblique configuration can be determined simply by

$$R_{a,oblique} = R_a \cos a \tag{2.20}$$

$$R_{\ell,oblique} = R_\ell \sin a \tag{2.21}$$

where a is the inclination angle between the orientation of the pipe axis and the direction of movement.

More recently, Sarvanis et al. (2017) reported full-scale, low-rate axial pull-out tests of steel pipes buried in sand. They developed the following functional form for the evolution of the axial resistance with relative axial displacement to capture observed behaviours in the tests, namely an increment in normal contact stress $\Delta\sigma'$

developing due to confined shear conditions in dilative sand, and a post-peak decay of axial resistance to a residual value

$$t(u_{rel}) = \begin{cases} \tan(\delta\varphi_{peak}) \left[\frac{\sigma'_v + \sigma'_h}{2} + \Delta\sigma'_{peak}\right] \frac{u_{rel}}{u_{rel}^{crit}} \pi D, & u \leq u_{rel}^{crit} \\ \mu(u'_{rel}) \left[\frac{\sigma'_v + \sigma'_h}{2} + \Delta\sigma'(u'_{rel})\right] \pi D, & u > u_{rel}^{crit} \end{cases} \tag{2.22}$$

in which $\delta =$ the interface strength reduction factor, $u_{rel}^{crit} =$ the relative soil-pipe displacement at peak axial resistance, $\varphi_{peak} =$ the peak friction angle of sand, $\mu(u'_{rel})$ and $\Delta\sigma'(u'_{rel})$ are exponential decay functions in terms of peak and residual soil parameters (not given here).

Sheil et al. (2018) conducted full-scale cyclic axial pull-out tests on a steel pipe embedded in two different sands for different cover depths. It was observed that redistribution of the initial contact stresses occurs as the pipe is cyclically pulled; the axial SPI resistance in loose sands tended to increase with the number of loading cycles, while the opposite was seen in dense damp backfills. An improved expression for cyclic axial resistance was proposed to address some of the limitations of Eq. (2.19) as

$$R_a = \mu\sigma'_N \beta\pi D + \mu w' \tag{2.23}$$

where $\sigma'_N =$ normal contact stress measured at the pipe crown, $w' =$ pipe self-weight, and $\beta =$ a calibration parameter estimated to fall in the range $0.2 \sim 0.6$.

Finite-element modelling

Numerical procedures for the analysis of engineering problems are rapidly gaining ground in recent years both in practice and research. Problems of virtually unlimited complexity, where analytical solutions do not exist or are cumbersome to use, can be effectively treated by numerical methods. Of all numerical methods of analysis available today, the finite-element method (FEM) has seen the widest acceptance in structural mechanics due to its versatility. In FEM, the continuum is subdivided (*discretised*) into smaller parts (*elements*) that are assigned individual constitutive behaviours and shape functions that approximate the spatial distribution

of the field variable (displacement) in the element; this strategy allows for modelling irregular geometries, material inhomogeneities, and localised response. Consequently, the set of partial differential equations describing the boundary value problem is replaced by a simpler set of either algebraic (for static loads) or ordinary differential equations in time (for transient loads); the latter are typically solved by a finite-difference scheme.

The FEM is especially powerful in handling problems of mechanical contact between deformable bodies. These problems involve boundary nonlinearities and discontinuities in addition to other potential nonlinearities, hence they bring in further computational complexity. Nonetheless, the FEM remains attractive for this class of problems in that, at model definition level, contact behaviour can be specified relatively easily and in a more intuitive way, as opposed to using equivalent springs and dashpots. Moreover, in most cases, directional coupling of contact behaviours is enforced automatically. **Figure 2-7** illustrates an example finite-element mesh for a common seismic soil-structure interaction problem where the applied load arises from propagation of seismic waves through the soil. It can be seen that three groups of finite elements are used to represent the complete dynamic soil-foundation system: soil elements, foundation elements, and interface elements. In a general 3-D SPI problem, the soil is modelled as a solid, the pipeline as a shell, and their interaction can be traced either by surface-based contact formulations or by contact elements.

There is a variety of commercial and non-commercial codes for finite-element analysis of structural systems available today, such as ABAQUS, ANSYS, LS-DYNA, MSC Nastran, Opensees to name a few, all of which are able to address efficiently a broad range of contact problems, including dynamic SPI. In this spirit, a large number of studies have explored the behaviour of buried steel pipelines under PGD effects using the FEM; a non-exhaustive list of references is provided here.

In a series of papers (Vazouras, Karamanos and Dakoulas, 2010, 2012; Vazouras, Dakoulas and Karamanos, 2015), 3-D continuum modelling was employed in ABAQUS to analyse the static axial and bending strains in buried steel pipelines crossing active

strike-slip faults under angle. Coupled SPI was modelled rigorously by virtue of contact pairs at the soil-pipe interface, while pipe continuity was also considered by assigning analytically derived nonlinear springs at the pipe ends. Soil plasticity was modelled using a Mohr-Coulomb constitutive law. The same strategy was followed by Daiyan et al. (2011) to validate centrifuge tests; their findings indicate that SPI can be strongly coupled under oblique loads. Vazouras & Karamanos (2017) modified their original numerical models to study the mechanical performance of pipe bends; their outcomes substantiated that bends are pipeline components of increased flexibility. Chaloulos et al. (2015) and Kouretzis et al. (2013) developed 2-D plane-strain SPI models to investigate the trench effects on the response of a pipe subject to PGD. Trifonov & Cherniy (2012) contributed a plane-stress plasticity model that accounts for internal pressure and temperature variation, to predict the stress and strain distributions over the section due to fault displacement. Tsatsis et al. (2018) also used 3-D continuum elements in ABAQUS to simulate the damage characteristics of a pipeline subject to slope sliding; the developed SPI models were validated against previous experimental results. Similar advanced models were developed by Sarvanis et al. (2017) to simulate soil-pipe pull-out and push tests, as well as a large-scale PGD test.

2.4 Spatially variable earthquake ground motion

Spatial variability in earthquake ground motion (SVEGM) connotes the differences in frequency content, amplitude and phase angle of seismic signals recorded from station to station on local scale. The effect was first studied in depth in the 1980s, when researchers started analysing the ample accelerogram data obtained from densely installed strong motion recording arrays, in particular the SMART-1 array in Taiwan (Loh, Penzien and Tsai, 1982; Abrahamson *et al.*, 1987). SVEGM as a process has stochastic character, in that it is not predictable with absolute certainty due to the randomness involved in a multitude of complex generating mechanisms. These mechanisms are known to be

a. the transmission of the waves at finite velocity (wave passage effect), which results in different arrival times at different recording stations at the ground surface;

b. the gradual reduction in the coherency of the waves as a result of (i) successive scattering, reflections and refractions occurring along their path through the inhomogeneous earth strata (ray-path effect), and (ii) the spatially irregular superposition of waves originating from different locations on an extended seismic source (extended source effect); (i) and (ii) are collectively termed the incoherence effect;

c. the different local soil conditions at remote stations that modify the amplitude and frequency content of the incoming waves (local site effects);

d. the attenuation of seismic waves along their path resulting from the gradual dissipation of wave energy across the medium;

e. the relative flexibility of the soil-foundation system, which can filter certain frequencies of the oncoming waves (Sextos, Pitilakis and Kappos, 2003).

Figure 2-8 displays schematically three of the above mechanisms, namely (a) to (c), which are believed to have an appreciable impact on buried pipelines. Mechanism (d) is in most practical cases not significant, whereas mechanism (e) can be influential only in soil-foundation problems.

The mathematical description of SVEGM is based on modelling the earthquake ground motion (acceleration) as a random process in time, $\ddot{u}(t)$. A number of statistical measures have been established to reflect the similarity between the motions at different recording stations (Zerva, 2009). The preferred descriptor of SVEGM is the complex-valued coherency function, expressed in the frequency domain. It is defined for the random processes $\ddot{u}_j(t)$ and $\ddot{u}_k(t)$ representing the seismic ground motions at recording stations j and k respectively. Assuming stationarity and ergodicity, coherency is expressed as

$$\gamma_{jk}(\omega) = \frac{S_{jk}(\omega)}{\sqrt{S_{jj}(\omega)S_{kk}(\omega)}} \tag{2.24}$$

where ω is the circular frequency, $S_{jk}(\omega)$ is the smoothed cross-spectral density between motions at j and k, and $S_{jj}(\omega)$ is the smoothed power spectral density at j. The (sample) cross-spectral density is the Fourier transform of the (sample) cross-covariance function $\widehat{R}_{jk}(\tau)$

$$\hat{S}_{jk}(\omega) = \frac{1}{2\pi} \int_{-\infty}^{+\infty} \widehat{R}_{jk}(\tau) e^{-i\omega\tau} \mathrm{d}\tau \tag{2.25}$$

$$\widehat{R}_{jk}(\tau) = \frac{1}{T} \int_{0}^{T-|\tau|} \ddot{u}_j(t)\ddot{u}_k(t+\tau) \mathrm{d}t \tag{2.26}$$

A more convenient expression for coherency that distinguishes between the incoherence and the wave passage effect is obtained by use of Euler's formula as

$$\gamma_{jk}(l,\omega) = \left|\gamma_{jk}(l,\omega)\right| e^{i\vartheta_{jk}(l,\omega)} \tag{2.27}$$

where the independent variable l is introduced to represent the station-to-station distance, $\vartheta_{jk}(\omega) = \tan^{-1}[\Re\{S_{jk}(\omega)\}/\Im\{S_{jk}(\omega)\}]$. The magnitude term $\left|\gamma_{jk}(l,\omega)\right| \in [0,1]$ is called lagged coherency and represents the phase variability as a result only of the incoherence effect. The term $\vartheta_{jk}(\omega)$ is called the phase spectrum and describes differences in phase attributed to the wave passage effect.

Random vibration analysis and deterministic time-history analysis using recorded or artificial SVEGM as input excitations are the basic tools to analyse the impact of the phenomenon on the response of structures. Geographically extended structures like bridges and dams are most sensitive to this type of excitation and have been investigated by analytical (Deodatis and Shinozuka, 1989) and numerical (Sextos and Kappos, 2009) means. Other methods of analysis have also been reported,

including field (Sextos *et al.*, 2015) and experimental (Norman *et al.*, 2006; Saiidi, Vosooghi and Nelson, 2013).

It is apparent that SVEGM is very relevant to buried pipeline systems. Considering the spatial scale of the structure, the input seismic excitation is in reality expected to be spatially variable and should be modelled as such. Research in this field has been devoted for the most part to the study of the effects of wave passage and spatial incoherence – local site effects have received less attention comparatively. A summary of past works is provided below.

2.4.1 Wave passage effect

SVEGM arising from the asynchronous arrival of a plane wave front at distant points along a buried pipeline has been addressed in many studies. The effect is reflected in Eqs. (2.6) and (2.7) in the phase velocity, $c = V/\sin\theta$, where V is the characteristic propagation velocity in the medium and θ the angle of incidence (see **Figure 2-8**a); apparently, for $\theta = 0$, $c \to \infty$, corresponding to a vertically propagating wave front. The standard modelling approach assumes a constant wave shape and uses a range of incidence angles to calculate the altered ground motions due to phase difference at supports along the pipeline. Indicatively, Shinozuka & Koike (1979), Hindy & Novak (1979), St John & Zahrah (1987), O'Rourke & Hmadi (1988), Mavridis & Pitilakis (1996), and Kouretzis et al. (2006) have all modelled the wave passage effect considering different types of elastic waves; details of these studies can be found throughout this chapter.

2.4.2 Incoherence effect

Buried pipelines subject to spatially incoherent ground motion have also been a topic of interest. Shinozuka et al. (1983) simulated the ground axial strain induced by horizontally propagating Rayleigh waves in a layered site as a Gaussian stationary process. The expected peak ground strain was evaluated by modifying Eq. (2.6), as a function of earthquake magnitude M, epicentral distance R and local soil conditions;

for instance, for $M = 8$, $R = 20$ km and soft soil, the expected peak ground strain was ~0.15%. It was concluded that soft soils amplify ground strain more strongly, and also that ground strain attenuates with distance from source, but at a slower rate than acceleration.

To examine the axial and transverse response of continuous buried pipelines to differential ground motion, Zerva et al. (1985) carried out random vibration analysis of BDWF models using as input ground motion data recorded at the SMART-1 array. By comparing the responses for partially and perfectly coherent input motions, a close match was found for the displacements, most likely because the same rigid-body mode was excited; however, partially correlated motions produced higher stresses in the pipe. It was also observed that axial stresses become dominant as the slenderness of the pipe increases, while bending stresses become sizable when the pipe diameter is large.

Outcomes from a similar work (Zerva, 1993) revealed that axial strains dominate over bending strains in continuous, large-diameter pipelines. It was also shown that the calculated pipeline response is sensitive to the lagged coherency parameters. The maximum calculated axial strains in this study were at least two orders of magnitude smaller than the typical yield strain of steel ($0.2\% \backsim 0.5\%$). Moreover, Zerva (1994), in studying the response of various lifeline structures, including buried pipelines, to spatially incoherent excitations, observed that pipe axial strains attain peaks when the motions are completely incoherent, i.e. the differential displacements at the input stations are maximised.

2.4.3 Local site effects

Local site effects on ground motions result from gradients in soil properties (medium inhomogeneity), features of irregular topography (e.g., hills, ridges, canyons and cut-and-fill slopes), and special subsurface geomorphic conditions, such as a soft surficial sediment bounded by stiff soil or rock (basin). The presence of any of the above along the route of a buried pipeline, combined with appropriately directed seismic excitation, can profoundly amplify the ground motion, alter its frequency

characteristics and spatial profiles, prolong its duration, and induce substantial ground strains and curvatures (Zhang and Papageorgiou, 1996; Assimaki, Kausel and Gazetas, 2005; Psarropoulos *et al.*, 2007; Scandella and Paolucci, 2010), which in turn can cause pipeline deformation.

To illustrate this further, two idealized site scenarios are sketched in **Figure 2-9**: (a) a site consisting of two horizontally adjacent soil layers of different characteristic wave velocities; and (b) a soft alluvial basin of trapezoidal shape. Both sites are swept by vertically propagating shear waves of varying polarization. In scenario (a), polarization in the x-direction (SV-waves) is expected to induce axial strain concentrations in the pipeline near the soil interface, while some uplifting motion will cause bending in the xz plane. In this situation, axial shell buckling, beam buckling and section ovalisation are all possible failures. Polarization in the transverse y direction causes only bending in the xy plane, with the largest curvatures expected near the soil interface. The flexural state of deformation in the pipe can cause ovalisation and bending shell buckling. The stress state is similar in scenario (b), the main difference being that peak strains and curvatures are located near the basin edges, as indicated in the figure. One immediately realizes that if the S-waves impinge under arbitrary angle, or if their polarisation is not aligned with an orthogonal axis, multi-directional ground motions will be simultaneously applied on the pipeline, thus the resulting deformation will be more complex.

The impact of SVEGM due to local site conditions on buried pipelines was first explored by Hindy & Novak (1979), who used a matrix-based approach to express the dynamic equilibrium of a linearly elastic SPI system subject to external support excitations. Two sets of soil conditions were examined, a homogeneous soil and a soil consisting of two different layers separated by a vertical plane, just as shown in **Figure 2-9**a. Earthquake excitation was assumed to be in the form of P and S-waves propagating along the pipe, and P-waves propagating vertically. In the inhomogeneous acase, large stress concentrations resulted close to the vertical boundary, with peaks

exceeding those predicted for the homogeneous case, with or without SPI considered (**Figure 2-10**).

Other early contributions in this area are from Nishio and co-workers who conducted laboratory tests of buried pipelines in valley and cut-and-fill settings subject to horizontal base excitation (Nishio, Ukaji and Tsukamoto, 1980; Nishio, Ishita and Tsukamoto, 1983). Analytical methods have also been used to study the deformation of buried pipelines laid through dipping soil layers (Akiyoshi and Fuchida, 1988), cut-and-fill embankments (Ando, Sato and Takagi, 1992), riverbeds (Liang, 1995b) and multiple soil media (Liang, 1995a). In all cases, it was observed that axial strains in a pipeline laid through inhomogeneous sites are considerably larger than in homogeneous ground.

A recent work (Papadopoulos *et al.*, 2017) addressed the combined effect of wave passage and local soil conditions on a gas pipeline crossing longitudinally a deep basin using the FEM; it was concluded that local site effects contribute the most to the induced axial strains and that these strains can exceed those obtained from Eq. (2.6) for zero interaction. Finally, Yu et al. (2018) derived a simplified closed-form solution for the elastic bending response of a pipeline due to SH-waves in ground with a sharp lateral change in stiffness.

2.5 Pipeline response analysis strategies

The choice of a suitable strategy for analysis of the pipeline response to strong ground shaking depends largely on the response parameter and damage mechanism of interest, as well as the sought degree of accuracy. In its entirety, the physical problem can be highly complex and uncertain depending on the context. It involves wave propagation in semi-infinite, spatially inhomogeneous media with uncertain dynamic properties, shell behaviour for the pipeline, geometric nonlinearities, material plasticity, nonlinear surface contact between deformable bodies, large dimensions, and time-dependent response. All the above complexities render a complete 3-D numerical

analysis not only computationally prohibitive, but also hardly justified in view of the involved uncertainties – simplification of the problem to within acceptable accuracy levels is therefore imperative. Typically, simplifying steps are taken in representing the two constituents of the physical system: (i) the pipeline, and (ii) the supporting soil and SPI. Modelling strategies for item (ii) have already been exposed in Section 2.3.

Regarding item (i), resort to the classical beam theory is preferred when one seeks a gross estimate of the expected seismic demand of the pipeline to compare with the respective code-prescribed capacity. Intrinsic in this approach is the assumption that axial and bending deformations are uncoupled, while the—important in most cases—hoop stress is neglected. Prediction of shell buckling modes or ovalisation mechanisms is not possible either; beam buckling can be captured, but only with 2nd-order beam formulations. Not surprisingly, the use of the classical beam theory to model buried pipelines has been widespread in research for its simplicity.

On the other hand, to check for the possibility of shell buckling or cross-section ovalisation and account for hoop stresses due to internal and external pressures, use of one of the available nonlinear shell theories is essential[1]. Hybrid approaches have also been reported, wherein a critical pipe segment is modelled as a cylindrical shell and the remaining pipe as a beam (Hamada, O'Rourke and Yoshizaki, 2000; Karamitros et al., 2007). Typically, stress analysis of shells is undertaken by FEM software.

All combinations between modelling variants of items (i) and (ii) have been reported in the literature.

2.5.1 Pipeline as a beam

A few notable works treating the pipeline as a beam are cited here. Sakurai & Takanashi (1969) were pioneers in studying the dynamic stresses in a buried pipeline by field experiments during the Matsushiro earthquake sequence. They observed that

[1] Exception to this is the non-linear tube finite element formulated by Karamanos and Tassoulas (1996) and other 1-D continua models, which can capture ovalisation, local buckling and plasticity effects due to multiple external loads.

pipe axial strains match ground strains when the earthquake intensity is mild and confirmed this through a solution for Eq. (2.8), ignoring the damping terms.

Shinozuka and Koike (1979) considered a BDWF model of a pipeline buried in homogeneous soil and derived dynamic factors to convert from the free-field axial strain ε_g to the maximum pipe axial strain ε_p assuming a sinusoidal P- or R-wave to propagate parallel to the pipeline. Factors were obtained for no-slippage (Eq. (2.28)) and partial slippage conditions (Eq (2.29)) as

$$\beta_0 = \frac{1}{1 + \left(\frac{2\pi}{\lambda}\right)^2 \frac{EA}{K_a} - \left(\frac{\omega}{\omega_o}\right)^2 - \left(\frac{\omega}{\hat{\omega}}\right)^2} \tag{2.28}$$

$$\beta_y = q\left(\frac{\gamma_{cr}}{\gamma_0}\right)\beta_0 \tag{2.29}$$

where $\omega_o = \sqrt{K_a/\rho A}$; $\hat{\omega} = 2\pi/\lambda\sqrt{E/\rho}$; $\gamma_0 \propto \varepsilon_g$ is the maximum free-field shear strain at the interface; $\gamma_{cr} = 10^{-3}$ is assumed the critical shear strain at slippage; and $1 \leq q \leq \pi/2$. As can be seen, the factor for partial slippage β_y is inversely proportional to ε_g. Comparison between the dynamic and respective static (ignoring the ω terms) conversion factors revealed a minor contribution of pipeline inertia.

By solving Eqs. (2.10) and (2.11) for an obliquely incident sinusoidal shear wave, St John and Zahrah (1987) derived similar quasi-static reduction factors to evaluate the restoring forces of an SPI system directly from the corresponding zero-interaction system. O'Rourke and Hmadi (1988), considering the frictional behaviour to be of elastic-perfectly plastic form, proposed a procedure for determining a pipeline design strain due to propagating R-waves, based on the use of dispersion curves and a calculated interface 'frictional' strain.

Mavridis and Pitilakis (1996) solved Eqs. (2.8)-(2.9) in the frequency domain assuming complex harmonic excitations and homogeneous ground. Using separation of variables to express the complex displacement, e.g. as $u(x,t) = U(x)e^{i\omega t}$ for the axial

component, they arrived at pipe-to-soil displacement ratios in the axial (Eq. (2.30)) and lateral (Eq. (2.31)) direction

$$R_a = \frac{S_a}{S_a - m\omega^2 + E_p A(\omega/c)^2} \tag{2.30}$$

$$R_\ell = \frac{S_\ell}{S_\ell - m\omega^2 + E_p I(\omega/c)^4} \tag{2.31}$$

in which $S_a = K_a + i\omega C_a$ and $S_\ell = K_\ell + i\omega C_\ell$ are the complex-valued impedances of the SPI system in the axial and lateral direction, respectively. It was found that when the wave passage is the only source of pipe deformation, analysis for horizontal shaking is critical – in this case, SPI effects can be critical.

2.5.2 Pipeline as a shell

From the perspective of structural stability, Chen et al. (1980) presented the first study on quasi-static elastic buckling of pipes buried in uniform ground. They used Donnell's and Flügge's shell stability equations to describe the pipe as a long, simply supported and radially restrained shell. The critical axial stress resultant from Donnell's equations was obtained as

$$N_{cr} = \sigma_{cr} t = \left[\frac{1 + k_r R^2/E_p t}{3(1 - {\nu_p}^2)}\right]^{1/2} \frac{E_p t^2}{R} \tag{2.32}$$

in which k_r is the radial elastic stiffness of the medium. It was found that the presence of the confining medium causes a substantial increase in P_{cr}.

Lee et al. (1984) used an elastic-plastic cylindrical shell formulation based on the simple flow plasticity theory to check the stability of the dynamic equilibrium of a pressurised pipe shell buried in an infinite homogeneous elastic medium. SPI was only considered in the lateral mode assuming a radial soil restraint as in Chen et al. (1980). It was shown that the critical axisymmetric buckling stress and strain computed for dynamic conditions do not differ much from those for static conditions. In a seminal

effort, Wong et al. (1987) considered theoretically the 3-D elastic response of a long pipeline shell buried in homogeneous elastic half-space to obliquely incident body or surface waves. Using eigenfunction expansions of wave potentials, a solution to the equations of elastodynamics was presented that gives the coupled motion of pipeline and soil.

In the work by Yun and Kyriakides referenced earlier, Sander's nonlinear thin-shell theory for infinitesimal membrane strains and finite small rotations was deployed to describe shell deformation, and incremental plasticity formulations to describe material response; both perfect and imperfect shells were examined. SPI was assumed as in Lee et al. (1984) but this time considering nonlinear elastic ground springs, whose force-deformation relationship was calculated by solving the problem of the uniform expansion of a circular cavity in infinite ground. Their findings suggest among others that bifurcation and limit axial loads decrease with increasing imperfection amplitudes, and that they are slightly higher with soil confinement than without it (**Figure 2-11**); the corresponding strains remain relatively unchanged.

Later, Kouretzis et al. (2006) combined the zero-interaction model with linear thin shell equations to derive exact distributions of all strain components over the pipe section due to plane harmonic shear waves impinging at an arbitrary angle; this approach was extended in Kouretzis et al. (2011) to cover the case of Rayleigh waves. These analyses showed that design of continuous spiral-welded buried pipes should be on the basis of the maximum principal and equivalent strain rather than the direct normal components, while that of segmented or butt-welded pipes should be based on axial strain due to Rayleigh waves. Hatzigeorgiou and Beskos (2010) developed the FEM code SINUS to perform direct analysis of seismic SSI effects in 3-D rock-tunnel systems, considering material inelasticity through the continuum theory of elastic damage. Focusing on the seismic performance of pipe bends, Saberi et al. (2013) employed ABAQUS to develop a hybrid 3-D shell-beam pipeline model where the bent part was represented by shell elements while the straight parts by beam elements. SPI was taken into account using the ALA spring models (presented in Subsection 2.6.2).

Performance was evaluated by nonlinear response history analyses using three-directional multi-support excitation input with phase difference.

2.5.3 Discussion

In view of the above survey, there are certain key considerations to be made first before we establish appropriate theoretical and numerical SPI models and gain confidence in their predictive power for situations that govern seismic design of buried gas pipelines.

Geological and geomorphological conditions

A major consideration is the overall geological and geomorphological conditions in the region of interest. Crucial to the choice of a suitable analysis methodology is the knowledge of the soil profiles traversed by the pipeline. To this end, geotechnical characterisation surveys can prove useful in identifying the real soil properties in a site. Where strong ground heterogeneities or topographic features, such as basins, hill crests and toes and cut-and-fill embankments, are present along the pipeline route, more elaborate models are necessary to accurately evaluate the details of the system response, more so where soil nonlinearity needs to be considered. 2-D and 3-D site response analysis can be effective in determining the differential surface free-field motion in such critical instances. The sub-structuring Domain-Reduction method (Bielak *et al.*, 2003) is also an option for special cases where large-scale simulations containing the seismic source, path, and local site effects, are desired. For sites characterized by relatively uniform properties, sophisticated modelling strategies, as the above, are rather unnecessary.

Distance to earthquake source

A second consideration is the proximity of the region of interest to the earthquake source, which controls the types of the arriving seismic waves and their frequency content. A pipeline passing near the epicentre of an earthquake is more likely to be stricken by high-amplitude, high-frequency, vertically propagating body waves. Pipeline stressing here would be mainly due to two causes: (i) the relative movement

between pipeline and soil, in which case a plane-strain SPI model should be sufficient to evaluate the lateral pipe response; (ii) local site effects, in which case advanced response models are a necessity as noted before.

In a different situation, a buried pipeline far away from the earthquake source is exposed to nearly-vertically propagating body waves and, additionally, high-amplitude, lower-frequency surface waves travelling along the earth surface. It has been observed that it is the latter waves that govern pipeline deformation (O'Rourke and Hmadi, 1988). The effects of the wave passage need to be modelled in this case. The remarks made here imply that the selection of input ground motions to represent a design earthquake scenario for the purposes of an SPI analysis should consider the distance of the site from the earthquake source.

Trench soil and external pipe walls

The condition of the trench soil and of the external pipe walls also deserves special attention, since these are two factors that determine the soil-pipe contact behaviour. In common pipeline trenching practice, the excavated trench soil is backfilled after laying in the pipeline, and compaction may or may not follow. The initial contact state between pipe and soil depends largely on the in-situ soil properties and the quality of compaction. Sometimes, compaction can lead to $k_0 > 1$; in turn, the frictional resistance, t_u, being dependent on soil confinement, increases, which permits the development of larger axial forces in the pipe. Further, it has been found that the uplift resistance of the pipeline depends strongly on the trench soil properties (Chaloulos, Bouckovalas and Karamitros, 2017), which is of interest for analysis and design for beam buckling.

The frictional contact behaviour is controlled in part by the coefficient of interface friction, μ. Some typical values for μ under different external pipe wall conditions are found in Brumund and Leonards (1973), where it is concluded that $0.5 \tan\varphi \leq \mu \leq \tan\varphi$, with φ being the angle of shearing resistance of the trench soil; for instance, polishing the outer pipe surface reduces μ to the lower limit. These values may be taken as a reference, but a case-by-case investigation is advisable in practice

as μ is difficult to determine reliably without laboratory testing (e.g., direct shear tests). Even if μ is known from tests, it would likely be unrepresentative of the prevailing conditions along the entire pipeline. The effect of steel scour on SPI has also been studied (Rajani and Tesfamariam 2004) and it was found that axial interaction depends on the unsupported pipeline length caused by scour.

Internal pressure

Another key factor in structural analysis of gas pipelines is the level of pressurisation. Pipelines belonging to the high-pressure transmission grid develop large initial circumferential tensile stresses ($30\% \sim 40\%$ of σ_y) as a result of the internal pressure. This can have mixed effects on the overall seismic performance of the pipeline.

In constraint-free circular cylindrical shells under uniform axial compression, the presence of internal pressure lowers the whole inelastic branch of the response, this reduction being sharper for higher pressures. Consequently, yield, bifurcation and collapse loads are reduced compared to the unpressurised case (Paquette and Kyriakides, 2006). For shells under axial compression, pressure also stiffens the pre-yield response. In buried pipelines, however, Lee et al. (1984) report that pressurization has the opposite effect, namely that it raises the critical stresses. It remains to be clarified in which situations consideration of internal pressure in analysis leads to conservative or unconservative results.

Geometric imperfections of the pipe walls

Wall imperfections pose well-known implications on the stability of shells. Cylindrical shells with high R/t_w are highly imperfection-sensitive structures, a behaviour manifested by the severe discrepancies between the elastic buckling loads from theoretical solutions and experiments (Weingarten, Seide and Peterson, 1968). This sensitivity is also evident in cylindrical shells with lower R/t_w, where buckling is expected beyond material yield.

Buried pipelines may be exposed to two types of geometric imperfections: 'load' imperfections caused by the varying soil pressures acting on the pipeline walls; and deviations of the wall geometry from the perfect state, induced by such operations as

manufacturing (residual stresses caused by uneven cooling of different material patches after the hot-rolling process), transportation, girth welding and laying. For instance, a well-known pipe manufacturer quotes in its API-5L X65 line pipe stock specifications a manufacturing tolerance for t_w of +15%, −12.5% (ArcelorMittal, 2013).

Traditionally, buckling analysis of shells considering imperfect geometry is facilitated by linearly superimposing eigenmode shapes on the perfect geometry. Other approaches include load perturbation and explicit definition of custom, stress-free imperfections (e.g. Castro et al. 2014). The shape and amplitude of imperfections adopted in shell buckling analysis are known to affect to a great degree the critical response parameters of the shell. Therefore, caution should be exercised during buckling analysis in establishing representative—but not overly conservative—imperfection patterns. It is also of interest to examine the combined effect of different imperfection patterns, internal pressures and soil confinement levels on the buckling response parameters of buried gas pipelines.

2.6 Code provisions for earthquake-resistant design of buried pipelines

In this section, the current standards of practice for design of underground pipelines to earthquakes are reviewed in order to identify key provisions and recommendations and evaluate how they align with the current state of knowledge of the field. The main normative documents reviewed are Eurocode 8, the American Lifeline Alliance guideline, and the Japan Gas Association recommendations.

2.6.1 Eurocode 8 (2006)

Part 4 of Eurocode 8 (European Committee for Standardization, 2006) provides a broad framework for the seismic design of pipelines among other utility infrastructure. The design philosophy following from previous Eurocodes is based on the Ultimate and Serviceability Limit States (ULS and SLS). ULS relates to a state of

structural collapse; design to ULS should also consider safety hazards incidental to an earthquake, such as explosion and fire in the event of a pipe breakage. For SLS, a two-level hierarchy is prescribed: the lower level requires the system to remain fully operational and leak-proof, whilst the higher one permits a certain level of damage to be sustained, without total loss of the supplying capacity.

The Eurocode makes a distinction between PGD and wave propagation effects. It recognises that pipe inertial forces are negligible in comparison with the restoring forces caused by ground deformation, allowing the use of a simpler analysis. Annex B recommends the use of the zero-interaction model for the determination of pipe axial and bending strains, provided that the soil is stable and homogeneous. It is also noted that pipelines buried in dense soil are allowed to be designed solely for the effects of wave propagation. No further guidance on SVEGM is given in relation to pipelines. However, in the section dealing with above-ground pipelines, it is suggested that SVEGM should be accounted for if the pipeline segment analysed is longer than 600 m or if the foundation ground exhibits longitudinal non-uniformities. One might presume this design rule can be extended to buried pipelines too.

For steel-welded pipelines, the Eurocode requires that the available ductility of the material is not exceeded and buckling is prevented by design. For the first requirement, it sets the maximum allowable strain at 3%; for the second, the maximum allowable compressive strain is proposed to be the smaller between 1% and $0.2 \times t_w/R$.

2.6.2 American Lifelines Alliance (2001)

The report published by ALA (American Society of Civil Engineers, 2001) emphasizes merely the same points as Eurocode 8. Notably, it recommends a set of relationships to describe the constitutive behaviour of Winkler-type nonlinear springs in four principal directions of SPI, i.e. axial, lateral, vertical uplift and vertical bearing. The nonlinear form of SPI is idealized as elastic-perfectly plastic, hence each spring model can be defined by two parameters, the maximum spring force and the mobilising (yield) relative displacement between the spring nodes (**Figure 2-12**). The

relationships, widely used in design practice, are valid for uniform soil and are listed in **Table 2-3**.

ALA allows to ignore flexural deformation of the pipe on the grounds that it is negligible compared to the axial response. Moreover, ground deformation can be assumed to result solely from surface waves for conservatism; it is postulated that ground axial strains will rarely exceed 0.3%. For PGD-induced loads, the guideline recommends 3-D nonlinear pseudo-static finite-element analysis considering SPI effects and inelastic material properties.

In terms of performance acceptance criteria, ALA prescribes a maximum allowable tensile strain of 0.5%, while the allowable strain in compression is adopted from Gresnigt (1986) as

$$\varepsilon_{cr} = 0.375\frac{t_w}{D'} - 0.0025 + 3000\left(\frac{PD}{2E_p t_w}\right)^2 \tag{2.33}$$

where $D' = D/[1-3(\Delta D/D)]$, with $\Delta D/D =$ diameter flattening. Additionally, the document specifies a maximum allowable value of $0.9\sigma_y$ for the bending stress in the pipe. These limits are in effect on the condition that strict welding procedures have been followed during construction.

2.6.3 Japan Gas Association (2000)

The "Recommended practice for earthquake-resistant design of gas pipelines" by Japan Gas Association (2000) features a simplified methodology for design of high-pressure transmission pipelines to 'Level 2' seismic motions. Level 2 is defined as the performance level corresponding to a deformed pipe, but free from content leakage. The design flow comprises two phases. In the first phase, the design seismic motion at the site of interest is determined, considering existence of active faults along the pipeline route, which may require fault analysis. In the second phase, a peak axial ground strain is estimated with the use of linear vibration parameters and the spectral velocity of the site, and from this the peak pipe axial strain is then obtained using the

quasi-static equivalent of the conversion factor given by Eq. (2.28) and a coefficient to account for sliding. The calculated pipe strain is checked against a maximum allowable strain of 3%.

2.6.4 Other provisions

According to the B31.8 standard of the American Society of Mechanical Engineers (2004), the maximum permissible value for the sum of all longitudinal stresses shall be $0.9\sigma_y$ to prevent buckling or other failure modes. Longitudinal strain is recommended to be kept below 2%.

2.7 Summary of the chapter and conclusions

This chapter dealt with the state-of-the-art and state-of-practice related to the design and response analysis of buried gas pipelines for seismic wave propagation effects. The key aspects of the problem revisited were the dominant damage mechanisms, soil-pipe interaction, spatially variable earthquake ground motion, strategies for pipeline response analysis, and the pertinent code provisions. The main points to be concluded from the above review are the following:

- Contrary to the commonly held view, buried pipelines can experience damage due to travelling seismic waves, a conclusion supported by the ever-increasing field evidence. The most likely—and most destructive—failure is shell buckling and thus design practice should be primarily directed towards the verification of buckling capacity of pipelines. It is not to be overlooked, though, that shell buckling, beam buckling and section ovalisation can affect the pipeline in coupled ways; this combined effect has not been investigated adequately.

- A number of approaches have been developed and applied to model the behaviour of buried pipelines subjected to seismic excitation. Ranging from the zero-interaction model in homogeneous ground to sophisticated FEM techniques

that can capture complex SPI behaviours, the existing models offer varying degrees of accuracy and practicality in use.

- The most commonly used BDWF model, although fairly easy to use, comes with some important deficiencies; the spring-to-spring interaction, as well as the directional coupling of SPI modes, are not normally considered. It is also unable to predict shell instabilities. Shell models of the pipeline bounded by solid continuum models of the ground can overcome these limitations, but they have been used almost exclusively for PGD problems.

- SVEGM is the primary source of distress in a buried pipeline. Research shows that local site conditions is the factor that can generate the heaviest distortion in a buried pipeline. Lateral gradients in the soil properties tend in general to 'attract' larger ground deformations, consequently imparting greater loads to the pipe. In continuation of the work by Hindy and Novak (1979), research needs to focus on identifying other unfavourable site conditions that can lead to critical seismic demands in the pipe.

- To analyse the effect of local site conditions on the ground surface response profile, it is most appropriate to use site-specific response analysis in two or three dimensions. This area of research is now mature and has to offer a range of capable analysis tools able to model soil nonlinearity, pore water pressure generation, wave radiation and other complex behavioural features.

- With regard to instability failures, it remains undetermined what the combined effect of internal pressure, soil confinement, and geometric imperfections is on the critical buckling loads of the pipe. Finite-element modelling using continuum elements, although computationally expensive, is essential to further our understanding into this issue.

- Existing design standards and guidelines do not reflect the latest research findings. The zero-interaction model recommended by the Eurocode is not appropriate in all situations, while the validity of the axial SPI spring model

proposed by the ALA is recently put to question by experiments. Further, little to no direction is provided on how to address cases of SVEGM on pipes, other than those due to the wave passage.

- Although significant effort has been expended to the investigation of the problem at hand for decades, some critical questions have not yet been addressed. For example, what is the effect of soil nonlinearity in the ground motion near the pipeline? What happens when nonlinear soil response occurs specifically in a laterally non-homogeneous site? Are pipe buckling modes more likely to develop in such cases? If yes, what are their characteristics and which parameters govern them? And are the existing code-prescribed performance criteria sufficient for these cases?

- In addition, very limited experimental work has been carried out to investigate the problem at hand. Physical testing under dynamic conditions is required to verify existing analytical outcomes and to increase understanding in areas that are still obscure, as is the pipeline seismic response considering local site effects.

To the above questions and several more, this research aims to provide answers by means of a systematic numerical and experimental methodology that is developed in the next three chapters.

Table 2-1. Database of steel gas transmission pipelines in Europe

ID	Pipeline name	Operator	Operating since	Current status	Capacity (10^9 m^3/year)	Transiting	Type	Total length (km)	Diameter (mm)	Operating pressure (MPa)
1	Trans Adriatic Pipeline	TAP AG	2020	UC	10.0	AL;GR;IT	OS;OB	878	1200	9.5
2	Nord Stream twin line	Nord Stream AG	2011	OP	55.0	DK;FI;RU;SE	OS	1224	1220	
3	Balgzand BactOP Line (BBL pipeline)	BBL Company	2006	OP	19.0	GB;NL	OS;OB	235	914	14
4	InterconnectOR (UK)	InterconnectOR (UK) Limited	1998	OP	20.0	BE;GB	OS	235	1016	15
5	JAGAL	Gascade Gastransport GmbH	1999	OP	24.0	DE	OB	338	1200	
6	Langeled	Gassco AS	2006	OP	25.5	GB;NO	OS	1166	1066	25
7	MIDAL	WINGAS GmbH	1993	OP	12.8	DE		679	1000	
8	MEGAL	Open Grid Europe	1980	OP	22.0	DE		1161	0	8
9	NEL	NEL Gastransport GmbH	2012	OP	20.0	DE		441	1422	10
10	NatiOPal TransmissiOP System (NTS)	NatiOPal Grid plc		OP	0.0	GB		7500	600	8.5
11	NETRA	jordgasTransport GmbH	1993	OP	21.2	DE		341	1200	
12	OPAL	OPAL Gastransport GmbH & Co. KG	2011	OP	36.0	DE	OB	472	1400	10
13	RHG (Rehden-Hamburg-Gasleitung)	Gascade Gastransport GmbH	1994	OP	0.0	DE		132	800	
14	SNIP (Scottish NatiOPal Pipeline)	Premier TransmissiOP Limited (PTL)	1996	OP	0.0	GB	OS	135	610	
15	STEGAL	Gascade Gastransport GmbH	1992	OP	0.0	DE		314	800	
16	South Wales Gas Pipeline	NatiOPal Grid plc	2007	OP	0.0	GB	OB	317	1220	9.4
17	TAG (Trans Austria Gas)	TAG GmbH	1974	OP	47.5	AT		380	1200	

ID	Pipeline name	Operator	Operating since	Current status	Capacity (10^9 m^3/year)	Transiting	Type	Total length (km)	Diameter (mm)	Operating pressure (MPa)
18	Trans Europa Naturgas Pipeline (TENP)	Trans Europa Naturgas Pipeline GmbH & Co. KG	1974	OP	15.5	DE		968	950	
19	Transitgas Pipeline	Transitgas AG	1974	OP	35.0	CH	OB	292	900	6.75
20	WAG (West-Austria-Gasleitung)	Gas COPnect Austria GmbH	1980	OP	0.0	AT		385	800	
21	WEDAL	Gascade Gastransport GmbH	1998	OP	10.0	DE	OB	321	800	
22	Franpipe	Gassco AS	1998	OP	19.6	FR;NO	OS	840	1067	
23	Greenstream pipeline	Agip Gas BV	2004	OP	11.0	IT;LY	OS	520	810	
24	Maghreb–Europe Gas Pipeline (MEG)	Metragaz, SOPatrach, Enagás, Transgas	1996	OP	12.0	DZ;ES;MA;PT	OS;OB	1620	1200	
25	MEDGAZ	MEDGAZ	2011	OP	8.0	DZ;ES	OS	210	610	
26	Trans-Mediterranean Pipeline (TransMed)	SOPatrach, Sergaz, TMPC	1983	OP	30.2	DZ;IT;TN	OS;OB	2475	1220	
27	South Caucasus Pipeline (SCP)	BP	2006	OP	25.0	AZ;GE;TR	OB	692	1067	
28	TANAP	SOCAR	2018	OP	16.0	TR	OB	1850		
29	Central Area TransmissiOP System (CATS)	CATS Management Limited	1993	OP	17.5	GB	OS	404	914	
30	Europipe I	Gassco AS	1995	OP	16.8	DE;NO	OS	620	1016	
31	Europipe II	Gassco AS	1999	OP	25.9	DE;NO	OS;OB	658	1067	
32	FLAGS (Far North Liquids and Associated Gas System)	Royal Dutch Shell plc	1982	OP	0.0	GB	OS	450	914	
33	Fulmar Gas Line	Royal Dutch Shell plc, ExxOPMobil	1986	OP	4.4	GB	OS	290	510	
34	Frigg UK System	Total E&P UK Plc	1977	OP	0.0	GB	OS	362	810	

ID	Pipeline name	Operator	Operating since	Current status	Capacity (10^9 m^3/year)	Transiting	Type	Total length (km)	Diameter (mm)	Operating pressure (MPa)
35	NOGAT (Northern UCshore Gas Transport)	GDF Suez	1992	OP	6.1	NL	OS	264		
36	Norpipe	Gassco AS	1977	OP	16.0	DE;NO	OS	443	914	
37	SAGE (Scottish Area Gas EvacuatiOP) System	Apache		OP	0.0	GB	OS	323	762	
38	SEAL System	Royal Dutch Shell plc	2000	OP	0.0	GB	OS		864	
39	Statpipe Rich and Dry Gas	Gassco AS	1985	OP	18.9	NO	OS	890	762	
40	Tyra West - F3 pipeline	Maersk Oil	2004	OP	5.5	DK;NL	OS	100	660	
41	Vesterled	Gassco AS	2001	OP	12.0	GB;NO	OS	361	813	
42	Zeepipe System	Gassco AS	1993	OP	67.2	BE;NO	OS	1416	1016	
43	Blue Stream	Gazprom, Blue Stream Pipeline B.V., BOTAŞ	2005	OP	16.0	RU;TR	OS;OB	1213	1400	25
44	Gazela Pipeline	Net4Gas	2013	OP	0.0	CZ	OB	166	1422	
45	Urengoy-Pomary-Uzhgorod ('Brotherhood') pipeline	Gazprom, UkrTransGaz	1967	OP	132.0	RU;SK;UA		4500	1420	
46	Soyuz Pipeline	Gazprom, UkrTransGaz		OP	26.0	RU;UA		1567	1420	
47	Yamal-Europe	Gazprom, Transgaz Belaru, EuRoPol Gaz	1997	OP	33.0	BY;PL;RU		4196	1420	
48	Northern Lights	Gazprom, Beltransgaz	1985	OP	51.0	BY;RU		7377	1420	

*Key: OP=operating; UC=under construction; OS=offshore subsea; OB=onshore buried

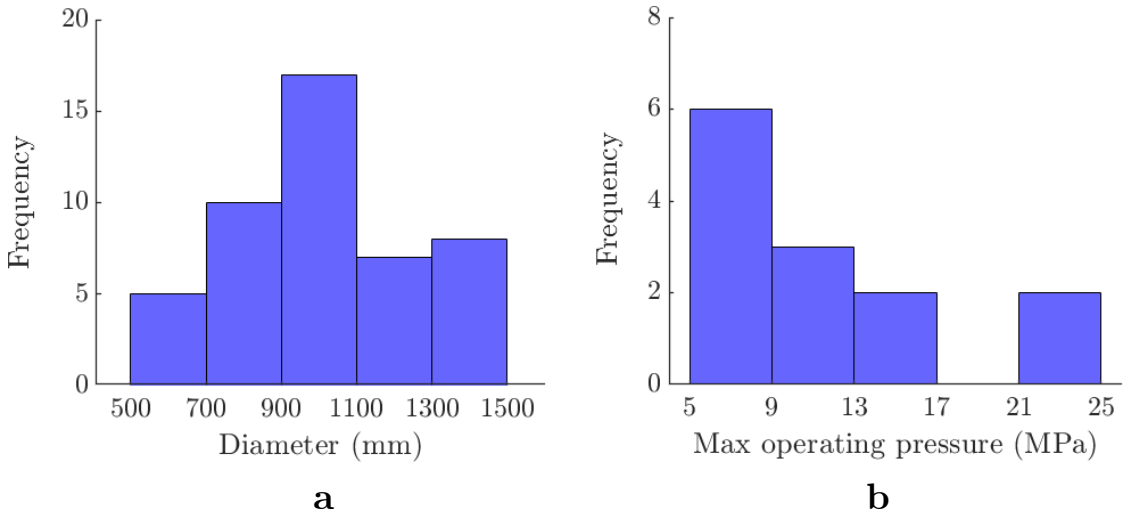

Figure 2-1. Histograms of (a) pipeline diameter and (b) maximum operating pressure based on data presented in Table 2-1

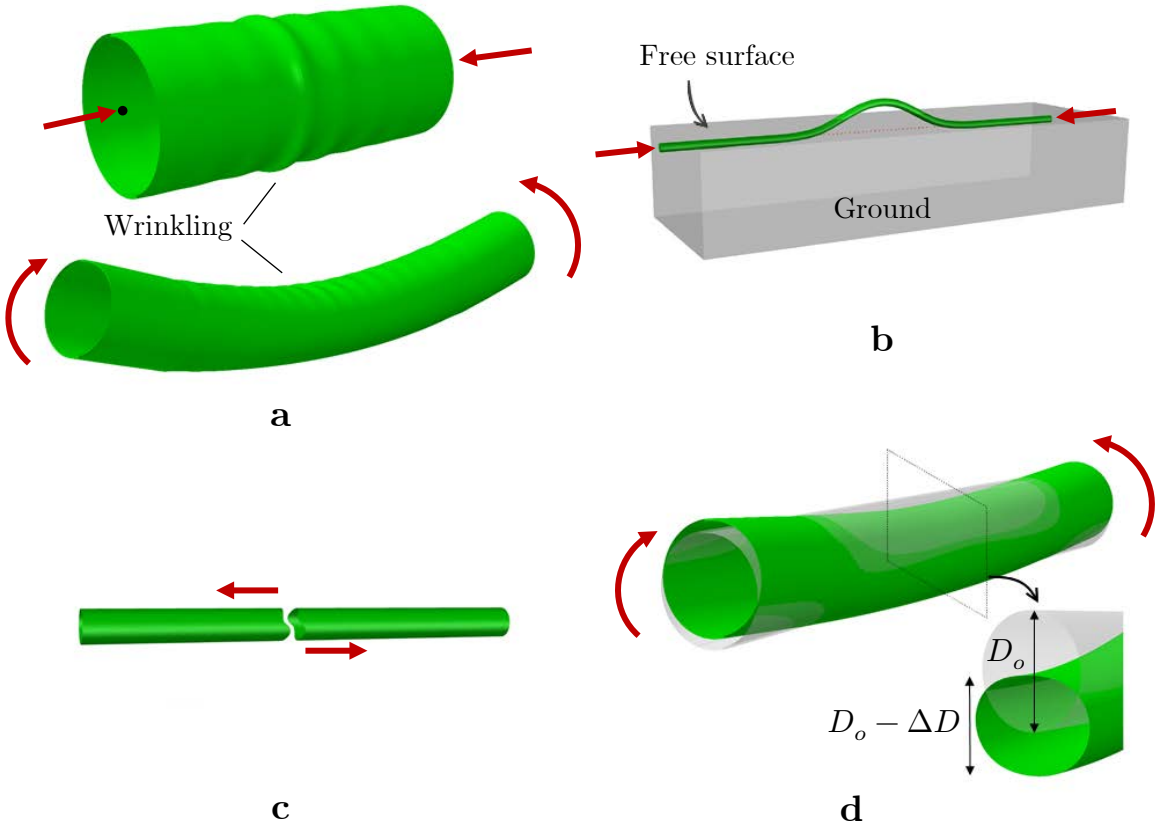

Figure 2-2. Common failure modes in buried continuous steel pipelines: (a) shell-mode buckling (wrinkling) due to uniform axial compression (top) and pure bending (bottom); (b) beam-mode buckling; (c) tensile rupture; (d) cross-section ovalisation

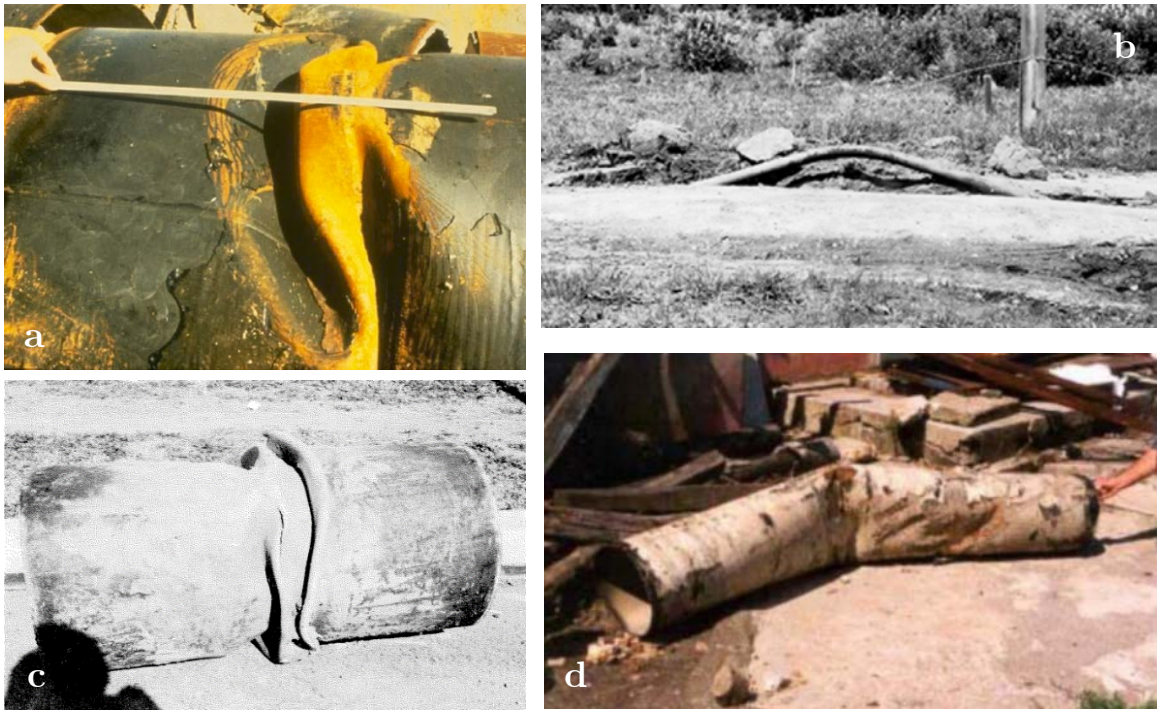

Figure 2-3. Failures of buried steel gas pipelines due to: (a) axial shell buckling; (b) beam buckling (c) axial shell buckling in the 1971 San Fernando earthquake (Jennings and Housner, 1971); (d) bending shell buckling in the 1999 Kocaeli earthquake (Vazinram and Rasti, 2006)

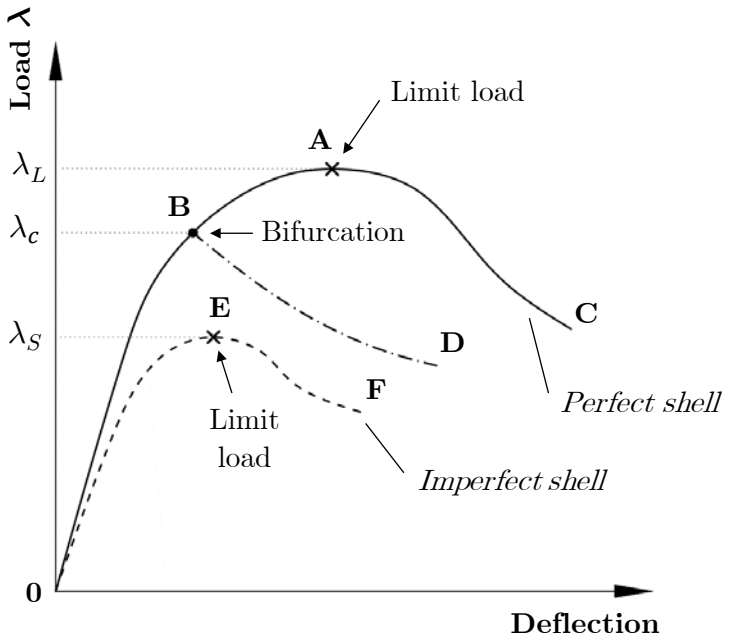

Figure 2-4. Characteristic load-deflection curves for perfect and imperfect shells, distinguishing different paths and critical points; adapted from Bushnell (1982)

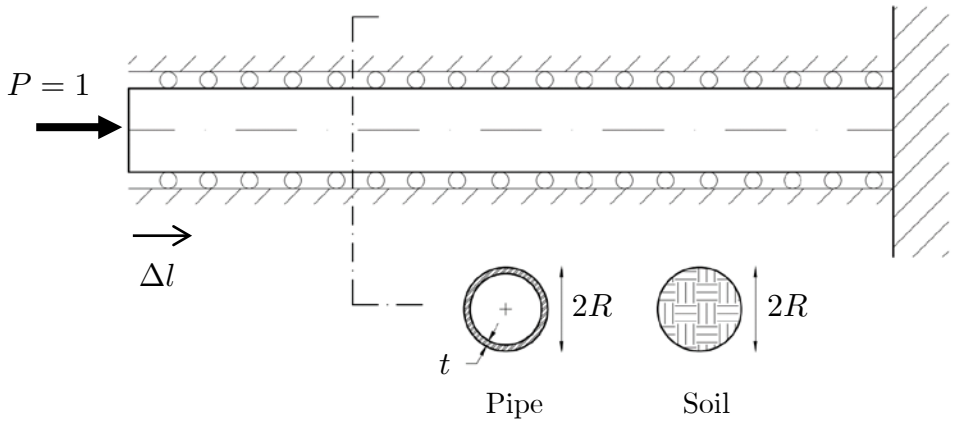

Figure 2-5. Idealisation of a confined portion of pipe or soil material as a tube or bar element clamped at one end and restrained from lateral movement (uniaxial strain conditions) under unit axial load

Table 2-2. Ground strain and curvature due to different types of seismic waves (St John and Zahrah, 1987)

Wave type	Longitudinal strain	Curvature
P-wave	$\frac{\dot{u}_{max}}{V_P}\sin^2\theta$ $\theta_{cr} = \pi/2$	$\frac{\ddot{u}_{max}}{V_P^2}\sin^2\theta\cos\theta$ $\theta_{cr} \cong \pi/5$
S-wave	$\frac{\dot{u}_{max}}{V_S}\sin\theta\cos\theta$ $\theta_{cr} = \pi/4$	$\frac{\ddot{u}_{max}}{V_S^2}\sin^3\theta$ $\theta_{cr} = \pi/2$
Rayleigh wave (dilatational component)	$\frac{\dot{u}_{max}}{V_R}\sin^2\theta$ $\theta_{cr} = \pi/2$	$\frac{\ddot{u}_{max}}{V_R^2}\cos\theta\sin^2\theta$ $\theta_{cr} \cong \pi/5$

Note: $\dot{u}_{max}$ = peak soil particle velocity in the direction of motion; $\ddot{u}_{max}$ = peak soil particle acceleration in the direction of motion; V_P = P-wave velocity; V_S = S-wave velocity; V_R = Rayleigh wave velocity

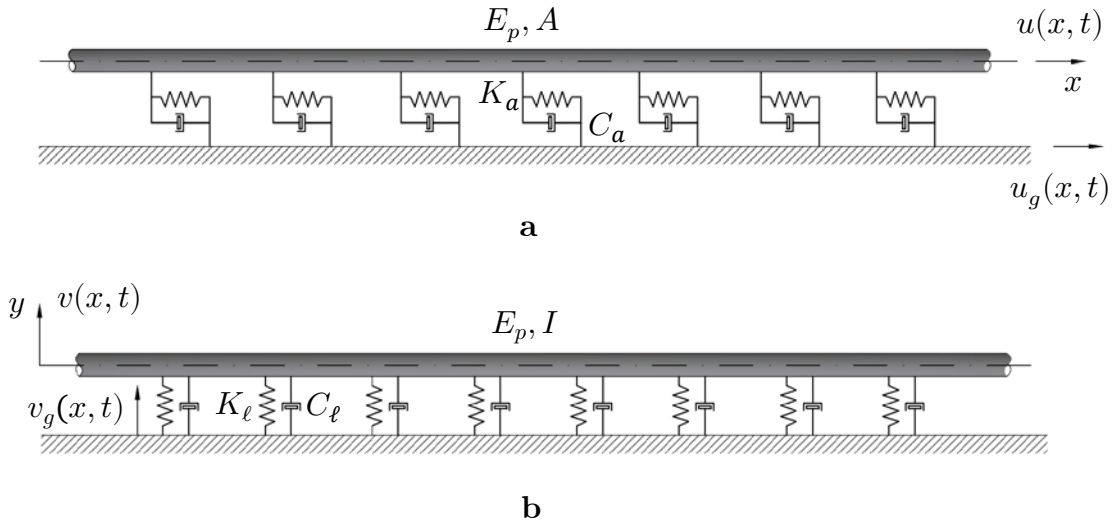

Figure 2-6. Dynamic model of beam on elastic foundation for continuous buried pipelines for (a) horizontal and (b) transverse ground excitation

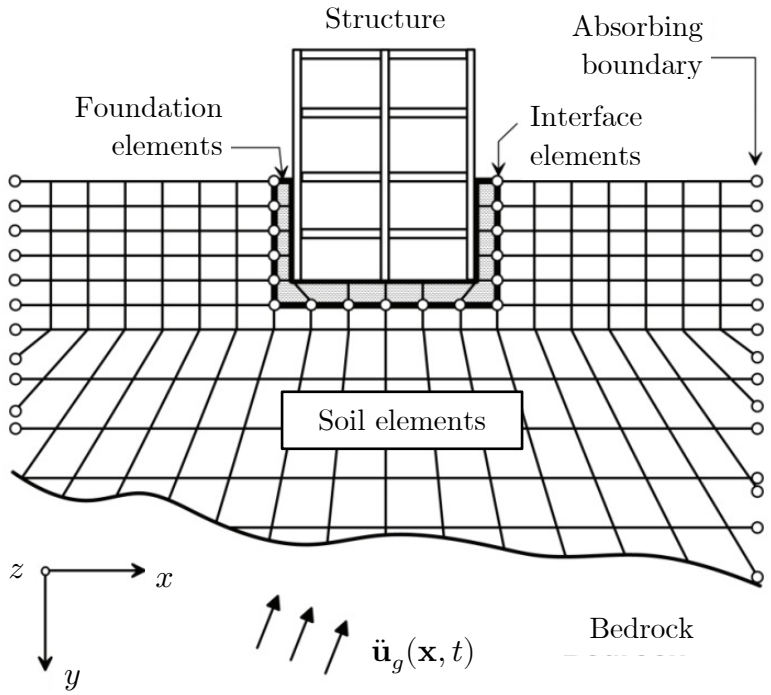

Figure 2-7. Example 2-D finite-element mesh configuration for direct seismic soil-structure interaction analysis; adapted from Kramer (1996)

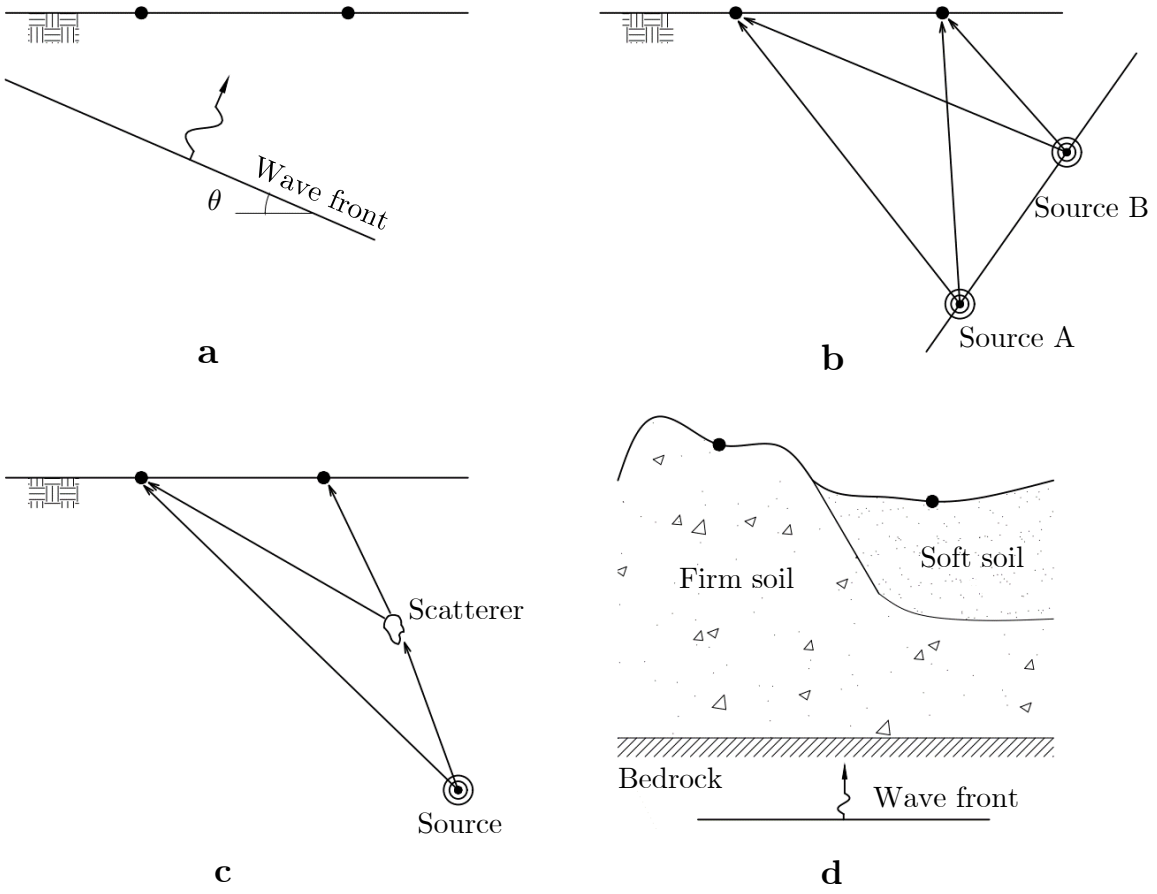

Figure 2-8. Sources of SVEGM potentially damaging for buried pipelines: (a) wave passage effect; (b) extended source effect; (c) ray-path effect; (d) local site effect

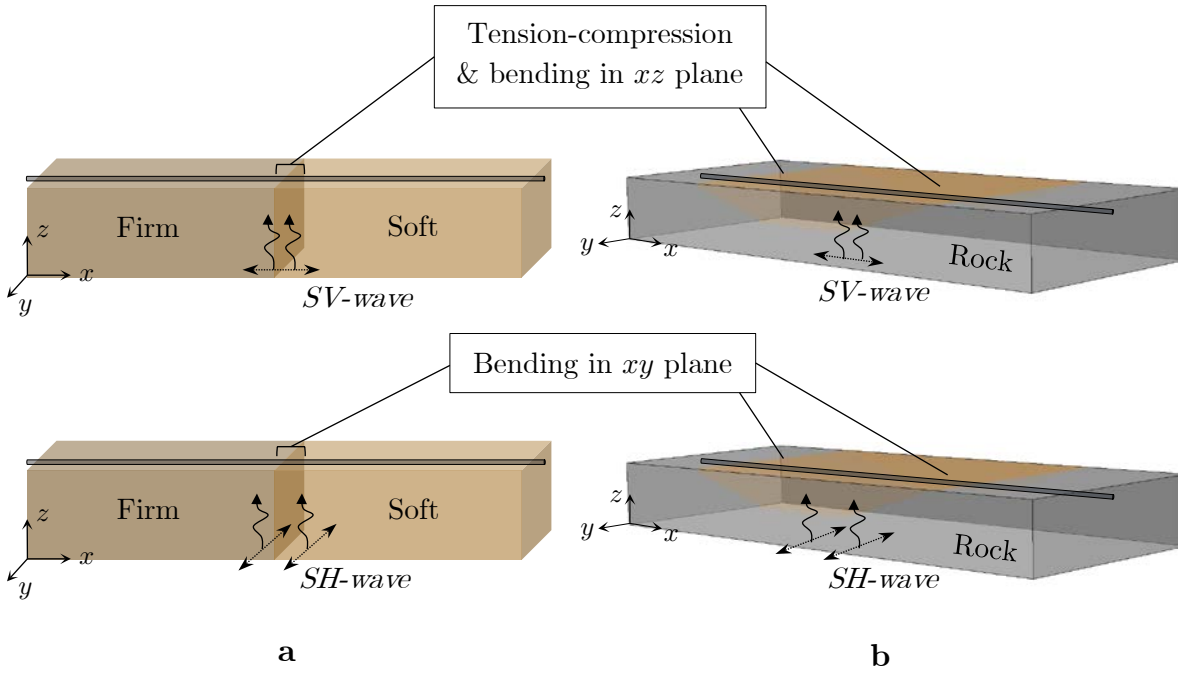

Figure 2-9. Modes of deformation of a buried pipeline crossing (a) two laterally adjacent soil layers of different softness and (b) an alluvial basin, due to two types of upward travelling seismic waves (plane of propagation is the $x - z$ plane)

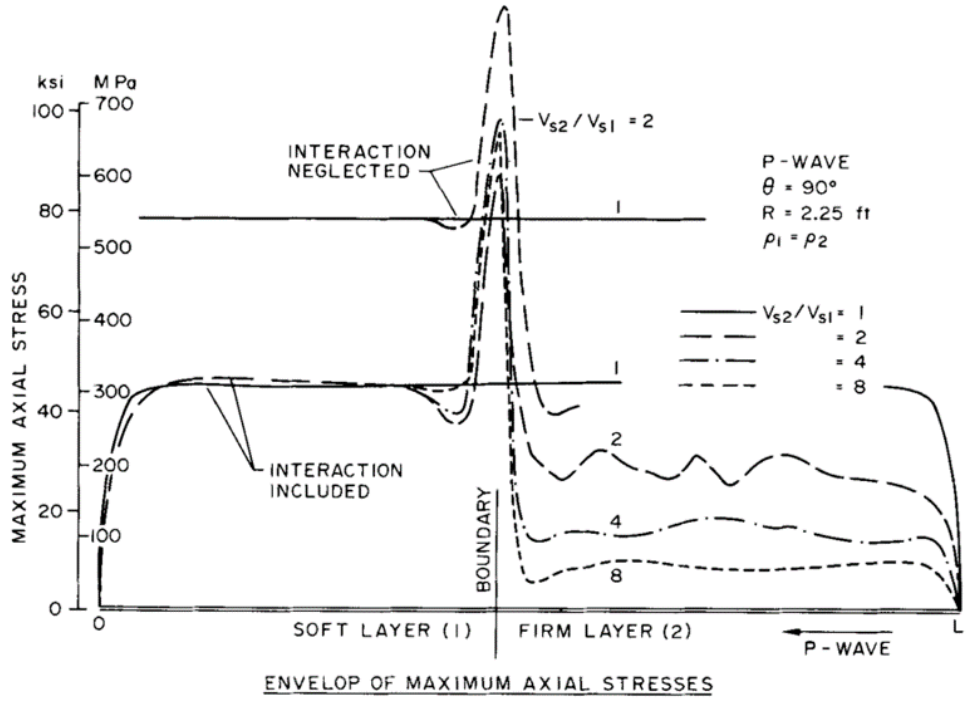

Figure 2-10. Spatial profile of maximum axial stresses in long buried steel pipe ($R/t = 62$) due to P-wave propagating from stiff to soft soil in the pipe direction, calculated by Hindy and Novak (1979) for various stiffness ratios V_{s2}/V_{s1} (reprinted)

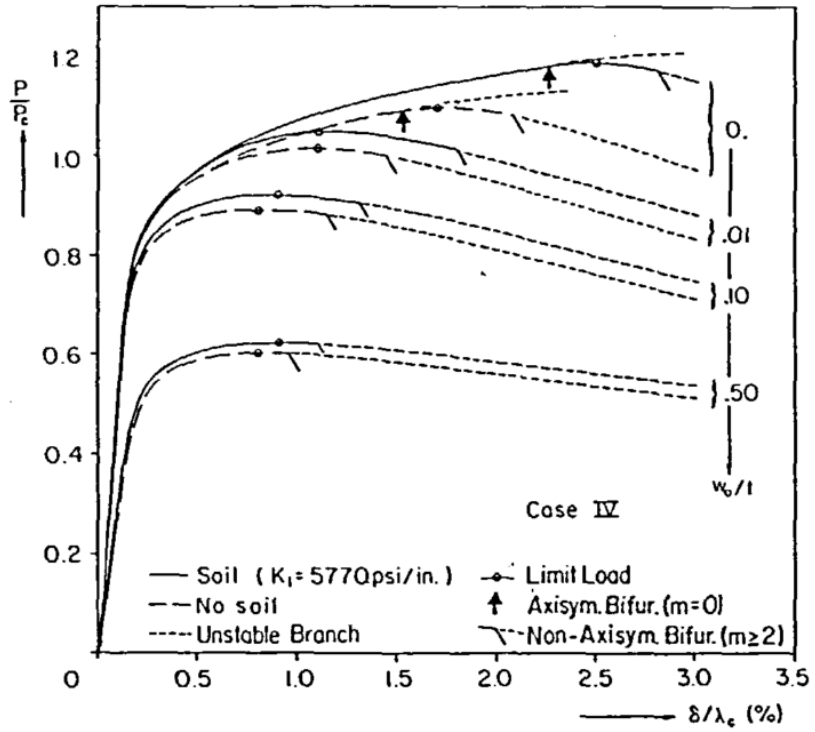

Figure 2-11. Normalised axial compressive load-average axial shortening curves for steel shell ($R/t_w = 32$; $\sigma_y = 276$ MPa) with different axisymmetric imperfection amplitudes, with and without soil confinement (Yun and Kyriakides 1990); reprinted

Table 2-3. Expressions for bi-linear SPI springs recommended by the ALA

Direction	Maximum soil force per unit length	Mobilising relative displacement
Axial	$t_u = \mu\gamma' H\left(\frac{1+k_0}{2}\right)\pi D + \pi Dac$	$3 \sim 10$ mm
Lateral horizontal	$P_u = \gamma' HDN_{qh} + DN_{ch}c$	$0.04(H + D/2) \leq 0.10D \sim 0.15D$
Vertical uplift	$Q_u = \gamma' HDN_{qv} + DN_{cv}c$	$\begin{cases} 0.01H \sim 0.02H < 0.1D \text{ (sand)} \\ 0.1H \sim 0.2H < 0.2D \text{ (clay)} \end{cases}$
Vertical bearing	$Q_b = \gamma' HDN_{qb} + DN_c c + \gamma \frac{D^2}{2} N_\gamma$	$\begin{cases} 0.1D \text{ (sand)} \\ 0.2D \text{ (clay)} \end{cases}$

Note: c =backfill cohesion; a = adhesion factor; N_{qh}, N_{ch}, N_{qv}, N_{cv}, N_{qb}, N_c, N_γ = bearing capacity factors in the corresponding directions (values retrievable from relevant tables)

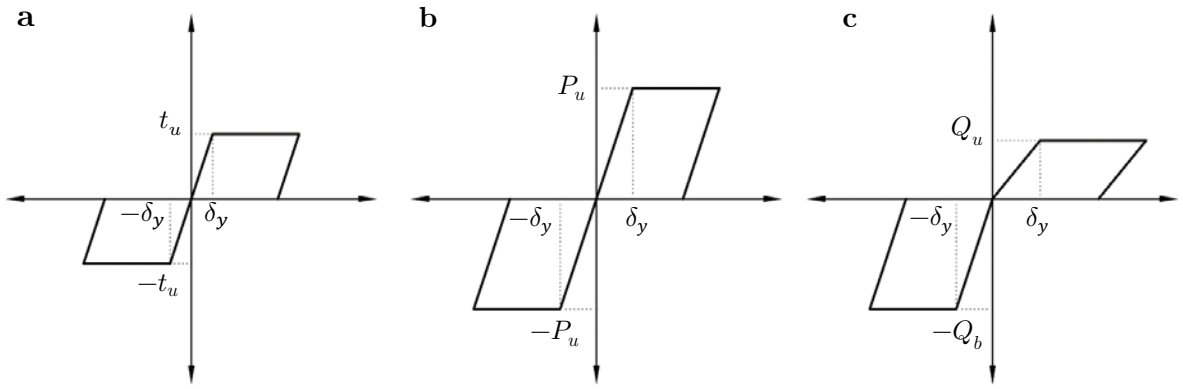

Figure 2-12. Plots of force-displacement relationships for SPI spring models proposed by the ALA: (a) axial spring; (b) lateral horizontal spring; (c) transverse vertical spring

Chapter 3

Numerical Substructure I: Site Response Models

3.1 Introduction

This chapter presents the first part of the numerical investigation into the seismic response of gas pipelines buried in laterally inhomogeneous soil. The problem at hand will be analysed by splitting it into two manageable numerical substructures, a global free-field model and a local SPI model. Here, the first substructure is addressed; the second substructure is developed in Chapter 4.

The chapter begins by outlining the proposed methodology, including presentation of the theoretical background and an account of the assumptions made and the limitations inherent in the approach. Following are the details of the baseline site scenarios chosen for analysis and the development of the respective numerical models. Finally, results, including outcomes of an extensive parametric study, are presented in graphical format and discussed. A summary of remarks concludes the chapter.

3.2 Overview of the numerical methodology

In view of the scarcity of new physical insights on the topic as concluded in Chapter 2, this thesis is a contribution towards the study of the behaviour of buried gas pipelines in laterally inhomogeneous soil during strong ground shaking. The problem will be approached through computer simulation and experiment, the latter

being the subject of Chapter 5. Emphasis will be placed on analysing the dynamic longitudinal response of the pipe, known to be the most crucial as it can result in buckling failures.

The core idea underlying the numerical methodology is to capture the response of the soil-pipe system at three levels: the site level, the SPI level, and the pipeline level. Until now, the literature has treated these basic constituents of the problem in isolation from each other (e.g., the zero-interaction model), in lumped terms (e.g., the Winkler foundation model), or based on simplifying assumptions about constitutive material laws (e.g., linearly elastic soil). This is a first comprehensive attempt to simultaneously overcome these limitations in order to improve our understanding of the mechanics of the problem. To achieve that, recourse to numerical methods is required. The finite-element method is chosen here for reasons mentioned in Subsection 2.3.2.

While a large-scale 3-D nonlinear simulation of the dynamic response of the soil-pipe system would be admittedly the most rigorous approach, it is hindered, as already noted in Section 2.5, by the immense solution cost, difficulties in reliably interpreting the results, and the large uncertainties involved in the definition of perplexing model parameters. An additional complication is the different dimensional scale characterizing the wide soil domain considered and the pipe. Besides, it has been observed that considering site amplification in three dimensions does not necessarily offer increased fidelity over a 2-D or even 1-D model (Makra and Chavez-Garcia, 2016). On the other hand, 1-D site response models, commonly used in practice, were discarded from the list of options because they are unable to capture strain gradients in a dimension other than the depth. It is thus imperative to make do with a number of compromises, seeking a trade-off between modelling sophistication and computational cost.

The relative insignificance of inertial and kinematic interaction in this type of problems allows one to decouple the soil-pipe system and to analyse it in two successive stages. The soil-pipe system in this study is partitioned into two substructures:

(1) the global model containing only the site (*substructure I*);

(2) a refined local model containing the pipeline, a near-surface portion of the soil surrounding the pipeline, and the interface contact (*substructure II*).

In this sub-structuring scheme, the local model depends on the global, but not the other way around – output from analysis of substructure I is used as input to analysis of substructure II. **Figure 3-1** illustrates the proposed sub-structuring scheme. The workflow of the scheme is detailed in the following. Note that, unless otherwise stated, all position-dependent variables are referenced in a Cartesian coordinate system.

3.2.1 Substructure I: 2-D site response model

The first step of the methodology is the determination of the dynamic ground response within laterally inhomogeneous geological structures overlying a semi-infinite layer of bedrock subjected to given excitation forms. Shear waves are solely considered as the source of disturbance in the ground, as they are known to carry most of the elastic energy released by a fault rupture.

Given that the ground motion components can be directed randomly relative to the pipeline axis, it appears reasonable to focus on the scenario that results in the maximum axial deformation in a laterally inhomogeneous site. This is the case where the ground motion vector and the propagation vector both lie in the plane defined by the pipeline axis and the vertical (plane $x-z$ in **Figure 3-1**a). Therefore, plane $x-z$ is the plane of propagation and vertically polarised S-waves (i.e., SV waves) will be considered to excite a plane-strain model of the site (**Figure 3-1**b). For context, this is the case with $\varphi = 0^\circ$ and $\beta = 90^\circ$ in the wave vector decomposition system employed in Kouretzis et al. (2006), for S-wave action represented there by SH-waves. The axial pipe strain for this scenario in homogeneous ground is as expected found to be zero, but the lateral inhomogeneity introduced here will modify this result. A secondary benefit resulting from this assumption is that the dimensionality of the problem is automatically reduced from three to two.

2-D site response analyses are performed in the time domain for two site scenarios, using simple pulses and real earthquake records as excitation forms at the model base. From the results, the time instant, t_{cr}, of the absolute peak ground strain occurring at any horizontal position x at depth h (a line coinciding with the fictitious pipe centreline) is detected

$$\max_{x,t}|\varepsilon_{xx}(x,h,t)|\,, \qquad x \in [-L, L] \tag{3.1}$$

where $2L$ is the total length of the analysed soil domain. The respective spatial profile of ground deformation along this horizontal line of points is obtained in terms of the in-plane displacement vector

$$\boldsymbol{u}_{cr} = [u_{cr}\ w_{cr}]^T = \boldsymbol{u}(x, h, t_{cr}) \tag{3.2}$$

This deformation profile is then used as input to substructure II as will be explained next (**Figure 3-1**c).

It is well-established that, unless highly plastic, soils exhibit nonlinearity in their shear stress-strain path even for low strain amplitudes (Vucetic and Dobry, 1991; Vucetic, 1994). This characteristic is of major importance as a drop in stiffness relates to heavier straining of the material. Modelling of the strain-dependent nature of the soil modulus is exposed in Section 3.5.

3.2.2 Substructure II: Nonlinear SPI model

In the second stage of the methodology, a detailed 3-D finite-element model is developed consisting of a long portion of the pipeline and a block of trench soil of equal length (**Figure 3-1**d). This local model is assumed to arise from truncation of substructure I and expansion to the third spatial dimension, y. A thin circular cylindrical nonlinear shell represents the pipeline, while the trench soil is modelled with solid continuum elements. This modelling approach allows for prediction of buckling modes in the pipe, while the initial stress state due to gravity and pipe internal pressure is determined prior to the application of the seismic load. The critical ground

displacement field $\boldsymbol{u}_{cr}$ computed in substructure I, now expanded to three-dimensional space $[u_{cr}\ 0\ \ w_{cr}]^T$ and satisfying $\partial \boldsymbol{u}_{cr}/\partial y = 0$, is imposed on the soil block in a pseudo-static manner. The dynamic character of the response of substructure II is suppressed, since pipeline inertia is negligible; in this way, the overall computing cost is minimised, as only the pipeline response at $t = t_{cr}$ is sought.

The evolution of contact between the soil and the pipe is predicted using a surface contact formulation able to capture slippage, separation, and the coupling between them explicitly, ensuring an accurate representation of the load transfer mechanism from soil to pipe. Further details on substructure II are found in Chapter 4.

3.2.3 Benefits of sub-structuring

There are multiple gains resulting from the proposed sub-structuring scheme. The most apparent one is a dramatic reduction in the computational time required to complete a single model analysis, compared to building and solving a full 3-D dynamic finite-element SPI model. The latter option was tested for the purposes of Chapter 5; a full analysis of a numerical model of the experimental setup required about 8 days, whereas the proposed sub-structuring scheme takes typically 3 to 8 hours depending on the mesh size and the allocated computing power.

Further, by partitioning the physical system and therefore reducing its complexity allows to analyse the sensitivity of its response to various parameters and trace the source of modelling errors more easily. If a large-scale model with both far- and near-field details was in place, it would be difficult to identify cause and effect relationships as a multitude of effects would superimpose and interact in complex ways. The proposed approach also offers versatility in that model refinement strategies can be implemented on a single substructure at a time, without the need to intervene on the other. Finally, it resolves the dimensional incompatibility between the large-scale seismic ground response and the localized character of the expected pipe failures.

3.2.4 Objectives of sub-structuring

The main objectives of the proposed sub-structuring scheme are to

a. predict the ground motion amplification in laterally inhomogeneous sites;

b. determine the range of response peaks and the profiles of ground deformation expected to develop along a buried gas pipeline under seismic excitations of different characteristics, with the aim to highlight critical cases;

c. study the dependence of ground deformation indicators to key problem parameters;

d. evaluate the pipeline demand resulting from the critical soil movements and compare with existing code-prescribed limit states;

e. analyse the interaction effects at the soil-pipeline interface;

f. ultimately explore the possibility of buckling failure in pipelines laid through such inhomogeneous sites, identify the circumstances that favour its occurrence and study its characteristics.

3.2.5 Assumptions and limitations

The adopted methodology relies on certain assumptions and has a number of limitations. These are acknowledged below.

- Only 2-D wave effects are captured by the simulation; 3-D effects are inevitably disregarded.

- The central assumption invoked is that inertial SPI (i.e., waves emitted by the vibration of the pipe through the soil) and kinematic SPI (i.e., the ground motion modification at pipeline bed due to the stiffness contrast between the soil and the pipe) can be ignored with negligible loss of accuracy. The error introduced by this approximation on the whole is not explicitly quantified – for that, a prohibitively costly 3-D dynamic SPI analysis would be required. However, a simple way to argue in quantitative terms about the error from ignoring inertial SPI is to consider the

ratio of the weight of the pipe to the weight of the soil it replaces, $w_p/w_s = 2(\rho_p/\rho)\, t_w/R$. For typical steel gas pipelines and soil grades, this ratio lies in the range 0.16~0.52, which implies a 'negative' inertial interaction. Regarding kinematic interaction, preliminary complex harmonic analysis is performed to quantify its effect on the response of a wide range of soil-gas pipe systems. From the findings presented in Appendix A, it is reasonable to conclude that the influence of the pipe stiffness on the free-field motion near the pipe is negligible for typical soil-pipe configurations and forcing frequencies in the examined range of 0.1~15.0 Hz, with the exception of very soft foundation soils ($V_s \leq 100$ m/s), whose vibratory response is altered for exciting frequencies higher than about 9 Hz.

- Ground deformation is confined in the plane defined by the pipeline axis and the vertical. Consequently, bending of the pipeline in other planes is not considered.

- Soil nonlinearity is approximately accounted for since neither yielding nor hardening effects nor permanent deformation can be captured with equivalent-linear analysis.

- For cases where soil nonlinearity is expected to be very pronounced (under extremely high-intensity motions, in liquefiable soils etc.), the equivalent-linear material model ceases to be a reliable assumption and more advanced models, such as cyclic nonlinear or plasticity models, become necessary (Kaklamanos *et al.*, 2015).

- Dry cohesionless soils are considered only, thus all quoted soil stresses are total stresses. The effect of ground water head is not examined.

- The time factor is not considered in substructure II. This means that the effects of time-dependent phenomena on the pipeline, such as fatigue and strength and stiffness degradation with loading cycles, are ignored.

- The critical loads and strains computed for the pipeline are representative to the degree that the assumption of equivalence between static and dynamic buckling response parameters holds true.

3.3 Equations of wave propagation in a continuum and the finite-element method approximation

3.3.1 Homogeneous, linearly elastic, isotropic continuum

For simplicity, consider first a homogeneous, linearly elastic and isotropic earth model and small deflections. The dynamic motion of an earth continuum occupying a volume Ω with boundary $\partial\Omega$ can be described by the system of Eqs. (3.3)-(3.5), expressed in index notation. The first equation is the momentum balance equation; the second equation is the general statement of Hooke's law; the third equation expresses the linearised strain-displacement relationship:

$$\sigma_{ij,j} + \rho f_i = \rho \frac{\partial^2 u_i}{\partial t^2} \tag{3.3}$$

$$\sigma_{ij} = \lambda \varepsilon_{kk} \delta_{ij} + 2\mu \varepsilon_{ij} \tag{3.4}$$

$$\varepsilon_{ij} = \frac{1}{2}(u_{i,j} + u_{j,i}) \tag{3.5}$$

where $\sigma_{ij,j}$ = stress tensor components; ρf_i = body force per unit volume; u_i = direct displacement components; $i, j = 1, 2, 3$ correspond to Cartesian coordinates x, y, z; λ and $\mu = G$ are Lame's elastic constants; δ_{ij} = Kronecker's delta; ε_{ij} = small-strain tensor components. Repeated indices imply summation, commas denote partial differentiation with respect to the indexed spatial coordinate.

After substitutions, the momentum balance equation can be expressed as in Eq. (3.6), which is known as the displacement equation of motion

$$\mu u_{i,jj} + (\lambda + \mu) u_{j,ji} + \rho f_i = \rho \ddot{u}_i \tag{3.6}$$

This is a system of linear, second-order, partial differential equations of the hyperbolic type. Switching to vector notation, Eq. (3.6) is written as

$$\mu \nabla^2 \boldsymbol{u} + (\lambda + \mu) \nabla \nabla \cdot \boldsymbol{u} + \rho \boldsymbol{f} = \rho \ddot{\boldsymbol{u}} \tag{3.7}$$

in which $\boldsymbol{u} =$ the displacement vector, $\nabla^2 =$ Laplacian operator, $\nabla =$ the gradient operator, $\ddot{\boldsymbol{u}} = \partial^2 \boldsymbol{u} / \partial t^2$ is the acceleration vector. Note that, in the above, all vector and tensor variables depend implicitly on the position vector, $\boldsymbol{x} = x\hat{\boldsymbol{\imath}} + y\hat{\boldsymbol{\jmath}} + z\hat{\boldsymbol{k}}$ **($\hat{\boldsymbol{\imath}}$, $\hat{\boldsymbol{\jmath}}$, $\hat{\boldsymbol{k}}$** are the components of the unit vector**)**, and the time, t. To completely define a boundary value problem, one must specify boundary conditions on the boundary $\partial\Omega$ of the medium and initial conditions over the whole domain Ω.

The body force term can be neglected for most applications where typical wavelengths are involved; if so, Eq. (3.7) is amenable to analytical solution. The classical solutions are those of the bulk longitudinal and shear wave propagating through an unbounded medium, which can be derived for example by taking the divergence and curl of both sides of Eq. (3.7) respectively (neglecting the body force). In this way, Eq. (3.7) is separated into the P- and S-wave equations given by

$$\frac{\partial^2 (\nabla \cdot \boldsymbol{u})}{\partial t^2} = a^2 \nabla^2 (\nabla \cdot \boldsymbol{u}), \qquad a^2 = \frac{\lambda + \mu}{\rho} \tag{3.8}$$

$$\frac{\partial^2 (\nabla \times \boldsymbol{u})}{\partial t^2} = \beta^2 \nabla^2 (\nabla \times \boldsymbol{u}), \qquad \beta^2 = \frac{\mu}{\rho} \tag{3.9}$$

Eq. (3.8) describes an irrotational (i.e., involving no shear or rotation) wave, with velocity equal to α, while Eq. (3.9) a distortional wave (i.e., involving no volumetric deformation), with velocity equal to β. The latter type of wave is usually assumed to be composed of the vector sum of SH (shear horizontal) and SV (shear vertical) waves, whose particle motions lie in planes perpendicular to each other.

When considering the free surface of the earth as a boundary condition, additional solutions to the elastic wave equation can be found that form the family surface seismic waves. The most relevant of them from an engineering point of view is that of the Rayleigh wave (Rayleigh, 1885) arising in a homogeneous elastic half-space. Considering plane time-harmonic waves in the xz plane with frequency ω, the Rayleigh wave displacement components are given by

$$u = A_1 \left(-ik_R e^{-qz} + \frac{2iqsk_R}{s^2 + k_R^2} e^{-sz} \right) e^{i(\omega t - k_R x)} \tag{3.10}$$

$$w = A_1 \left(\frac{2qk_R^2}{s^2 + k_R^2} e^{-sz} - qe^{-qz} \right) e^{i(\omega t - k_R x)} \tag{3.11}$$

in which A_1 = arbitrary horizontal displacement amplitude, $s^2 = k_R^2 - \omega^2/V_s^2$, $q^2 = k_R^2 - \omega^2/V_p^2$, $k_R = \omega/V_R$ where V_R is the Rayleigh wave velocity. This velocity is related to the body wave velocities through the Poisson's ratio and is found to be slightly lower than the S-wave velocity. The particle motion trajectory represented by Eq. (3.14)-(3.15) is a retrograde ellipse near the earth surface, being a combination of a P- and S-wave. The two displacement components are out-of-phase by $\pi/2$. Rayleigh waves in homogeneous half-space are non-dispersive, but become dispersive when propagating in layered media, that is, their different frequency components travel at different speeds.

3.3.2 Inhomogeneous, linearly elastic, isotropic continuum

In the general inhomogeneous case, the material parameters λ, μ and ρ are not constant over the continuum, rather they are functions of $\boldsymbol{x}$. The displacement equation of motion assumes then the form

$$\nabla\lambda(\nabla \cdot \boldsymbol{u}) + \nabla\mu \cdot [\nabla \boldsymbol{u} + (\nabla \boldsymbol{u})^T] + \mu\nabla^2 \boldsymbol{u} + (\lambda + \mu)\nabla\nabla \cdot \boldsymbol{u} + \rho \boldsymbol{f} = \rho \ddot{\boldsymbol{u}} \tag{3.12}$$

It is obvious that the equation of motion now includes two new terms representing gradients in Lame's parameters (first two terms on the left-hand side).

This equation is very complicated to solve analytically. Some analytical solutions have been obtained for special cases where restrictive assumptions have been made for the spatial profiles of material parameters, most commonly requiring inhomogeneity only in the depth direction (e.g. Manolis et al. 1999).

3.3.3 Inhomogeneous, nonlinear, isotropic continuum

When the medium is neither homogeneous nor linearly elastic, an explicit expression of the displacement equation of motion is not obtainable, as Eq. (3.4) is no longer valid. Solutions to this case are possible by numerical approximation, for instance by the use of the FEM or finite differences to discretise the spatial domain. An appropriate incremental constitutive model is also essential in this case to determine inelastic deformations based on the history of the response, such as classical flow plasticity or gradient elastoplasticity (Zervos, Papanastasiou and Vardoulakis, 2001), combined with a numerical scheme to discretise the time dimension and compute the response at the end of each time step.

3.3.4 Finite-element equilibrium equations

The equation of equilibrium of a single finite element can be obtained in various ways, such as by using the principle of virtual work or Hamilton's principle for a deformable body. The underlying concept is that the displacement field, $\mathbf{u}(\mathbf{x})$, within each element is interpolated from values calculated at the nodal points of the element, $\mathbf{u}_{\mathrm{I}}$, based on a predefined shape function matrix $\mathbf{N}$. The resulting matrix equilibrium equation for a linearly elastic element, including damping effects, is stated as

$$\mathbf{m}\ddot{\mathbf{u}} + \mathbf{c}\dot{\mathbf{u}} + \mathbf{k}\mathbf{u} = \mathbf{f}_{\mathrm{ext}} \tag{3.13}$$

where

$$\mathbf{u} = \mathbf{N}\mathbf{u}_{\mathrm{I}}; \qquad \dot{\mathbf{u}} = \mathbf{N}\dot{\mathbf{u}}_{\mathrm{I}}; \qquad \ddot{\mathbf{u}} = \mathbf{N}\ddot{\mathbf{u}}_{\mathrm{I}} \tag{3.14}$$

and the element mass, damping and stiffness matrices, and the external force vector are given by

$$\mathbf{m} = \int_{\Omega} \rho \mathbf{N}^T \mathbf{N} \, \mathrm{d}V \tag{3.15}$$

$$\mathbf{c} = \int_{\Omega} c \mathbf{N}^T \mathbf{N} \, \mathrm{d}V \tag{3.16}$$

$$\mathbf{k} = \int_{\Omega} \mathbf{B}^T \mathbf{E} \mathbf{B} \, \mathrm{d}V \tag{3.17}$$

$$\mathbf{f}_{\mathrm{ext}} = \int_{\partial\Omega} \mathbf{N}^T \mathbf{t} \, \mathrm{d}A \tag{3.18}$$

where $\mathbf{B} = \boldsymbol{\partial}_{\mathbf{x}} \mathbf{N}$ is called the strain-displacement matrix, containing the spatial derivatives of the shape functions ($\boldsymbol{\partial}_{\mathbf{x}}$ is a differential operator), so that $\boldsymbol{\varepsilon} = \mathbf{B}\mathbf{u}_{\mathrm{I}}$; $\mathbf{E} =$ the constitutive matrix; $\mathbf{t} =$ the traction vector.

In modern computer implementation of the FEM, the global matrix is assembled by the direct stiffness method, where transformed coefficients of the various element matrices are directly placed at the appropriate locations of the global matrix based on global node numbering. The matrix equation of global equilibrium takes the form of Eq. (3.19) for linearly elastic material and of Eq. (3.20) for nonlinear material

$$\mathbf{M}\ddot{\mathbf{U}} + \mathbf{C}\dot{\mathbf{U}} + \mathbf{K}\mathbf{U} = \mathbf{F}_{\mathrm{ext}} \tag{3.19}$$

$$\mathbf{M}\ddot{\mathbf{U}} + \mathbf{C}\dot{\mathbf{U}} + \mathbf{F}_{\mathrm{int}}(\mathbf{U}) = \mathbf{F}_{\mathrm{ext}} \tag{3.20}$$

where symbols in capitals now represent quantities referred to in the global reference frame. When seismic wave propagation is modelled with the FEM, a line or point source disturbance in the form of a time-history of stress or displacement is usually prescribed at boundary or internal nodes of a finite domain representing the region of interest.

Note that, in the above, the solution variable **U** is still a continuous function of time, therefore time-integration of Eqs. (3.18)-(3.19) is required to obtain a discrete solution in the general case. In problems involving material nonlinearity, iterative algorithms—most often the modified Newton-Raphson scheme—are employed in conjunction with implicit numerical time-integration schemes to approximate the restoring force vector $\mathbf{F}_{\text{int}}(\mathbf{U})$ at each time step according to specified convergence criteria. The same solution strategy applies to problems involving large deformations (i.e., geometric nonlinearity), where **K** also varies across time as it depends on the spatial coordinates and the current geometric configuration of the system is updated at every time instant.

3.4 Selection of site structures

In an effort to broaden the scope of this study, a scenario-based approach is taken. To this end, the following generic geological structures are considered:

a. a site composed of two laterally adjacent soil deposits of dissimilar shear wave velocities, their boundary being vertical (*Site 1*), as in Hindy & Novak (1979);

b. a symmetric trapezoidal sediment-filled valley (*Site 2*).

The two sites and their long sections are illustrated in **Figure 3-2**. In both structures, inhomogeneity manifests as abrupt transitions between distinct homogeneous layers sharing an interface. Common geological formations in nature exhibiting lateral inhomogeneities are alluvial basins of various shapes and aspect ratios. Other cases are surface fault sites and cut-and-fill embankments.

The following assumptions are made to simplify the subsequent analysis:

- The vertical interface in Site 1 is assumed to extend to infinity in the out-of-plane direction.

- The out-of-plane valley dimension of Site 2 is assumed very long, a reasonable assumption for valleys formed around rivers. On these grounds, plane-strain conditions for analysis purposes can be warranted.

- The sites are treated as a single continuum, therefore continuity of stresses and displacements is enforced at all shared interfaces.

- Both sites have level surfaces, thus topographic effects are not considered.

- Ground motion occurs in the xz plane as the plane is swept by upward travelling SV-waves. The seismic motions applied at bedrock level are assumed to be fully correlated, except a phase shift where non-vertical incidence is considered.

3.5 Site characterization, stratigraphy and material constitutive modelling

Due to their particulate and multi-phase nature, the mechanical behaviour of soil media is quite complex to understand and model with accuracy. Two categories of site response models will be considered here based on the constitutive behaviour of the soil, namely linearly viscoelastic and equivalent-linear. The distinction is made in order to facilitate evaluation of the impact of different levels of ground excitations—classified here as weak and strong—applied at the site bedrock, and to identify the limits of applicability of each constitutive model in this context.

Site 1

Figure 3-2 identifies the geometric and material parameters for each site. The free parameters for Site 1 are the following: the S-wave velocity of the left deposit, $V_{s,1}$; the depth to bedrock, H; the length of the stiffness transition zone, l_t; the small-strain damping ratio, ξ; and the wave incidence angle, θ. An invariant $V_{s,2} = 100$ m/s is assumed across all Site 1 instances and a uniform mass density of 1.7 Mg/m^3 is assigned to both deposits.

The half-width, L, of the domain and is set equal to 250 m. Note that, while L is not actually a parameter of the physical problem, it appears in the numerical model because sidewise truncation of the laterally infinite domain is necessary to render it finite. In the absence of known characteristic patterns in nature, a linear variation of soil stiffness (or, equivalently, V_s) is assumed within a transition zone, and this zone's width $l_t = x_2 - x_1$ is varied. The expression giving the soil shear modulus, G, at each horizontal coordinate is then

$$G(x) = \begin{cases} G_1, & x \leq x_1 \\ G_1 + \dfrac{G_2 - G_1}{l_t} x, & x_1 \leq x \leq x_2 \\ G_2, & x \geq x_2 \end{cases} \tag{3.21}$$

Site 2

For Site 2, a 300-m-wide, 30-m-deep valley is considered, giving a depth-to-width ratio of 0.1; this aspect ratio characterises a shallow and wide valley (Kramer, 1996). Independent parameters are taken to be the following: the S-wave velocities of the basin soil, $V_{s,1}$, and the surrounding rock/soil, $V_{s,2}$; the projected length of the dipping edge on the surface, L_e, which controls the dipping slope; the small-strain damping ratio, ξ; and the wave incidence angle, θ. The mass densities of the basin and the surrounding rock are fixed at 1.7 Mg/m^3 and 2.0 Mg/m^3, respectively. The half-width of the analysed domain is again $L = 250$ m.

Bedrock

The underlying bedrock is assumed to possess a mass density of 2.4 Mg/m^3 and an S-wave velocity of 1000 m/s, thus representing a typical sandstone. The Poisson's ratio for all soils in this study is taken constant at $\nu = 1/3$. Note that modest modifications in the stratigraphy of the baseline sites as of **Figure 3-2** are implemented in the nonlinear models.

3.5.1 Linearly elastic models

The first group of models concerns damped linearly elastic behaviour. As displayed in **Figure 3-2**, the soil layers in both sites are described by uniformity in material properties in the z-direction. In reality, soils usually exhibit increasing stiffness with depth, but, for the sake of simplicity and ease of interpretation, the elastic deposits considered here will have constant S-wave velocity profiles, namely $\partial V_s/\partial z = 0$. A uniform small-strain damping ratio is assumed across all deposits.

To consistently present the results of the parametric study in unitless terms, the following dimensionless variables are introduced for Site 1:

- the dimensionless frequency

  $$a_0 = \frac{\omega}{\omega_{0,2}} = 4\frac{fH}{V_{s,2}}$$

  (ω = central excitation frequency)

- the site impedance ratio, which reduces to the velocity contrast

  $$\frac{\rho_1 V_{s,1}}{\rho_2 V_{s,2}} = \frac{V_{s,1}}{V_{s,2}}$$

- the dimensionless transition zone length

  $$\frac{l_t}{H}$$

For Site 2, it is possible to construct dimensionless variables as below:

- the dimensionless frequency

  $$a_0 = \frac{\omega}{\omega_{0,1}} = 4\frac{fH_V}{V_{s,1}}$$

- the site impedance ratio

  $$\frac{\rho_1 V_{s,1}}{\rho_2 V_{s,2}} = 0.85\frac{V_{s,1}}{V_{s,2}}$$

- the slope of the dipping edge

$$s = \frac{H_V}{L_e}$$

In the above, $\omega_{0,1}$ represents the first natural frequency of a 1-D soil column with the properties of the valley, $H_V = 30$ m is the valley depth. The influence of the above parameters will be quantified and discussed in Subsection 3.7.1. **Table 3-1** summarises the values these parameters assume in the parametric study.

The commercial finite-element code ABAQUS is employed to develop and solve the linearly elastic models. A user-subroutine is written in Fortran to introduce the desired linear stiffness gradients in the transition zone, l_t, of Site 1; the user-subroutine is listed in Appendix B.

3.5.2 Equivalent-linear models

3.5.2.1 Background

A linear shear stress-strain relationship is rarely a valid assumption for a soil. Typical soils are known to exhibit strongly nonlinear hysteretic response under cyclic loading, even when subjected to strains as low as ~0.0003% (Kramer, 1996). To capture this behaviour, the equivalent-linear model is a common approach. **Figure 3-3** shows qualitatively an ideal hysteresis loop characterising the cyclic stress-strain response $\tau - \gamma$ of the soil. The equivalent-linear model uses two simple parameters to approximately describe this loop, namely the secant shear modulus, G_{sec}, and the hysteretic damping ratio, ξ or D. Parameter G_{sec} characterises the average slope (stiffness) of the loop over a loading cycle and its initial, elastic value is termed G_{max}. Parameter ξ quantifies the size of the loop, which reflects the amount of hysteretic energy dissipated over a loading cycle; it is given by

$$\xi = \frac{1}{4\pi}\frac{E_D}{E_s} = \frac{1}{2\pi}\frac{A_{loop}}{G_{sec}\gamma_c^2} \tag{3.22}$$

in which E_D = dissipated energy in a cycle; $E_s = {}^1\!/_2\,\tau_c\gamma_c$ = maximum strain energy stored in a cycle; A_{loop} = the area of the loop; γ_c = peak shear strain amplitude; τ_c =

$G_{sec}\gamma_c$ = peak shear stress amplitude. Parameters G_{sec} and ξ are commonly referred to as strain-compatible. A number of factors bear influence on the variation of G_{sec} and ξ with cyclic shear strain, most importantly, the mean effective confining stress of the soil $p' = (\sigma'_1 + \sigma'_2 + \sigma'_3)/3$, the soil type, and the plasticity index, *PI*. Some or all of these dependencies are reflected in various moduli degradation and damping curves (known as G–γ–D curves) that have been developed based on laboratory test data.

To incorporate this behavioural model in analysis practice, linear site response analysis iterations are performed to determine the values of G_{sec} and ξ that are compatible with the effective shear strain level induced by a given excitation in each layer of material. This procedure will be better illustrated in the next.

3.5.2.2 Implementation

In light of the fundamental dependence of G_{max} on p', variation of G_{max} with depth is additionally introduced in the equivalent-linear models using the empirical relationship proposed for sands by Seed & Idriss (1970)

$$G_{max}(z) = 220 K_{2,max} \sqrt{p'} \tag{3.23}$$

where $K_{2,max}$ = empirical parameter that depends on the relative density, D_r, of the soil.

To generate a $V_s(z)$ profile, a different ρ corresponding to a different density state—loose, medium or dense—is specified for each soil deposit of Site 1, according to **Table 3-2**. Using then Eq. (3.23) and the relationship $V_s = \sqrt{G_{max}/\rho}$, three different vertical wave speed profiles are generated and equal number of Site 1 cases is drawn from their combinations, all other factors unchanged and excluding the homogeneous cases. The continuous and discretized V_s profiles derived for one of these cases are plotted in **Figure 3-4**a. To discretise the continuously nonlinear V_s profiles, each soil deposit is divided into layers with depths not exceeding 10 m. For Site 2, only the valley response is assumed equivalent-linear; again, different ρ are assigned to it to

generate the vertical V_s profile. The bounding stiff soil is assumed linearly elastic and homogeneous.

A four-parameter model proposed by Darendeli (2001) is chosen to represent the G–γ–D relationships over others available in the literature for it is analytic, pressure-dependent, and generally statistically robust. The normalised modulus degradation curves derived from this model are based on a modified version of the hyperbolic model (Hardin and Drnevich, 1972) for cyclic nonlinear soils, and are calculated as

$$\frac{G}{G_{max}} = \frac{1}{1 + \left(\frac{\gamma}{\gamma_{ref}}\right)^{a}} \tag{3.24}$$

where $\gamma_{ref} = \gamma_{G/G_{max}=0.5}$, $a =$ curvature coefficient to correct the shape of the backbone curve. The expression providing the material damping curves includes a hysteretic part, which is calculated assuming Masing behavior, and a small-strain part; it is given by

$$D = b\left(\frac{G}{G_{max}}\right)^{0.1} D_{Mas} + D_{min} \tag{3.25}$$

in which the first term on the right represents the hysteretic part and D_{min} the small-strain part.

To generate a family of Darendeli curves for each soil deposit, an averaged p' is estimated for each discretised layer and a different G–γ–D curve is assigned to it, as illustrated in **Figure 3-4**b for a soil of a Site 1 model case. The sensitivity of the results to the number of curves used was evaluated and it was found that generating curves for p' taken every 10 m is a nearly-optimal choice.

For the actual computation of the site response, QUAD4M (Hudson et al., 1994) is employed, which is a unique computer code that is capable of time-domain finite-element analysis of the equivalent-linear response of 2-D site domains. QUAD4M operates only with a CLI that accepts model input files with a predefined syntax, lacking a graphical mesh generator. To facilitate the creation of irregular meshes, a

one-way interface is developed between QUAD4M and GiD, a Windows-based pre- and post-processor providing capacity for generic mesh generation. Details of this interfacing is provided in Appendix B, along with the necessary scripts and instructions to implement it.

The computation procedure encoded in QUAD4M is described in the following steps:

(1) An initial linear model is set up with ${G_{sec}}^{(1)}$ and $D^{(1)}$ corresponding to the low-strain values G_{max} and D_{min}, respectively. This model is solved for the input excitation and the histories of *maximum* shear strain are computed for each soil element j as

$$ {\gamma_{max}}^{(1)} = \sqrt{(\varepsilon_{xx} - \varepsilon_{yy})^2 + \varepsilon_{xy}^2} \tag{3.26} $$

(2) An *effective* strain measure to characterise the overall induced strain level in each soil element is defined by factoring down the peak amplitude of γ_{max} over the history as

$$ {\gamma_{eff}}^{(1)} = f_\gamma \max_t \left| {\gamma_{max}}^{(1)} \right| \tag{3.27} $$

where the factor f_γ is given the empirical value 0.65.

(3) From ${\gamma_{eff}}^{(1)}$, new equivalent-linear ${G_{sec}}^{(2)}$ and $D^{(2)}$ are traced in the specified G–γ–D curves. The updated ${G_{sec}}^{(2)}$ and $D^{(2)}$ are used for the second analysis iteration and steps (1)-(3) are repeated until strain-compatible properties are achieved.

The convergence to strain-compatible properties should normally be verified by comparing at the end of each iteration the percentage difference between the previous and the updated properties to a certain threshold. Since there is no built-in routine for this in QUAD4M, a prescribed number of iterations is set. This number is varied

empirically between 12 and 25 across the models and convergence is judged by inspection of ${G_{sec}}^{(i)}$ and $D^{(i)}$.

3.6 Aspects of the finite-element models

3.6.1 Discretization and mesh convergence

A critical aspect in the development of credible finite element models for seismic wave propagation is the choice of the element size. This is determined by the shortest wavelength of interest and is practically limited by the available computing power and time. Apparently, a coarse mesh with element nodes located far apart from each other in the direction of wave propagation is inadequate to resolve fine wavelengths.

In this study, the mesh resolution in the z-direction is chosen in a way to ensure representation of wave frequencies up to 12.5 Hz for the range of the examined V_s. For this purpose, the rule of thumb is adopted that at least eight elements must resolve the shortest wavelength of interest (Kuhlemeyer and Lysmer, 1973). This means that the smallest element length used is about 1 m. A mesh of comparable refinement is implemented in the x-direction to ensure low element aspect ratios. A structured mesh with bi-linear, reduced-integration quadrilateral elements is used for Site 1. Triangular elements are additionally used for Site 2 models to accommodate discretisation of the regions around the dipping slopes. A mesh with progressively decreasing element size towards the ground surface is adopted for the equivalent-linear sites that have a non-constant V_s profile.

Indicative meshes for both site scenarios are pictured in **Figure 3-5**. The lateral truncation of the medium is carried out so as to satisfy convergence of the axial ground strain profile at the surface, $\varepsilon_{xx}(x,0)$, and of the first natural frequency of the site. To illustrate this approach, **Figure 3-6** shows the results of the convergence study undertaken to identify the ideal domain width for Site 1 equivalent-linear models. Distributions $\varepsilon_{xx}(x,0)$ and $u_x(x,0)$ are plotted for models with $L = 100, 150, 250$ m,

all other conditions being identical. For simplicity, the G–γ–D curves by Seed and Idriss are employed here, which are independent of p'. Clearly, $\varepsilon_{xx}(x,0)$ converge for all model widths inside a 200-m-wide zone, while $u_x(x,0)$ for the 300-m-wide model approaches better that of the more accurate 500-m-long model. Consequently, equivalent-linear models are assigned a half-width of $L = 150$ m to limit the computing time.

3.6.2 Boundary conditions

The choice of boundary conditions is a crucial decision in any dynamic finite-element analysis. This is particularly true for the case of unbounded media, where fictitious boundaries need be introduced to make the model finite and controllable in terms of size. In problems of wave propagation through the ground, wave radiation is an important physical mechanism of energy dissipation (geometric damping) and should be duly considered in numerical models to prevent trapping of wave energy inside the finite domain, an effect that would cause unphysical response. Elementary boundaries imposing conditions of zero traction or displacement at the boundaries of the finite domain are unable to serve this purpose, unless they are placed very far from the region of interest. Exception to this is when fully rigid layers, such as stiff bedrock at the base, are assumed to bound the analysed domain, causing total reflection of all travelling waves.

There is a plethora of methods for modelling so-called absorbing or transmitting boundary conditions. Here, local absorbing boundaries (Lysmer and Kuhlemeyer, 1969) in the form of normal and tangential viscous dashpots are assigned at the base of the linear and equivalent-linear models to model radiation of downward propagating seismic waves to infinity. Considering without loss of generality a bottom horizontal boundary as shown in **Figure 3-7**, these boundary viscous dashpots are formulated in terms of stresses as

$$\sigma_n = \rho V_p \frac{\partial w}{\partial t}; \quad \tau = \rho V_s \frac{\partial u}{\partial t} \tag{3.28}$$

where σ_n, τ represent the normal and tangential stress components at the boundary; ρ, V_p, V_s refer to the layer of material immediately outside the bounds. They yield exact results, i.e. perfect energy absorption, only for non-dispersive waves incident at the boundary at a normal angle. For all other wave cases, their effectiveness is reduced, but better results can be obtained again by placing them at a distance from the region of interest. Regardless, viscous dashpots offer a fair balance between accuracy and computational efficiency; they are also well suited for finite-element implementation in the time domain and for these reasons are preferred here.

For the lateral boundaries of the linear elastic models, a hybrid approach was chosen with viscous dashpots connected one-to-one to the nodes of a 1-D soil column representing the far-field soil, as proposed in Papadopoulos *et al.* (2017). As QUAD4M does not offer a similar facility, horizontal sliders were assigned at the nodes of the lateral boundaries which allow unrestrained horizontal motion while preventing vertical motion. Despite the obvious shortcoming of this approach, it is believed that the width of the domain is large enough to allow effective dissipation of any spurious wave reflections by material damping, an expectation that is strengthened by the amplified ξ due to equivalent-linear response.

3.6.3 Damping

While soil damping is known to be frequency-independent even at low strains, the reliance of this study on time-domain analysis tools necessitates the use of frequency-dependent damping. Small-strain damping in the linear models and hysteretic damping in the equivalent-linear models are assumed to be of the viscous Rayleigh type. According to this classical damping model, the damping matrix of the system is determined by linear superposition of the mass and stiffness matrices as

$$\mathbf{C} = a_M \mathbf{M} + b_K \mathbf{K} \tag{3.29}$$

where the mass- and stiffness proportional coefficients, a_M and b_K, are tuned to achieve a match between the Rayleigh damping ratio, ξ, and a target hysteretic damping ratio, ξ_{target}, at two significant frequencies ω_i and ω_j. A system of algebraic equations results from this approach that can be solved to yield the Rayleigh coefficients as

$$a_M = \xi \frac{2\omega_i \omega_j}{\omega_i + \omega_j}; \qquad b_K = \xi \frac{2}{\omega_i + \omega_j} \tag{3.30}$$

In this case, the significant frequencies are taken to be the frequency of the first (undamped) vibration mode $\omega_{N,0}$ and $n \times \omega_{N,0}$, where n is the next greater odd integer than $\omega/\omega_{N,0}$, ω being the predominant exciting frequency. This choice of frequencies is adopted by default in QUAD4M and is motivated by the fact that the higher natural frequencies of a soil column responding as a shear beam are odd multiples of the fundamental one. The value of ξ_{target}, as already mentioned, is either 2% or 5% in linearly elastic models, while it is strain-compatible in equivalent-linear models.

3.6.4 Input excitations

To gain understanding into how the induced ground deformation patterns of the sites may be influenced by the characteristics of the excitation, pulse-like waveforms with a narrow frequency bandwidth and a dominant frequency are used as input to the linearly elastic models. Specifically, Ricker wavelets are employed for this purpose, with their acceleration history expressed as

$$\ddot{u}(t) = a[1 - 2\pi^2 f_o^2 (t - t_0)^2] e^{-i\pi^2 f_o^2 (t-t_0)^2} \tag{3.31}$$

where a = amplitude, f_o = the characteristic frequency and t_0 = the time instant that the peak occurs.

Preliminary dynamic elastoplastic analyses with incrementally adjusted shaking intensities revealed that appreciable nonlinear response is not triggered in the sites considered until the bedrock acceleration exceeds roughly 0.05g. The elastoplastic soil models used in these analyses employed a pressure-dependent von Mises yield criterion,

an associated plastic flow rule and nonlinear kinematic hardening, and were calibrated to given G–γ–D curves (Anastasopoulos *et al.*, 2011). Representative results in the form of shear stress-strain loops are shown in **Figure 3-8**. The response is plotted at element locations where the maximum and minimum shear strain is computed throughout the straining history. It is seen that a 0.05 g input generates essentially linear soil response at both locations. All input accelerations are scaled to this threshold amplitude for the linear elastic analyses to remove the effect of shaking amplitude on ground deformation.

The same wavelets are used for equivalent-linear analysis but scaled to $a = 0.2$g and $a = 0.3$g in order to trigger nonlinear effects (**Figure 3-9**). Although in strict terms a pulse-like ground excitation (characteristic of near-source sites) and a plane wave front (prevalent in far-source sites) appear somewhat contradicting assumptions, they are both adopted in this study to simplify modelling and facilitate interpretation of results. In addition, three strong, far-source ground motion records (with distance to source $d_w > 10$ km) with varying mean periods, T_m, calculated according to Rathje et al. (1998), are selected as input to the equivalent-linear models (**Figure 3-10**). Their properties are presented in **Table 3-3**.

The use of local absorbing boundaries requires application of the input excitation as equivalent nodal force histories proportional to velocities, as $f_b(t) = \rho V_s \dot{u}_b(t) A_{trib}$, where A_{trib} is the tributary area of each node. Therefore, the earthquake acceleration records retrieved from online databases are integrated in time to obtain the velocity records first.

The system of N simultaneous algebraic equations, where N is the number of degrees of freedom (DOF) in the system, to be solved in this case is given in Eq. (3.19) and is restated here

$$\mathbf{M}\ddot{\mathbf{U}}(t) + \mathbf{C}\dot{\mathbf{U}}(t) + \mathbf{K}\mathbf{U}(t) = \mathbf{P}_{\text{ext}}(t) \tag{3.32}$$

where

$$\mathbf{P}_{\text{ext}}(t) = \boldsymbol{\mathcal{I}} \mathrm{c_d} \dot{\mathbf{U}}_{\mathrm{b}}(t)$$

in which $\mathrm{c_d} = \rho V_s$ is the absorbing dashpot coefficient per unit area; $\dot{\mathbf{U}}_{\mathrm{b}}(t)$ = the vector of applied velocity histories at the base nodes; $\boldsymbol{\mathcal{I}}$ = the 'influence' vector containing ones for all base nodal DOFs and zeros for all other DOFs.

3.6.5 Time-integration scheme

Direct numerical integration of Eq. (3.32) is carried out using the Newmark-β method for $\beta = 1/4$ and $\gamma = 1/2$ (constant average acceleration), which is an implicit method made explicit for linear systems and is unconditionally stable. This choice of parameters ensures zero numerical damping, quadratic convergence, and no upper bound on the time step, Δt.

For $\beta = 1/4$ and $\gamma = 1/2$, the system responses in step $i+1$ are written in terms of the known response in step i as

$$\ddot{\mathbf{U}}_{i+1} = \frac{4}{(\Delta t)^2}(\mathbf{U}_{i+1} - \mathbf{U}_i) - \frac{4}{\Delta t}\dot{\mathbf{U}}_i - \ddot{\mathbf{U}}_i \tag{3.33}$$

$$\dot{\mathbf{U}}_{i+1} = \frac{2}{\Delta t}(\mathbf{U}_{i+1} - \mathbf{U}_i) - \dot{\mathbf{U}}_i \tag{3.34}$$

$$\widehat{\mathbf{K}}\mathbf{U}_{i+1} = \hat{\mathbf{P}}_{i+1} \tag{3.35}$$

where

$$\widehat{\mathbf{K}} = \mathbf{K} + \frac{4}{(\Delta t)^2}\mathbf{M} + \frac{2}{\Delta t}\mathbf{C}$$

$$\hat{\mathbf{P}}_{i+1} = \mathbf{P}_{i+1} + \left(\frac{4}{(\Delta t)^2}\mathbf{M} + \frac{2}{\Delta t}\mathbf{C}\right)\mathbf{U}_i + \left(\frac{4}{\Delta t}\mathbf{M} + \mathbf{C}\right)\dot{\mathbf{U}}_i + \mathbf{M}\ddot{\mathbf{U}}_i$$

For accuracy and resolution, the value of Δt in all linear analyses is taken equal to the time step of the time-histories of the input excitations.

3.6.6 Model verification

In the absence of exact elastic or viscoelastic solutions for the particular wave propagation problem at hand, the accuracy of the predictions obtained from the 2-D site response models is gauged against 1-D closed-form, frequency-domain solutions (transfer functions), for laterally uniform soil layers subjected to unilateral base shear excitation.

A 1-D site response model of a typical flat-layered site over elastic half-space, with strain-compatible properties predicted by the Seed and Idriss curves, is developed in DeepSoil (Hashash *et al.*, 2016). The site is subjected at its base to a suite of two recorded earthquake ground motions: one from the 1994 Northridge earthquake (CDMG station) and one from the 1979 Friuli earthquake (Tolmezzo station); their properties are listed in **Table 3-3**. The computed response is compared to that obtained by the 2-D site analogue modelled in QUAD4M.

Figure 3-11 shows the surface-to-bedrock transfer functions. Although the 2-D model over-predicts the response by a maximum of 27% at an intermediate frequency range bounded by the target Rayleigh frequencies, a good match in terms of shape is observed. The above marked discrepancies are attributed to underdamping of the 2-D response as a result of the frequency-dependent nature of the Rayleigh damping formulation.

3.7 Results for free-field response

Due to the breadth of the produced output, results are presented in various formats to highlight different features of interest each ctime. Response parameters are plotted against the transformed horizontal coordinate $\bar{x} = (x - L)/L \in [-1,1]$.

The parameters used for all equivalent-linear models are found in **Table 3-4** for Site 1 and

Table 3-5 for Site 2, respectively. The site impedance ratio is the ratio of the products $\rho \times V_{s,30}$ of two adjacent deposits, where $V_{s,30}$ is the average S-velocity of the uppermost 30 metres of the deposit. The different models are identified with the notations $[SiLj]$ and $[SiELj]$, where S stands for site, L/EL stand for linear/equivalent-linear soil and i, j are integers denoting the site and the case ID, respectively.

3.7.1 Linearly elastic models

Figure 3-12 shows the envelopes of the peak tensile and compressive axial strains along a horizontal path of nodes located at a depth $h = 1$ m from the surface for a number of Site 1 cases. **Figure 3-13** shows the same for Site 2 cases. Note that the values plotted are not concurrent. All cases exhibit peak strains in the softer of the two soils, in close proximity to their vertical interface. Tensile strains are nearly exact reflections of the compressive strains. Considerable strains are observed near the lateral

boundaries in some cases and this might indicate influence of the imperfect absorbing boundary conditions.

With regard to Site 2, peak surface strains are identified over the wedge toes; strain values become very small in the stiff soil and in the middle, where the horizontal displacements attain their peaks due to the constructive interference of Rayleigh waves, whose presence will be explained later. In both sites, strains are greater for higher impedance ratios and lower a_0. Note also that when $\rho_1 V_{s,1}/\rho_2 V_{s,2} = 1$ and $\theta = 0$, all normal ground strain fields become everywhere zero as both sites collapse to the homogeneous soil case subjected to vertically propagating SV-waves.

Figure 3-14 plots seismogram synthetics of the horizontal accelerations at the surface of the sites for cases of synchronous bedrock input. It can be seen for Site 1 that a coherent input generates highly non-synchronous ground motions at the surface, associated with pronounced axial strains. A clearer picture of the wave patterns for Site 1 is provided in **Figure 3-15**, where contours of the shear and vertical normal strain fields are displayed at different times. As can be seen in the top left figure, the wave front forms an oblique transition zone at the inhomogeneity boundary due to the different propagation velocities in the soft and firm soils. Mode conversion occurs inside the transition zone generating a P-wave that travels upwards and gives a so-called 'parasitic' vertical motion component at the surface. Apparent in the softer deposit are the successive reflections of the oblique SV- and P-wave fronts at the surface and the bedrock interface.

The situation for Site 2 with $V_{s,1} = 70$ m/s and $V_{s,2} = 800$ m/s is more complex, as pictured in **Figure 3-14**b. Upon the first incidence of the wave at the sloping interface, mode conversion produces SV- and P-waves. The refracted rays arrive at the surface and interfere with the vertically impinging rays arriving from the valley centre (focusing effect). Further mode conversion of the oblique wave fronts occurs at the free surface and subsequently at the valley-rock interface, resulting in trapping of the waves inside the valley and prolongation of the response. More importantly, Rayleigh waves—identified with green dashed lines—are locally generated at the top of the basin edges,

as first shown in great detail by Bard & Bouchon (1980) for 'Type 2' basins, which closely resemble the basin geometry adopted here. In fact, two phases of these waves are generated and are seen to travel back and forth along the basin surface, with phase velocities graphically estimated at 120 and 67 m/s. The symmetry of the domain results in maximum motion amplification at the valley mid-span due to constructive interference of the Rayleigh waves.

To demonstrate the presence of Rayleigh waves in a more illustrative way, particle trajectories in the xz-plane of three different valley nodes located 13 metres away from the left valley edge are plotted in **Figure 3-16** at successive time windows. It is observed that the nodes undergo retrograde quasi-elliptical trajectories with motion amplitudes decreasing with depth, as expected of a fundamental Rayleigh mode. The dominant displacement component in this case is the horizontal. The ground motion synthetics display similar qualitative characteristics as found in other studies (e.g. Gelagoti *et al.*, 2010; Makra and Chavez-Garcia, 2016).

Figure 3-17 presents the time-evolution of the elastic ground axial strains at the surface of a Site 1 model with $H = 60$ m, $V_{s,1}/V_{s,2} = 1.4$, $l_t/H = 0.16$, $\theta = 0$ and $\xi = 2\%$. As one would expect, the out-of-phase horizontal movement of the two deposits generate alternating tensile-compressive strain near the vertical boundary, and more so towards the softer of the two deposits. The axial strains attain their peaks early during the first direct pulse arrival and then decay with time. In **Figure 3-18**, the instantaneous longitudinal distributions of the axial strains and horizontal displacements at depth h, corresponding to time instant t_{cr}, are plotted for the most unfavourable model cases of the two sites. While the axial strain magnitudes for the two sites are comparable, the distributions are different; a pipeline buried in Site 1 would be primarily subjected to axial compression at the critical timeframe, while the same pipeline buried in Site 2 would experience an anti-symmetric state of stress with respect to the middle of the site.

An interpretation of the results of the parametric study for the linearly elastic models is provided next. The influence of the dimensionless parameters established in

subsection 3.5.1 on the peak axial compressive strains, $\varepsilon_{c,max}$, is investigated. Representative results are collectively illustrated in **Figure 3-19**.

Effect of exciting frequency

The effect of the frequency content of the seismic input on $\varepsilon_{c,max}$ is found to be major in all cases. Low-frequency disturbances produce consistently larger peak axial strains, regardless of the soil impedance ratio and ξ, as illustrated throughout **Figure 3-19**. This is accentuated by the fact that *PGA*-scaling of the input motions is adopted, thus, for the same PGA, a high-frequency acceleration, when integrated twice, will naturally give smaller displacements than a low-frequency acceleration. Another feature of interest prevalent in many plots (e.g. a, b, d, h) is that the curves attain their maxima at the fundamental resonant frequency, that is, when $a_0 \approx 1$. Therefore, it can be said for the overall soft soils examined here that it comes as no surprise that low-frequency excitations tend to induce larger surface motion and deformations.

Effect of site impedance ratio

The site impedance ratio proves to be a defining factor for the level of $\varepsilon_{c,max}$ induced in both sites. The larger the impedance ratio, the greater the axial strain at the interface (**Figure 3-19**a and b). However, it is not only the relative stiffness of the site that controls the strain magnitudes, but also the absolute stiffness. This is inferred from the fact that sites with similar velocity contrasts but different absolute velocities sustain different axial strain levels. Overall, softer sites of type 1 or 2 develop larger normal strains than stiffer ones with similar velocity contrasts under the same bedrock excitation. **Figure 3-19**a demonstrates this fact: a Site 1 model with velocities of 70 and 100 m/s develops 1.36 to 2.14 times larger normal strains than a model with velocities of 140 and 100 m/s – depending on the exciting frequency, the two sites having roughly the same velocity contrast ($1/0.7 = 1.43 \approx 1.4$).

Effect of the spatial rate of change of stiffness (Site 1)

For Site 1, the impact of the extent of the transition zone between the two deposits was investigated. Introducing a transition zone for G_{max} as a parameter and varying G_{max} linearly from value G_1 to G_2 had imperceptible effects on the computed

$\varepsilon_{c,max}$ as compared to the case of abrupt transition, as depicted in **Figure 3-19**e. For this reason, all equivalent-linear models henceforth employ an abrupt transition to simplify modelling.

Effect of dipping slope (Site 2)

Figure 3-18f shows that steeper basins produce lower $\varepsilon_{c,max}$ for an intermediate range of wavelengths; on the other hand, $\varepsilon_{c,max}$ appears insensitive to s for other frequencies in the bandwidth examined. To provide further insight into the ambiguous effects of s on $\varepsilon_{c,max}$, complex steady-state analysis is performed in ABAQUS (based on the formulations detailed in Appendix A) for two Site 2 models with identical impedance ratios but different dimensionless frequencies a_0. Two s values are examined for each case as in the previous. The results are plotted in **Figure 3-20** in the form of distributions of surface axial strain magnitudes along the left half of the valley, since the response is symmetric. The strain magnitudes are normalised with respect to the peak magnitude in each graph. It can be seen that the effect of s on $\varepsilon_{c,max}$ depends in complex ways on a_0. For $a_0 < 1$, the steeper basin produces higher strain peaks, whereas for $a_0 > 1$ and up to ~2.5, the trend reverses. For a_0 higher than ~2.5, the distributions become complex and it is impossible to identify trends.

Effect of wave incidence angle

An obliquely impinging wavefront seems to have a somewhat obscure effect on the axial strains, depending on whether the wave passage contribution is additive or not to the local site effect contribution, but is in general terms minor for both sites (**Figure 3-19**g and h). The additional strains due to oblique incidence are smaller by an order of magnitude than those attributed to material inhomogeneity; this has been verified by direct comparison of the peak strains induced in homogeneous sites for $\theta \neq 0$ to the peak strains induced in inhomogeneous sites for $\theta = 0$. For instance, for the equivalent homogeneous soil case to the one whose results are plotted in **Figure 3-19**g and with $a_0 = 2.4$, $\varepsilon_{c,max}$ was computed 1.2×10^{-4} and 1.7×10^{-4} for $\theta = 20°$ and $\theta = 30°$, respectively. One may also consider the analytical expression for the peak normal

ground strain in homogeneous elastic isotropic soil due to SV-waves incident at an angle θ, given in **Table 2-2** as

$$\frac{\dot{u}_{max}}{V_s}\sin\theta\cos\theta$$

where $\dot{u}_{max}$ is the maximum ground velocity; the difficulty here lies in determining $\dot{u}_{max}$ without resort to 2-D site response analysis. NCHRP (National Academies of Sciences, 2008) recommends an empirical expression that correlates $\dot{u}_{max}$ with spectral acceleration at a period of 1s. Alternatively, exact solutions for the ground strain field exist for plane time-harmonic waves propagating in elastic half-space (Achenbach, 1973).

3.7.2 Equivalent-linear models

In employing equivalent-linear models, the focus is shifted from qualitatively investigating the key attributes of the site deformation under low-amplitude vibration to determining the levels of deformation that can be experienced by the ground surrounding a buried pipeline during likely strong earthquakes. A suite of analyses of sites with equivalent-linear properties is conducted in order to identify the cases generating the most critical load on the pipeline.

Before presenting results in terms of deformation, a qualitative comparison of the spatial distribution of the obtained ground response with similar studies in the literature is warranted. Gelagoti *et al.* (2010) developed and validated numerical models of the Ohba Valley, a very soft valley in Japan, to study the seismic wave propagation effects. This valley is similar in geometry and soil properties with Site 2 of this thesis. Using both linear and equivalent-linear soil properties, they produced peak ground response distributions at the surface in terms of 'aggravation factors', that is, the ratio of PGA from 2D analysis to the equivalent result from 1D analysis, due to Ricker wavelet excitations of various frequencies. To facilitate a plausible juxtaposition, **Figure 3-22** plots the surface horizontal PGA distribution for model S2EL10 assuming both equivalent linear and linear elastic soil properties. These

distributions are to be contrasted to Figures 6a and 13a in Gelagoti *et al.* (2010) which refer to response to a 3-Hz Ricker wavelet. A fair agreement is observed between the two sets of results, with PGA amplification diminishing when considering an equivalent-linear model. Amplification in the equivalent-linear soil is seen to peak above the valley edges while attenuating in the centre. Note that the two studies use different G–γ–D models.

Figure 3-21 plots the ground axial strain field on the surface for two typical site models (S1EL10 and S2EL8) subject to 0.2 g Ricker pulses. Clearly, for Site 1, the strain distribution shows heavy localisation towards the middle boundary, with large positive and negative peaks reaching 2.1% and -1.3%. For Site 2, one may observe that the focusing-induced strain peaks above the wedge toes seen in the case of the elastic models are now suppressed, while strains towards the sharp valley-rock interface are amplified, with peak magnitudes comparable to those of Site 1.

Figure 3-23 presents the critical distributions of $\varepsilon_{xx}(x)$ and $u_x(x)$ of the site models with the highest impedance ratios and subjected to recorded strong ground motions; the peak values of compressive strains are marked as well. It is seen that, for Site 1, the critical $u_x(x)$ occurs when the vibrations of the adjacent soil deposits are nearly out of phase, as manifested by the step-like shape of the profile. At this time instant, a sharp strain spike develops almost right at the boundary, as shown in the top left plot. This behaviour is a direct consequence of the degradation of G-modulus with increasing strain levels, assuming that an incremental change in the Young's modulus, E, is linearly related to an incremental change in G.

This effect is better illustrated in **Figure 3-25**, which plots the longitudinal profiles of the converged G/G_{max} for two Site 1 cases subjected to 1-Hz-Ricker wavelets, one at 0.2 g and one at 0.3 g. In the converged solution for the 0.2 g pulse, the ground experiences at depth h an average maximum shear strain of roughly 0.3% in the soft and 0.04% in the firm deposit, resulting in mean G/G_{max} of 33% and 68%, respectively. It is observed that G/G_{max} drops significantly as $x \to 0$, more so for the

0.3g-pulse, with unrealistically small values computed right at the interface of the soils. This can be explained by considering that, during a marked axial contraction phase, an increment in the horizontal normal stress $\Delta\sigma_h{}'$ develops locally, which raises the confining pressure to $p' + \Delta p'$; recalling the dependence of G/G_{max} on p' (see **Figure 3-4**), it is to be expected that G/G_{max} would drop more mildly. These observations point to the conclusion that the 2-D equivalent-linear site response models developed here yield rather conservative results, and the very large axial strains computed at the soil interfaces should not be taken at face value.

The deformation pattern in the soil is not so simple for Site 2. A state of anti-symmetry with respect to the middle of the valley is apparent in the critical strain profile shape, meaning that a sharp compressive strain peak develops at one valley edge while a sharp tensile strain peak of roughly equal magnitude at the other edge.

To illustrate some further important characteristics of the response, **Figure 3-26** plots the critical profiles $\varepsilon_{xx}(x)$, $u_x(x)$, $\kappa_x(x)$ (= axial curvature) and $u_y(x)$ of models S1EL11, S1EL12, S1EL14, which refer to 0.3g-Ricker pulse input. It is seen that significant vertical dislocation of soil mass, comparable to the horizontal one, occurs at the critical time instant in a short zone around the soil border, producing a sharp curvature peak. This is to demonstrate the importance of the vertical component of motion (thrust), which can potentially modify the pipe response. It is also observed that model S1EL12 undergoes the largest deformation among the three models; this is due to mechanical resonance, as the first natural frequency of this site is very close to 1 Hz, which is the characteristic frequency of the exciting Ricker pulse.

The above numerical results have been obtained using a varying number of iterations. To corroborate the converging nature of the equivalent-linear soil properties, it is mentioned at this point that in all cases examined, the final (at the last iteration) average absolute deviation over all elements for both G_{sec} and ξ did not exceed 0.1% in Site 1 models and 0.98% in Site 2 models. A few outliers were present though in most analyses, as it is understood that it is very difficult to satisfy absolute convergence simultaneously in a mesh consisting of more than 5000 elements. Nevertheless, the

maximum deviations recorded were not excessive: 19% for G_{sec} and 7% for ξ for Site 1, and 15% for G_{sec} and 4% for ξ for Site 2. The equivalent material properties converged always worse for the stronger input excitations as expected. For illustration purposes, the degree of convergence G_{sec} and ξ in all elements is mapped in **Figure 3-27** and **Figure 3-28** for models S1EL3 and S2EL0. The contours represent the percent deviation of the final values of the equivalent linear properties from the previous iteration. It is observed that for model S1EL3, ξ converges very well everywhere, while G_{sec} exhibits deviations of up to 19% in a limited number of elements close to the surface. A similar situation is evident in model S2EL0, where generally convergence is slightly better. For these models, the material properties were iterated 12 times.

Summarising the key observations, the most severe soil deformation for both sites is found to result from input motions with low frequency content (such as the Imperial Valley record), just as in the linearly elastic sites. Most notably, the deformation is maximised when the excitation contains dominant frequencies close to the resonant frequencies of the site, while it is beyond doubt that higher impedance contrasts lead to larger deformation.

3.8 Summary of the chapter

In this chapter, the principal aspects of the adopted numerical methodology were highlighted, followed by development of numerical substructure I (global free-field model). A systematic study comprising 2-D site response analyses was conducted to determine the patterns of soil deformation due to seismic wave propagation in two laterally inhomogeneous sites, considering different material models and input excitations. The main findings drawn from the results are described below:

Linearly elastic soil

- In Site 1 models featuring a ramp lateral transition in soil stiffness, $\varepsilon_{c,max}$ develops in the softer soil deposit, very close to the separating interface, with

values from as low as 0.01% to 0.15%, which is in relative agreement with predictions for homogeneous sites reported elsewhere, e.g. Shinozuka et al. (1983). Wave mode conversion occurs inside the transition zone from the soft to the stiffer deposit, generating a P-wave that travels upwards and produces considerable vertical motions at the surface. Therefore, the critical load pattern for a pipeline buried in Site 1 would consist of a combination of differential horizontal soil displacements and a localized vertical displacement inside the transition zone.

- In Site 2, valley-type, cases, the anti-symmetric axial strain field at the surface is dominated by local wave scattering inside the valley, predominantly Rayleigh waves generated at the valley edges and propagating back and forth along the surface. The absolute peaks occur above the wedge toes and vary roughly from 0.01% to 0.11%. A pipeline buried in such a site would be subjected simultaneously to compression and tension along successive segments.

- The peak axial ground strain values depend mainly on the impedance contrast of the soil deposits and the resonant frequencies that greatly amplify oscillations. The absolute stiffness of the deposits is also a critical parameter, as the softer soils experienced consistently larger deformations. The worst-case soil deformations are obtained for a combination of large impedance ratios, soft soil deposits and long-period input motions. In contrast, the additional strains due to the wave passage effect are much smaller than those due to local site effects. Geometric parameters examined such as the transition zone length in Site 1 and the boundary slope in Site 2 are shown to also have minor influence on the deformation levels.

Equivalent-linear soil

- It is shown that, when considering nonlinearity in the cyclic soil behaviour under higher-intensity motions, the induced axial ground strains can be as much as two orders of magnitude larger (up to ~15%) than in linearly elastic soil, a difference attributed to the sharp decrease of the G-modulus with increasing cyclic shear strain.

- In Site 1, the axial strain profiles tend to be more localized towards the boundary of the two soils, producing a sharp peak. The horizontal displacement load pattern could be approximated with certain functional forms, such as a logistic or step function of x, to facilitate parametric pipeline buckling analyses. There is also considerable vertical ground movement concentrated around the separating interface, which would cause bending of a buried pipe

- In Site 2, wave-scattering effects are suppressed by the nonlinearity of the soil response and strain peaks are shifted towards the inclined rock-valley interface, with magnitudes comparable to Site 1. The anti-symmetric axial deformation shape remains.

- The severity and spatial profile of soil deformation as estimated using equivalent-linear soil models poses potentially greater risk to underground pipes cutting through the soil material interfaces.

- The degree of degradation of the G-modulus is overestimated very close to the material interfaces. Bearing in mind that the higher the level of confining pressure p', the slower the reduction of G with increasing shearing, it is understood that the increased soil pressure developing during compressive vibration would slow down the reduction of G. However, in the currently available analysis platforms, there is no capability to adaptively switch between different $G\text{–}\gamma\text{–}D$ curve during analysis according to the current p'.

- The computed axial ground strain profiles were found to be quite sensitive to the number of $G\text{–}\gamma\text{–}D$ curves assigned to the various layers of the model. Apparently, the larger the number of the curves used, the more refined the representation of the material properties is, which is particularly necessary at low depths from the surface where the rate of change of G is larger.

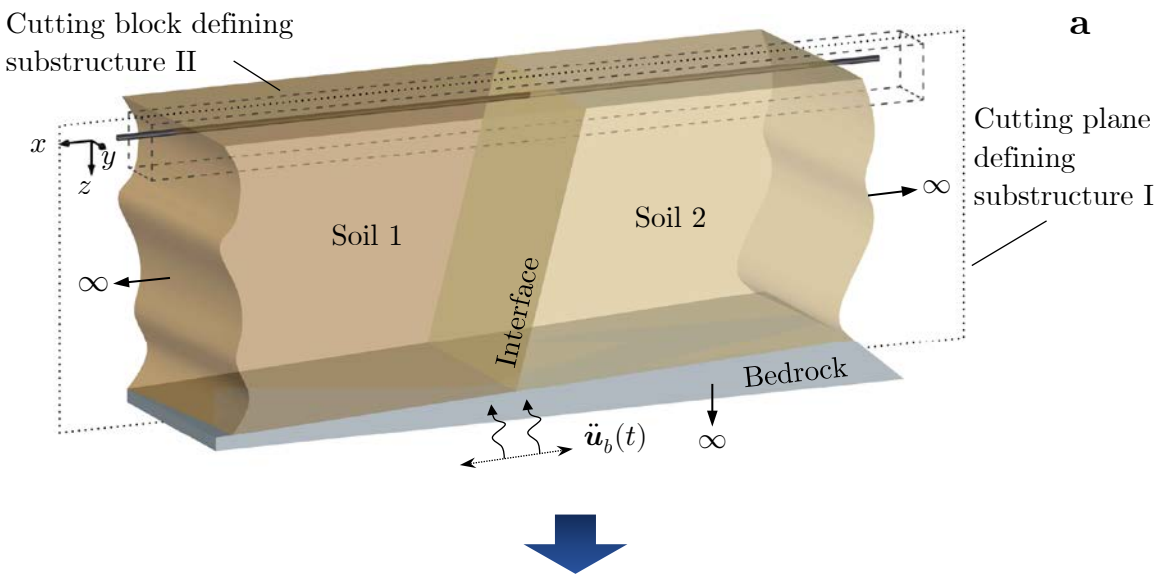
a
Cutting block defining substructure II
Cutting plane defining substructure I
x
y
z
Soil 1
Soil 2
Interface
Bedrock
∞
$\ddot{u}_b(t)$

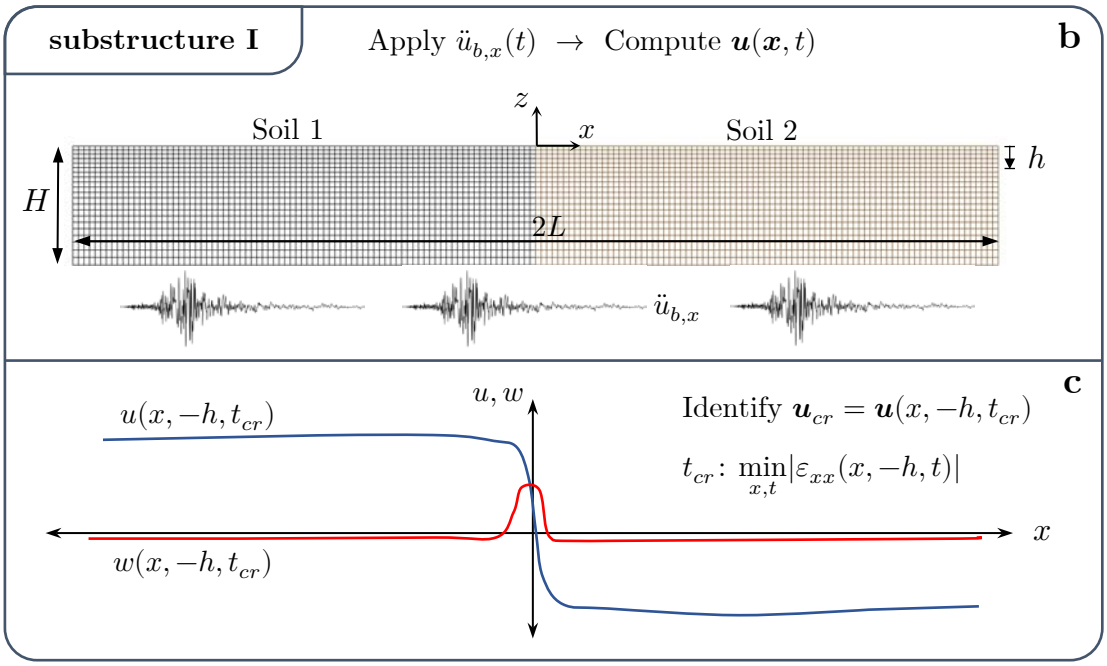
substructure I
Apply $\ddot{u}_{b,x}(t)$ → Compute $\boldsymbol{u}(\boldsymbol{x},t)$
b
Soil 1
Soil 2
H
h
2L
$\ddot{u}_{b,x}$
c
$u(x,-h,t_{cr})$
$w(x,-h,t_{cr})$
u, w
Identify $\boldsymbol{u}_{cr} = \boldsymbol{u}(x,-h,t_{cr})$
t_{cr}: $\min_{x,t}|\varepsilon_{xx}(x,-h,t)|$

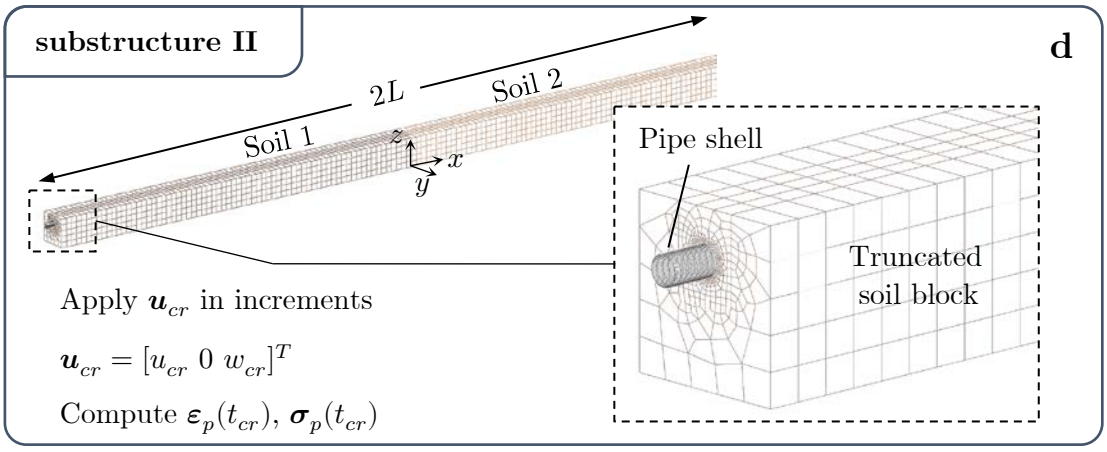
substructure II
d
2L
Soil 1
Soil 2
Pipe shell
Truncated soil block
Apply $\boldsymbol{u}_{cr}$ in increments
$\boldsymbol{u}_{cr} = [u_{cr}\ 0\ w_{cr}]^T$
Compute $\boldsymbol{\varepsilon}_p(t_{cr})$, $\boldsymbol{\sigma}_p(t_{cr})$

Figure 3-1. Flowchart of the proposed sub-structuring scheme: (a) idealization of the physical problem at hand; (b and c) substructure I: plane-strain site response analysis to earthquake excitation and extraction of the critical soil deformation profile at depth h; (d) substructure II: application of this profile as an incremental displacement field $\boldsymbol{u}_{cr}$ on the truncated 3-D soil portion to evaluate the pipeline response $\boldsymbol{\varepsilon}_p(t_{cr})$, $\boldsymbol{\sigma}_p(t_{cr})$ (meshes are indicative)

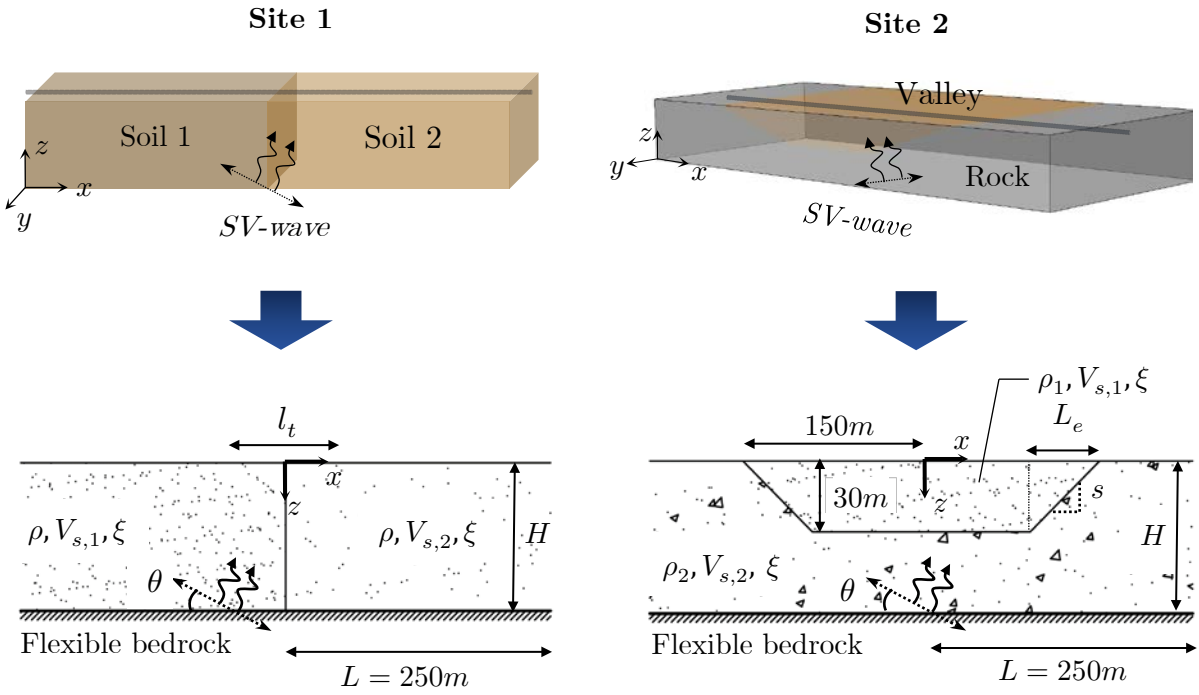

Figure 3-2. Perspective illustrations of the two sites considered and identification of key problem parameters for linearly elastic conditions: (a) Site 1 and (b) Site 2

Table 3-1. Values considered for the dimensionless parameters of the linearly elastic models

Scenario 1		Scenario 2	
a_0	0.6, 1.2, 2.4, 6, 12	a_0	0.43, 0.86, 1.7, 3.43, 4.3, 8.6
$V_{s,1}/V_{s,2}$	0.7, 1.4, 2, 4	$V_{s,1}/V_{s,2}$	0.0875, 0.175, 0.35
θ	0°, 10°, 20°, 30°	θ	0°, 10°, 20°
l_t/H	0.33, 1, 1.66	s	30%, 60%
ξ	2% , 5%	ξ	2%, 5%

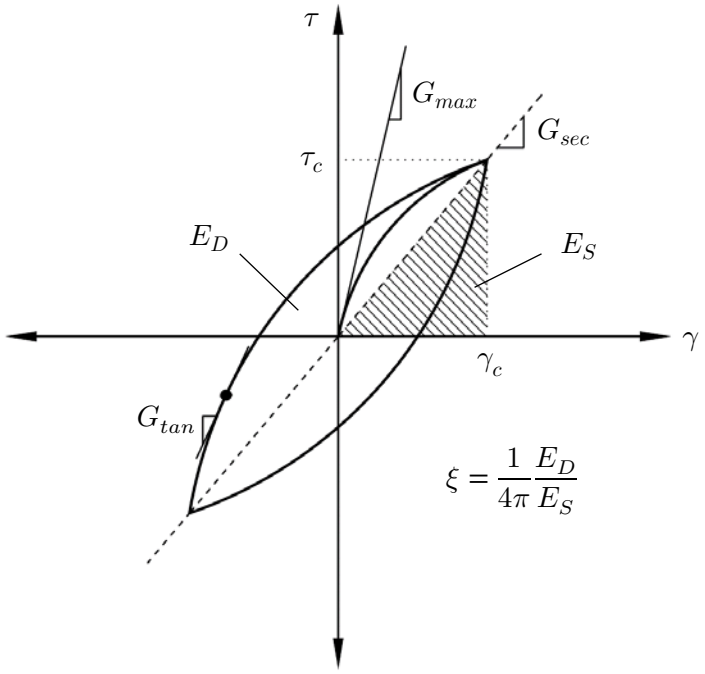

Figure 3-3. Ideal hysteretic loop of a soil under cyclic loading, showing the key descriptors of the response in the equivalent-linear approach

Table 3-2. Specification of parameters for the definition of vertical G_{max} profiles of the equivalent-linear models according to the relationship by Seed & Idriss (1970)

Sand state	ρ (Mg/m³)	D_r (%)	$K_{2,max}$ (-)
Loose	1.4	30	34
Medium	1.65	52.5	48
Fine	2	90	70

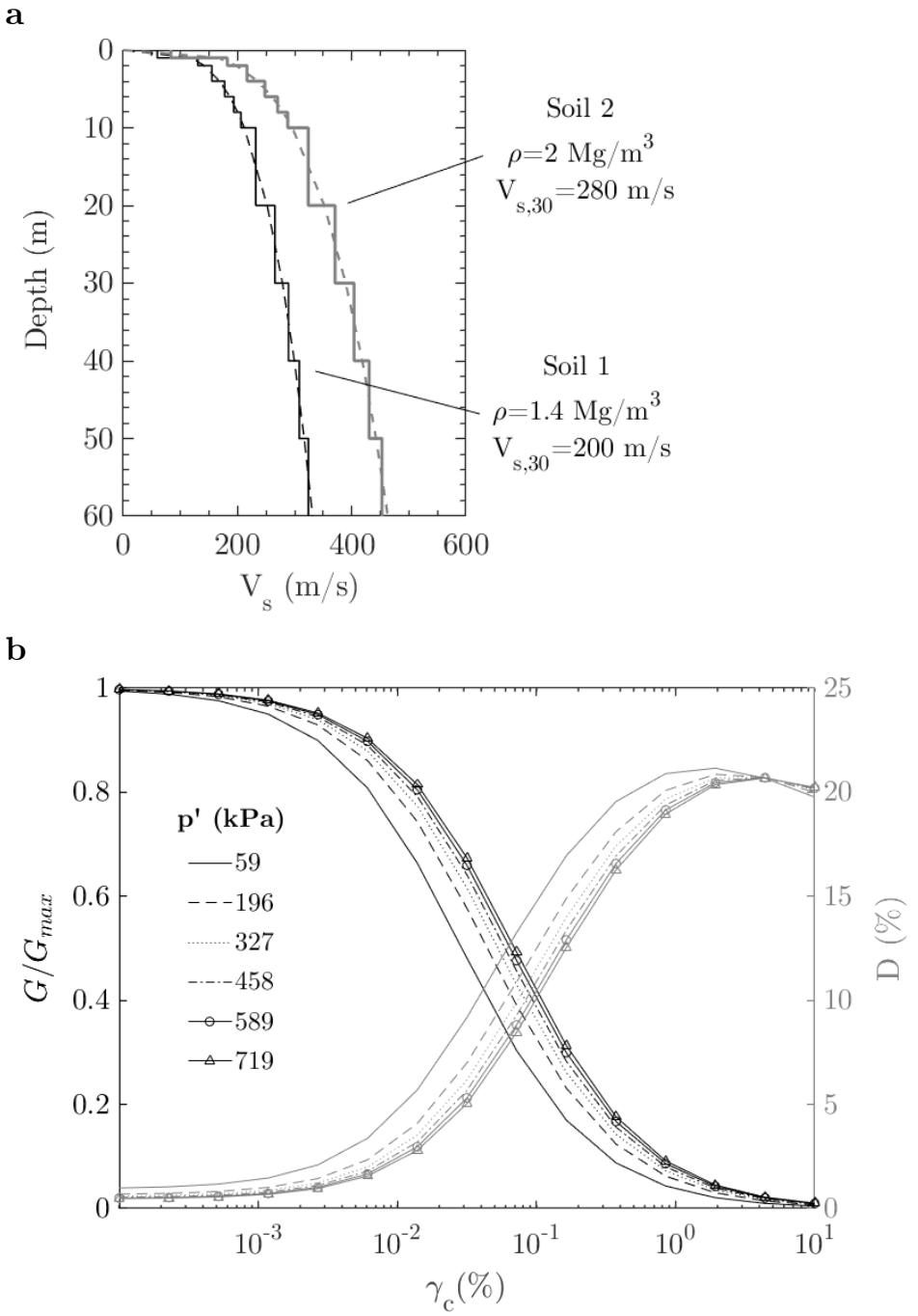

Figure 3-4. (a) V_s profiles generated for the two soils of a typical Site 1 model case; (b) G–γ–D curves calculated for different confinement levels in the firm soil (averaging is applied every 10 metres)

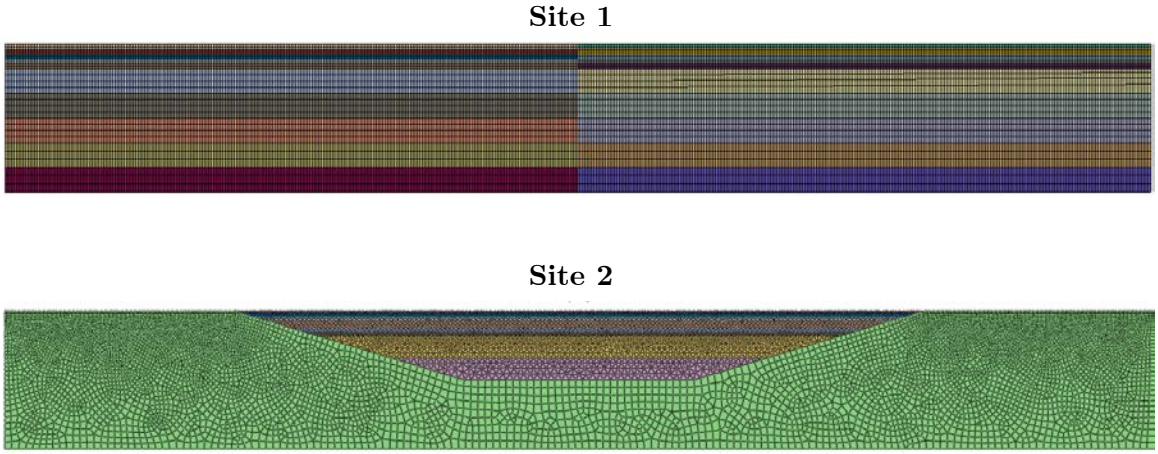

Figure 3-5. Element discretization and layering for typical equivalent-linear models of Site 1 (top) and Site 2 (bottom); visible is the progressive reduction in element size towards the softer material at the surface

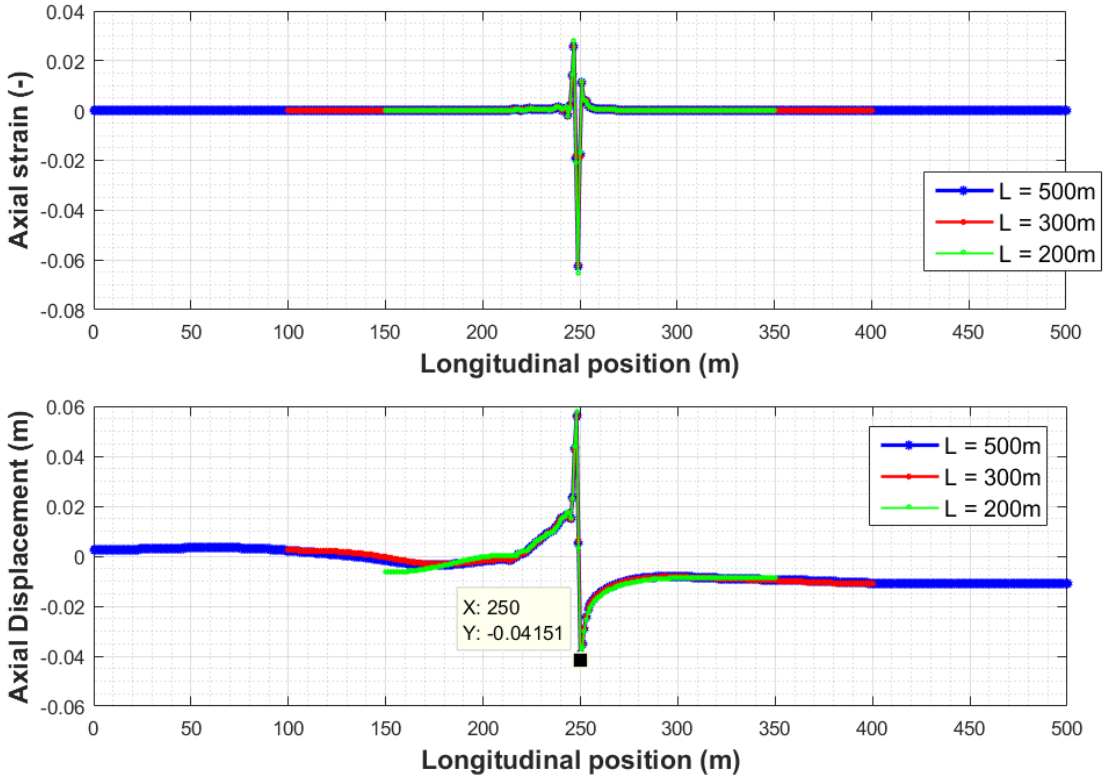

Figure 3-6. Mesh convergence study for equivalent-linear Site 1 models based on convergence of the longitudinal profile of (a) axial strain and (b) displacement at ground surface; shown are the results for three different domain half-widths: $L = 100, 150, 250$ m

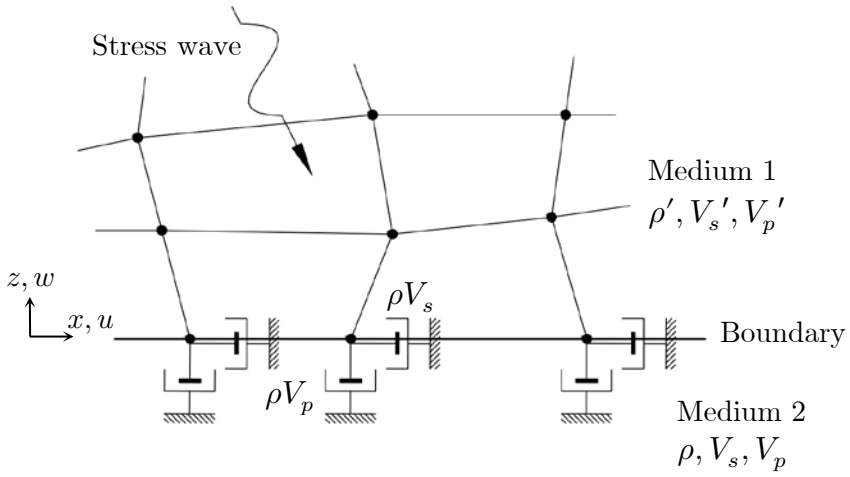

Figure 3-7. Example application of viscous dashpots as local absorbing boundaries along the lower horizontal boundary of a two-dimensional finite element mesh; the dashpots are defined by the dashpot coefficient per unit area

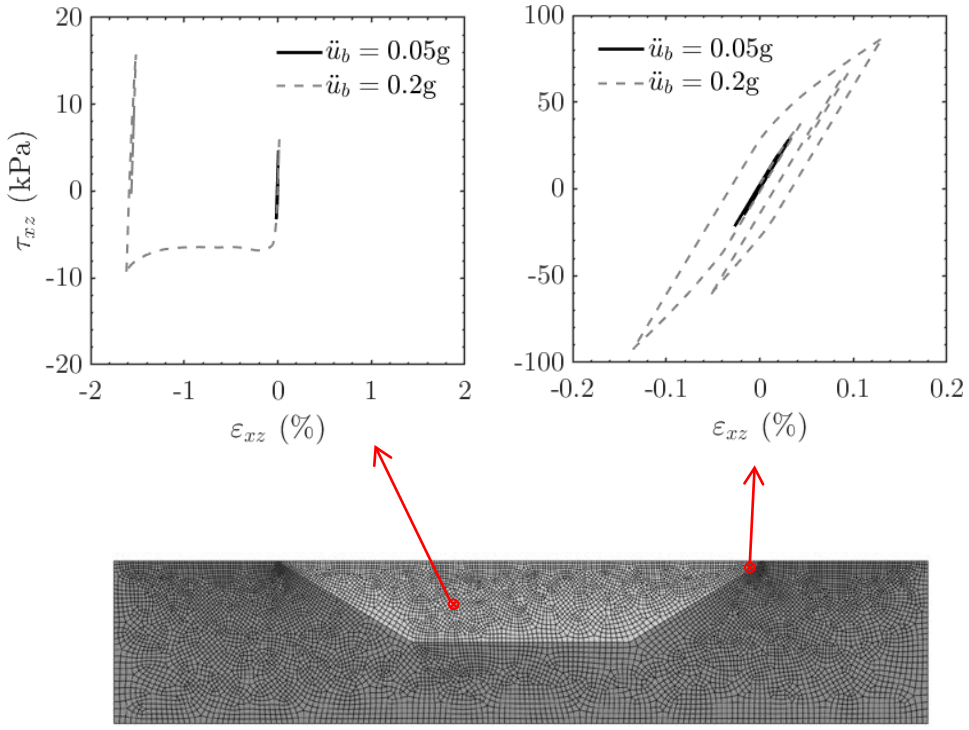

Figure 3-8. Shear stress-strain loops at two element locations due to elastoplastic response of Site 2 to a 1-Hz Ricker base excitation of varying amplitudes; these locations yield the maximum and minimum shear strain throughout the loading history of the domain

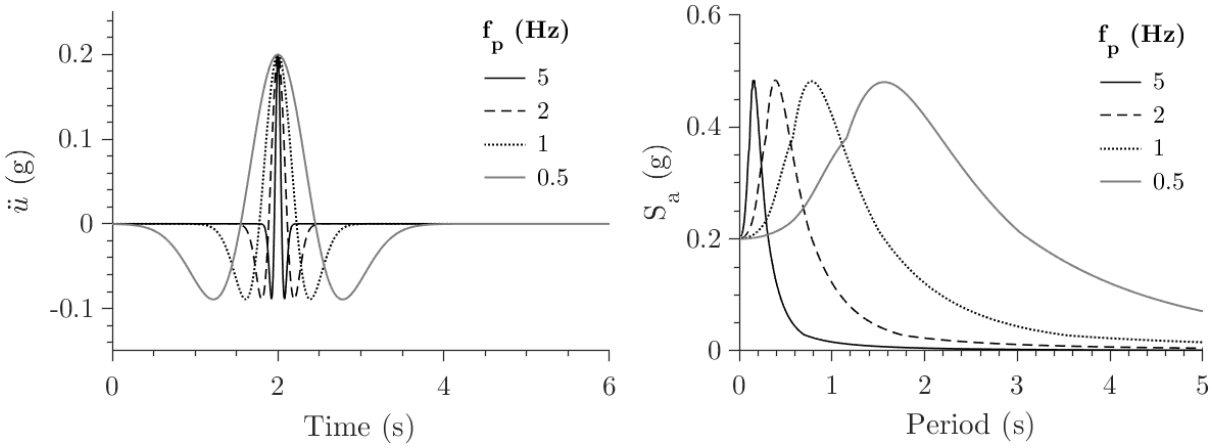

Figure 3-9. Acceleration time-histories of four Ricker wavelets with amplitude of 0.2 g and different characteristic frequencies (left) and their 5% damped elastic spectra (right).

Table 3-3. List of real outcrop earthquake records used as input motions

ID	Event	Moment Magnitude	PGA (g)	Mean period (s)	Predominant period (s)
EQ1	Imp. Valley (1979)	6.4	0.32	0.40	0.26
EQ2	Chi-Chi (1999)	7.7	0.18	0.97	0.54
EQ3	Kocaeli (1999)	7.6	0.35	1.25	0.31

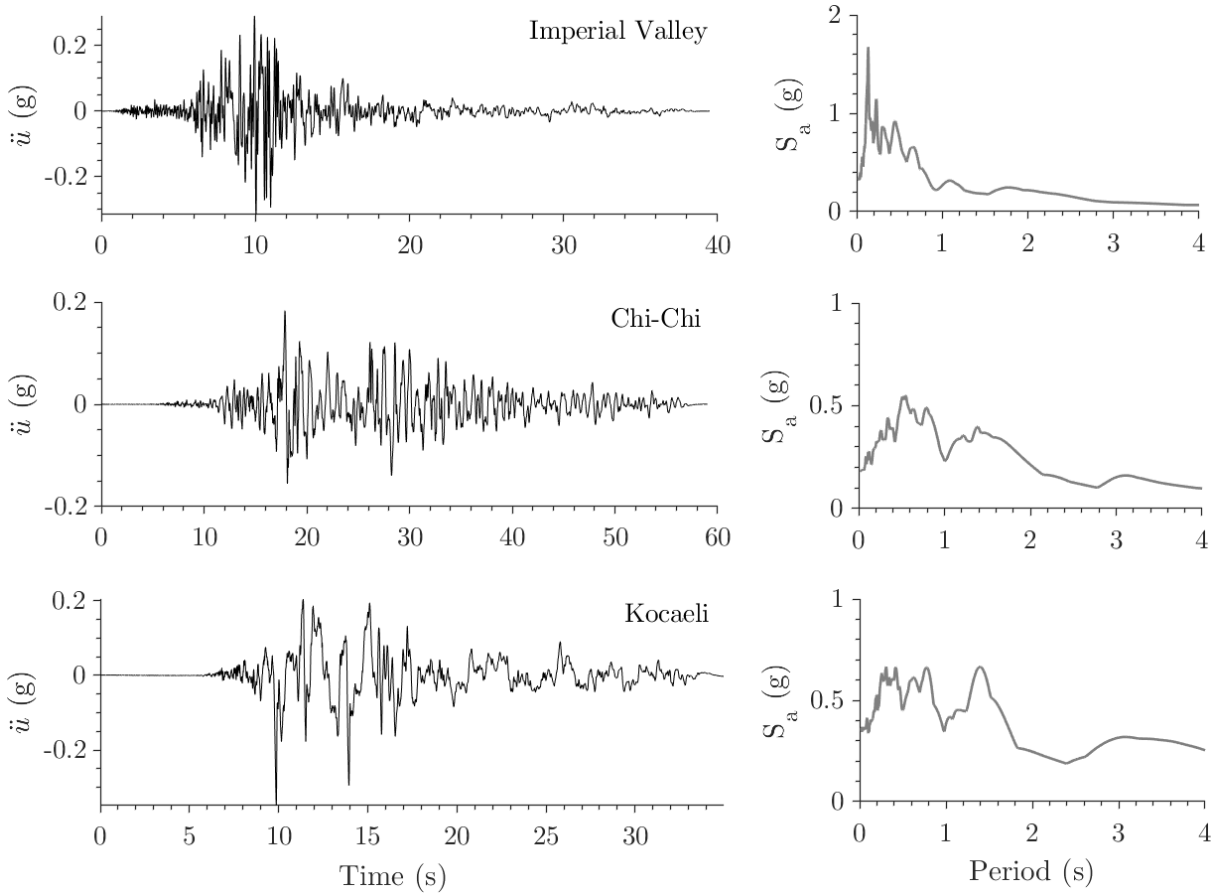

Figure 3-10. Acceleration time-series (left) and the corresponding 5% damped elastic spectra (right) of the earthquake records used as bedrock input motions

Table 3-4. List of parameters used for equivalent-linear Site 1 models

Case ID	ρ_1 (Mg/m³)	ρ_2 (Mg/m³)	Depth-to-bedrock (m)	Impedance ratio	Input motion
S1EL0 (base)	2.00	1.4	60	0.5	EQ1†
S1EL1	2.00	1.65	60	0.7	EQ1
S1EL2	1.65	1.4	60	0.7	EQ1
S1EL3	2.00	1.4	30	0.5	EQ1
S1EL4	2.00	1.4	90	0.5	EQ1
S1EL5	2.00	1.4	60	0.5	EQ2
S1EL6	2.00	1.4	60	0.5	EQ3
S1EL7	2.00	1.4	30	0.5	R05_02*
S1EL8	2.00	1.4	30	0.5	R1_02
S1EL9	2.00	1.4	30	0.5	R2_02
S1EL10	2.00	1.4	30	0.5	R5_02
S1EL11	2.00	1.4	30	0.5	R05_03
S1EL12	2.00	1.4	30	0.5	R1_03
S1EL13	2.00	1.4	30	0.5	R2_03
S1EL14	2.00	1.4	30	0.5	R5_03

†**EQ[*X*]: Earthquake record from Table 3-3**
*R[*X*]_[0*Y*]: Ricker wavelet with $f_o = X$ Hz and amplitude $a = 0.Y$ g

Table 3-5. List of model parameters used for equivalent-linear Site 2 models

Case ID	ρ_1 (Mg/m3)	$V_{s,2}$ (m/s)	s (%)	Impedance ratio	Input motion
S2EL0 (base)	1.4	400	30	0.5	EQ1[†]
S2EL1	1.65	400	30	0.6	EQ1
S2EL2	2	400	30	0.7	EQ1
S2EL3	1.4	400	60	0.5	EQ1
S2EL4	1.4	800	30	0.35	EQ1
S2EL5	1.4	400	30	0.5	EQ2
S2EL6	1.4	400	30	0.5	EQ3
S2EL7	1.4	400	30	0.5	R05_02[*]
S2EL8	1.4	400	30	0.5	R1_02
S2EL9	1.4	400	30	0.5	R2_02
S2EL10	1.4	400	30	0.5	R5_02
S2EL11	1.4	400	30	0.5	R05_03
S2EL12	1.4	400	30	0.5	R1_03
S2EL13	1.4	400	30	0.5	R2_03
S2EL14	1.4	400	30	0.5	R5_03

[†]EQ[X]: Earthquake record from Table 3-3
[*]R[X]_[0Y]: Ricker wavelet with $f_o = X$ Hz and amplitude $a = 0.Y$ g

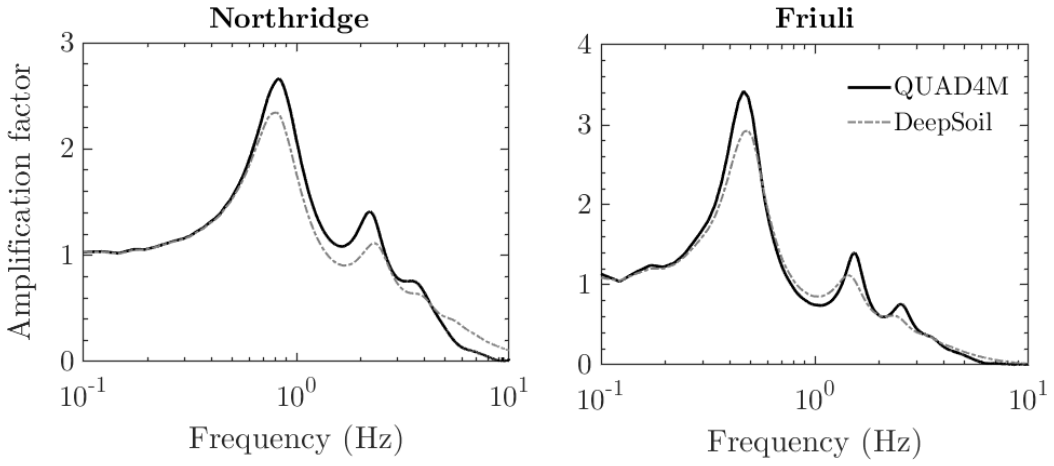

Figure 3-11. Comparison of surface-to-bedrock amplification factors of horizontal acceleration for 1-D (DeepSoil) and 2-D (QUAD4M) equivalent-linear site response models

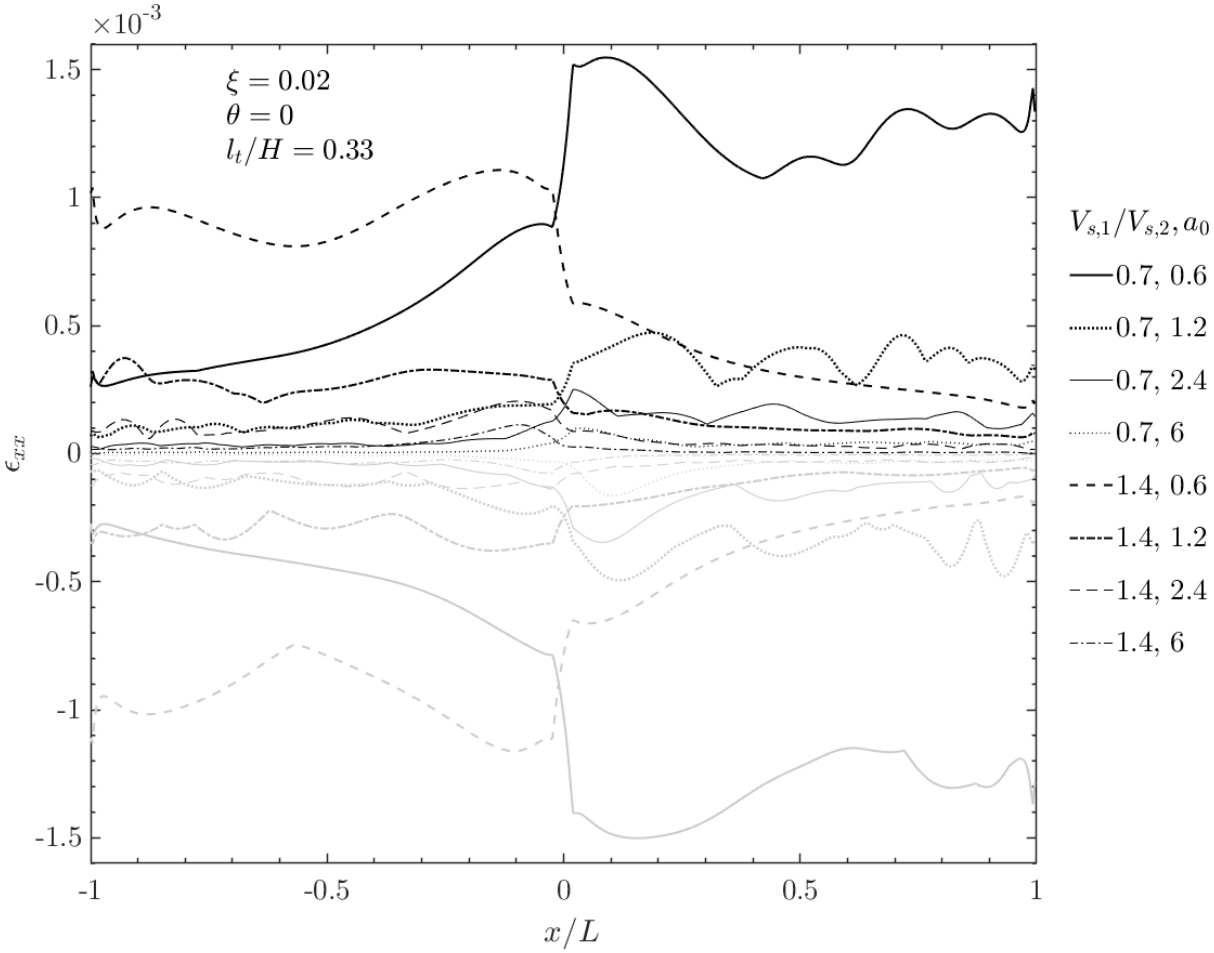

Figure 3-12. Envelopes of peak tensile (positive) and compressive (negative) axial ground strains along the surface for different Site 1 cases

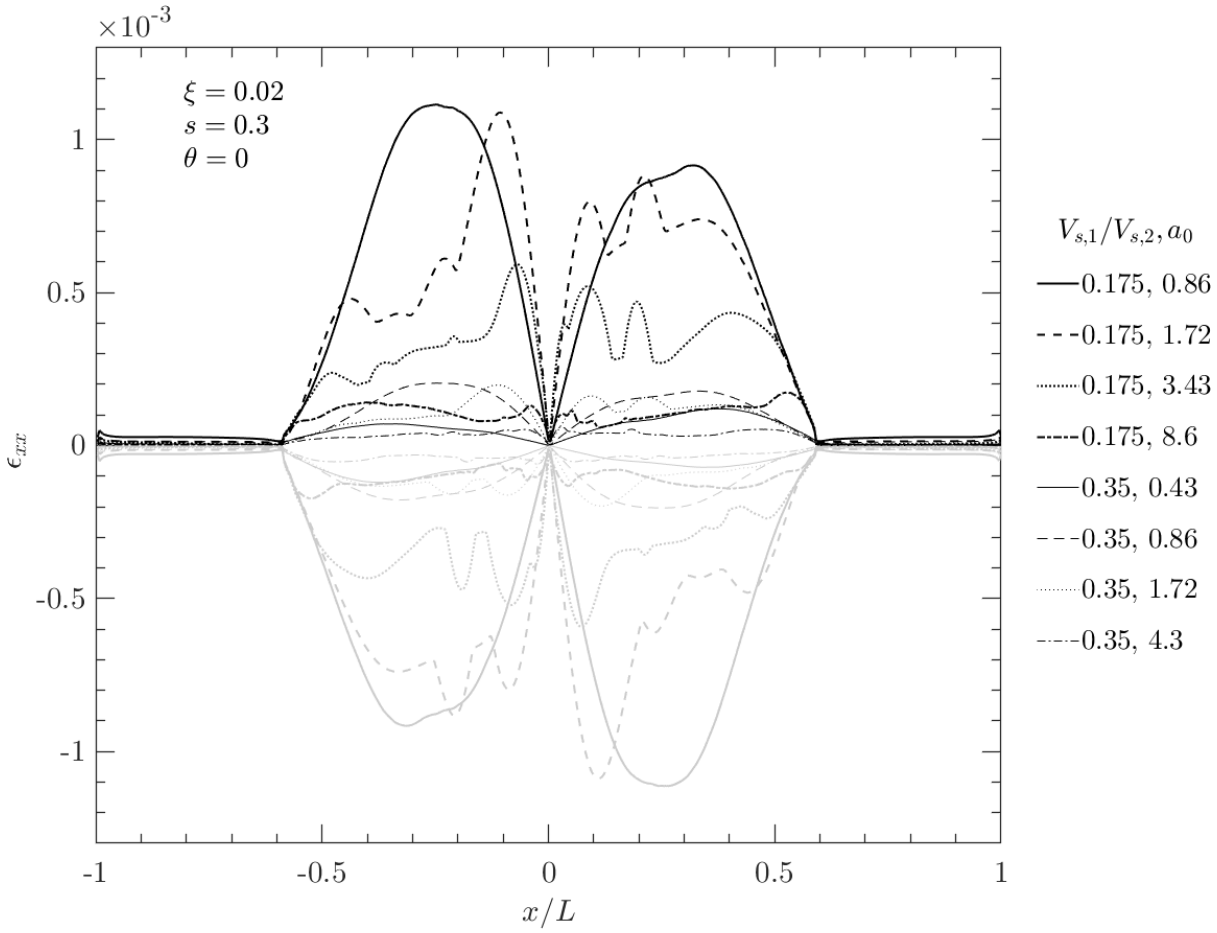

Figure 3-13. Envelopes of peak tensile (positive) and compressive (negative) axial ground strains along the surface for different Site 2 cases

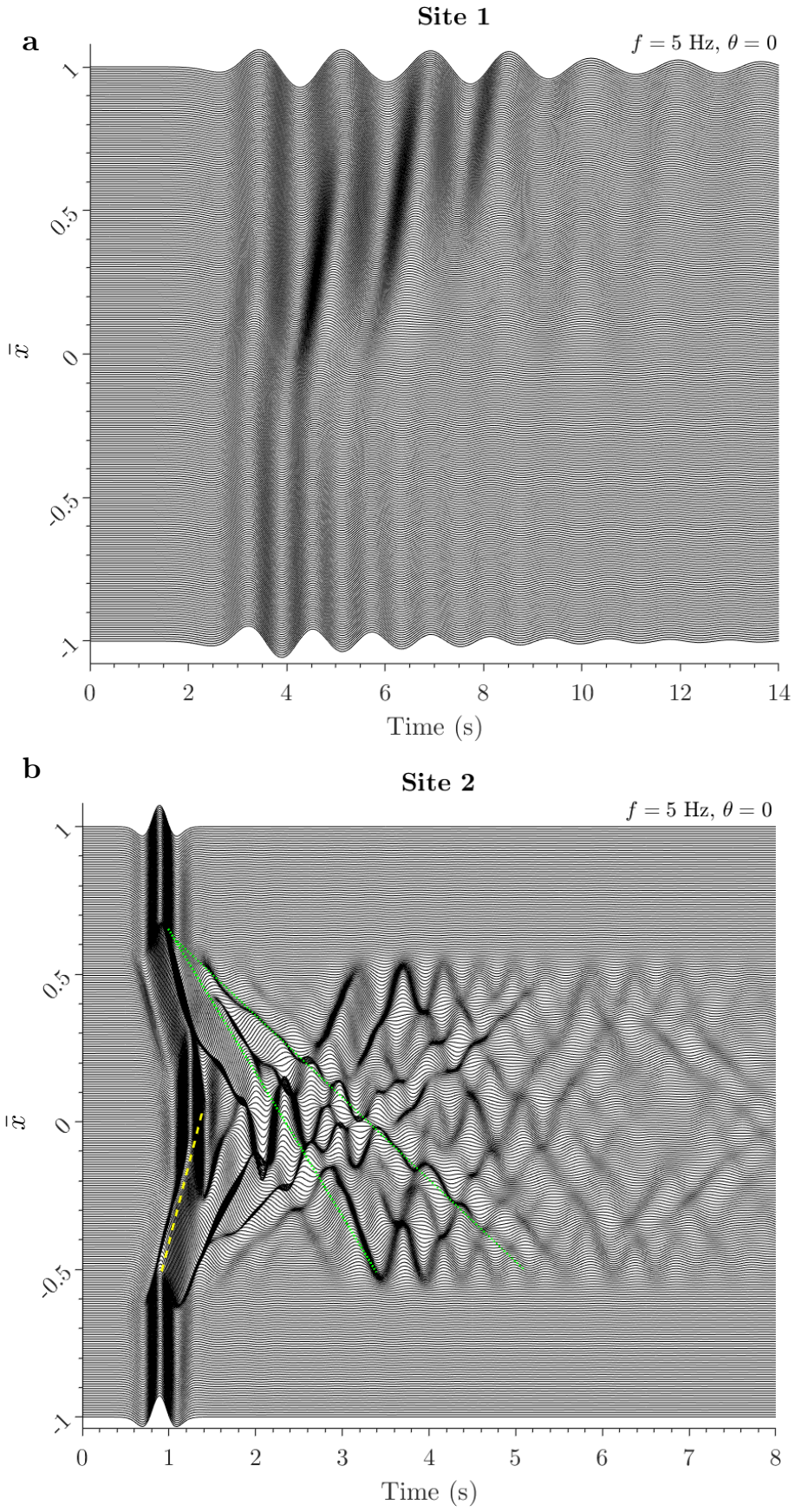

Figure 3-14. 2-D synthetics of horizontal surface acceleration for (a) Site 1 and (b) Site 2, with $f = 5$ Hz and $\theta = 0$; the yellow dashed line identifies the refracted wave front along the

dipping interface, while the green dotted lines trace the Rayleigh wave phases generated at the valley edges

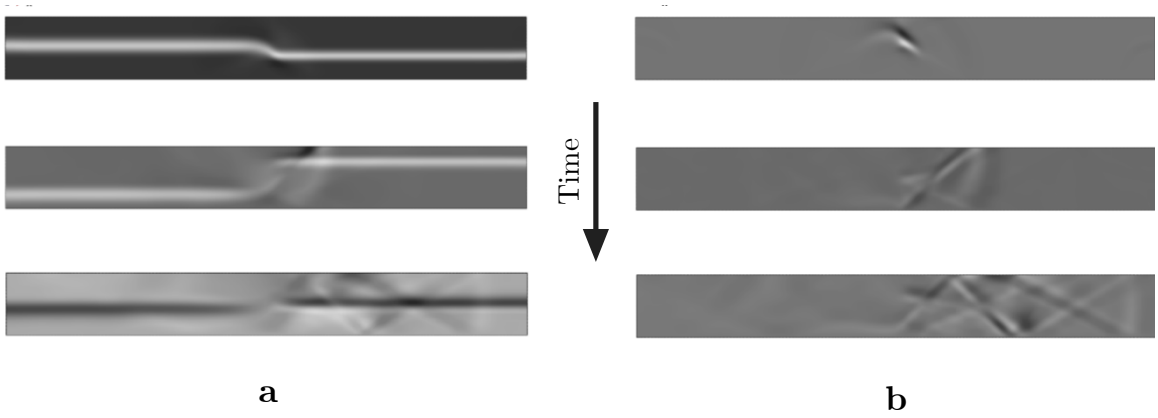

Figure 3-15. Snapshots of the complete (a) shear strain field (SV-waves) and (b) vertical normal strain field (P-waves) in a Site 1 model subject to a vertically incident 5-Hz Ricker SV-pulse; discernible are the upward travelling inclined wave fronts at the vertical boundary and the ensuing successive reflections in-between the surface and the bedrock; vertical vibrational components are seen propagating in the top right snapshot

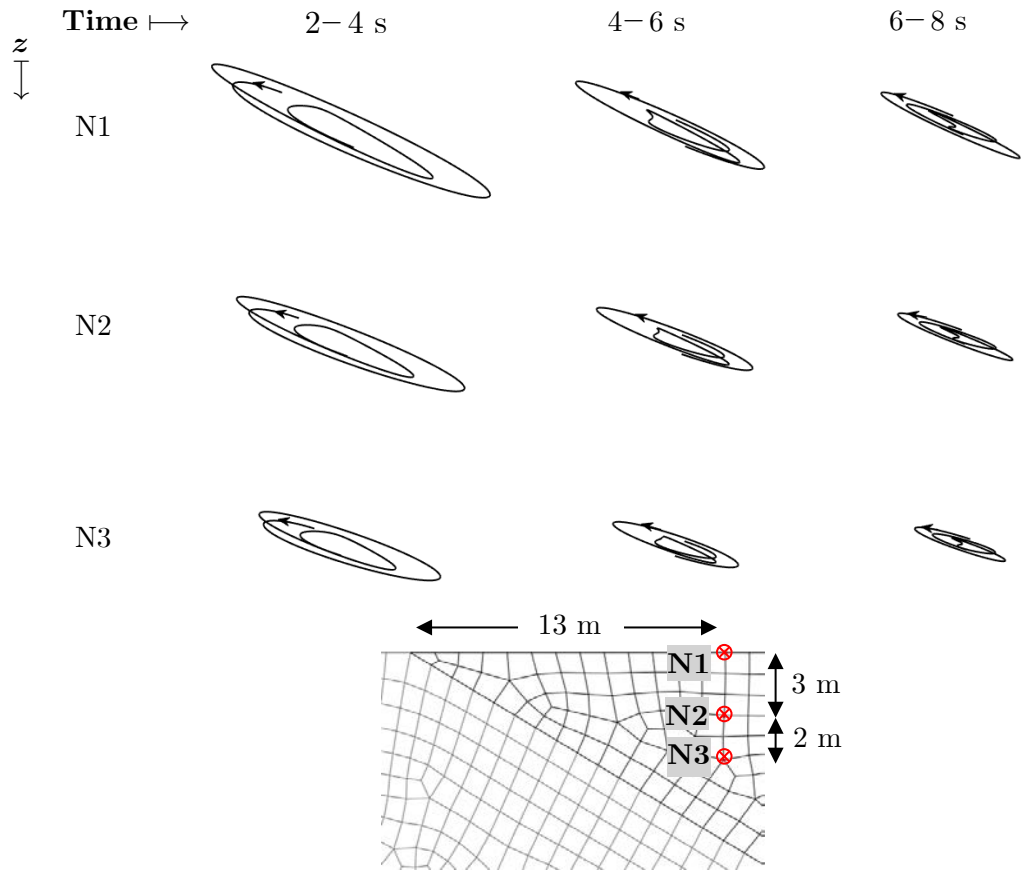

Figure 3-16. Particle motion trajectories on xz plane at different time windows for three points of a Site 2 model with $f = 5$ Hz and $\theta = 0$; arrows indicate the rotation sense of the particle motion

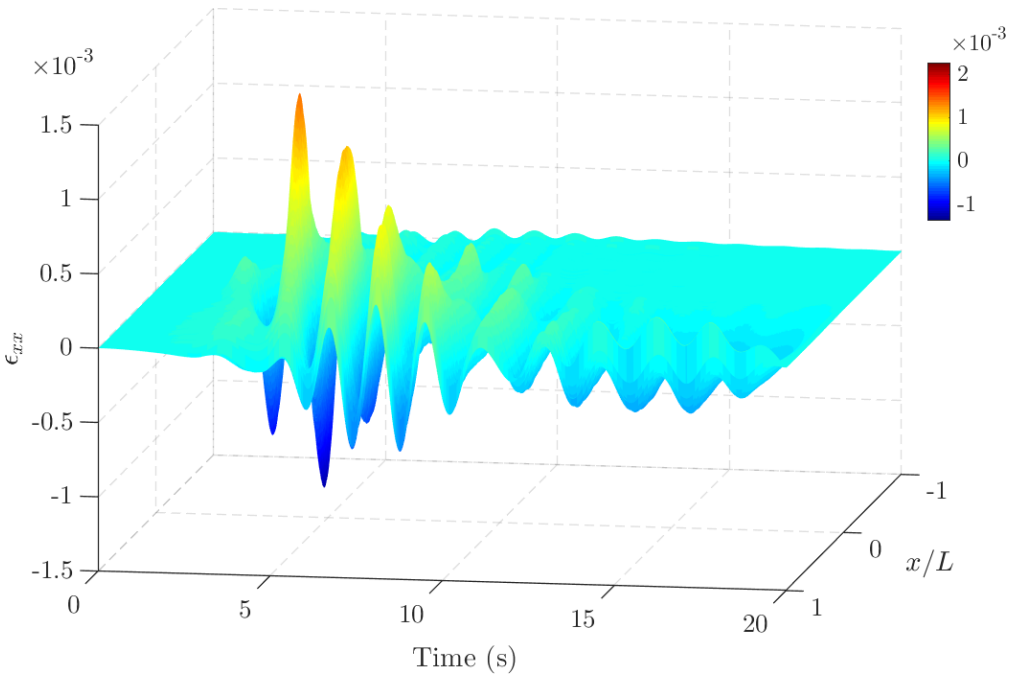

Figure 3-17. Time-variation of ground axial strain field at the surface of a Site 1 model with $H = 60$ m, $V_{s,1} = 140$ m/s, $l_t = 10$ m, $\theta = 0$ and $\xi = 2\%$.

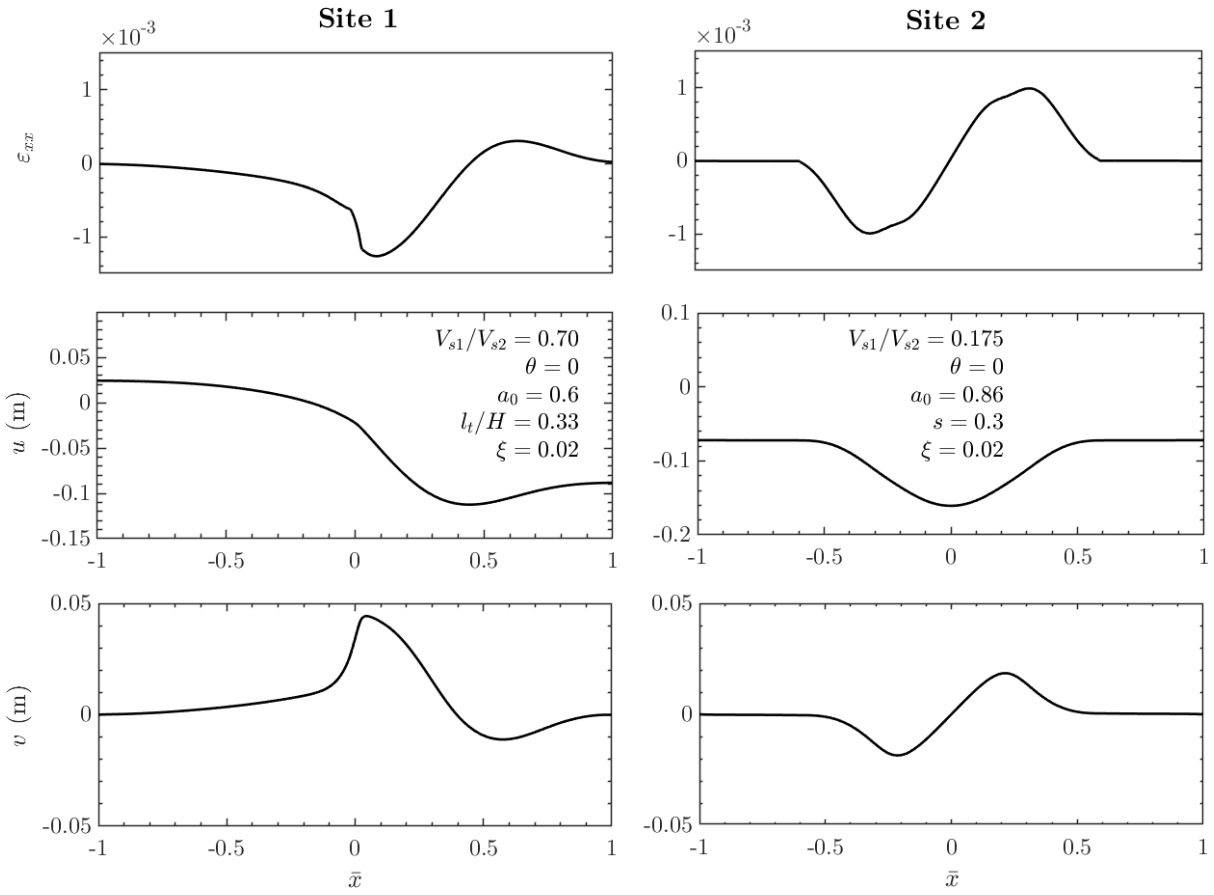

Figure 3-18. Time-critical longitudinal profiles of axial ground strain, horizontal and vertical ground displacement at depth h for Site 1 and Site 2 linear elastic models

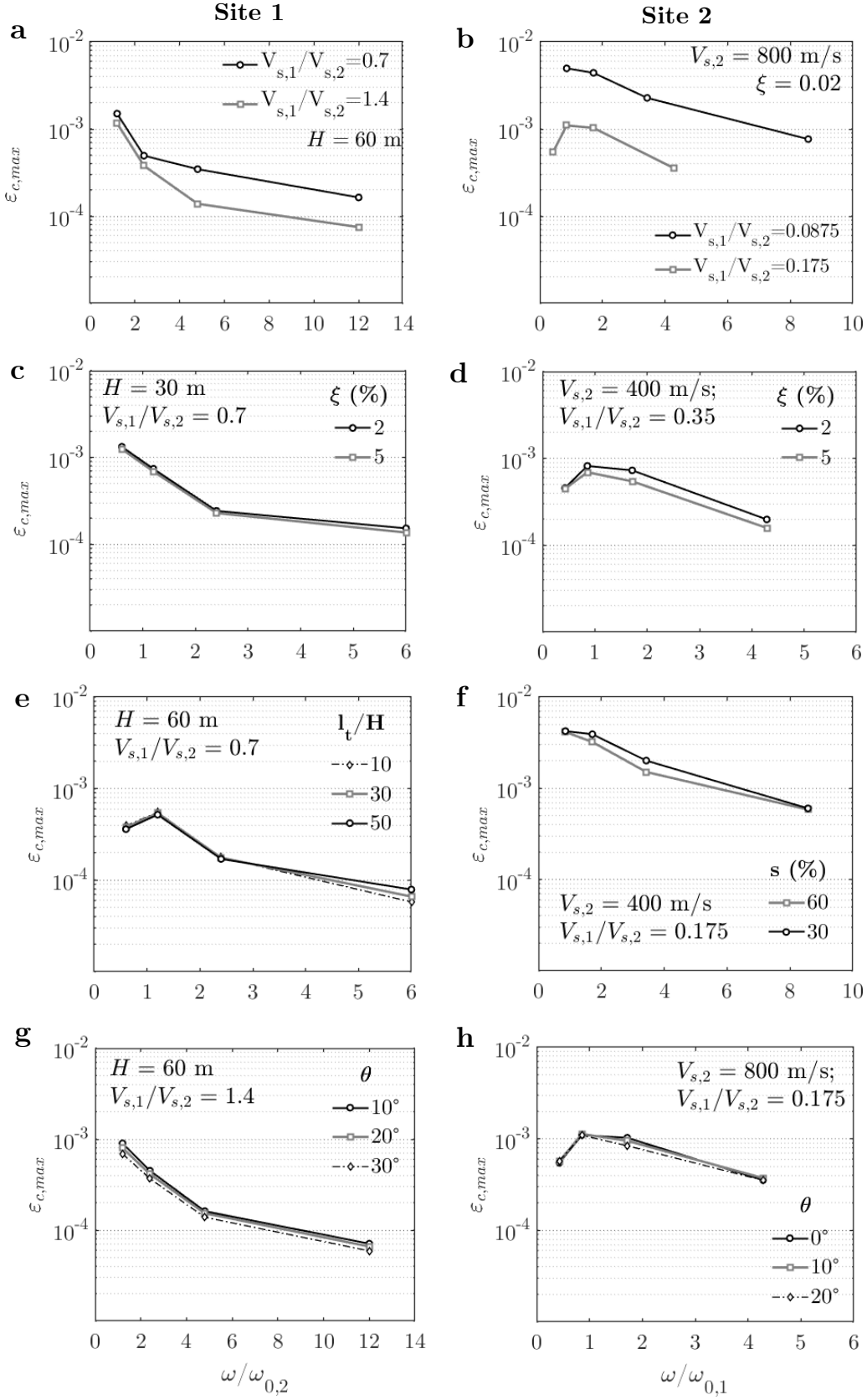

Figure 3-19. Variation of peak compressive axial ground strains with normalized frequency a_0 for different: (a-b) impedance ratios; (c-d) viscous damping ratios; (e) normalised transition zone lengths for Site 1, (f) dipping slopes for Site 2, and (g-h) wave incidence angles; where

not mentioned, reference parameters are implied as follows: for Site 1, $\xi = 2\%$, $\theta = 0$, $l_t/H = 0.33$; for Site 2, $\xi = 2\%$, $\theta = 0$, $s = 30\%$

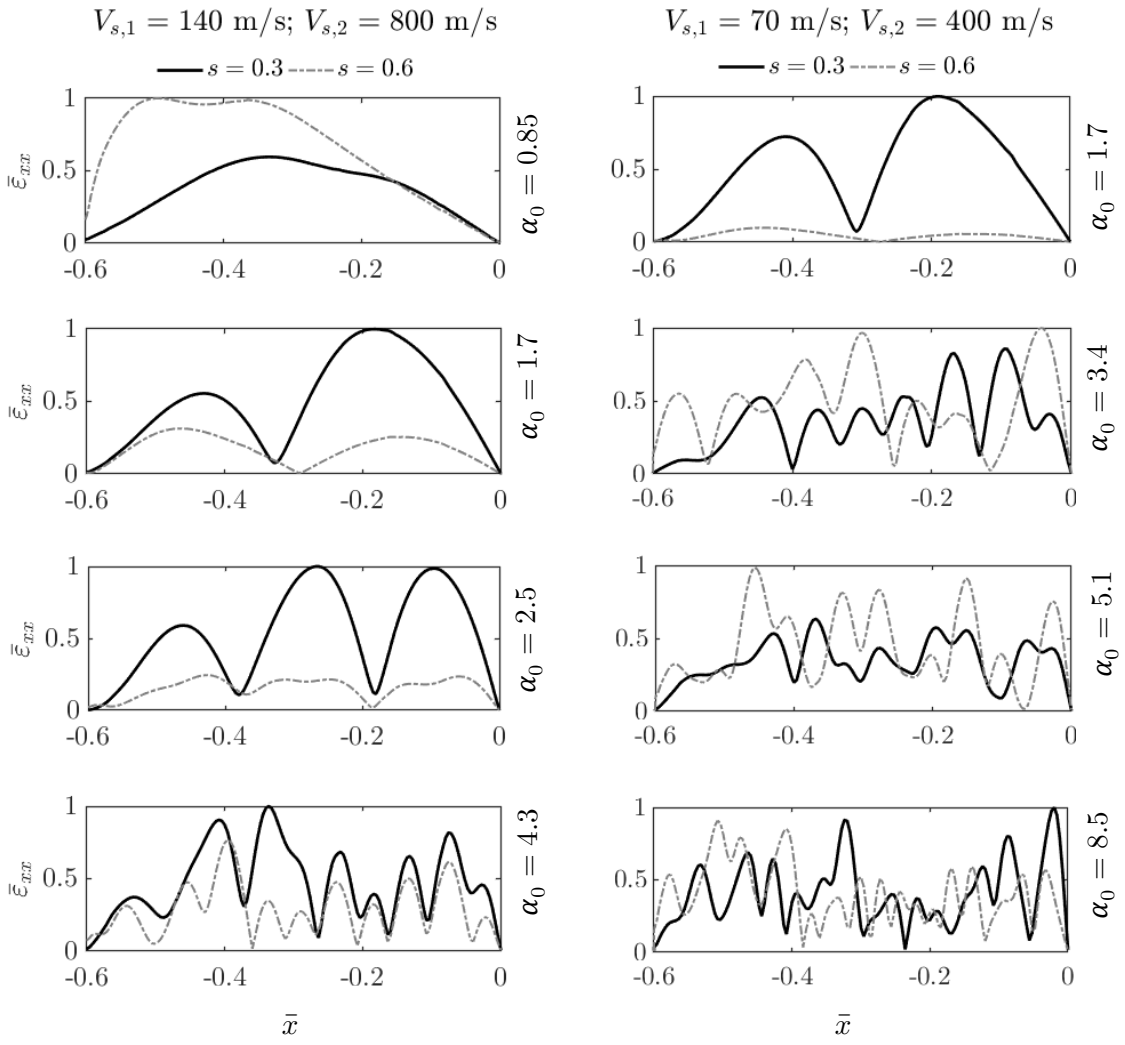

Figure 3-20. Steady-state profiles of axial strain along the valley surface for two Site 2 models with different dipping slopes and $\xi = 2\%$, obtained from complex harmonic analysis

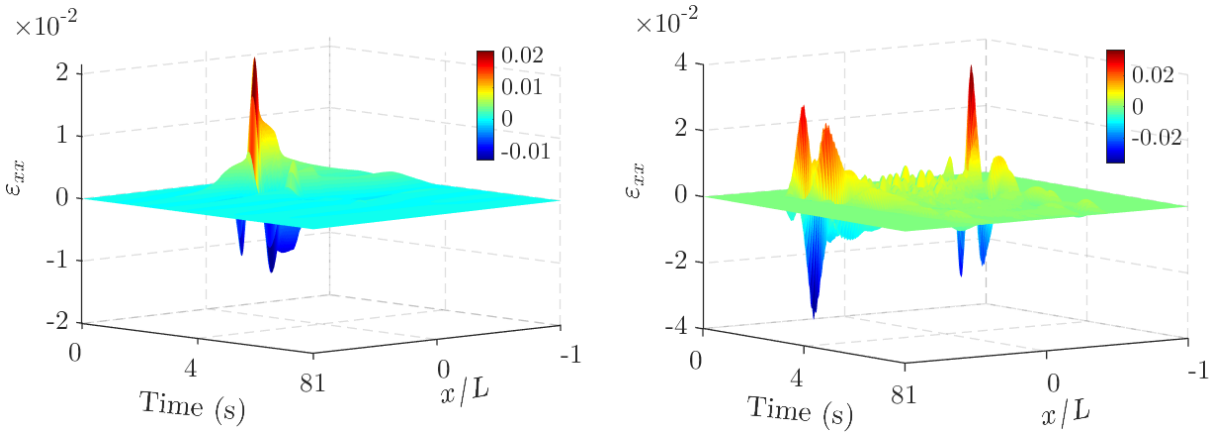

Figure 3-21. Time-variation of ground axial strain field at the surface for cases S1EL10 (left) and S2EL8 (right)

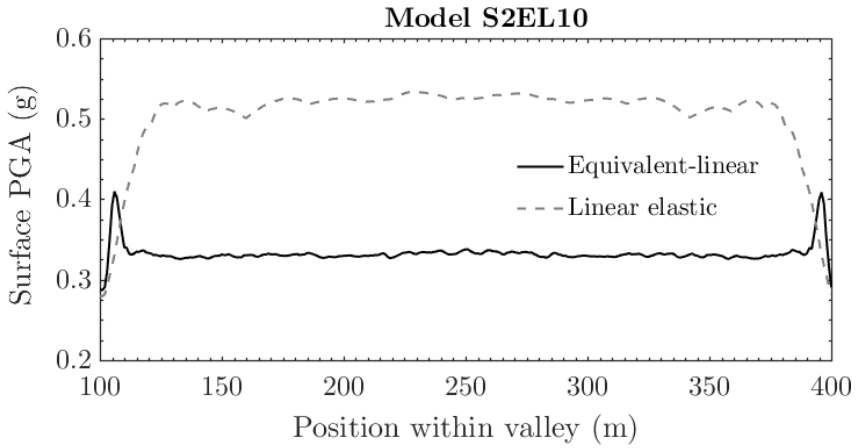

Figure 3-22. Horizontal PGA distribution at the surface of valley model S2EL10 considering both linear and equivalent-linear site response

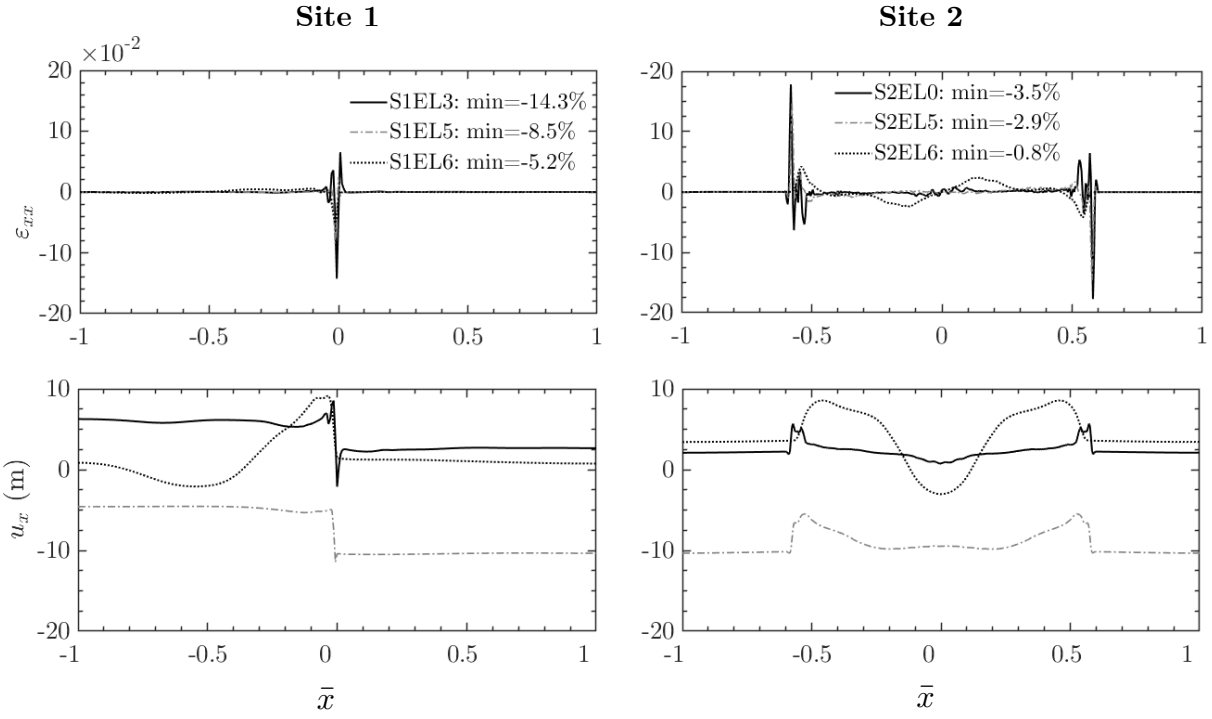

Figure 3-23. Time-critical spatial profiles of axial ground strain and horizontal ground displacements computed for the equivalent-linear models with the highest impedance ratios, for all three input earthquakes

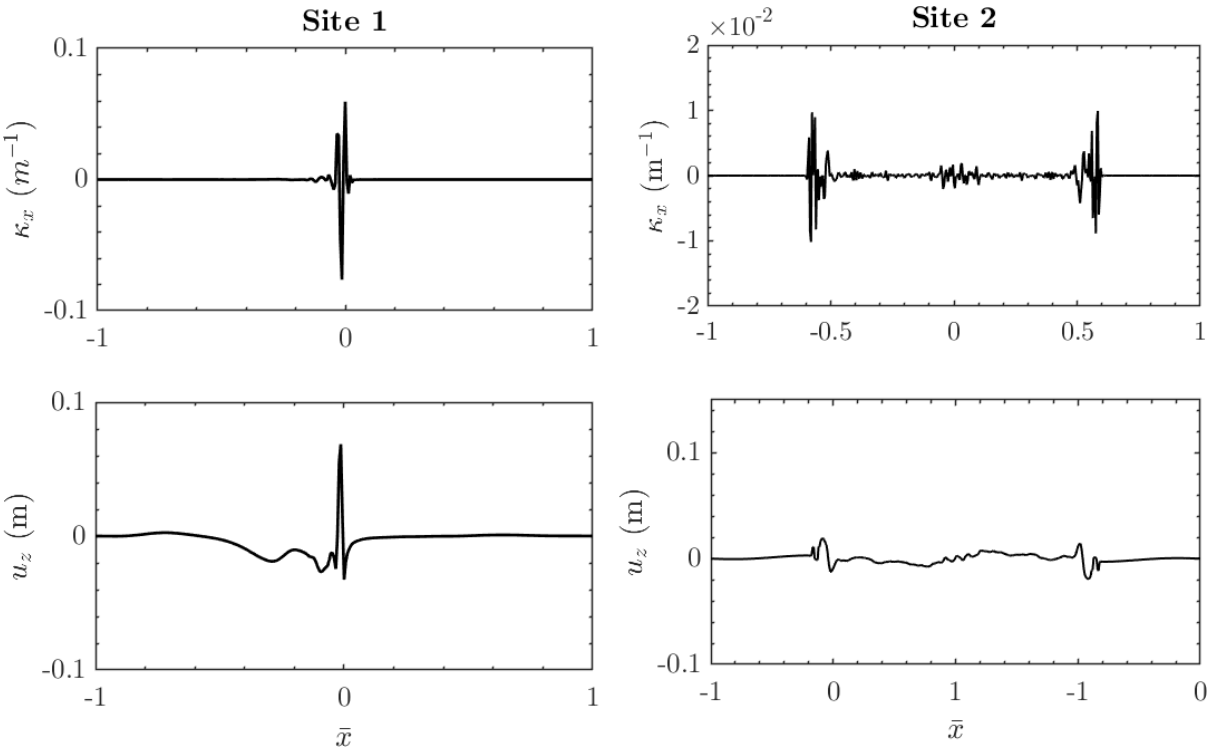

Figure 3-24. Time-critical spatial profiles of axial curvature and vertical displacement at pipeline depth for Site 1 model S1EL3 and Site 2 model S2EL0

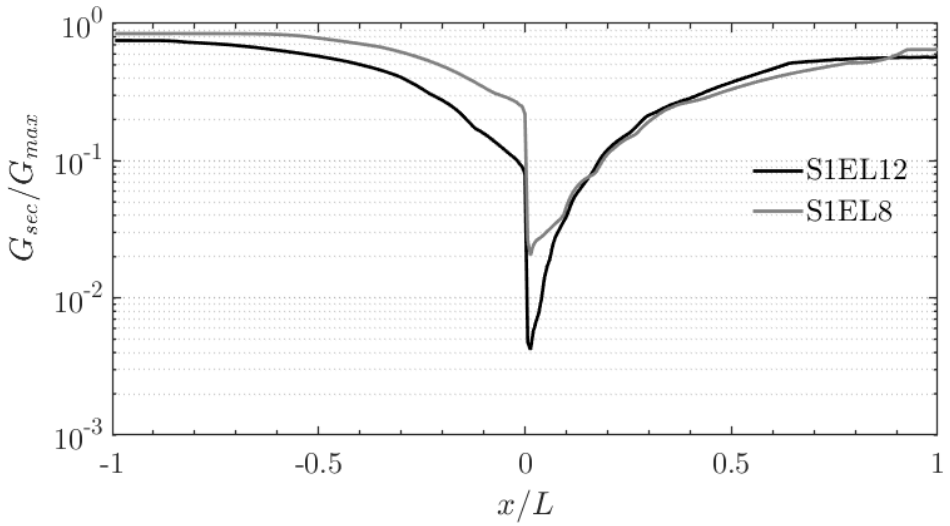

Figure 3-25. Plot of the spatial profile of G/G_{max} at the final (converged) analysis iteration for two equivalent-linear models of Site 1

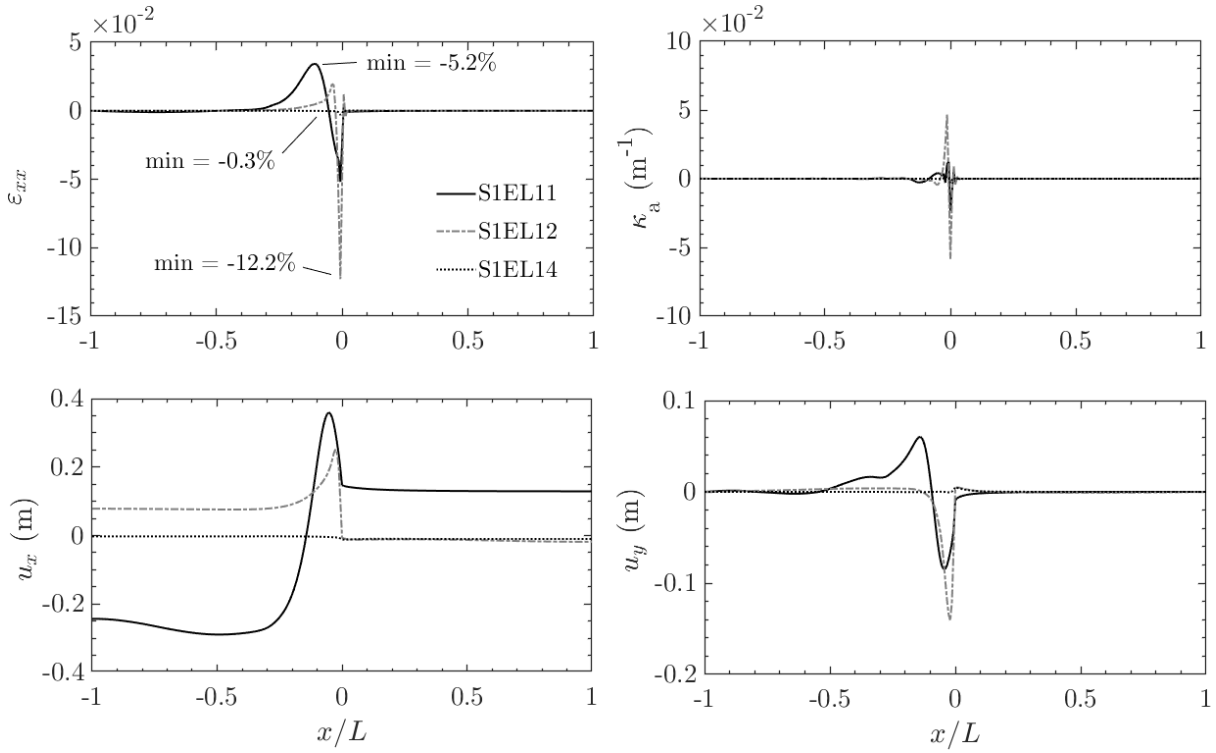

Figure 3-26. Time-critical spatial profiles of axial ground strain, axial displacement, axial curvature and vertical displacement for models S1EL11, S1EL12, S1EL14 (Ricker wavelets with amplitude 0.3 g)

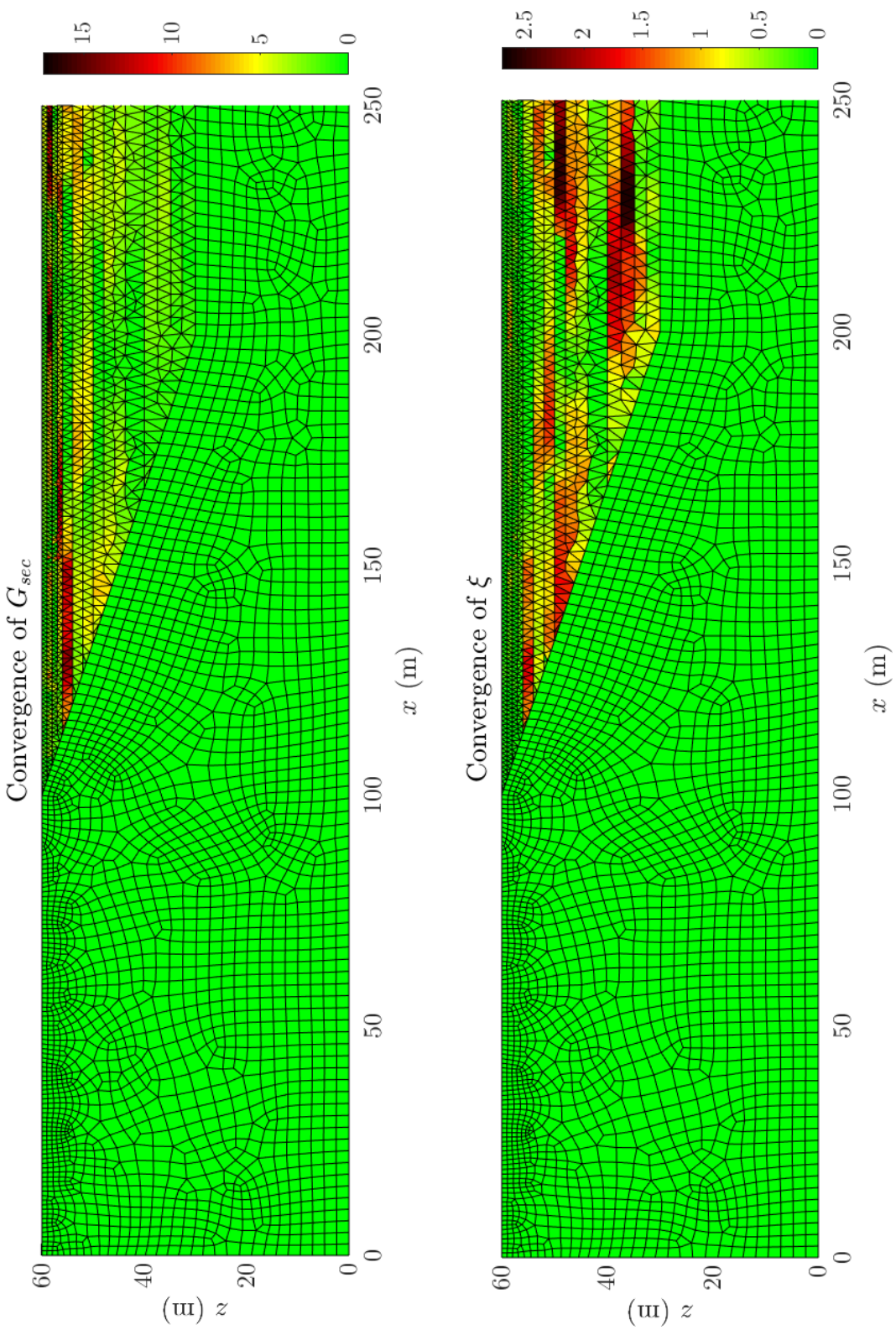

Figure 3-27. Mesh contours of % deviation of G_{sec} and ξ between the last and second to last iteration of the equivalent linear analysis for model S2EL0

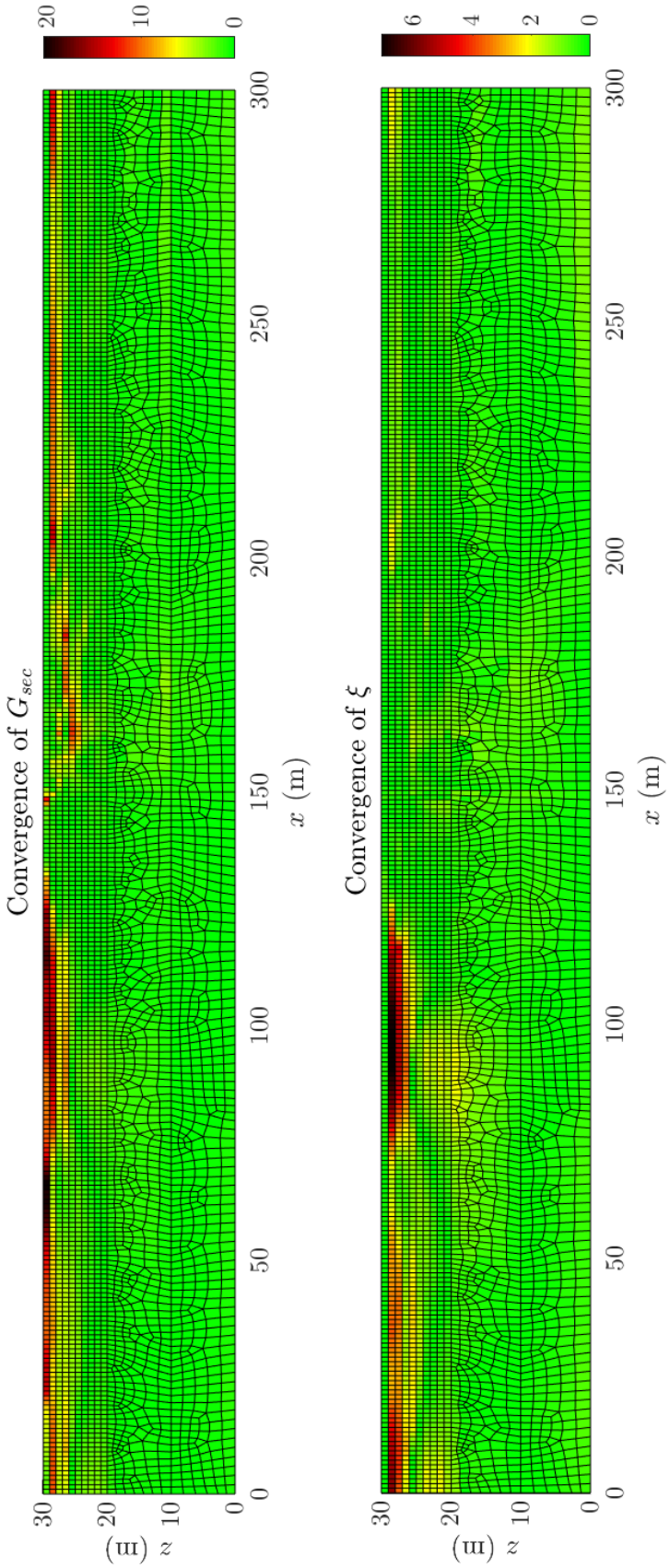

Figure 3-28. Mesh contours of % deviation of G_{sec} and ξ between the last and second to last iteration of the equivalent linear analysis for model S1EL3

Chapter 4

Numerical Substructure II: Nonlinear Soil-Pipe Interaction Model

4.1 Introduction

In the previous chapter, the first substructure of the proposed FEM-based response analysis methodology for soil-pipe systems was developed. This chapter addresses analysis of the second substructure, which captures the structural response of the buried gas pipeline subject to the free-field load computed in the first substructure.

The chapter is organised in five parts. First, the key components of substructure II are presented and the points of connection with substructure I are explained. Second, an introduction to plastic buckling of circular cylindrical shells is provided in order to set the necessary background for subsequent developments. Third, the fundamental aspects of the finite-element models of substructure II are described and the relevant modelling choices are reasoned. Representative outcomes from analysis of these models are then discussed and characterisation of the structural performance of the pipeline is sought. A comparison of the peak evaluated pipe demands with standard performance criteria adopted in practice is also carried out to assess the validity of those criteria. The chapter ends with a sensitivity analysis of a generalised model that captures the major factors affecting the critical loads of the pipeline.

4.2 Overview of numerical substructure II

Following the determination of the free-field response from plane strain analysis of substructure I and the identification of critical ground deformation profiles $\boldsymbol{u}_{cr}$ at pipeline depth, it remains to analyse the structural response of the buried pipeline and the possibility of failure when subjected to these ground deformations. Illustrated in **Figure 3-1**, a 3-D model consisting of shell and solid finite elements is employed to predict the response of the buried pipeline. The reasons for choosing this kind of representation were discussed in section 2.7.

4.2.1 General

Figure 4-1 depicts the geometry and global coordinate system of substructure II associated with Site 1 models. Truncation of the initial soil domain of substructure I is possible in view of three conditions, that is, the absence of kinematic and inertial interaction, the assumed plane strain conditions, and the shallow embedment of the pipeline. Starting from the ground surface, a subdomain with a width of $2L$ and a depth $d > H + R$ is cropped and then extruded by $2b$ in the y direction to form a surficial block of soil. The transverse dimension $2b$ is taken large enough (several times the pipe radius) to allow development of the expected in-situ soil stress field as well as unobstructed pipe deformation in the transverse horizontal plane. The values of d and b will be found by a sensitivity study on a case-by-case basis. A circular cylindrical cavity, whose centreline is parallel to the x-axis with $(y, z) = (0, -H)$, accommodates a nonlinear circular cylindrical isotropic shell model of the pipeline; the surrounding soil block is idealised as a 3-D solid body.

The differential soil displacement field extracted at the critical time frame from the ground response history at the critical time instant, now expanded to three dimension as $[u_{cr}\ 0\ \ w_{cr}]^T$, is prescribed on the soil block. For simplicity in modelling, this field is taken independent of the depth coordinate over the whole soil domain $(\partial \boldsymbol{u}_{cr}/\partial y = 0)$, on the grounds that d is small compared to the minimum predominant

wavelength, $\lambda_{o,min}$, contained in the incident waves, therefore the in-plane motion of the soil particles will not vary appreciably with depth. It has been established that the error introduced by this assumption is not significant for $d/\lambda_{o,min} < 0.1$. Application of the soil loads is preceded by application of permanent loads; these are the gravitational load on the whole system and the internal pressure on the pipe.

Considering that the problem at hand is in reality a dynamic one, a careful account of the major energy dissipation mechanisms of the soil-pipe system is necessary. Material damping in problems of SPI comes predominantly from soil action. In the proposed approach, soil material damping has already been modelled in substructure I. Radiation damping has also been considered in substructure I by means of absorbing boundaries in the ground response models. Another important form of energy dissipation is due to sliding and gap formation at the soil-pipe interface; this behaviour is explicitly modelled in substructure II and is detailed in subsection 4.4.4. Energy release due to internal plastic work in the pipe is also considered by employing an elastoplastic constitutive law for steel.

The adopted 3-D model encompasses three types of nonlinearities: nonlinear kinematics for the pipe shell, material plasticity for the pipe steel, and nonlinear interface contact behaviour. All of them can be addressed relatively efficiently by the large-deformation elastoplastic total Lagrangian finite-element formulation implemented in ABAQUS. The solution of the resulting system of equations is traced incrementally by an arc-length algorithm, which is capable of detecting smooth instabilities along the nonlinear equilibrium path. The analysis of substructure II yields the pipe strains $\boldsymbol{\varepsilon}_p(t_{cr})$ and stresses $\boldsymbol{\sigma}_p(t_{cr})$, as well as the response at the soil-pipe interface in terms of contact pressure $\sigma_n(\vartheta, x, t_{cr})$, shear longitudinal contact stress $\tau_x(\vartheta, x, t_{cr})$ and axial slip $\delta u(\vartheta, x, t_{cr})$. Note that subscript p will be dropped for clarity henceforth.

4.2.2 Restatement of objectives

Objectives (a) to (c) as outlined in subsection 3.2.4 have been met in the previous chapter through analysis of substructure I. In the present chapter, the centre of attention is on the last three objectives, repeated here for convenience:

a. evaluation of the pipeline demand due to critical soil displacement fields obtained from substructure I and comparison with standard performance criteria proposed in codes of practice;

b. analysis of the interaction effects at the soil-pipeline interface;

c. investigation of the possibility of buckling failure in pipelines laid through such inhomogeneous sites, identification of the circumstances that favour its occurrence and description of its characteristics.

4.3 Plastic buckling of circular cylindrical isotropic shells

Since emphasis is on finding whether buckling failure can occur in buried pipelines under certain unfavourable earthquake scenarios and subsurface conditions, it is prudent to supply at this point a brief survey of the state of knowledge on plastic buckling of tubes under different external loadings and boundary conditions, so as to furnish a frame of reference for the analysis to follow.

Buckling of circular cylindrical isotropic shells is a stability problem that has concerned engineers for decades owing to its salient characteristics and often sudden and catastrophic consequences to high-performance structures. In analysis of buckling problems, the parameters of greatest interest from a design point of view are the critical loads, the general nature of which has been discussed in subsection 2.2.1. Reliable prediction of these loads in the plastic range requires simultaneous consideration of large-deflection (nonlinear) shell theories and material plasticity. A long known behaviour of great importance is the sensitivity that these loads exhibit to initial

geometric imperfections. This sensitivity tends to be extreme for elastic buckling but is moderated if buckling occurs in the plastic regime.

The literature is abundant in shell theories able to describe the pre- and post-buckling response of tubes with various levels of accuracy. Notable examples are the Donnel-Mushtari-Vlasov (DMV) theory (Donnell, 1933; Galimov and Mushtari, 1961) which assumes small strains, moderate out-of-plane rotations, small rotation about the normal and short-wavelength deformations; and Sanders's general nonlinear theory for finite strains (Sanders, 1963), which includes as subsets the widely used formulations for small strains-moderate rotations, small strains-moderate rotations-small rotation about the normal, as well as the DMV theory. The second-order strain-displacement relationships based on the assumptions of small strains and small finite (moderate) rotations are supplied in Appendix C, contrasted against the 'best' first-order approximation (Sanders, 1959).

A variety of constitutive models for plasticity are available to predict the onset and evolution of yielding in metal solids under multiaxial stress conditions. The most commonly used models for plastic buckling analysis are the classical J_2 flow theory and the J_2 deformation theory. The latter becomes equivalent to the J_2 flow theory under monotonic proportional loading, that is, when all stress components increase at constant ratios.

4.3.1 Buckling under uniform axial compression

The problem of buckling of tubes loaded in uniform axial compression is the simplest one to track analytically and experimentally and has stimulated the greatest research interest. The basic case is met when the tube deforms axisymmetrically beyond bifurcation and until the collapse (limit) load, if the latter occurs after the bifurcation load. Depending on details such as the type of edge support and the presence of imperfections, non-axisymmetric modes of buckling might be triggered before or after the collapse load (Bushnell, 1982).

In early years, the tangent modulus theory was the way to approximately determine the critical plastic buckling loads of shells (Timoshenko and Gere, 1961). Von Karman & Tsien (1941) first explained the observed discrepancies between buckling load predictions of the classical thin shell theory and experiments with thin shells by ascribing them to the highly unstable character of the post-buckling behaviour. Asymptotic analysis of the initial post-bifurcation behaviour of elastic shells as pioneered by Koiter was extended to study post-buckling in the plastic range (Hutchinson, 1973; Hutchinson and Budiansky, 1976; Needleman and Tvergaard, 1976).

Bushnell (1976) contributed to the field by developing a special computer program BOSOR5 for the nonlinear buckling analysis of axisymmetric structures. The aim was to determine the pre-buckling equilibrium path, as well as the bifurcation point. The plastic bifurcation load and half-wavelength of a perfect cylindrical shell were first derived by Batterman (1983) considering both the J_2 incremental and the J_2 deformation theory of plasticity. The solutions based on the J_2 deformation theory can be expressed as

$$\sigma_c = \frac{2Et_w}{R\sqrt{3}} \frac{1}{\sqrt{\zeta(5+3\psi-4\nu)-(1-2\nu)^2}} \tag{4.1}$$

$$\lambda_c = \frac{\pi\sqrt{Rt}}{4\sqrt{3}} \sqrt[4]{\frac{(\zeta+3\psi+3)^2}{\zeta(5+3\psi-4\nu)-(1-2\nu)^2}} \tag{4.2}$$

where $\zeta = E/E_T$; $\psi = E/E_S - 1$; $E_T = d\sigma/d\varepsilon$ is the tangent modulus; $E_S = \sigma/\varepsilon$ is the secant modulus. By setting $\psi = 0$, the solutions for the J_2 incremental theory are recovered. From the form of Eqs. (4.1) it is trivial to observe that the critical bifurcation stress is always larger for the J_2 incremental theory. For $\zeta = 1$ and $\psi = 0$, Eqs. (4.1) and (4.2) reduce to the well-known classical linear theory results. Note that the foregoing solutions assume simply supported shell edges.

A somewhat more elegant form of σ_c and λ_c is given by

$$\sigma_c = \left(\frac{C_{11}C_{22} - C_{12}^2}{3}\right)^{1/2} \frac{t_w}{R} \tag{4.3}$$

$$\lambda_c = \left\{\frac{C_{11}^2}{12(C_{11}C_{22} - C_{12}^2)}\right\}^{1/4} \pi\sqrt{Rt} \tag{4.4}$$

where $C_{\alpha\beta}$ are the instantaneous moduli of the material at buckling. The constitutive matrix used to obtain these moduli is for the deformation theory

$$\boldsymbol{C}_d = \begin{bmatrix} \frac{1}{E_T} & \left(\frac{1}{2} - \nu\right)\frac{1}{E} - \frac{1}{2}\frac{1}{E_T} \\ sym & \frac{1}{4}\frac{1}{E_T} + \frac{3}{4}\frac{1}{E_S} \end{bmatrix}^{-1} \tag{4.5}$$

and for the flow theory

$$\boldsymbol{C}_f = \begin{bmatrix} \frac{1}{E_T} & \left(\frac{1}{2} - \nu\right)\frac{1}{E} - \frac{1}{2}\frac{1}{E_T} \\ sym & \frac{1}{4}\frac{1}{E_T} + \frac{3}{4}\frac{1}{E} \end{bmatrix}^{-1} \tag{4.6}$$

The above forms are supplied to draw analogies with solutions for other loading cases.

A long-standing paradox in plastic buckling analysis stems from the apparent insufficiency of the flow theory to reproduce the experimentally measured plastic bifurcation loads of shells. While physically sounder, the flow theory of plasticity is known to overestimate the plastic buckling loads of perfect shells, whereas the theoretically weaker deformation theory produces consistently lower values, closer to experimental results (e.g., Bardi & Kyriakides 2006a; Bardi & Kyriakides 2006b). Many different interpretations have been proposed for this mismatch without general consensus to date. To resolve the paradox, Bushnell (1982) proposed the use of the flow theory together with the reduced shear modulus as predicted by the deformation theory. Hutchinson & Budiansky (1976) suggested that considering very small geometric imperfections in flow theory analysis tends to smooth out these discrepancies. Recently, Shamass et al. (2014) presented carefully conducted finite-element simulations of published axial compression tests of shells using both theories,

and found that results with the flow theory were consistently in excellent agreement with the test results. They concluded that any cited divergence stems from the kinematic assumptions adopted in the analytical solutions with respect to the expected buckling mode, which introduce excessive stiffness in the model.

4.3.2 Buckling under combined internal pressure and axial compression

Gas pipelines operate under very high internal pressures, therefore the effect of pressurization is an essential consideration when determining their buckling resistance. Generally, the qualities of the plastic buckling and collapse behaviour of cylindrical shells under combined axial compression and constant pressure resemble those in pure axial compression. Under increasing axial load, the pipe develops uniform axisymmetric wrinkles, which grow steadily leading eventually to a limit load instability. This event can be considered to mark the failure of the pipe shell, since localized deformation ensues. The presence of hoop stresses due to internal pressure lowers the axial stresses in the inelastic region, while bearing little effect on the axial strains. Pressurization also inhibits the development of non-axisymmetric buckling modes by providing a stabilizing effect to the response.

Paquette & Kyriakides (2006) studied the problem both experimentally and analytically. In their analytical treatment, the anisotropic flow theory was used to trace the history-dependent axisymmetric pre-buckling response, whereas the anisotropic deformation theory was employed for establishing the bifurcation point. The bifurcation stress and wavelength can be obtained again by Eqs. (4.5)-(4.6), but the biaxial state of stress is now taken into account through the equivalent stress $\sigma_{eq} = \sqrt{\sigma_x^2 - \sigma_x\sigma_\vartheta + \sigma_\vartheta^2}$, where σ_x is the axial stress and

$$\sigma_\vartheta = P\frac{R}{t_w} \tag{4.7}$$

is the hoop stress due to internal pressure P. The constitutive matrix that gives the deformation theory moduli at each loading increment for isotropic yield conditions is

$$\boldsymbol{C}_d^{-1} = \frac{1}{E_S}\begin{bmatrix} 1+q(2\sigma_x-\sigma_\vartheta)^2 & -\frac{1}{2}+\left(\frac{1}{2}-\nu\right)\frac{E_S}{E}+q(2\sigma_x-\sigma_\vartheta)(2\sigma_\vartheta-\sigma_x) \\ sym & 1+q(2\sigma_\vartheta-\sigma_x)^2 \end{bmatrix}^{-1} \tag{4.8}$$

in which

$$q = \frac{1}{4\sigma_{eq}^2}\left[\frac{E_S(\sigma_{eq})}{E_T(\sigma_{eq})}-1\right]$$

Note that the corresponding matrix for J_2 flow theory, $\boldsymbol{C}_f^{-1}$, is recovered from Eq. (4.8) by substituting $E_S = E$. Results from their experiments of axially compressed stainless steel cylinders were found in good agreement with numerical analysis results.

4.3.3 Buckling of radially supported shells under axial compression

The case of a buried gas pipeline can be viewed from a modelling perspective as one of a radially supported shell. To the author's knowledge, this class of buckling problems was first addressed comprehensively by Yun (1988). A numerical analysis strategy was formulated based on a periodic domain of an inelastic circular cylindrical shell representing the pipeline and a set of nonlinear elastic radial springs representing the soil support. The relationship between the equivalent stress, σ_e, and strain, ε_e, of the soil was expressed according to the Duncan and Chang parametric model of triaxial soil tests as

$$\sigma_e = E_S\varepsilon_e = \frac{\varepsilon_e}{a+b\varepsilon_e} \tag{4.9}$$

where a and b are functions of the confining stress, the strength parameters and the hardening of the soil. This uniaxial model was generalized for plane strain and was used to solve a boundary value problem of a circular soil cavity expanding uniformly, from which the nonlinear radial pressure-displacement response of the desired springs was computed. The pre-buckling response was incrementally solved for by employing the J_2 flow theory to model the plastic behaviour; a plastic bifurcation check was performed after each pre-buckling solution increment was completed. The critical

(bifurcation or limit) loads were found to slightly increase because of the presence of the soil support, with the increase being larger for higher R/t_w ratios, but the respective increase for the corresponding strains was more pronounced. The imperfection sensitivity of the critical loads was evaluated to be significant.

A thesis (Zhang, 2009) has presented a series of analytical solutions for the critical plastic buckling loads of infinitely long cylindrical shells with elastic or rigid cores and perfect geometry. The core has been represented as a continuous one-way spring foundation of constant k operating only in compression. These solutions can also be applied to the case of a buried pipeline shell, where the resistance of the surrounding soil is active in compression. Due to the complexity of the expressions, only the results for the extreme case of a rigid core ($k = \infty$) are cited here as

$$\sigma_c = \frac{5}{3}\left(\frac{C_{11}C_{22} - C_{12}^2}{3}\right)^{1/2}\frac{t_w}{R} \tag{4.10}$$

$$\lambda_c = \sqrt{3}\left[\frac{C_{11}^2}{12(C_{11}C_{22} - C_{12}^2)}\right]^{1/4}\pi\sqrt{Rt} \tag{4.11}$$

It is seen that a rigid support raises the bifurcation buckling stress of the pipeline by a factor of 5/3 and the buckling half-wavelength by a factor of $\sqrt{3}$ compared to the case of a constraint-free pipeline (Eqs. (4.3) and (4.4)).

In reality, a pipeline of the kind studied here is subjected to four different loading and boundary conditions at least within its critical segment. These are the internal pressure; the axial soil load; an uplift profile applied by the soil; and continuous confinement from the soil. It is then sensible to expect therefore that the mechanics of such a problem will exhibit features from all the above discussed relatively simpler buckling problems.

4.4 Development of the 3-D solid-shell finite-element model

Essential details of the modelling strategy adopted for substructure II are exposed in this section. The finite element models are developed in ABAQUS 6.14.

4.4.1 Model geometry and material properties

Two actual gas pipelines listed in **Table 2-1** are simulated, namely the Transitgas (*TG*) pipeline crossing Switzerland, and the currently under construction Trans-Adriatic Pipeline (*TAP*) crossing Greece, Albania, the Adriatic and Italy. Geometric and material data for these pipelines are presented in **Table 4-1**. Note that data fields marked with asterisk were unavailable, so typical values were assumed for these. The TG and TAP pipelines are deliberately chosen as they belong to two rather distinctive R/t_w regimes as far as gas transmission applications are concerned. The pipeline models developed based on these data are referred to as the *baseline* models in the context of this thesis.

The inelastic material behaviour of steel is simulated using the flow theory of plasticity with isotropic strain hardening and a von Mises yield criterion; the accuracy of this approach is justified in the previous section. Following common practice, a Ramberg-Osgood power-law model is used to parametrise the uniaxial monotonic stress-strain response of the material as

$$\varepsilon = \frac{\sigma}{E}\left[1 + a\left(\frac{\sigma}{\sigma_y}\right)^{n-1}\right] \tag{4.12}$$

with a yield offset of 0.5%, appropriate for carbon steel, and a hardening exponent $n = 12$. Parameter a is then estimated as $0.5\% \times E/\sigma_y$. The resulting uniaxial $\sigma - \varepsilon$ curve representing true values is plotted in **Figure 4-3**. Notice that this model represents the response of a continuously nonlinear elastic material and therefore lacks an initial linearly elastic branch. To make the uniaxial $\sigma - \varepsilon$ curve compatible with the traditional definition requirements of an elastic-plastic material in ABAQUS, the plastic branch

is specified directly from Eq. (4.12) for stresses corresponding to plastic strains as small as 10^{-6}. Although these stresses are lower than the nominal σ_y, this is an indispensable approximation that allows to determine an initial elastic branch and establish equivalence between the flow and deformation theory of plasticity.

The soil medium is modelled in this phase as linearly elastic, with spatially averaged strain-compatible moduli as obtained from analysis of substructure I. The dimensions of the soil block are discussed in section 4.4.3.

4.4.2 Mesh design and mesh convergence

The reduced-integration finite-strain S4R shell element is chosen from the software element library to discretize the pipe shell. This element is equipped with both membrane and bending stiffness and is appropriate for modelling the post-buckling response of thin or thick shells. Its merits are its accuracy and computational efficiency, since it only uses one integration point. Its formulation is based on the nonlinear Sanders-Koiter shell theory. Five integration points are used across the thickness of the element.

Zones of different mesh density are specified along the x-axis of the model (**Figure 4-4**). Within the zones of the anticipated critical deformation, that is, around the separating interfaces of the soil materials, the mesh is made fine enough to adequately resolve the plastic axisymmetric buckling modes of an axially compressed unconstrained circular cylindrical shell. The elastic axial half-wavelength of such a shell made of steel with $E = 200$ GPa and $\nu = 0.3$ is given by the below classical result

$$\lambda_c \cong 1.72\sqrt{Rt_w} \tag{4.13}$$

However, buckling in the post-yield regime is generally associated with shorter half-wavelengths. Eq. (4.2) is used to establish the plastic buckling half-wavelength for the models considered. Then, this result is divided by 5 (10 elements per wavelength) to obtain the maximum axial element dimension. With this strategy, maximum axial element dimensions $l_{x,max} = 30$ mm and $l_{x,max} = 100$ mm are sufficient for the TG

and TAP pipeline, respectively. The critical zone, L_{cr}, where the foregoing element dimension applies is taken to extend 2 metres from either side of the separating interfaces. Note that in the presence of internal pressure, the axial wavelength of the wrinkles is longer than without pressure, therefore for the pressurized cases the chosen mesh is conservative.

Sufficiently away from the critical zone, the mesh is made progressively coarser, with element sizes up to 1 metre matching the substructure I models, to minimize the computational burden. Besides, in these low-interest regions, ground strain and curvature amplitudes are very small and hence the pipeline is not expected to deflect appreciably. For element division along the ϑ coordinate, a constant element length $l_\vartheta = 40$ mm is used.

A mesh convergence study confirmed the robustness of the numerical model of the pipe. A pipe shell about $3\lambda_c$ long with the properties of the unpressurised TG pipeline was modelled in ABAQUS using flow plasticity under axial compression conditions; as customarily done, the nodes at one edge of the shell were fully fixed, while the nodes at the other edge were tied rigidly to a reference node at the centre of the section which was displaced axially. Meshes with element sizes from 100 mm to 10 mm were employed and the computed plastic bifurcation stress was compared to the theoretical one of 469 MPa (Eqs. (4.3) and (4.6)). The mesh with $l_x = 30$ mm and $l_\vartheta = 40$ mm gave a solution deviating from the theoretical one by only 2%, therefore it was deemed the most efficient one for substructure II as smaller element sizes would greatly increase the computational effort.

Reduced-integration linear eight-node solid continuum elements C3D8R are used to discretize the soil domain. To ensure mesh compatibility between the two bodies and eliminate penetration issues, the mesh of the soil on the contact with the pipe is made identical to the mesh of the pipe shell in the undeformed configuration. Details of the soil and pipe mesh are displayed in **Figure 4-5**.

4.4.3 Boundary conditions and boundary extents

Pipeline ends

A matter of concern considering that only a portion of the entire pipeline is modelled is what type of kinematic restraints will better represent the conditions at the artificial ends of the pipeline. If the two limiting boundary conditions for the pipeline end sections are considered, namely clamped ends and completely unrestrained ends, it is sensible to prefer the unfavourable one and allow the pipeline end sections move freely in all directions in the baseline models. This choice is driven by the expectation that, away from any lateral ground heterogeneities or man-made boundaries (e.g., compressor stations), a pipeline will displace as a rigid body in tandem with the soil mass under coherent ground motions parallel to the pipe axis. For increased accuracy, some level of longitudinal restraint should be enforced at the pipeline ends, such as by introducing nonlinear end springs to account for the pipeline continuity (e.g., Vazouras et al. 2015). Across the bounding xz and xy faces of the soil block, elementary boundary conditions are prescribed during the static gravity step; during the seismic load step, the normal to the xz face displacements are set to zero.

Effect of external boundary extents

Since the soil block represents a finite portion of an unbounded medium, the operation of truncation may have undesirable effects on the stress state in the soil and consequently the response of the pipe, if made too close to the pipe. It is therefore essential to examine the sensitivity of the 3-D model response to the distance of the soil boundaries from the pipe. This is done by analysing models of different dimensions in the y and z direction and identifying the one that offers a fair balance between accuracy and model size.

Figure 4-6 illustrates four different model sizes that are considered; dimensions are given as functions of pipe diameter D. The total number of elements generated by the user (not including internal elements to model the contact) in each model are also provided; the model with the most elements, namely model d, is assumed the most accurate one. The soil load from model S1EL3 is used as input and comparison among

the models is performed based on the magnitude and distribution of the accumulated effective plastic strain (PEEQ) and the longitudinal profiles $\varepsilon_{xx}(x)$ at $\vartheta = 0°, 90°, 180°$ (corresponding to the crown, east side, and invert points), since the loading is displacement-controlled. From the results for models a and b, it is seen that switching from the narrowest to a wider soil block results in some strain relief as expected, so the narrowest model is rejected as unrealistic. Model c, which is as wide as model b but deeper, gives a higher strain demand; model d, which is as deep as model c but even wider, does not yield substantial differences compared to model c. Therefore, accounting also for the total number of elements in each model, size c with $2b = 5D$ and $d_1 = 2D$ is selected as the optimum for specifying the soil block boundary extents in all substructure II models.

4.4.4 Modelling of interface contact

Contact modelling is a crucial aspect of the overall finite-element modelling strategy for substructure II in the attempt to accurately capture the seismic SPI effects. Initially, the soil cavity and the external pipeline walls are considered to be in perfect contact. The surface-to-surface contact discretization scheme is preferred in ABAQUS, which enforces contact constraints between designated master and slave surface sets in an average sense rather than individually at contact nodes. Surface-based discretization generally yields more accurate stresses than node-to-surface discretization, while preventing large penetrations of master nodes into slave surfaces. Relative tangential motions and rotations are allowed to be arbitrarily large, while loss of contact, i.e. formation of gaps, is permitted at the same time. This modelling approach ensures coupling between the tangential and normal components of interaction. Coupling is here understood in the sense that tangential contact is undefined where a gap has formed. This is not captured by the directionally independent SPI springs proposed by ALA.

4.4.4.1 Tangential contact

The basic isotropic Coulomb friction law is employed to determine the state of frictional contact. At its simplest form, the Coulomb friction law postulates that the shear stress generated between two bodies in contact is a fraction of the contact pressure. As long as a critical shear stress, τ_{cr}, is not exceeded, the two bodies stick together; when τ_{cr} is exceeded, sliding initiates between the bodies with $\tau = \tau_{cr}$ during sliding. Hence, the Coulomb friction law is a rigidly plastic model. The magnitude of τ_{cr} is determined by

$$\tau_{cr} = \mu\sigma_n \tag{4.14}$$

Here, μ is the static interface COF, defined at zero slip rate. Upon sliding initiation, that is, at non-zero slip rates, it has been experimentally observed that μ may change, typically decaying to a residual value, the kinetic interface COF. No distinction between static and kinetic interface COFs is made in this study. The kinetic interface COF is assumed equal to the static one. Note that, in the 3-D models developed herein, $\tau = \sqrt{\tau_x^2 + \tau_\vartheta^2}$.

From the available constraint enforcement schemes available in ABAQUS, the robust penalty formulation is chosen to resolve the constraints for tangential contact. With this formulation, the interface COF is the critical model parameter to be specified. τ_{cr} is automatically determined by the program within each region across the contact interface as a function of the local pressure, σ_n. Moreover, an additional upper bound is enforced on τ_{cr}, as it is physically impossible for τ_{cr} to be higher than the lowest of the strengths of the two materials in contact. In this case, the upper bound is the shear strength of the sands, s_u, therefore:

$$\tau_{cr} \leq s_u = \sigma_n{}' \tan\varphi + c \tag{4.15}$$

where $\varphi =$ friction angle and $c =$ cohesion of sand according to the Mohr-Coulomb model. Assuming $\varphi = 40°$ and $c = 0$ for the uppermost sand layer where the pipeline is laid, a uniform s_u at $z = -H$ is established accordingly for all substructure II models.

Invoking the empirical relationship $0.5\tan\varphi \leq \mu \leq \tan\varphi$ (Brumund and Leonards, 1973), and that, for sands, it is typically $\varphi = 29° \div 41°$, a gross range for μ is obtained as 0.28~0.78. Sheil et al. (2018) also infer from cyclic loading tests a value range of 0.55~0.6. For the baseline models, a moderately high $\mu = 0.6$ is assumed which lies within the quoted ranges. Note that the Coulomb friction model introduces non-symmetric terms to the tangent global stiffness matrix of the soil-pipe system. For this reason, the non-symmetric matrix storage is chosen in ABAQUS, which is optimum for improving convergence when $\mu > 0.2$ (Dassault Systèmes, 2014b).

4.4.4.2 Normal contact

For modelling the normal interaction, a 'hard' pressure-overclosure relationship is adopted, defined by the set

$$\sigma_n = 0 \quad for \quad u_n < 0 \qquad (4.16)$$

$$u_n = 0 \quad for \quad \sigma_n > 0$$

where u_n is the measure of penetration (assumed positive) of the two surfaces at a contact point. The first condition defines a gap (=negative penetration) while the second denotes contact. A linear penalty method, which introduces a constant penalty stiffness into the system equations, is used in this case too to enforce the constraints. **Figure 4-9** displays graphically the interaction models described above.

4.4.5 Initial geometric imperfections of shape

As discussed in section 4.3, unavoidable wall imperfections can drastically lower the theoretical critical loads of an ideally perfect pipe shell. To model this effect in the context of this study, a variation of the perfect models is considered later by introducing a stress-free axisymmetric imperfection pattern. This pattern is expressed by Eq. (4.17), where radial deflections are taken positive in the outward direction:

$$\tilde{w}(x) = w_0 \sin\left(\frac{\pi x}{\lambda_c}\right), \qquad -\frac{L_{cr}}{2} \leq x \leq \frac{L_{cr}}{2} \qquad (4.17)$$

λ_c is here the critical axial half-wavelength corresponding to the plastic bifurcation stress of the perfect pipe and w_0 is the amplitude assumed as a fraction of t_w. This imperfection shape is applied over the critical zone L_{cr} and is illustrated in **Figure 4-10** for $w_0 = 0.5t_w$. However, note that imperfection amplitudes in reality tend to be smaller for smaller R/t_w because in this case it is practically easier to manufacture perfect geometries.

The soil mesh across the contact surface is exactly matched with the perturbed pipeline mesh to prevent formation of gaps during application of the permanent loads. It should be mentioned that this study does not consider residual stresses induced during the manufacturing process, the effect of which on the material response of the pipe may be significant in certain cases.

4.4.6 Loading phases

The loading sequence is implemented in two steps. In the first step, gravity is applied as a static load to establish the in-situ soil stress state and to ensure that the interface contact model is activated; the internal pressure is also applied at this step on the pipe. In the second step, large-deformation incremental stress analysis is performed for the imposed soil displacements. The soil displacement profiles computed from substructure I correspond invariably to nodal spacing of 1 m, hence linear interpolation is performed to fit them to the denser mesh zones of substructure II.

To trace potentially unstable static equilibrium paths past limit points, where the load-deflection curve exhibits negative slope, an arc-length procedure is used in the seismic step. This is based on the modified Riks algorithm (Crisfield, 1981) as implemented in ABAQUS. This algorithm is powerful for solving for smooth equilibrium paths—those that do not involve discontinuities, i.e., bifurcation. Its formulation introduces an additional unknown, the 'load proportionality factor' λ, into the system of equations so that

$$\Delta l = \sqrt{\Delta \mathbf{u}^T \Delta \mathbf{u} + \Delta \lambda^2 \mathbf{p}^T \mathbf{p}} \tag{4.18}$$

is a fixed incremental arc length traversed in the $N+1$-dimensional space of the solution, where N is the number of DOFs. This constraint requires that all externally applied loads are proportional. Effectively, with the modified Riks method, both the incremental displacements and loads are sought simultaneously during analysis. The standard Newton-Raphson scheme is employed in the background to find the solutions for $\boldsymbol{p}$ and λ in the nonlinear system of equations

$$\mathbf{p}_{int}(\mathbf{u}, \lambda) - \lambda \mathbf{p}_{ext} = \mathbf{0} \tag{4.19}$$

In code implementation, the initial increment in arc length is set to 0.01 and from that $\Delta\lambda_{in}$ is estimated also at 0.01. While subsequent $\Delta\lambda$ are computed automatically by the algorithm, bounds on Δl are enforced to control the solution performance, with $\Delta l_{min} = 10^{-5}$ and $\Delta l_{max} = 0.01$. It was found that further reduction in Δl_{min} does not improve the solution accuracy, therefore this set of parameters is used for all analyses.

4.5 Pipeline response to critical soil loads

4.5.1 Response to weak ground motion

The maximum demand-to-capacity ratio in terms of equivalent stress across all linear elastic site scenarios, where the capacity is defined as the steel yield limit, was found to be 0.45, indicating that the pipeline responds in the elastic regime. This is depicted in **Figure 4-11**, which plots the equivalent stress contours on the TG pipeline due to soil loads from the worst low-intensity excitation case in Site 1.

Generally, the amount of ground shaking generated due to low-intensity inputs is unlikely to cause the pipeline to yield. The stress induced in the pipe is not negligible, but is largely due to the internal pressure, which is a known service load. It is noted that the pipeline is found to retain contact with the soil (no separation) under this level of ground loads.

4.5.2 Response to strong ground motion

Sets of results are reported for the two baseline pipeline models of **Table 4-1** subjected to input loads from two substructure I variants corresponding to strong bedrock excitation in nonlinear soil—modelled as equivalent-linear. Therefore, there will be four case studies presented in the following.

4.5.2.1 Pipeline in Site 1

The critical soil loads used as input are those from model S1EL3. To provide a sense of the magnitude and directionality of the imposed loads, the resultant displacement vectors $\boldsymbol{u}_{cr}$ representing the ground motion at the critical time instant of the excitation are illustrated in **Figure 4-12**. Clearly, the load is predominantly axial, with an increasing perpendicular component approaching $\bar{x} = 0$ from the soft side, as seen in the inset. Results are presented for both the TG and the TAP pipelines having perfect geometries.

Figure 4-13 plots the deformed shapes of the pipelines over the critical zone of deformation; note that deformations are magnified by a factor of 10 for clarity. The deformation shapes tend to follow the soil load directions; this is especially evident around $\bar{x} = 0$ and $\bar{x} = -0.1$ on the soft side, where upward bending is observed, driven by the strong vertical load component. On the stiff side, the pipes are less deformed. Between the two pipes, TG undergoes more severe bending deformations than TAP due to its higher R/t_w and hence lower bending stiffness.

To gain understanding into the stress distribution over the pipelines, the equivalent (von Mises) stress contours are plotted on a 3-D snapshot of the deformed structures in **Figure 4-14**. As expected, the material is found to be more heavily stressed around $\bar{x} = 0$ and where the uplift profile attains its peak; there are patches of material that are stressed beyond the yield limit of 448 MPa in both pipelines, but stresses are more localised in TG. In terms of deformation, **Figure 4-15** displays the axial strain distributions along longitudinal fibres at $\vartheta = 0°$ (crown), 90°, and 180°. While away from the soil interface the section fibres experience uniform straining,

within the critical zone the top and bottom fibre strains follow similar patterns but with opposite signs, confirming that bending dominates in this zone. There is significant compressive strain concentration on the bottom side of a critical section as evidenced by the single sharp downward peak in both pipes, with the TG experiencing nearly three times larger strain.

Figure 4-16 shows the axial and hoop strain circumferential profiles of the critical sections. For TG, the peak compressive axial strain of ~2% occurs at 180° (compressed side); the peak tensile hoop strain also occurs at the same location of the section and is of similar magnitude (1.9%). This amount of tensile strain, a result of the fairly high internal pressure (6.75 MPa), is not far from typically used tensile strain limits in design (see section 2.6). Moreover, the non-uniformity of the hoop strain profile is indication of section ovalisation.

The trends are similar for TAP, but now strain profiles diverge from symmetry with respect to the vertical. Note also that, interestingly, for TAP, the peak hoop strain is larger than the peak axial strain. For further insight, **Figure 4-17** portrays the ovalisation of three sections along the pipe length, alongside the maximum flattening parameter attained. Ovalisation is as expected found to be most substantial at the section acted upon by the maximum upward soil movement, with $\Delta D/D_o$ ratios very close to 4%; however, this level of ovalisation is not critical as it falls short of the conventional limit of 15%.

Overall, the pipes seem to not have reached a critical limit state in either case under the imposed loads (neither wrinkling nor localised bulging nor excessive ovalisation is observed). However, the strain distribution along TG reveals significant concentration, which means that a critical limit state is to be found very close on the traversed equilibrium path, as will be seen in the following. The first-order observations made above underscore the complexity of the pipe deformation response as well as the distinct details governing in the two classes of gas pipelines.

Load-deformation response

The study of the performance of buried pressurised pipelines under SVEGM would not be complete without analysis of the load-deformation response at the cross-section level. This shall be especially useful here as it will illuminate the salient characteristics, such as the nature of instabilities, of the incremental shell response up to collapse. To accomplish this, the previous two substructure II models are solved again for the same load patterns scaled up until collapse (or numerical non-convergence) occurs.

Given the two loading components acting on the pipelines, the axial force versus axial shortening ($P^*-\bar{\varepsilon}$) and bending moment versus axial curvature ($M^*-\bar{\kappa}$) responses of the two buried shells are calculated within a critical segment of length about equal to L_{cr} measured from $\bar{x}=0$ in the soft soil (the superscripted asterisk denotes normalised quantity). The kinematic quantities used on the horizontal axis are averaged over this critical segment (i.e., $\bar{\varepsilon}=\Delta u/l$ and $\bar{\kappa}=\Delta\varphi_y/l$). To obtain P and M, normal stresses are integrated over the critical section located approximately in the middle of the critical segment. Along this segment, the distribution of φ_y (nodal rotation about the global y axis) is almost linear, thus the axial curvature is approximately constant, resembling a pure bending situation. Moreover, P is approximately constant over the same length. Note that $\bar{x}=0$ could be roughly seen as a fixed end for the pipeline. Following Corona & Kyriakides (1988), the normalization factors used in the subsequent presentation are as follows:

$$P_o = 2\pi R t_w \sigma_y$$

$$M_o = D_o^2 t_w \sigma_y \text{ with } D_o = D - t_w$$

$$\kappa_o = t_w / D_o^2$$

where P_o and M_o represent the yield axial load and the plastic moment of the shell section, respectively.

Figure 4-18 plots the shell responses for the TG pipeline (compression is positive); this figure should be examined alongside **Figure 4-19**, which shows snapshots of the pipeline deformation states at various load levels marked in **Figure 4-18**. It is observed that P and M increase proportionately until the first yield in the material, beyond which a nonlinear branch is traced. A uniform wrinkling pattern does not emerge with the gradual reduction in axial and bending stiffness, but, as seen in the deformed shape marked as state (3), plastic strain starts to localize on the compressed side of the shell. Suddenly, as the load increases, snap-through buckling develops in the $M^*-\bar{\kappa}$ path at $M = 0.68M_o$ causing a single wrinkle to form on the compressed side (invert); separated by only a small amount of deformation, a second bifurcation in the $P^*-\bar{\varepsilon}$ path ensues at $P = 0.3P_o$, precipitating deformation localisation, as shown in deformation state (4). These events mark the collapse of the shell which manifests as a localised outward bulge—characteristic of pressurised shells—resulting to an unbounded increase in axial shortening in the post-buckling regime. Localised strains develops at a second location exactly at the soil interface, leading to a second localised bulge on the crown. A more detailed illustration of the growth of the ripple is provided in **Figure 4-20**, where the profile of the radial component of pipe displacement at $\vartheta = 180°$ is plotted. Parameter λ symbolises the proportion of the full nominal load applied at each increment.

The axial load-carrying capacity of the shell is exhausted at $\bar{\varepsilon}_{cr} \approx 0.5\%$, which can be considered the critical axial buckling strain in this case. The above described sequence of events showcases the strong $P-M$ interaction within L_{cr} through geometric and material nonlinearity. For this intermediate R/t_w ratio, the shell response is governed by two bifurcation instabilities in the axial force and bending moment occurring at very short distance from each other.

As far as the thicker TAP pipeline is concerned, its response is presented in **Figure 4-21** and **Figure 4-22**. In this case, a fundamentally different behaviour is exhibited by the shell: upon first yielding, the shell is seen to experience a sudden loss in axial load. Beyond that point, the behaviour of the shell is governed by bending.

The $M^* - \bar{\kappa}$ response traces an ovalisation path, with the shell ovalizing fairly uniformly in the critical length (see deformation state (2)). As the slope of the response curve gradually reduces, a limit moment $M = 0.58M_o$ is attained at $\bar{\kappa} = 0.44\kappa_o$ and, beyond this instability, ovalisation growth begins to localise around $\bar{x}_{cr}$, as seen in deformation state (3), and moment slowly drops with further load. This is better shown in **Figure 4-23**, where deformed shell rings at different x coordinates are sketched over the undeformed configurations; the maximum flattening factor calculated is 15.2%, exceeding the limit of 15%.

It is not straightforward to identify an appropriate performance measure in this case. $\bar{\varepsilon}_{cr}$ corresponding to the axial limit load alone is probably not the most representative parameter because the dominant response is in bending. That said, $\bar{\kappa}_{cr}$ corresponding to the limit moment appears more suitable to describe the limit load type of instability exhibited by TAP.

Contact response

Figure 4-24 shows the state of contact (sticking, sliding or gap) over the soil-pipe interface under the full soil loads from model S1EL3. It is evident that a highly non-uniform contact state prevails. For the most part outside the critical zone in the soft soil, pipe and soil slide against each other but remain in contact. Therefore, shear stresses are transferred from soil to pipe along a large length. Inside the critical zone, though, there are gaps at various locations resulting from the non-compliance of the pipes to the vertical soil movement. On the other hand, in the stiff soil, where axial ground movement dominates, no gaps are present. This state of contact demonstrates the strongly local character of the SPI problem, which is hard if not impossible to analyse with conventional spring models.

To further analyse the level of SPI in this problem, the horizontal and vertical displacement profiles of the soil block and the pipelines are plotted together in **Figure 4-25**. The left plot clearly shows the horizontal translation of the pipelines diverging from that of the ground, significantly more so for the stiffer TAP pipeline; the abrupt change in ground displacement at mid-span translates through frictional interaction

into smoother profiles in the pipelines. The right plot confirms that both pipelines are unable to conform to the soil uplift pattern in the region close to $\bar{x} = 0$, and for this reason gaps open both over the top and the bottom side. This type of behaviour is of course favourable as it acts as a strain relief for the shells, but bending is the dominant mode of response in this region.

4.5.2.2 Pipeline in Site 2

To evaluate the seismic performance of a gas pipeline crossing Site 2, the critical soil load profiles from model S2EL0 are used as input. Results are again computed for the baseline TG and the TAP pipelines having perfect geometries.

Figure 4-26 provides a graphical illustration of the ground displacement field imposed incrementally on the soil block. Contrary to Site 1, the vertical components are considerably smaller. Focus in analysis of the performance will be placed on the compression zone of the system, as this can be the critical one in terms of buckling. On examination of **Figure 4-27**, it is observed that under the S2EL0 soil loads in Site 2, both pipelines experience very small deformation (note that deformation has been scaled up by a factor of 10). The deformed shapes are characterised by downwards bending occurring inside the valley, close to the interface with the stiff soil. **Figure 4-28** provides further evidence of the relatively low stress levels developing in the pipelines. Both pipelines remain elastic with maximum equivalent stress not exceeding 315 MPa, the most part of which is attributable to $\sigma_{\vartheta\vartheta}$ caused by internal pressure. The axial strain profiles for TG presented in **Figure 4-29** show a peak of 0.05% (compressive), strikingly lower than the deformation levels experienced in Site 1.

Because the response of the pipelines buried in Site 2 is gauged non-critical, no further effort is expended into the analysis of their load-deformation paths. However, the contact response is further studied in the following to trace the causes of the reduced response.

Contact response

In **Figure 4-30**, the state of contact predicted at full load application is identified for TG with different colours. While the two bodies remain in contact outside the valley—with the frictional strength not moblised—inside the valley the two bodies are separated over a very extended zone. This is because the pipeline cannot follow the quite jagged pattern of the vertical soil displacement, thus allowing gaps to open. This in turn blocks the transmission of shear contact stresses to the pipe, hence the unexpectedly low axial strains. **Figure 4-31** plots together the displacement profiles of the soil block and the TG pipeline; striking is the deviation of the horizontal motion of the pipe from that of the soil. Apparently, the loss of contact over a great portion of the interface leads to this situation of low pipe demand.

4.5.3 Demand-to-capacity ratios

At this point, it is instructive to show how the peak computed pipe demands compare against design and performance limits proposed in standards of practice, which will allow to assess their reliability. The critical response of the pipeline is presented in the form of demand-to-capacity (D/C) ratios—equivalent to the inverse of the factor of safety—along a straight line of nodal points at $\vartheta = 180°$. The following strain and stress limits are used to represent pipeline capacity:

a. the allowable compressive strain $\varepsilon_{c,max}$ under seismic wave load as defined by

- Eurocode 8: $\min\{1, 20\,t/R\}$ (%)
- ALA: $0.75 \cdot [0.25\,t/R - 0.0025 + 3000(PR/Et)^2]$ (%)
- Japan Gas Association: 3%

b. the allowable longitudinal stress as specified by ASME: $0.9\sigma_y$

c. the von Mises yield stress criterion: $\sigma_{eq} < \sigma_y$

d. the criterion for prevention of ovalisation: $\Delta D/D_o < 0.15$

Compression limits were chosen over tension limits because emphasis is placed on buckling – tensile failure is not examined.

Figure 4-32 plots the D/C ratio profiles in terms of (local) compressive axial strain, with the capacity calculated according to (a) above, for pipelines in Site 1 under load from model S1EL3. Significant exceedance of the EC8 limit (0.53%) is seen to occur in the critical zone of TG. Although no buckling arises under the imposed load, performance evaluation based on the EC8 non-buckling limit yields buckling. However, according to the more extensive load-deformation analysis, the first shell bifurcation occurs at 1.27 times the nominal load at an average compressive strain of 0.5%, which agrees very well with the EC8 limit. Therefore, from the perspective of average pipe strain, the EC8 non-buckling limit seems very relevant. On the other hand, the ALA and JGA limits (2.1% and 3% respectively) are far less conservative in terms of average strain, leading to $D/C < 1$ and therefore failing to capture the buckling limit.

As for the TAP pipeline, all three metrics prove reliable to gauge its performance as revealed by the D/C curves being upper-bounded by the threshold line. Obviously, a fixed limit strain for buckling as the one proposed by JGA is not robust, regardless of the fact that it is effective for this case. The ALA threshold appears more accurate for characterising the capacity as it incorporates the effect of internal pressure, whereas the EC8 threshold is independent of it.

As mentioned earlier, σ_y is exceeded in both pipelines, but this is by no means indication of failure in such highly ductile structures. Along the same lines, while the longitudinal stress D/C ratio based on the ASME condition locally exceeds unity for TG, as seen in **Figure 4-33**, this stands in contrast to the fact that the pipeline is still able to carry further load. In general, strength limits are too conservative measures for ultimate limit state design or performance evaluation of carbon steel pipelines, particularly when the action under consideration is displacement-controlled like ground movements.

In relation to section ovalisation, the performance of the pipelines has been assessed in the previous section where it was found that the maximum $\Delta D/D_o$ experienced is about 3.75 times less than the limit.

4.6 Parametric investigation

In an effort to clarify how some key parameters may alter the critical buckling load, a sensitivity analysis is carried out by varying the R/t_w ratio, the internal pressure, the imperfection amplitude, the plastic hardening exponent, the interface COF and the end conditions of the pipeline shell when subjected to SVEGM due to site inhomogeneity. In the interest of simplicity and to aid a generalised approach to analysing substructure II, idealised analytical shapes for the horizontal and vertical seismic ground movement will be considered based on curve-fitting of the computed profiles from Chapter 3. In this way, analysis of substructure II will be disconnected from the specificities of each site scenario dealt with in substructure I, therefore allowing to make general observations on the pipeline response. Additionally, it will enable to correlate a suitable metric of ground motion intensity to a performance metric of the pipeline.

4.6.1 Curve-fitting of soil movement profiles

By careful inspection of the Site 1 displacement profiles in **Figure 3-23** and **Figure 3-26**, it can be seen that u_g may be well approximated by a logistic function of x, while v_g by a bell-shaped function of x. Using nonlinear regression analysis, the computed $u_g(x)$ profiles are fitted to a logistic model $f\colon \mathbb{R} \to [0, +\infty)$ given by

$$f(x) = \frac{Q}{1 + e^{-k(x-x_0)}} \tag{4.20}$$

This functional form belongs to the class of sigmoid (S-shaped) functions, saturating to zero as $x \to -\infty$ and to Q as $x \to +\infty$. For this reason, a zero baseline is first enforced for all $u_g(x)$ profiles before fitting; where necessary, the order of ordinates is

reversed to obtain an increasing function of x. Parameters Q, k and x_0 are estimated with iterative least-squares fitting using MATLAB. Results are presented in Figure **Figure 4-34**; a good fit is obtained as revealed by the R-squared statistics ($\geq 92\%$). It is also useful to note that parameter k controls the steepness of the curve.

The computed $v_g(x)$ profiles are fitted to a Gaussian curve expressed as

$$g(x) = ae^{-\left(\frac{x-b}{c}\right)^2} \tag{4.21}$$

with parameters a, b, $c \in \mathbb{R}$. These are estimated in the same way as for $u_g(x)$. Results are shown in **Figure 4-35**. The goodness of fit is satisfactory, with R^2 close to 90% in most cases. Note that the fitting parameters estimated for both models correspond to the transformed independent variable $\bar{x}$ and that the absolute load magnitudes are irrelevant as the loads will be incrementally ramped up to pipe failure. What matters though is the ratio of the horizontal to the vertical load magnitude, or Q/a, which has to be within physically realizable limits. This ratio is estimated from the above Figures to range between approximately 2 and 5 and is added to the parameter set but note that it will greatly depend on the physics of the seismic site response. Furthermore, to resolve some numerical difficulties encountered, a small rigid-body component is added to $u_g(x)$.

Having established the general analytical forms of the ground loads to be applied to the parametric SPI model, it remains to define the parameter space as follows: $P/P_y = 0.5, 0.56, 0.8$; $w_0/t_w = 0, 0.01, 0.1, 0.5$; $n = 9, 12, 20$; $\mu = 0.3, 0.6, 0.8$; pipe ends = free or both clamped; $R/t_w = 19.7, 37.5, 51.5$; $Q/a = 2, 5$. **Table 4-2** lists the parameters used for each model generated for this study. Case 1 is the base model and all others are drawn from it by varying one parameter at a time. The fitting parameters used in this study are $k = 56$, $x_o = 0.01$, $b = -0.08$, $c = 0.04$. Results will be presented in the form of arc length-internal axial force and arc length-moment curves at the critical section within L_{cr}, where the arc-length is equivalent to Q (i.e., the magnitude of the horizontal differential ground displacement). The P^*-Q and M^*-Q curves can

alternatively be interpreted as load versus vertical deflection of the bottom part of the pipe, since $Q/a = \text{const}$. Where not otherwise mentioned, model parameters are those of the base model.

To gauge how representative these curve-fitted shapes are of the actual input ground displacement profiles due to given excitations, a comparison is performed between the responses of the baseline case from **Table 4-2** and the TG pipeline presented in subsection 4.5.2.1. For the load from site S1EL3 it is $Q/a \approx 2$, therefore a comparison between these models (the 'approximate' and the 'accurate' one) at the same mobilised ground load is warranted, since all other parameters are the same. **Figure 4-33** shows the longitudinal pipe strain profiles along fibres at $\vartheta = 0°$ (crown), 90° (side), and 180° (invert) at full application of the load from case S1EL3, which corresponds to a relative axial ground movement of 0.21m locally in the transition zone. It is seen that that the distributions agree fairly well. The approximated model captures sufficiently the bending strains in the critical zone, though it underpredicts the peak values. This is however expected because the fitted forms tend to smooth out the local peaks and troughs in the true ground movements. Generally, one would expect that the lower the nonlinearity in the soil response and the degree of lateral soil inhomogeneity, the better the representation of the input ground loads by the proposed fitted forms.

4.6.2 Effect of internal pressure

Three pressure levels in the high regime are examined. Although from a design point of view pressurising a pipe to $P/P_y > 0.72$ is in violation of the ASME provisions for maximum allowable hoop stress, it serves to study to what extent a strongly multiaxial loading state modifies the critical performance states of the pipe. It is observed in **Figure 4-37** that higher pressures greatly lower the axial and moment capacities of the pipeline, as also reported in several other studies. At the same time, higher pressures can significantly delay the critical loads, in the sense that these will occur at larger Q, as is clearly the case with $P/P_y = 0.8$, where the bifurcation load is

preceded by a limit load. Given though that Q in reality is unlikely to exceed 0.3 m, this case has only theoretical relevance.

The unusual shapes of the response curves for $P/P_y = 0.5$ require explanation. At $Q = 0.2$, the axial load path displays branching downwards while the moment path branches upwards tracing high values. This behaviour is interpreted as the pipe attaining its beam mode plastic limit load, followed by a mild decay in the axial load. For reference, this graph may be compared with figure 2.14b in Yun (1988), which plots axial load against crown deflection calculated from analytical beam models on elastic foundation for different beam imperfections. Here, the beam load imperfection is effectively the Gaussian uplift profile due to the vertical ground motion component, which increases in amplitude. Beyond the identified limit point, the pipeline sustains much greater moment because of the increasing vertical deflection consisting of two components, the nonlinear beam uplift and the directly applied ground uplift. Effectively, the pipeline experiences a transition from a mixed beam-shell response mode to a predominantly beam mode.

4.6.3 Effect of imperfection amplitude

Figure 4-38 shows the P^*-Q and M^*-Q curves obtained for different values of the imperfection amplitude as this was defined in subsection 4.4.5. For the perfect pipeline, a limit bending moment is attained at increasing axial load – the analysis terminated at an arc-length of 0.29, a fact that probably implies the presence of a bifurcation or limit point impossible to overcome for the arc-length algorithm. The same observations can be made for the pipeline with 1% imperfection amplitude, only in this case the imperfection results in a slight decrease in the moment capacity.

When larger imperfections are introduced, results of greater engineering significance are obtained: buckling and collapse of the pipeline occur as revealed by the branching in the P^*-Q curve. Specifically, for $w_0/t_w = 10\%$, the axial response curve is seen to bifurcate at a differential horizontal ground displacement of 0.22 m. At this point, a ripple develops on the bottom of the critical section; with further axial

compression, deformation starts to increase rapidly while moment drops precipitously. The critical event of collapse showing as a downward-facing buckle happens at a differential horizontal ground displacement of 0.29 m. For $w_0/t_w = 50\%$, the first ripple forms at $Q = 0.15$ m whereas collapse comes at 2/3 of the value for $w_0/t_w = 10\%$—in this case, accompanied by development of a second upward-facing buckle very close to the initial one. The characteristics of the localised buckles formed are generally similar to those described in subsection 4.5.2.1.

4.6.4 Effect of material hardening

The effect of material hardening for constant yield stress on the load paths of the critical section is illustrated in **Figure 4-39**. Steel with higher hardening levels (i.e., lower n values) generally results in a moderately raised response. The Riks algorithm was unable to trace the response paths for the models with $n = 9$ and $n = 12$ beyond a certain point which is believed to be the bifurcation point of the beam mode of buckling. The existence of these bifurcation points is confirmed by analysing equivalent models with imperfections, which allowed to identify the corresponding limit points lying in close proximity to the bifurcation points of the perfect models. For instance, **Figure 4-40** shows a comparison of the responses between the perfect pipe and one with 10% imperfection for $n = 9$. It is seen that the perfect pipe traces nearly the same axial load path as the imperfect pipe—the response of which is similar to those plotted in **Figure 4-38**—while the presumed bifurcation load occurs virtually at the same Q as the buckling load of the imperfect pipe. Based on this rationale, the response curves $n = 9$ and $n = 12$ should qualitatively follow the trend of the curve for $n = 20$. As the hardening parameter is reduced, critical loads increase moderately and occur at progressively lower Q.

4.6.5 Effect of radius-to-thickness ratio

Three pipelines with different R/t_w ratios covering a wide range of gas applications are examined, all other properties being equal, and their responses are

compared in **Figure 4-41**. Two types of responses are identified: the first refers to the model with $R/t_w = 19.7$ (very thick pipe), for which the response is predominantly flexural while the internal axial force decays after attaining a limit value; the second refers to the two thinner models, which exhibit a response dominated by axial load with the moment experiencing a maximum, as described in subsection 4.6.2.

4.6.6 Effect of COF

Figure 4-42 shows how the response of the pipeline is affected by the interface COF – the interface shear strength is kept constant across the models at 25 kPa. For $\mu = 0.3$, the axial force displays a cut-off at about 0.1 m relative displacement, a consequence of the bilinear shear stress model. At this point, the moment curve obtains a steeper slope and bending—under constant axial compression—becomes dominant in the critical zone of the pipe. For $\mu = 0.8$, the response curves follow the trends of the base model, but in this case the pipeline experiences higher internal forces as the higher COF allows larger stresses to be transmitted from the soil.

4.6.7 Effect of pipe end conditions

As shown in **Figure 4-43**, a pipeline with assumed fixed end conditions exhibits a drastically different response than one with free ends, which has been the standard assumption until this point. Specifically, the internal axial force at the critical section presents a peak and then follows a decaying path, which means that slipping occurs earlier and over greater lengths. Consequently, the pipeline responds virtually in bending as pictured in the M^*-Q curve, accommodating quite large relative ground displacements without experiencing instabilities or loss of strength.

4.6.8 Effect of magnitude ratio of loading components

The dependence of the pipe response on the relative magnitudes of horizontal and vertical ground motion profiles is illustrated in **Figure 4-44**. When a is raised to

$0.5Q$, the flexural response of the pipe is amplified, with the bifurcation buckling load expected to occur at higher Q.

4.6.9 Discussion

From the foregoing parametric analysis, it becomes obvious that the response of a buried gas pipeline to spatially variable seismic ground motions along its length is governed by the interaction between the shell and the beam modes. The degree to which each mode bears influence seems to depend on a number of factors, most prominently the R/t_w ratio and D, the interface conditions and the internal pressure (the embedment depth is not examined). In the cases examined and for the majority of pipe typologies, the beam mode will not be dominant due to the large diameters used. It is worth noting that each pair of P^*-Q and M^*-Q curves plotted above represents only one possible loading path in the $P-M$ interaction space, that resulting from proportional increments in horizontal and vertical ground displacements. To construct the complete $P-M$ interaction diagram of the pipe section, a large number of different loading paths need be analysed to identify the failure point on each path, thereby allowing to draw the complete failure curve that would demarcate the buckling capacity of the section under combined P and M loads. This task is beyond the scope of this thesis.

To further demonstrate how significantly the non-uniform soil load profiles alter the pipe response, the TG baseline model buried in homogeneous ground with properties of one of the deposits used above is analysed for uniform horizontal ground movement, assuming free or fixed pipe ends. **Figure 4-45** shows the axial stress distribution along the pipeline for different levels of soil displacement. It is seen that in the free-end case, the pipe is very lightly stressed over its length, with the distribution being constant away from the ends, whereas in the fixed-end case, the distribution is linear and the pipeline ends are more heavily stressed, albeit below yield. However, the fixed-end case is not realistic, as even if a very stiff and heavy body

restrains a pipeline end, this body will be subject to motion due to ground shaking and hence the restraint will be inevitably relaxed.

4.7 Comparison with other studies

Due to the scarcity of published research on the same problem, comparison is restricted to results from simpler combination of loadings. The scope is to assess how the critical shell response parameters determined in this study differ from those calculated elsewhere.

The most relevant study to this thesis is that of Yun (1988). Although its results are not directly comparable to this chapter's analysis due to the different assumptions employed, there are certain common attributes that make a qualitative comparison valid. Yun briefly studied the interaction between the shell and beam buckling mode of buried steel pipes by using an approximate analytical beam model which assumed that buckling occurs when the maximum compressive stress in the beam section due to combined axial compression and bending reaches the theoretical critical buckling stress in axial compression only. His results for a family of models are shown in **Figure 4-46** in terms of normalised local shell buckling load against normalised uplifted length for different beam imperfection amplitudes (Δ_o/D) assumed over a segment 50 diameters long. Overlaid in dashed lines are the corresponding critical buckling loads under pure axial compression. Note that R/t_w is comparable to that of TG studied here. It is seen that a pipeline with a very mild initial uplift and $w_0/t_w = 10\%$ is predicted to buckle locally at only 68% of the corresponding critical buckling load in axial compression; for larger initial uplifts, the critical buckling load drops even lower.

For consistency, the critical (limit) loads are established here for the baseline TG pipeline supported radially by elastic soil springs representing the soil restraint, and subjected to axial compression; they are shown in **Figure 4-47**. The values of the springs are determined using the modulus of subgrade reaction, k_s, a soil parameter obtained from plate bearing tests commonly used to describe soil compliance. As it is

not straightforward to relate k_s with E_s, a range of values are considered to establish an upper and lower bound. An initial imperfection of axisymmetric shape is also considered with a 10% amplitude.

In the previous, critical axial buckling loads were established for the TG pipeline under combined P–M due to seismic soil movements. For the worst Site 1 scenario, buckling of the perfect pipeline occurred for $P = 0.3P_o$ at $\bar{\varepsilon} = 0.5\%$; this axial load is only 30%-35% of the buckling load under pure axial compression, while the critical average strain 36%-50% of that under pure axial compression. For the idealised load profiles, the axial buckling load for the TG pipeline with $w_0/t_w = 10\%$ was $P = 0.46P_o$; this value amounts to 47%-59% of the buckling load under pure axial compression. The load reductions estimated here are larger than those calculated by Yun, but of similar order. The loading combination considered here is more unfavourable as it involves first-order bending moment (whereas Yun's model considers only second-order moments) as well as internal pressure. The different pipe diameters and embedment depths are also factors influencing the governing response mode. In Yun's model, $h/D = 0.9$ and the diameter is small, conditions that favour the beam mode, whereas here $h/D = 1.67$ and the diameter is twice as large as in Yun's model, conditions that render the shell response dominant.

4.8 Summary of the chapter and conclusions

This chapter dealt with the development of the second substructure of the two-step numerical methodology for the seismic response analysis of buried gas pipelines, and its application to various site-specific and generic scenarios. The analysis undertaken offers new insights into the mechanical behaviour of gas pipelines crossing laterally inhomogeneous soil and subjected to seismic excitation. It has been demonstrated that such pipelines can display a variety of critical performance states depending on certain governing parameters. The existing performance criteria found in

major standards of practice have also been assessed for their applicability under these complex loading conditions. Specifically, the below conclusions are derived:

- Both baseline pipeline models performed to satisfactory levels on application of the critical soil displacement profiles from Site 1, as they did not suffer instabilities or other critical limit states. The loading pattern consisted of differential ground motions of 15 cm in the axial direction and 4 cm in the vertical direction on average. Nevertheless, both pipelines responded in the inelastic regime and significant stress concentrations were estimated near the soil block interface; considerable bending deformations were also present within the ground uplift zone, more so for the thinner TG pipeline. Section ovalisation was found to be appreciable, but within code-prescribed limits.

- From load-deformation analysis up to pipeline failure, profound differences were found between the responses of TG (representing an intermediate R/t_w buried steel pipe) and TAP (representing a thick one) to combined frictional and thrust seismic soil loads. Specifically, TG exhibited snap-through buckling at a load 1.23 times the nominal substructure I load, resulting in two sharp local buckles within the critical zone of loading. The interaction between axial load and bending moment at the worst affected section was strong in this case. The response of TAP on the other hand was predominantly in flexure, characterised by ovalisation which initiated uniformly and later localised at a very high load (2.3 times the nominal substructure I load).

- The contact state between soil and pipe was found to be highly non-uniform. Soil and pipe slip against each other for the most part off the critical zone. Therefore, shear stresses are transferred from soil to pipe over a great portion of the interface and that contributes to the internal axial force. Both pipelines were unable to conform to the soil uplift pattern, and for this reason gaps formed mainly over the top side.

- A number of performance limits in terms of stress and strain were evaluated for the above two cases. It was established that the Eurocode 8 no-buckling axial strain limit captures best the critical buckling condition under combined P– M load, when referring to average strain over a critical pipe portion. The respective thresholds by ALA and JGA are less conservative, with the latter also being theoretically unfounded. However, notice that for an imperfect pipeline the critical buckling axial strain is expected to be lower than that estimated for the perfect case, therefore the applicability of all three metrics remains under question.

- Using as input load the critical soil displacement field from Site 2, the responses of both the TG and TAP pipelines were computed to be entirely within the elastic regime, therefore non-critical. This odd behaviour was found to be due to the lack of contact over an extended pipe segment in the valley caused by the extremely jagged vertical ground motion profile, which prevented stress transfer from the soil.

- The possibility of buckling also depends on how spread out the differential displacements are. It is easy to realise that a differential movement spread over a long soil zone is not likely to impact the pipeline, as the induced load will be more uniformly spread in the pipeline. This aspect is related to the steepness fitting parameter k.

- The parametric study showed that circumstances that favour the development of instabilities in a buried gas pipeline are identified as the following:

    - relatively high R/t_w
    - the presence of initial shell imperfections
    - high interface COF (e.g, due to high pipe surface roughness or soil internal friction)
    - spiked ground load profiles, especially those with a vertical component of the same order of magnitude with the axial (along the pipe) component
    - low pressures
    - absence of any restraints along the pipeline

Buckling instabilities were found to occur at differential axial soil movements of 15 to 25 cm combined with local uplifts of 4 to 12 cm. The corresponding critical axial loads were found to be 40% to 70% lower than the ones for pure axial compression conditions, considering internal pressure and soil confinement.

- When combinations of the above conditions can exist for a buried gas pipeline crossing inhomogeneous soil, it is recommended that transient earthquake loads be a consideration for design. It is envisaged that the presented analysis methodology will be the tool or serve as a reference for such design and assessment applications, especially where a compromise between modelling sophistication and computational demand is sought.

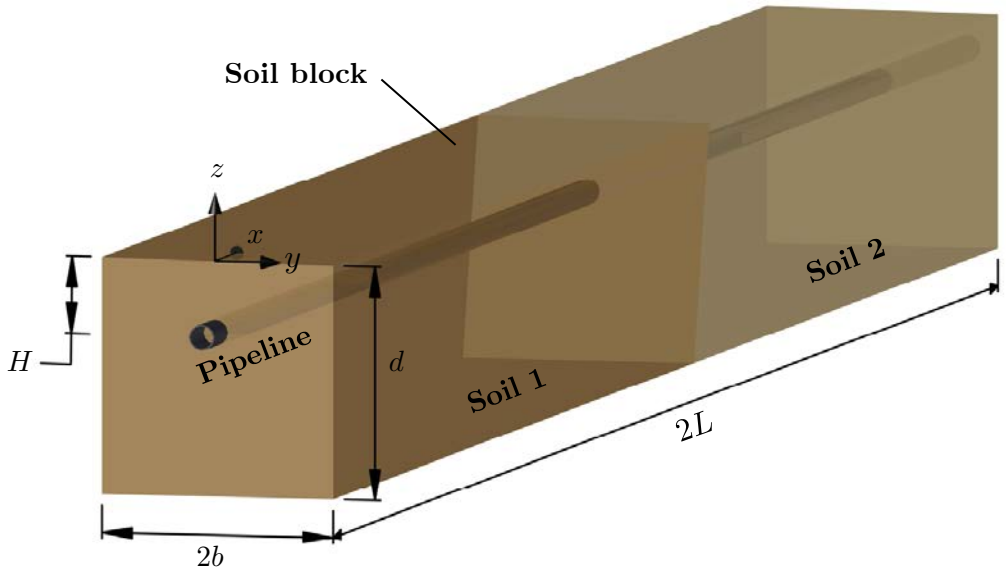

Figure 4-1. Three-dimensional illustration of the truncated local soil-pipe model; shown are characteristic lengths and the global coordinate system; note that the pipeline extrudes the soil block only for illustration purposes, also that dimension $2L$ is not to scale

Table 4-1. Geometric and material properties of the baseline gas pipeline models

Pipeline	R (mm)	t_w (mm)	R/t_w	h (m)	P (MPa)	P/P_y	E (GPa)	σ_y (MPa)	ε_{ult} (%)	w_0
TG	450	12	37.5	1.0*	6.75	0.56*	200	448*	10*	0
TAP	610	31	19.7	1.0	9.5	0.4*	200	448*	10*	0

*Postulated or inferred from other data

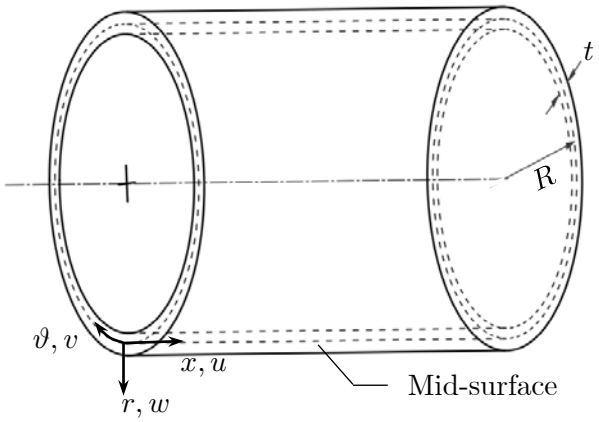

Figure 4-2. Geometry of a pipe shell segment and local cylindrical coordinate system (r, ϑ, x)

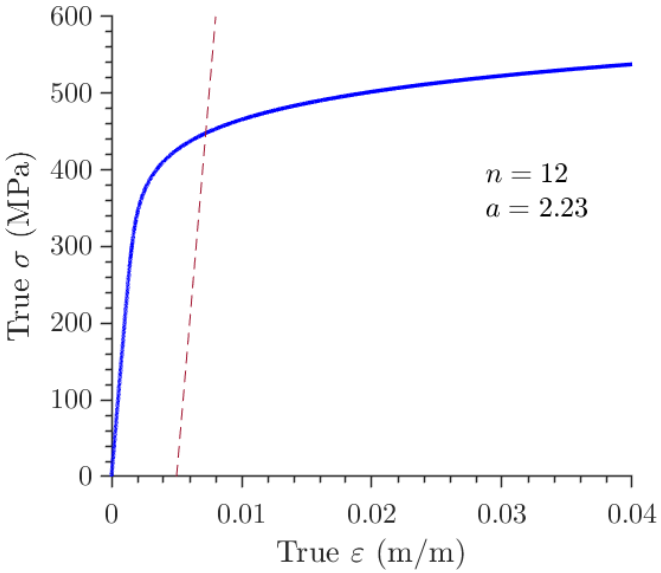

Figure 4-3. Uniaxial true stress-strain law adopted for API X65 steel of the baseline models; the red dashed line indicates the 0.5% yield offset

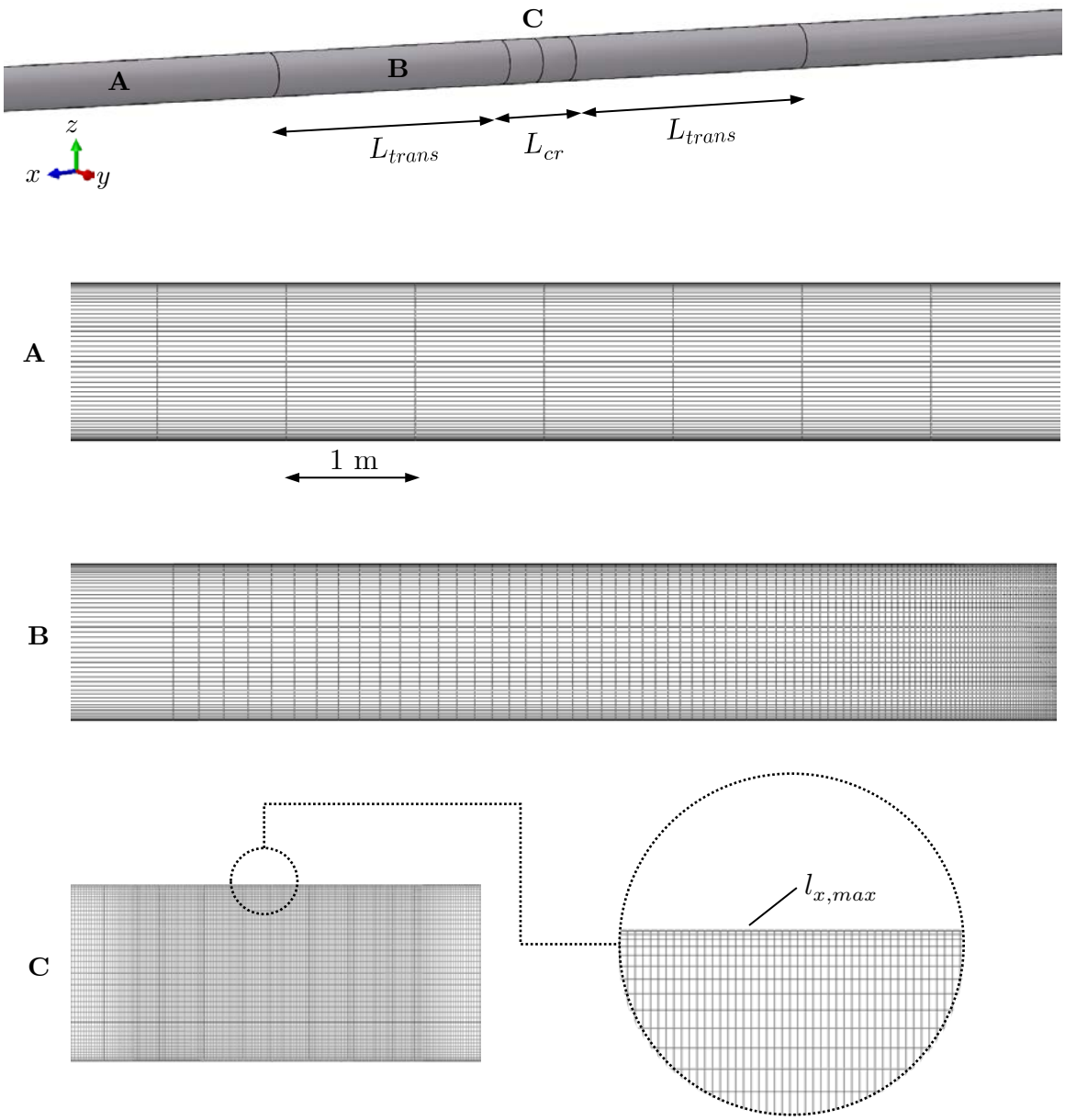

Figure 4-4. Details of the modular pipeline mesh design in the x direction; region C indicates the expected critical zone of deformation; region B is the transition zone from the dense to the coarse mesh

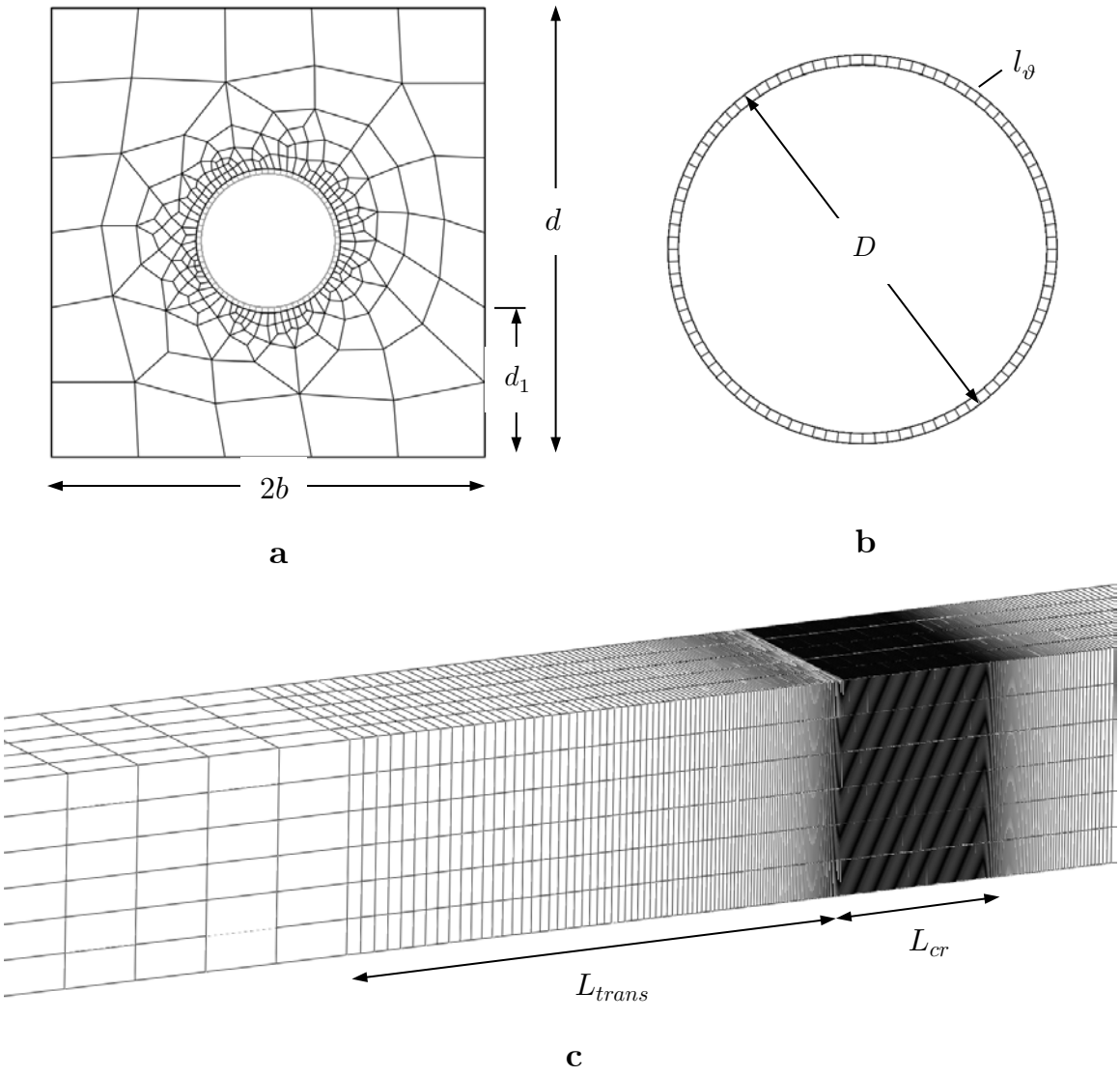

Figure 4-5. (a) yz section of the soil-pipe mesh of the baseline TG model; (b) discretisation of the pipeline ring; (c) aspect of the axial mesh zonation along the soil block

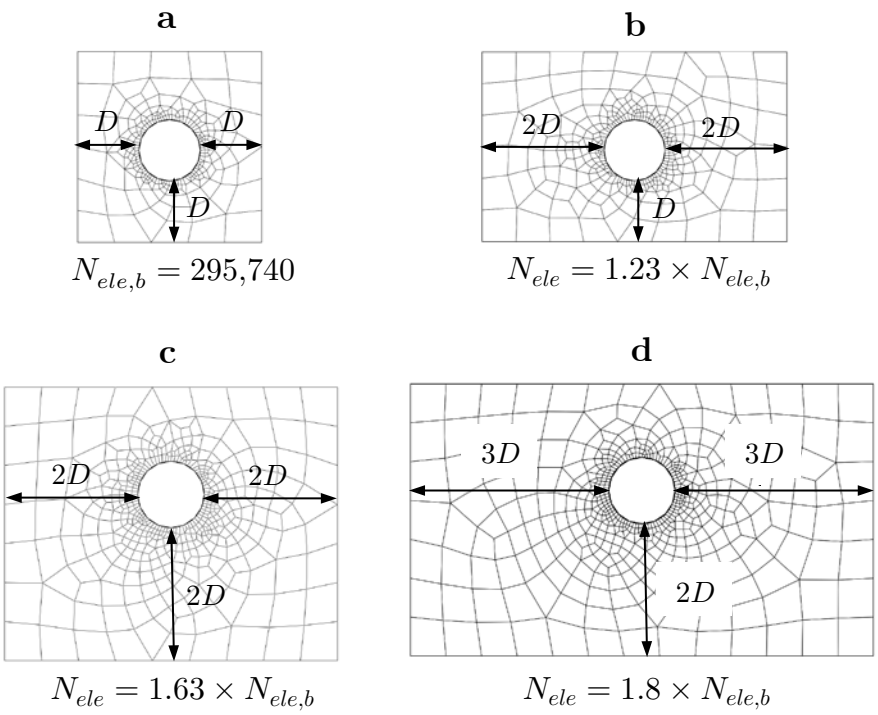

Figure 4-6. Alternative substructure II model sizes tested to gauge the effect of boundary extents; N_{ele} is the total number of user-generated elements

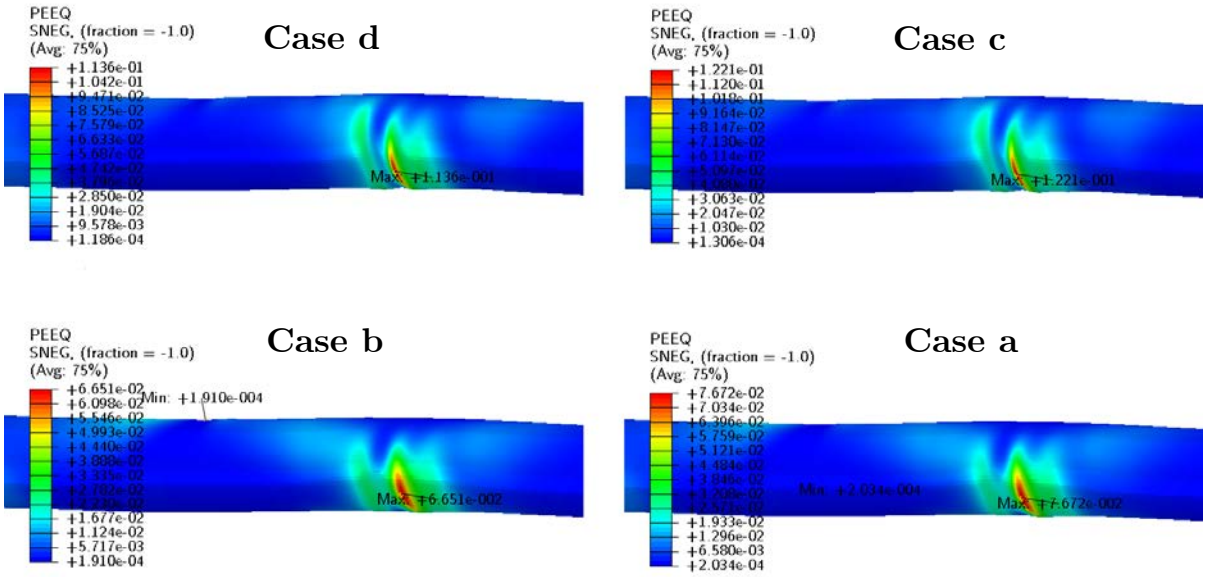

Figure 4-7. Contours of accumulated effective plastic strain on TG pipeline due to imposed load from model S1EL3 computed for the four different model sizes of **Figure 4-6** (bottom face shown)

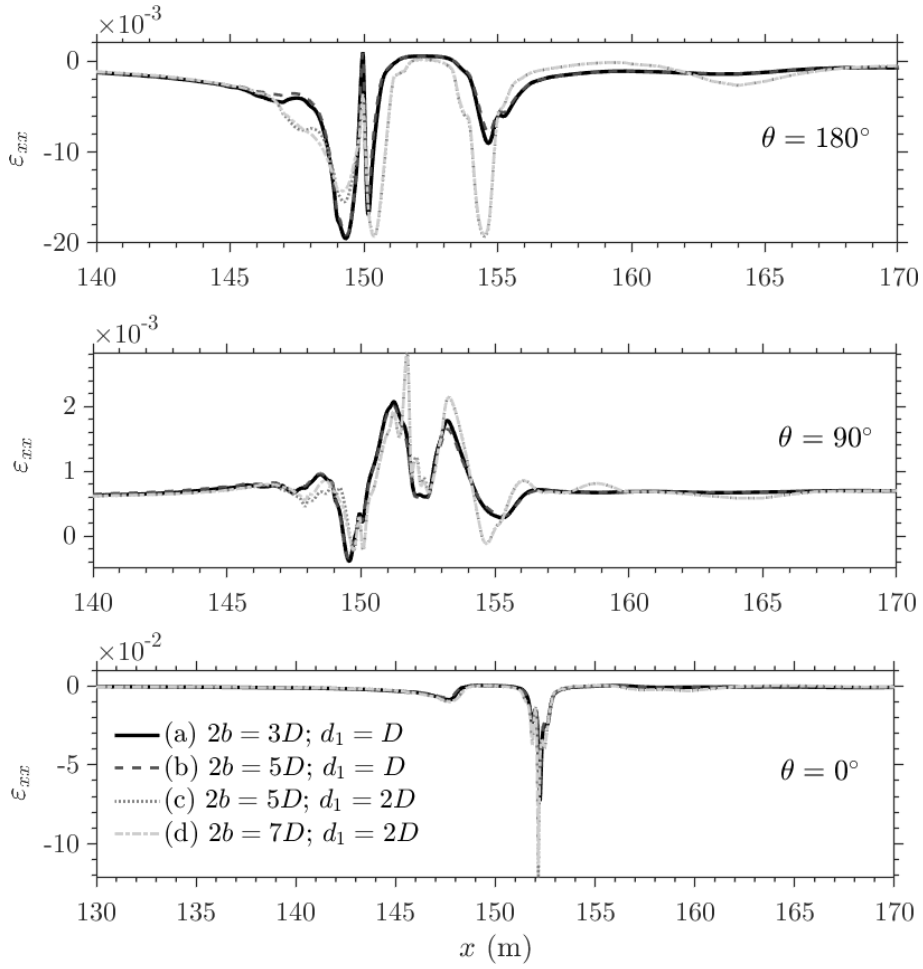

Figure 4-8. Axial (meridional) strain profiles along three straight nodal lines at different circumferential coordinates, for four different model sizes

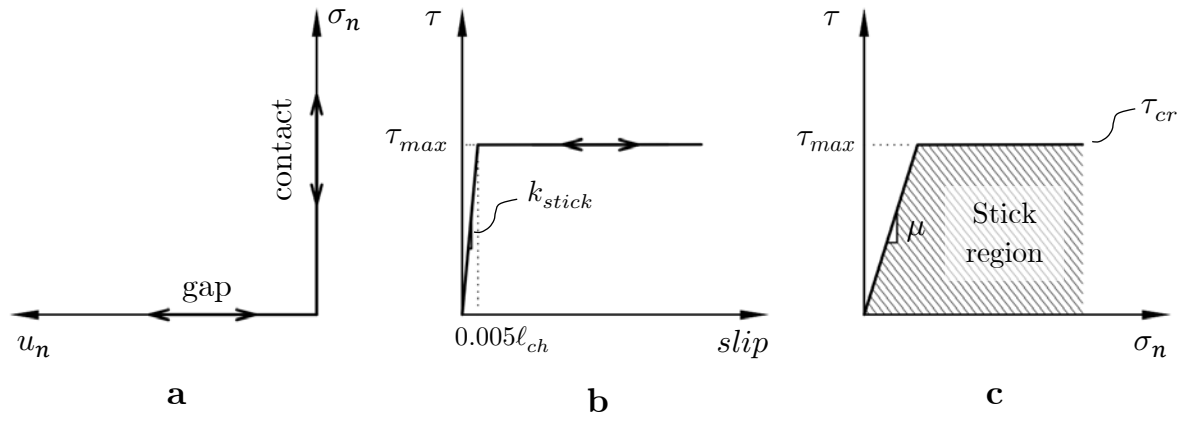

Figure 4-9. Contact theories adopted for modelling the quasi-static interaction between soil and pipe: (a) contact pressure-penetration relationship; (b) contact shear stress-slip relationship; (c) contact shear stress-pressure relationship

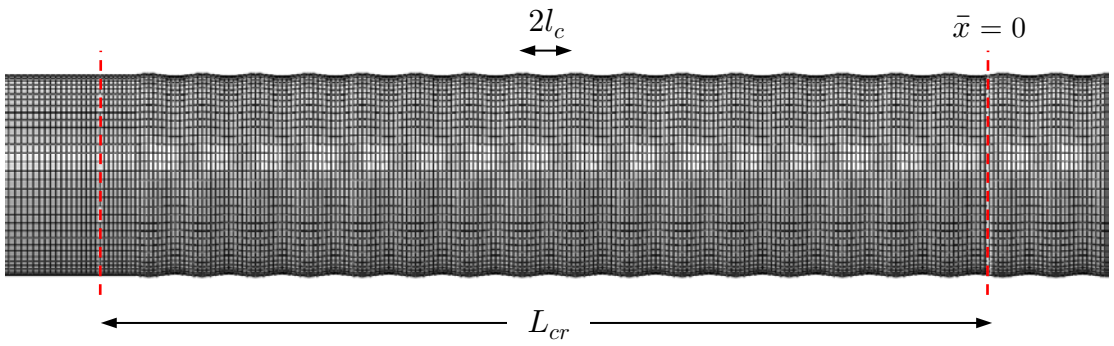

Figure 4-10. Axisymmetric imperfection shape assumed for the pipeline shell

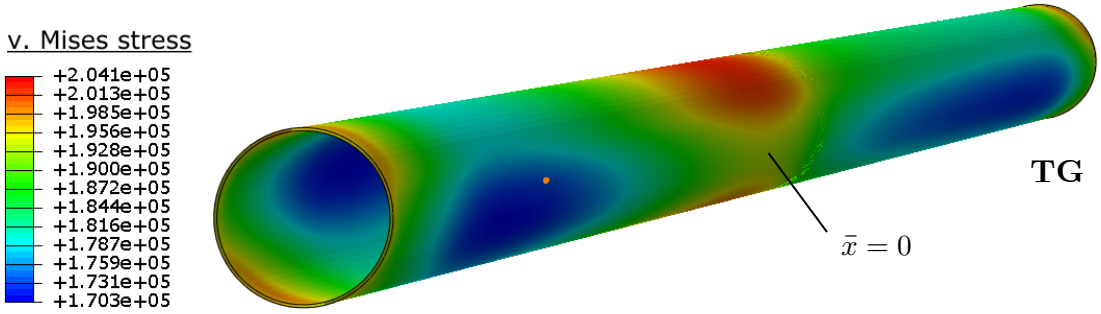

Figure 4-11. Equivalent stress in TG pipeline due to soil loads from the critical weak input excitation in Site 1

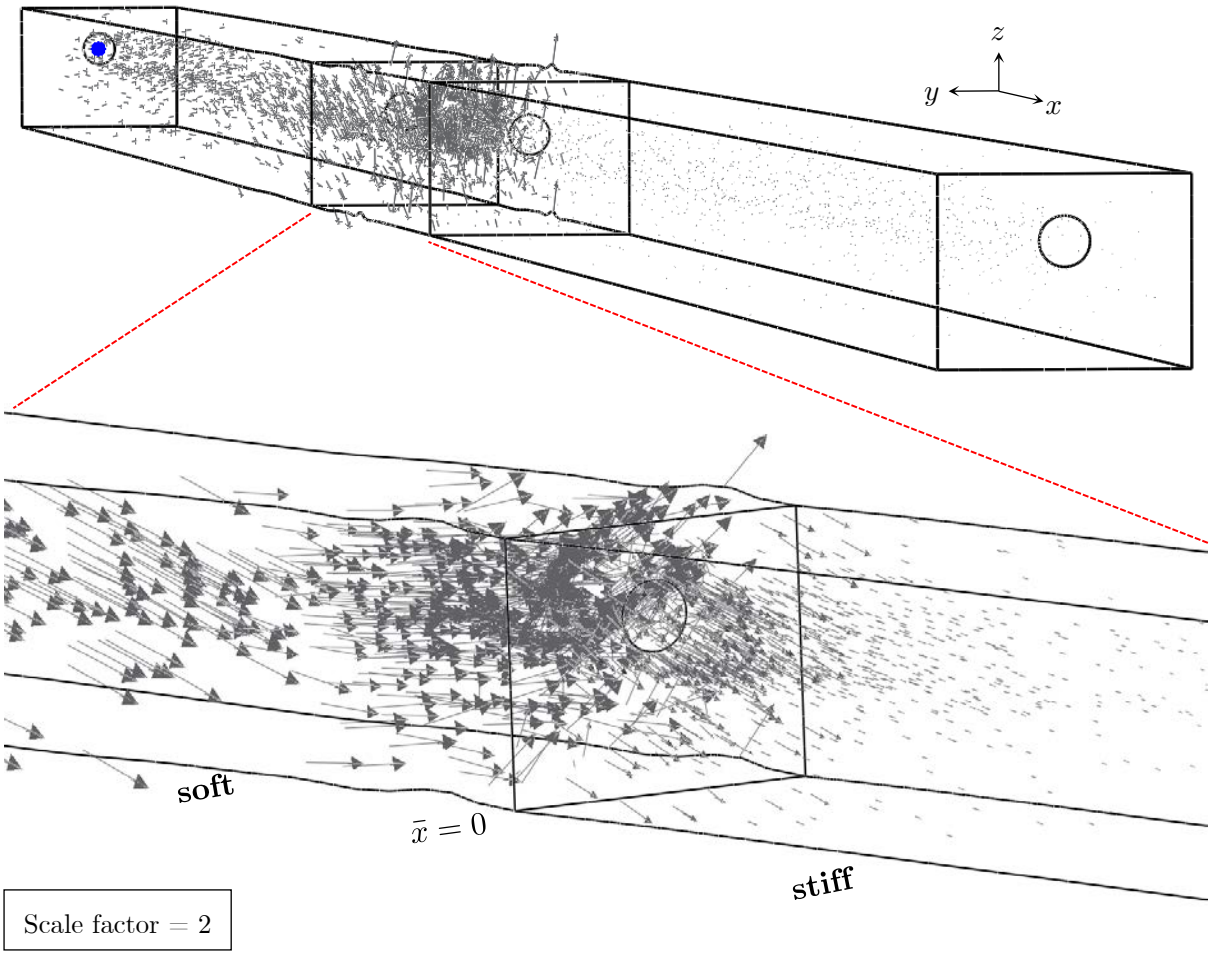

Figure 4-12. Resultant displacement vectors of soil block representing the input load from model S1EL3

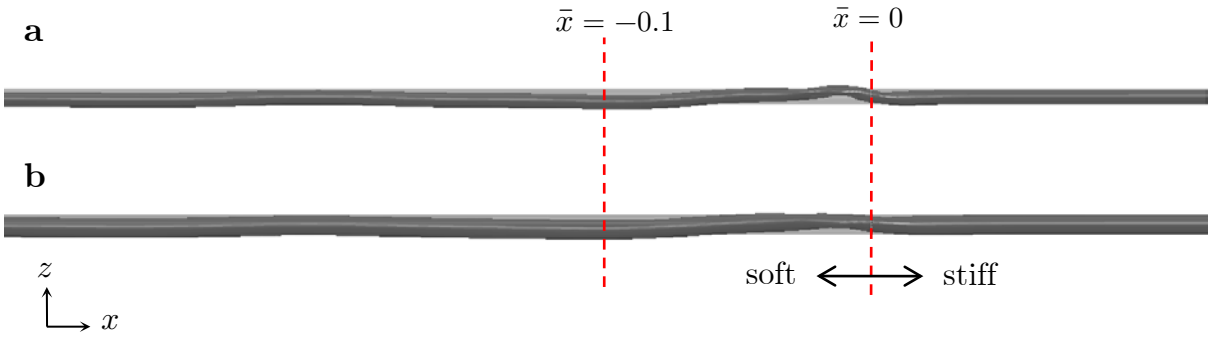

Figure 4-13. Deformed shapes of pipelines overlaid with undeformed ones due to bidirectional soil loads from model S1EL3: (a) TG and (b) TAP; (scale factor = 10 for better visibility)

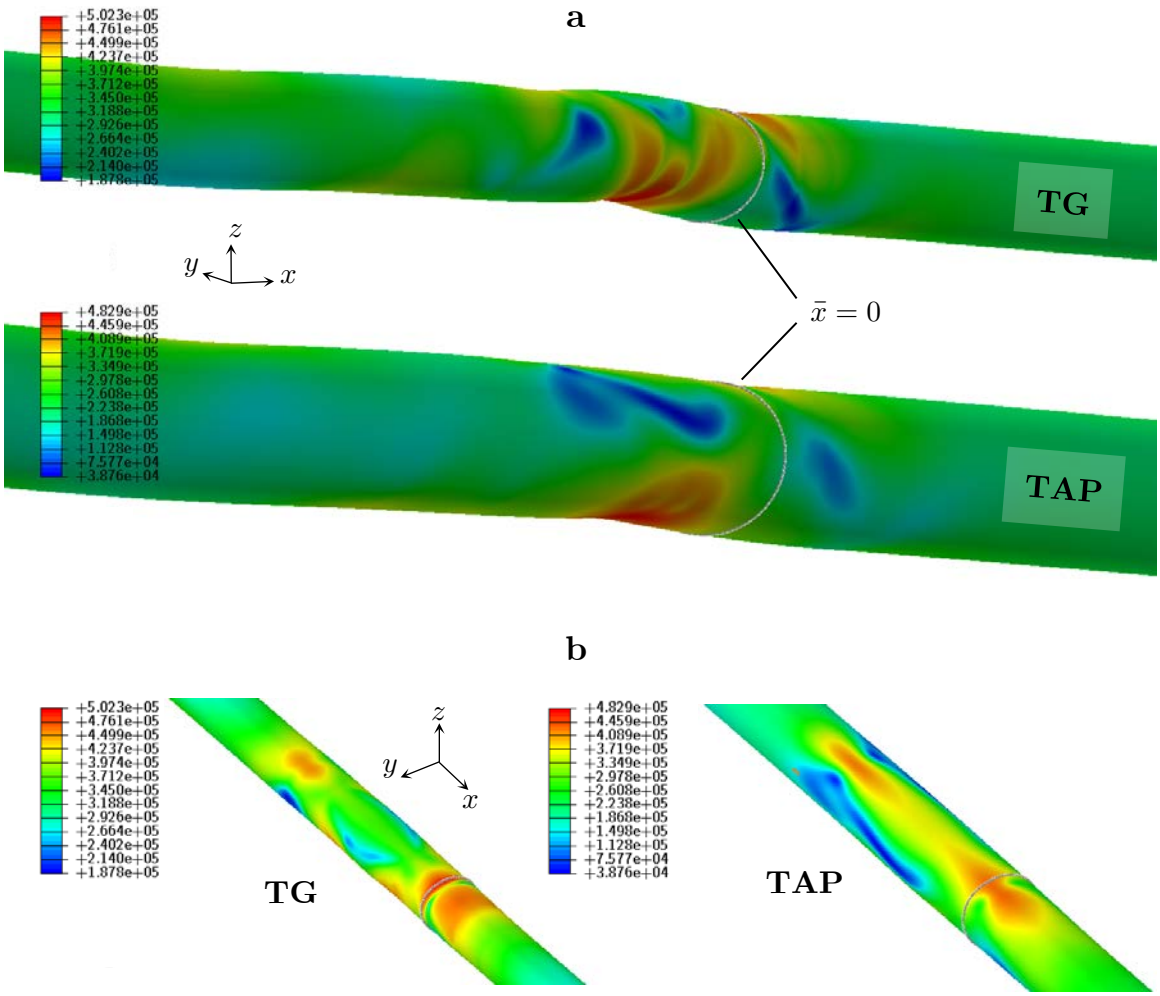

Figure 4-14. Equivalent stress contours over the critical pipe segments due to soil loads from model S1EL3: (a) side view and (b) top view

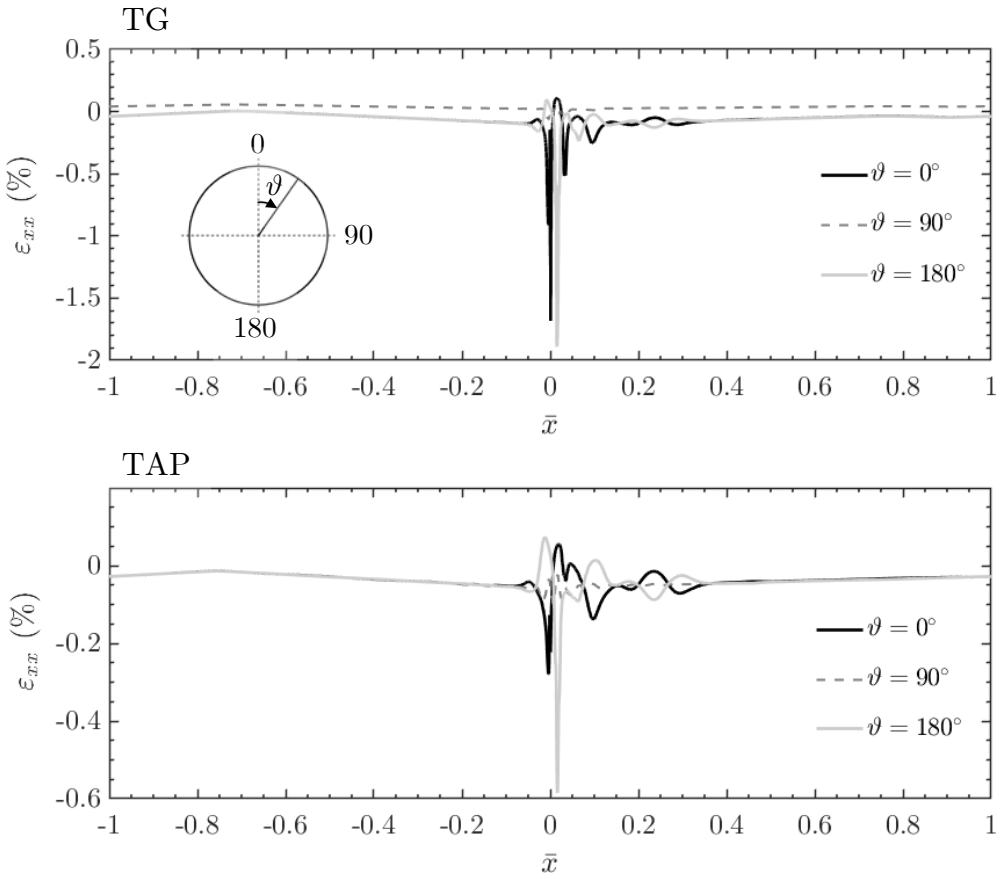

Figure 4-15. Meridional (outer-surface) strain profiles along longitudinal lines at $\vartheta = 0°, 90°$ and 180° for the baseline TG and TAP pipelines subject to S1EL3 load

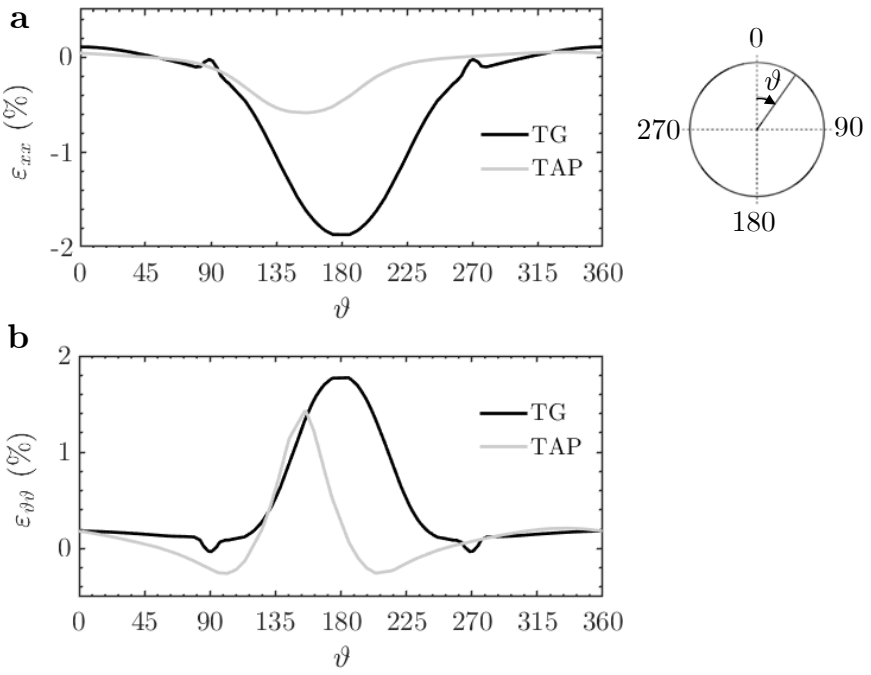

Figure 4-16. (a) Axial strains and (b) hoop strains around the circumference of the critical sections for soil load from model S1EL3 (values computed at integration points located on the outer surface of the shell)

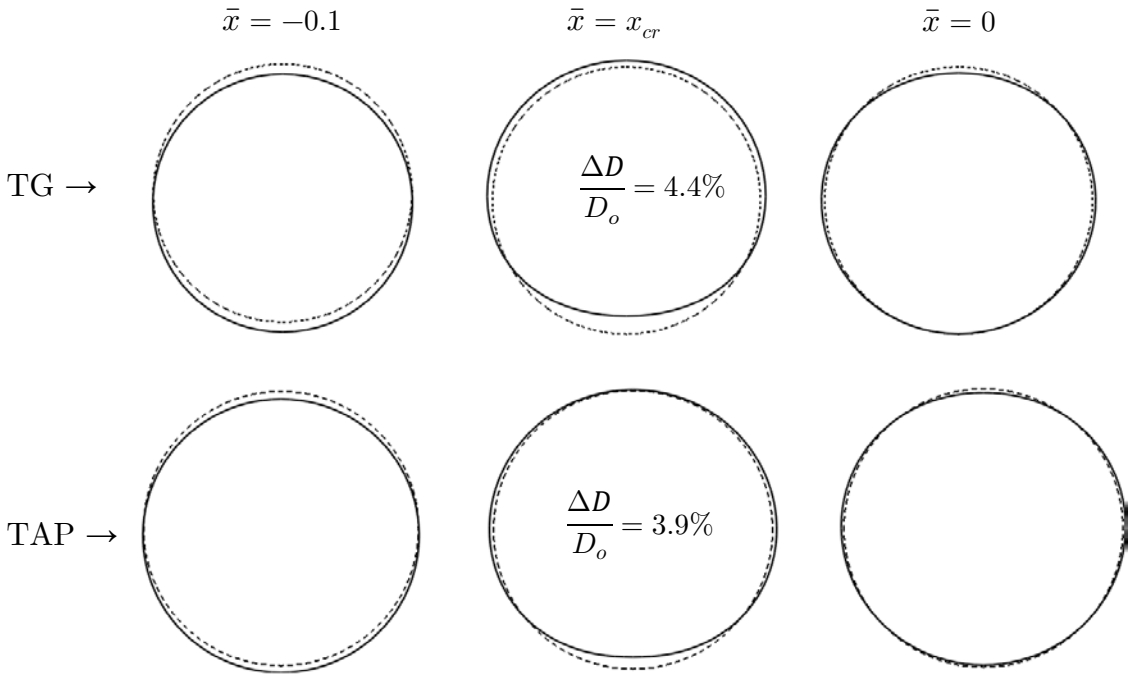

Figure 4-17. Deformed pipe cross-sections at different locations under the S1EL3 soil loads; maximum section flattening indicated

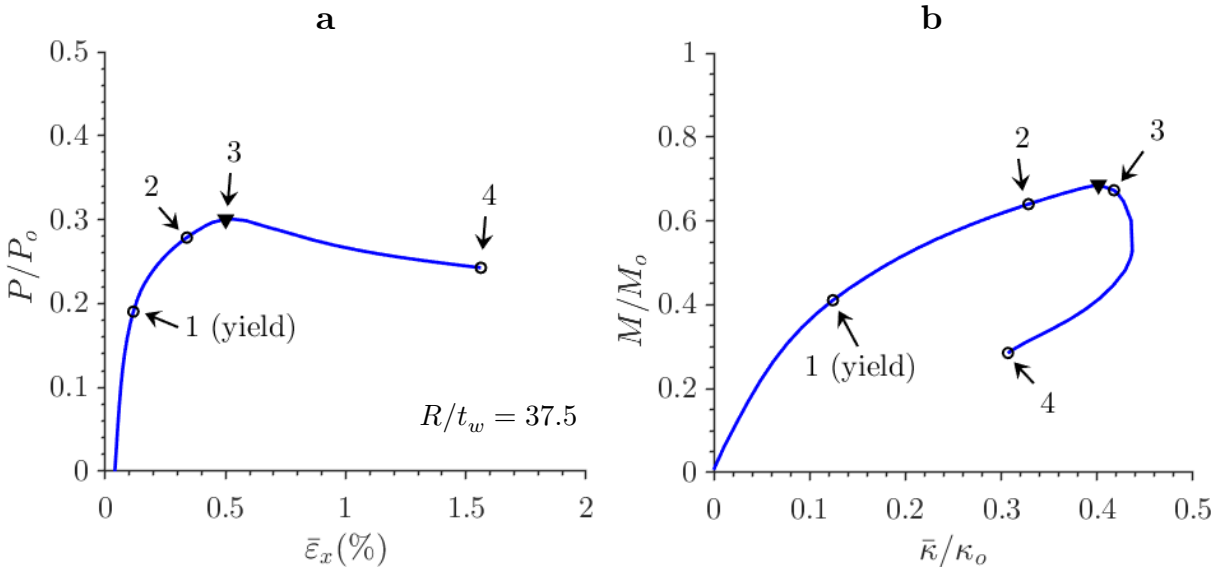

Figure 4-18. (a) Average axial load-deformation response and (b) average bending moment-axial curvature response of the TG pipeline shell within the critical segment due to load from case S1EL3; numbers on the paths identify events of interest visualized in **Figure 4-19**

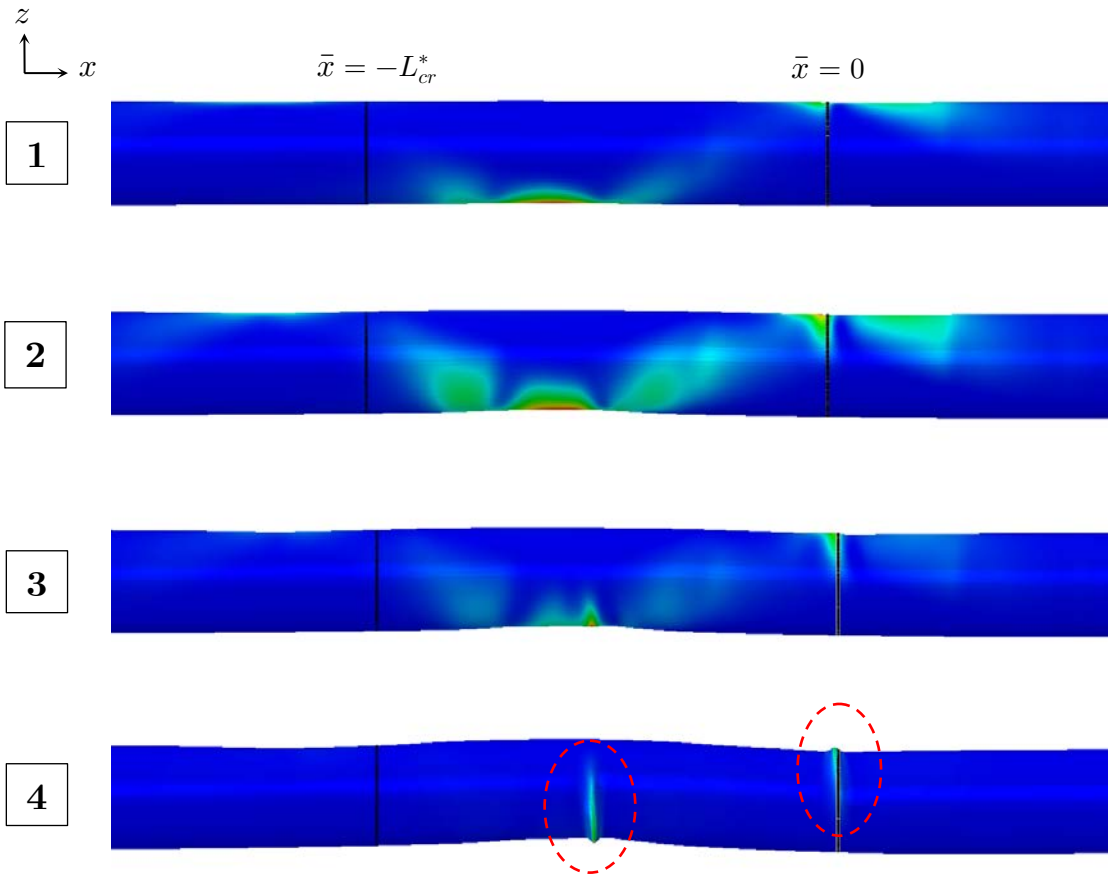

Figure 4-19. Evolution of deformation in the TG pipeline due to $P-M$ interaction; equivalent plastic strain contours overlaid

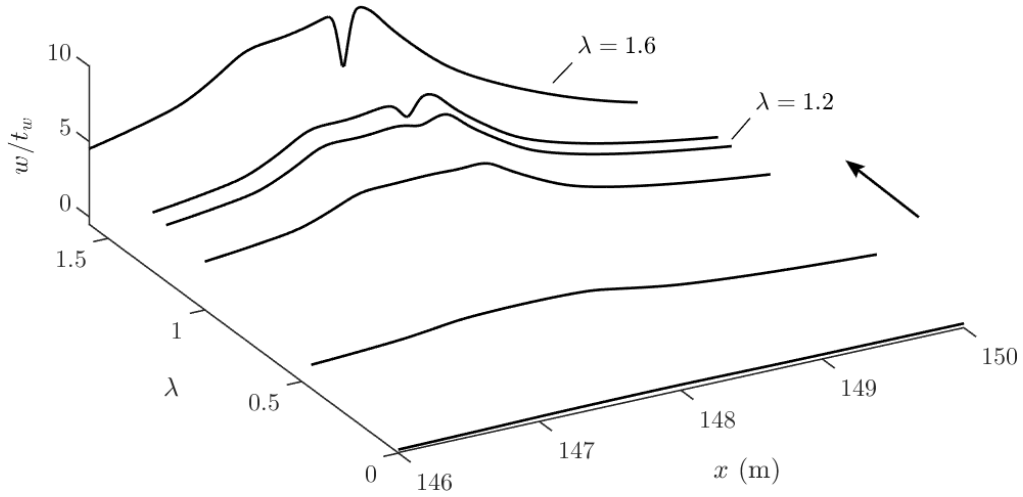

Figure 4-20. Evolution of radial displacements on the compressed side within L_{cr} of the TG pipeline due to scaled-up load from case S1EL3

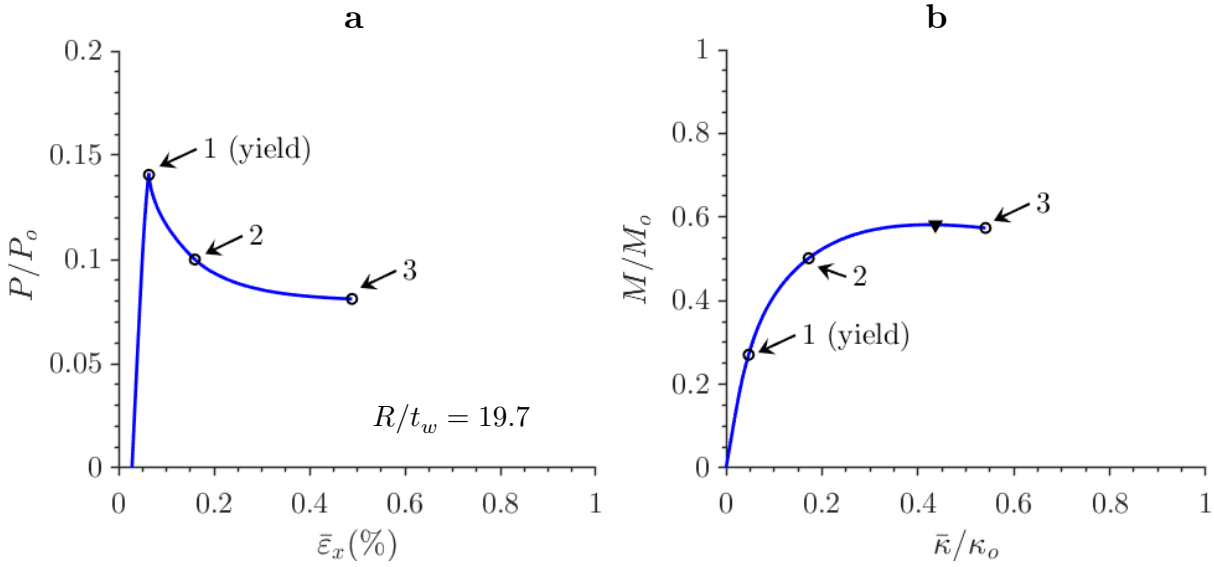

Figure 4-21. (a) Average axial load-deformation response and (b) average bending moment-axial curvature response of the TAP pipeline shell within the critical segment due to load from case S1EL3; numbers on the paths identify events of interest visualized in **Figure 4-22**

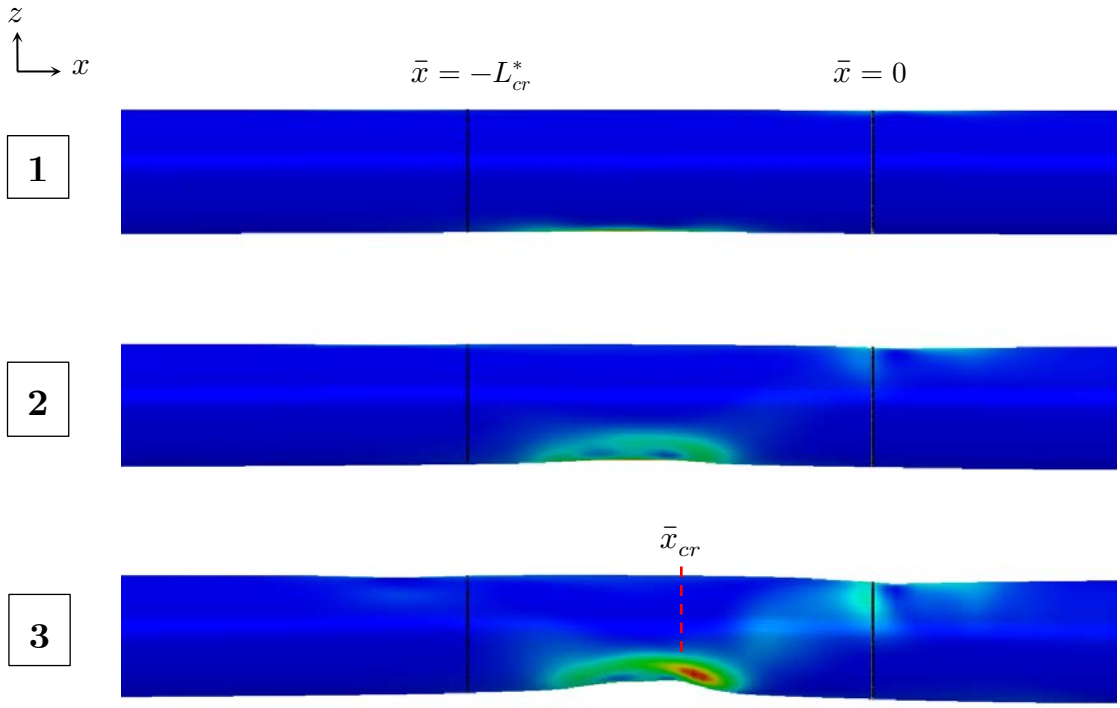

Figure 4-22. Evolution of deformation in the TAP pipeline due to $P-M$ interaction; equivalent plastic strain contours overlaid

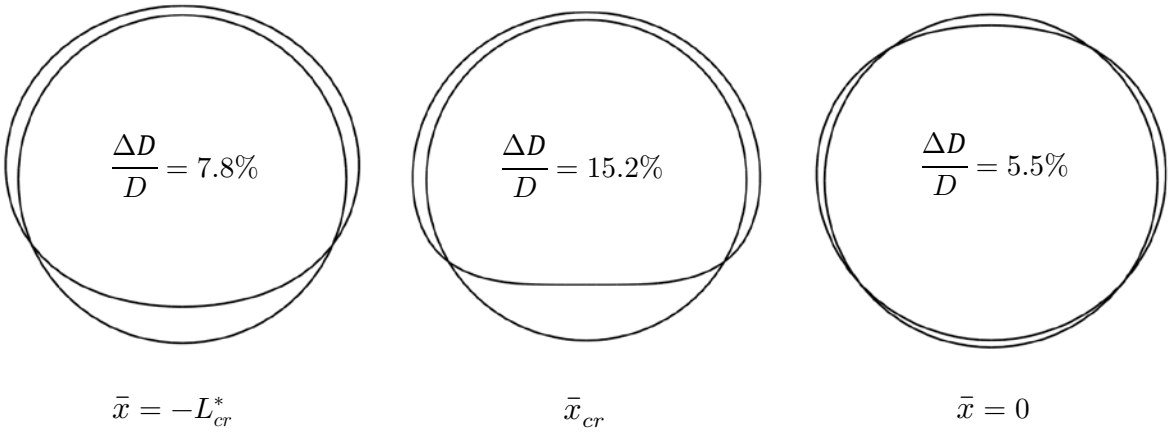

Figure 4-23. Deformed pipe cross-sections for TAP at collapse due to amplified (2.5x) S1EL3 soil loads; maximum section flattening indicated

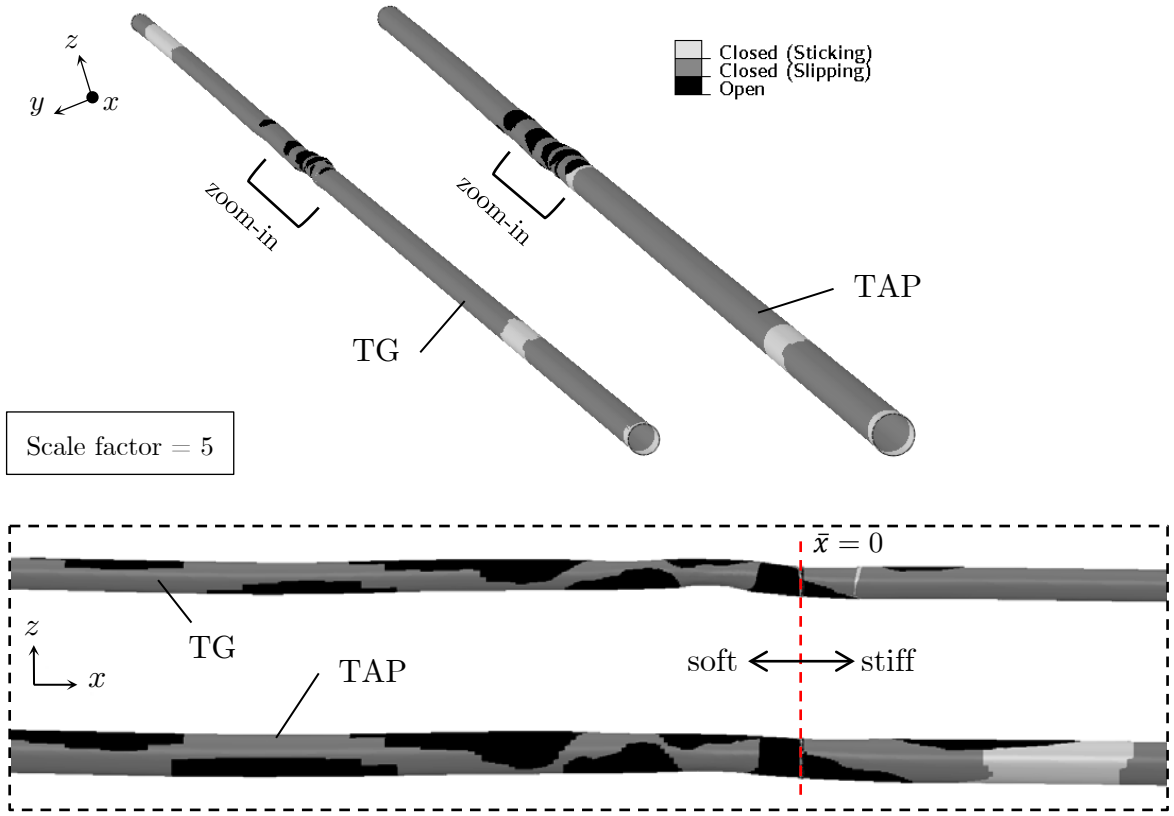

Figure 4-24. Pipe contours indicating the contact status (sticking, sliding or gap) at the soil-pipe interface upon application of soil loads from model S1EL3; inset shows close-up views of the critical regions

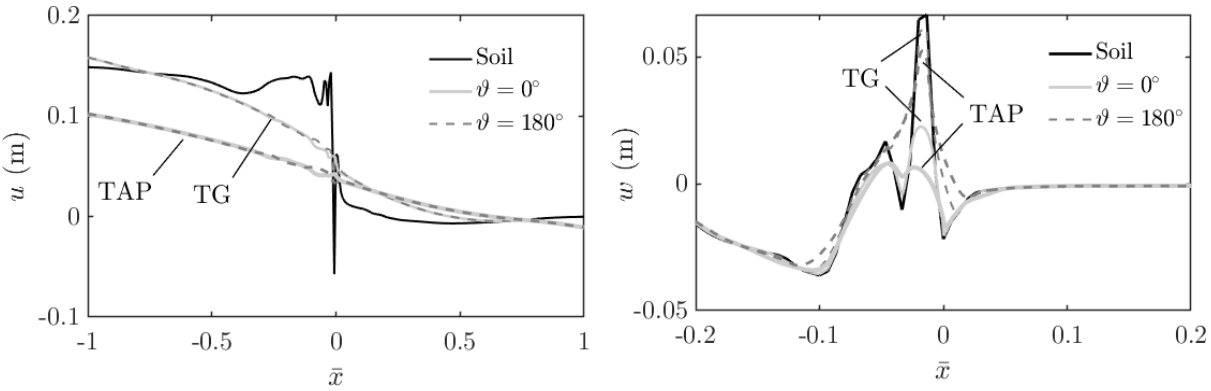

Figure 4-25. Horizonal and vertical displacement profiles of soil and baseline pipeline along the crown ($\vartheta = 0°$) and invert ($\vartheta = 180°$) due to loads from model S1EL3

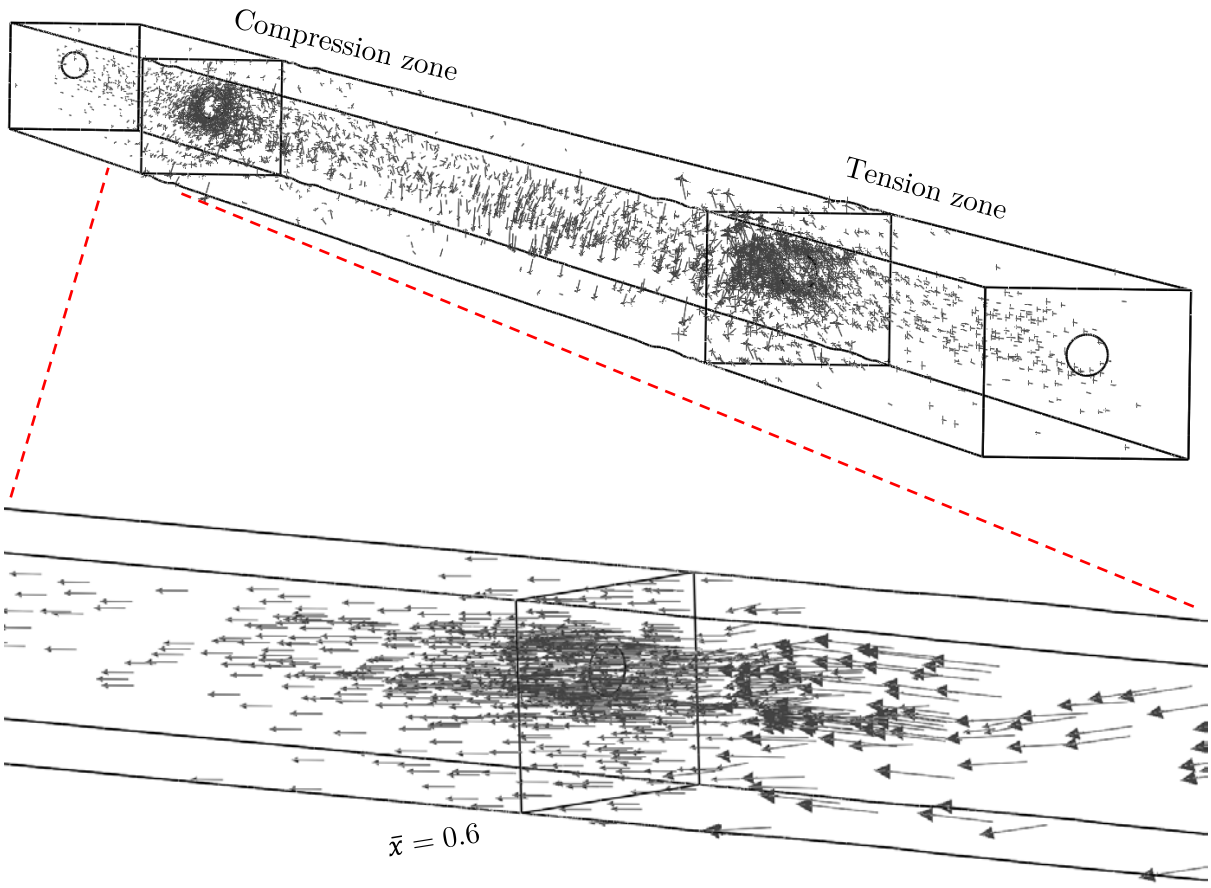

Figure 4-26. Resultant displacement vectors of soil block representing the input load from model S2EL0

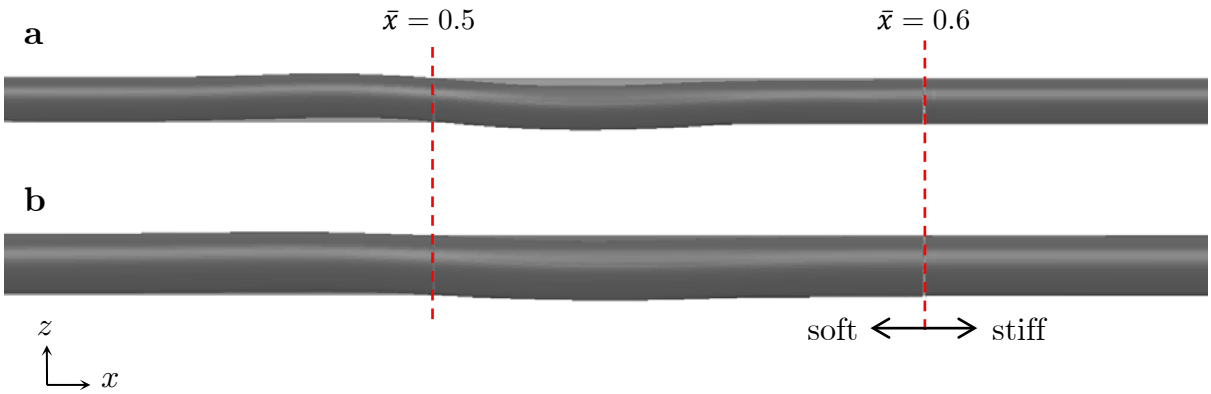

Figure 4-27. Deformed shapes of pipelines overlaid with undeformed ones due to bidirectional soil loads from model S2EL0: (a) TG and (b) TAP; (deformation scale factor = 10 and z coordinate scale factor = 2 for better visibility)

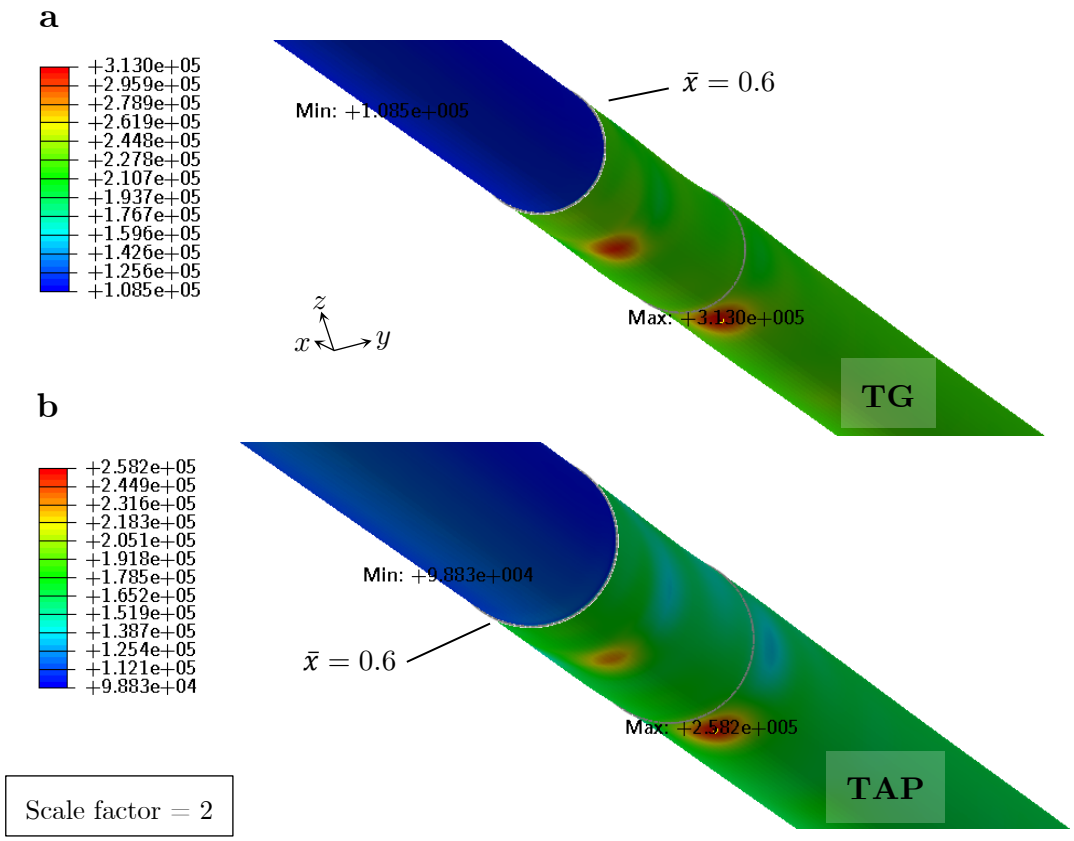

Figure 4-28. Equivalent stress contours (in kPa) over the critical pipe segments due to soil loads from model S2EL0: (a) TG and (b) TAP pipeline

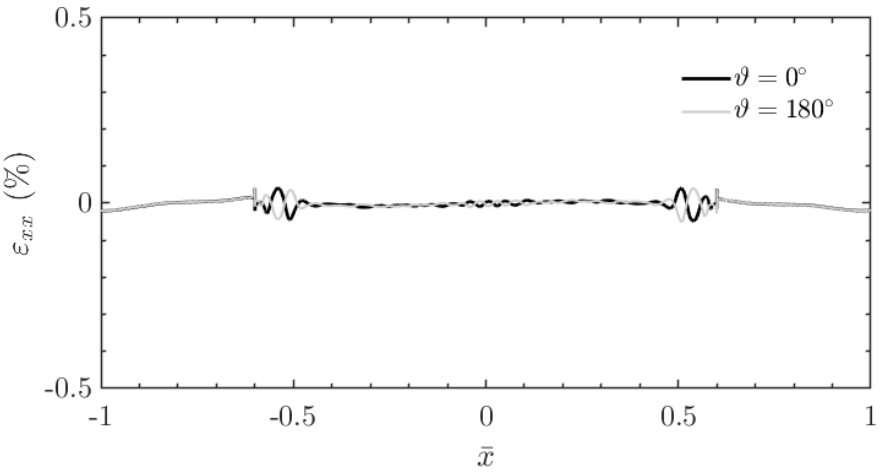

Figure 4-29. Meridional (outer-surface) strain profiles along longitudinal lines at $\vartheta = 0°$ and 180° for the baseline TG pipeline subject to S2EL0 load

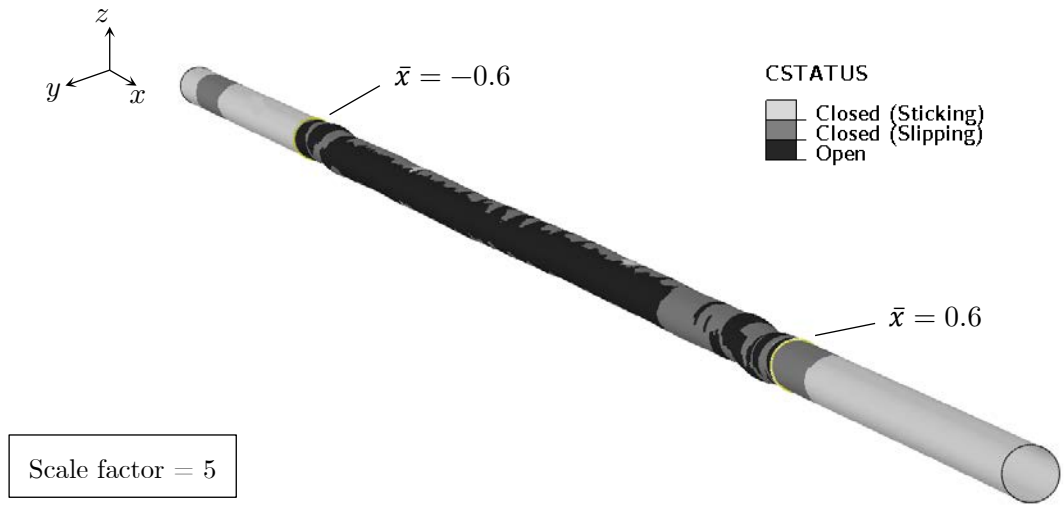

Figure 4-30. Contours indicating the contact status (sticking, sliding or gap) at the soil-pipe interface upon application of soil loads from model S2EL0 on TG

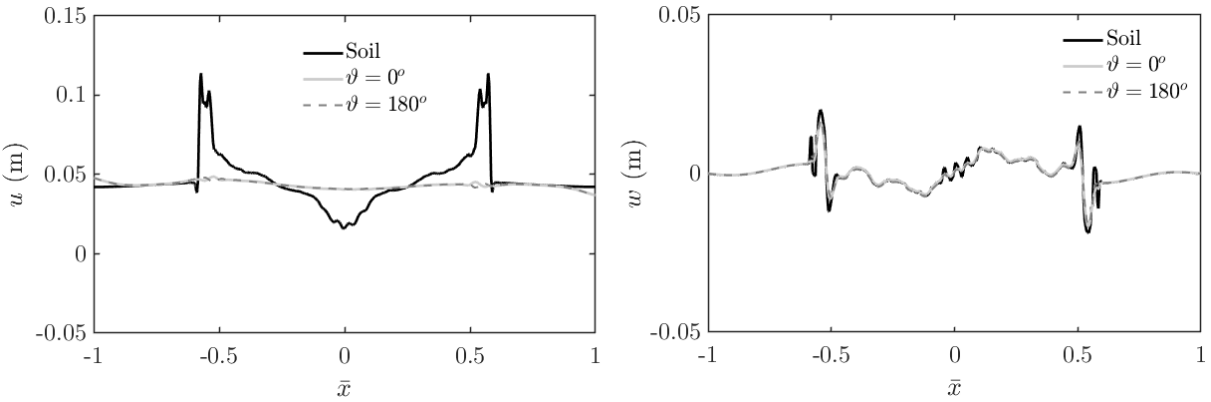

Figure 4-31. Horizonal and vertical displacement profiles of soil and pipeline along the crown ($\vartheta = 0°$) and invert ($\vartheta = 180°$) due to loads from model S1EL3 on the TG pipeline

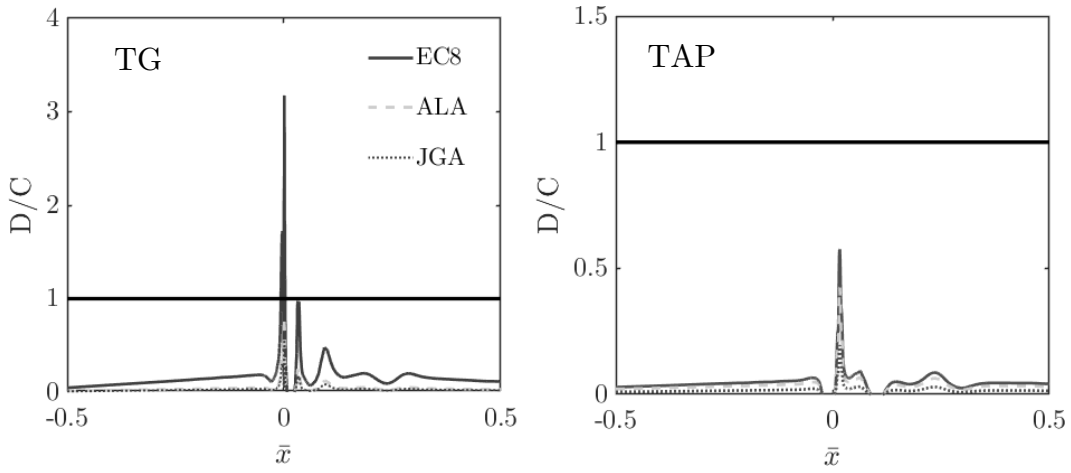

Figure 4-32. Demand-to-capacity ratios in terms of compressive axial strains for pipelines in Site 1

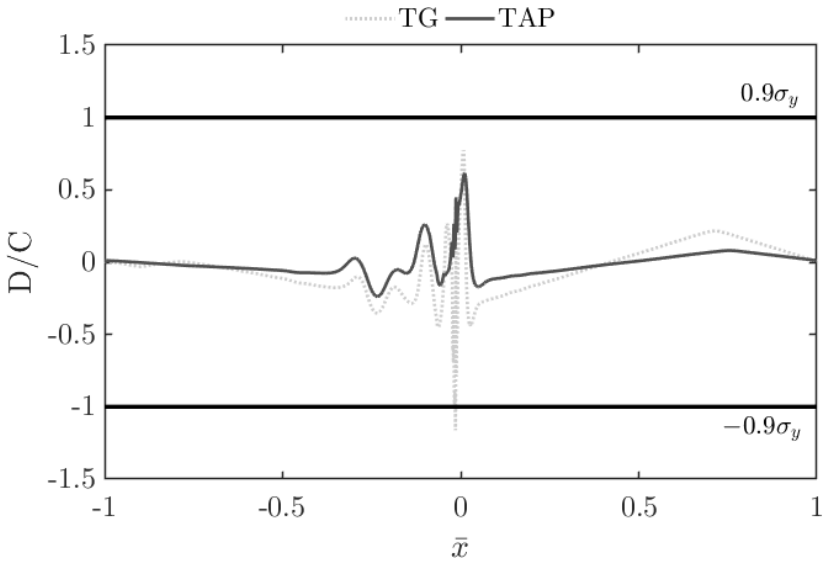

Figure 4-33. Demand-to-capacity ratios in terms of axial stress (based on ASME limits) for pipelines in Site 1

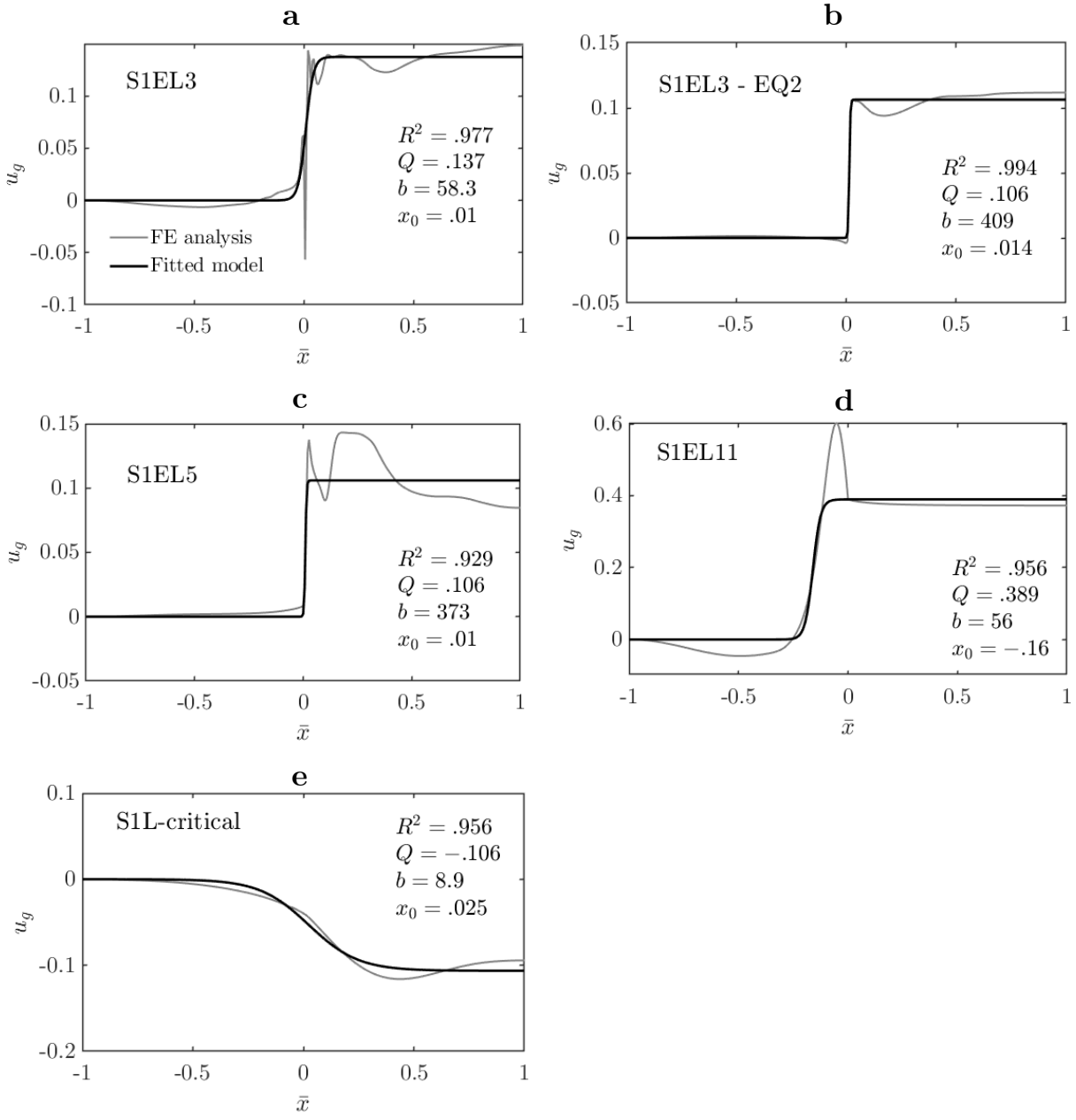

Figure 4-34. Fitted logistic curves to $u_g(x)$ profiles computed from FE analysis in Chapter 3; coefficient estimates and goodness-of-fit displayed for each case

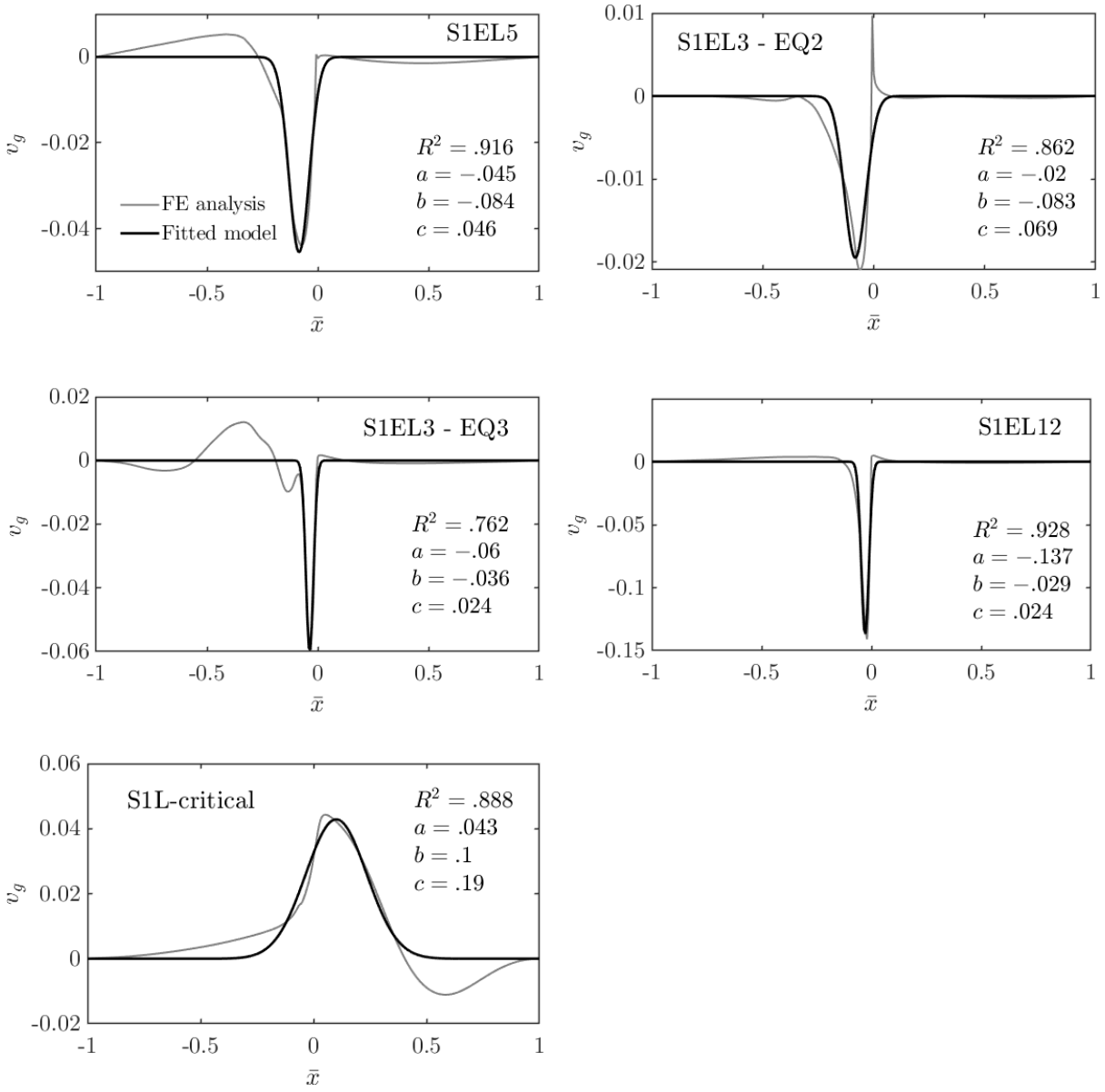

Figure 4-35. Fitted logistic curves to $v_g(x)$ profiles computed from FE analysis in Chapter 3; coefficient estimates and goodness-of-fit displayed for each case

Table 4-2. Parameters used in each SPI model of the parametric study

Case	R/t_w	P/P_y	w_0/t_w	n	μ	BCs	Q/a
1 (base)	37.5	0.56	0	12	0.6	Free	2
2	37.5	0.5	0	12	0.6	Free	2
3	37.5	0.8	0	12	0.6	Free	2
4	37.5	0.56	0.01	12	0.6	Free	2
5	37.5	0.56	0.1	12	0.6	Free	2
6	37.5	0.56	0.5	12	0.6	Free	2
7	37.5	0.56	0	9	0.6	Free	2
8	37.5	0.56	0	20	0.6	Free	2
9	37.5	0.56	0	12	0.3	Free	2
10	37.5	0.56	0	12	0.8	Free	2
11	37.5	0.56	0	12	0.6	Fixed	2
12	37.5	0.56	0	12	0.6	Free	5
13	51.5	0.56	0	12	0.6	Free	2
14	19.7	0.56	0	12	0.6	Free	2

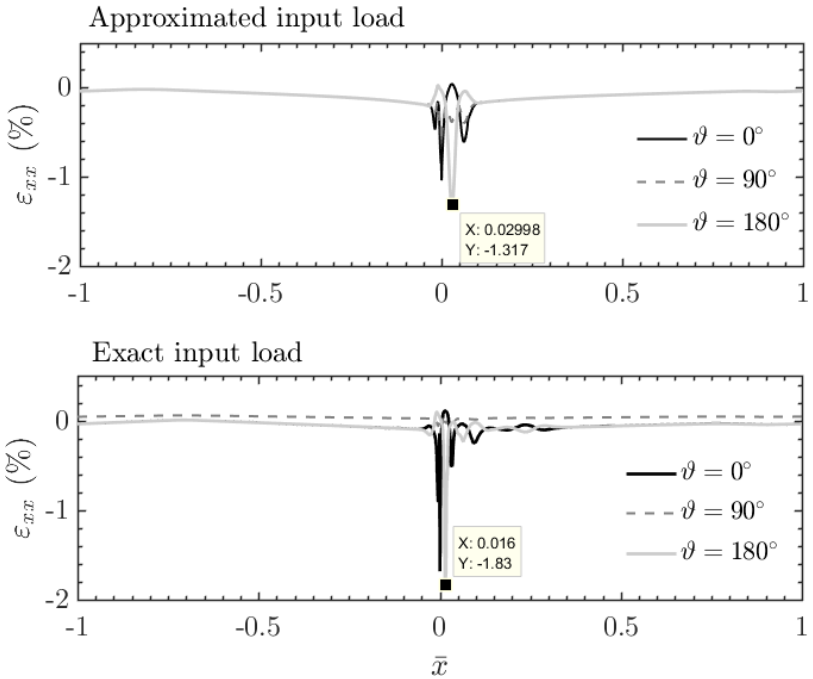

Figure 4-36. Axial strain profiles for the TG pipeline due to the exact ground displacement profiles computed in Chapter 3 and the approximated fitted forms

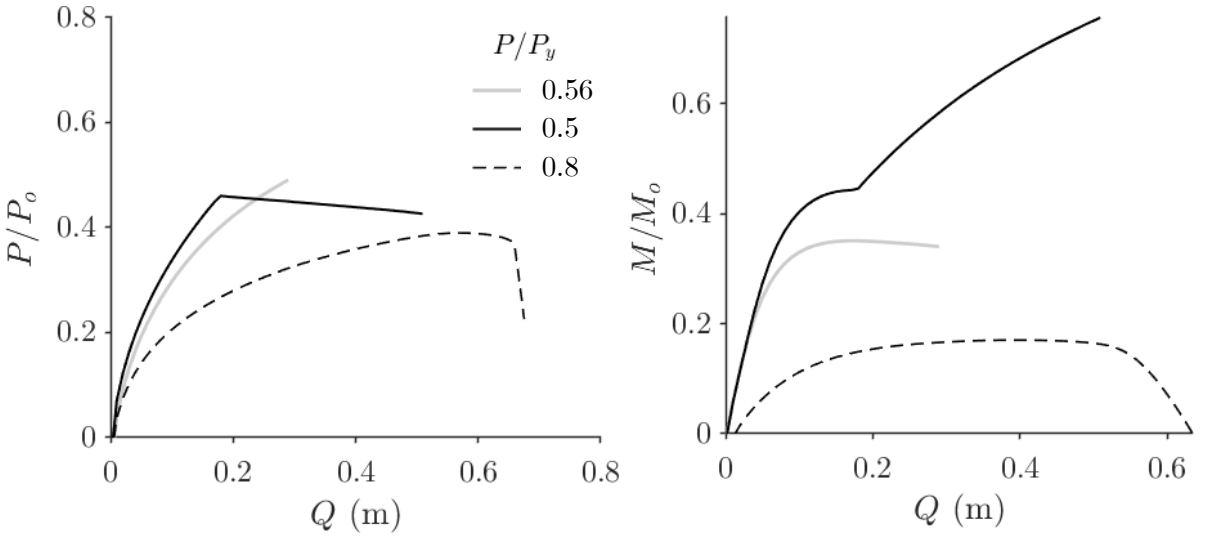

Figure 4-37. Axial load (left) and bending moment (right) versus imposed horizontal differential ground displacement for different internal pressure levels

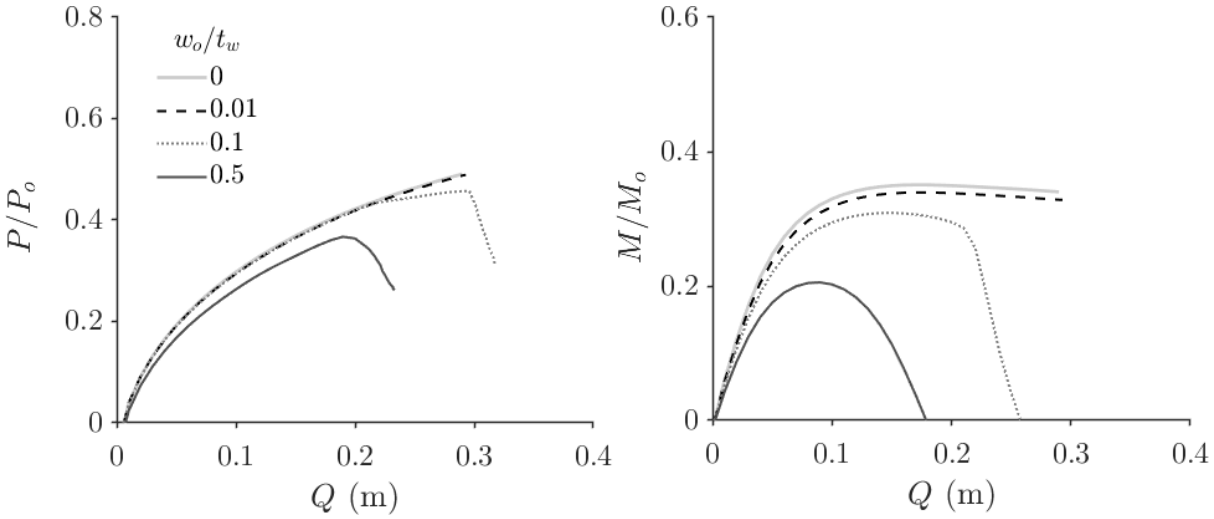

Figure 4-38. Axial load (left) and bending moment (right) versus imposed horizontal differential ground displacement for different imperfection amplitudes

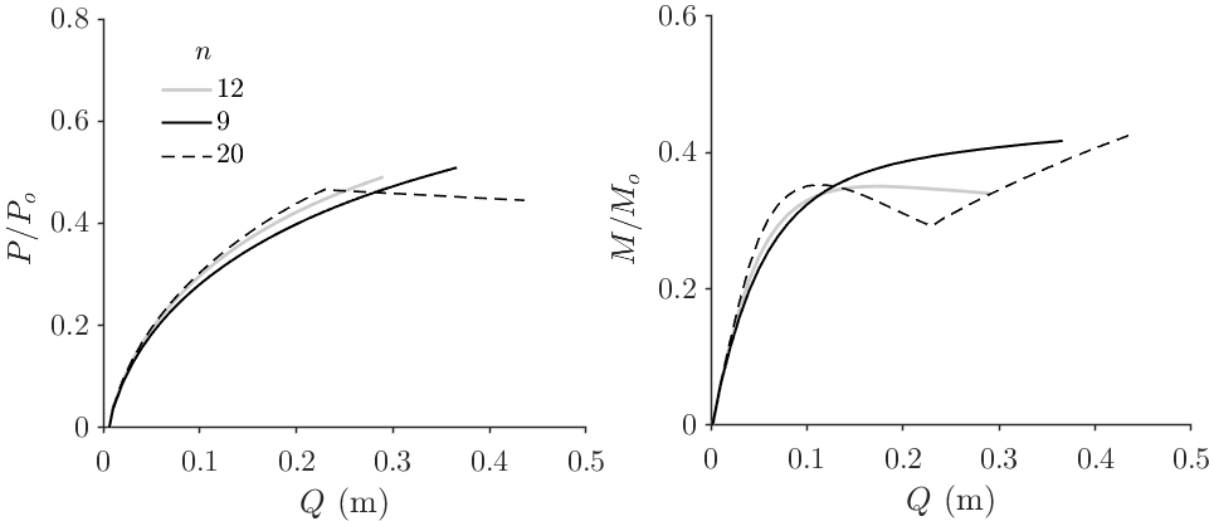

Figure 4-39. (a) Axial load (left) and bending moment (right) versus imposed horizontal differential ground displacement for different values of the hardening exponent of steel n

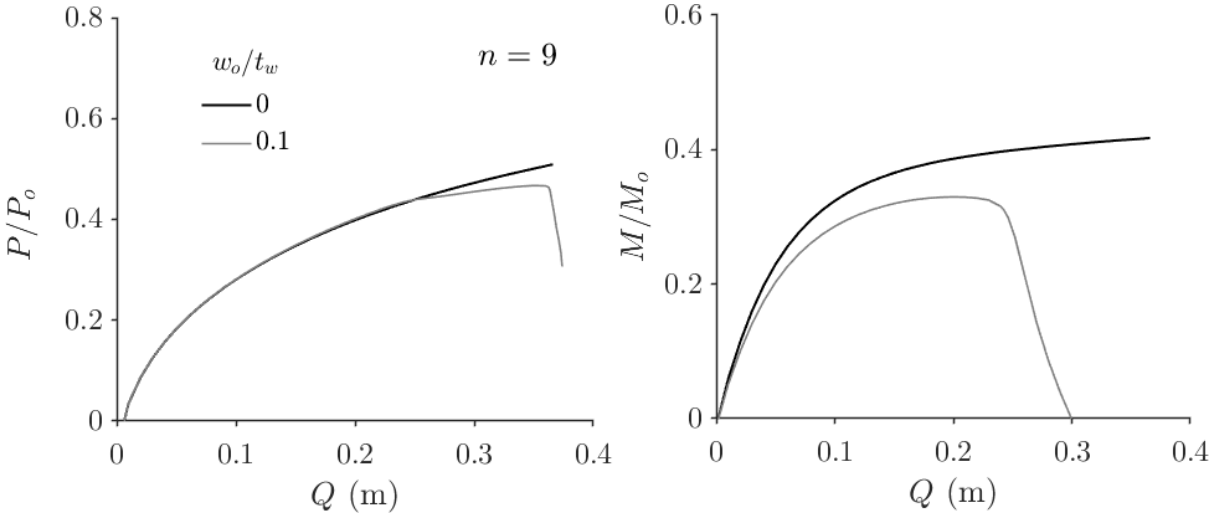

Figure 4-40. Critical section responses for model with $n = 9$ for perfect and imperfect geometry

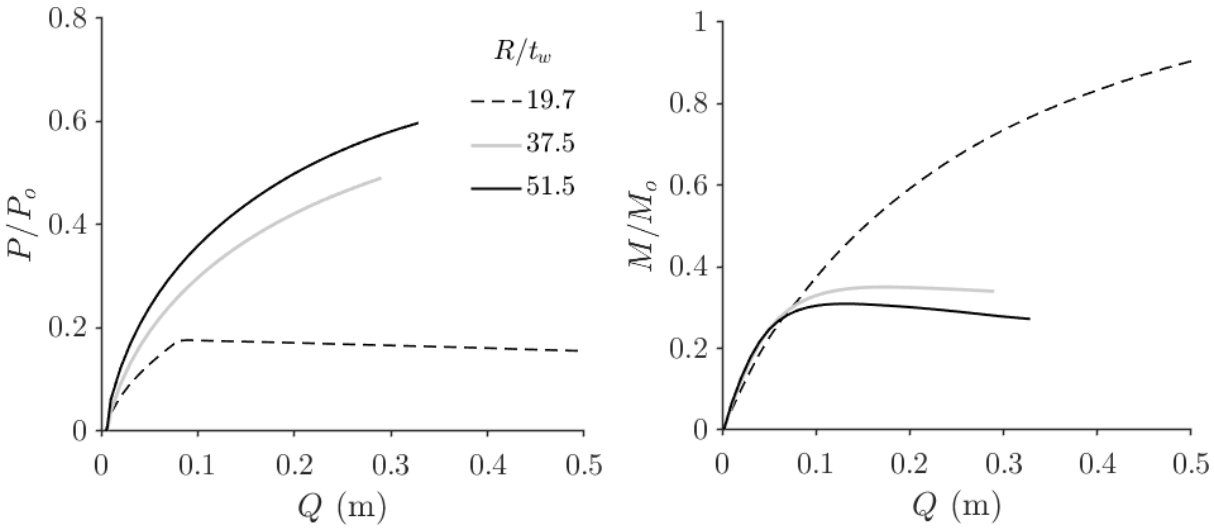

Figure 4-41. Axial load (left) and bending moment (right) versus imposed horizontal differential ground displacement for different shell slenderness ratios

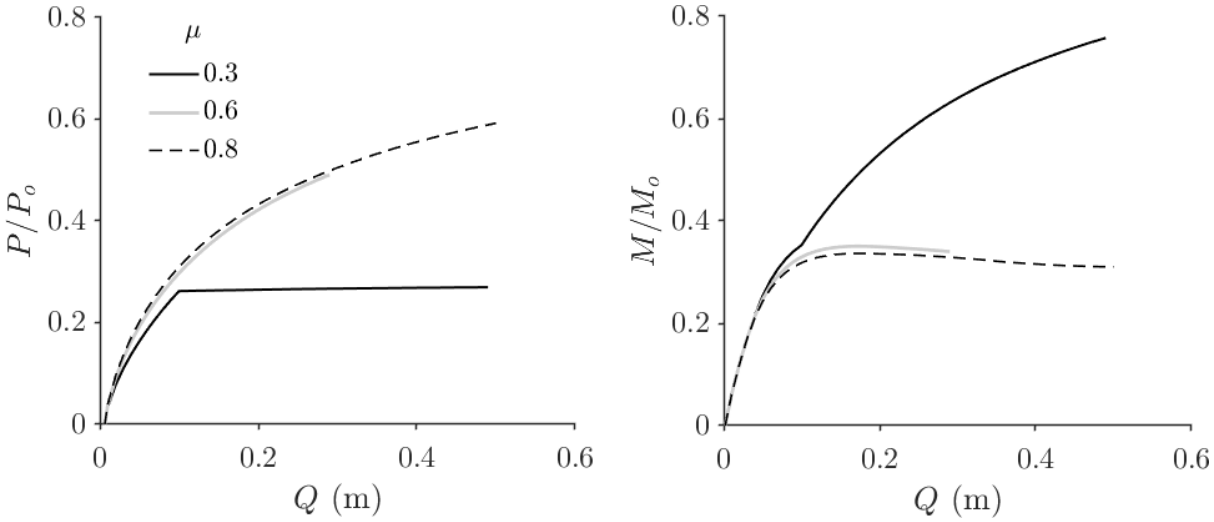

Figure 4-42. Axial load (left) and bending moment (right) versus imposed horizontal differential ground displacement for different values of the interface COF

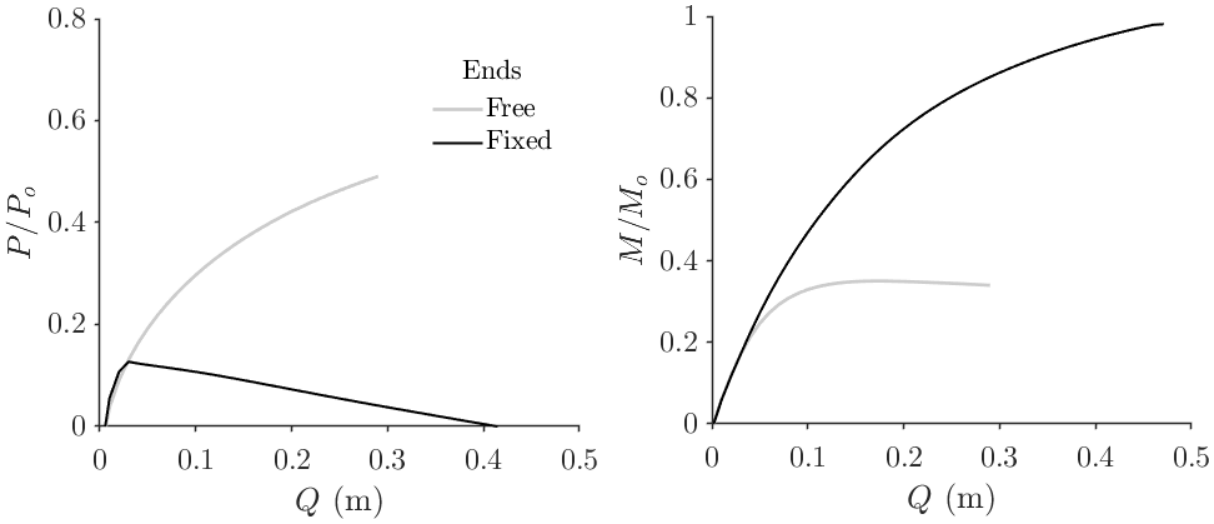

Figure 4-43. Axial load (left) and bending moment (right) versus imposed horizontal differential ground displacement for different pipe end conditions

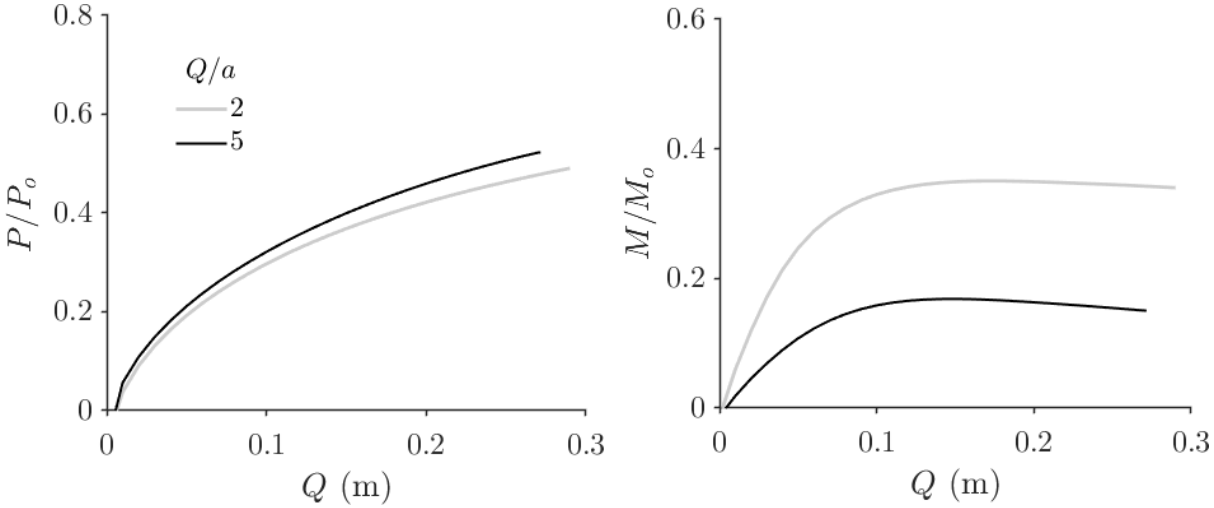

Figure 4-44. Axial load (left) and bending moment (right) versus imposed horizontal differential ground displacement for different ratios of horizontal to vertical differential ground displacement magnitudes

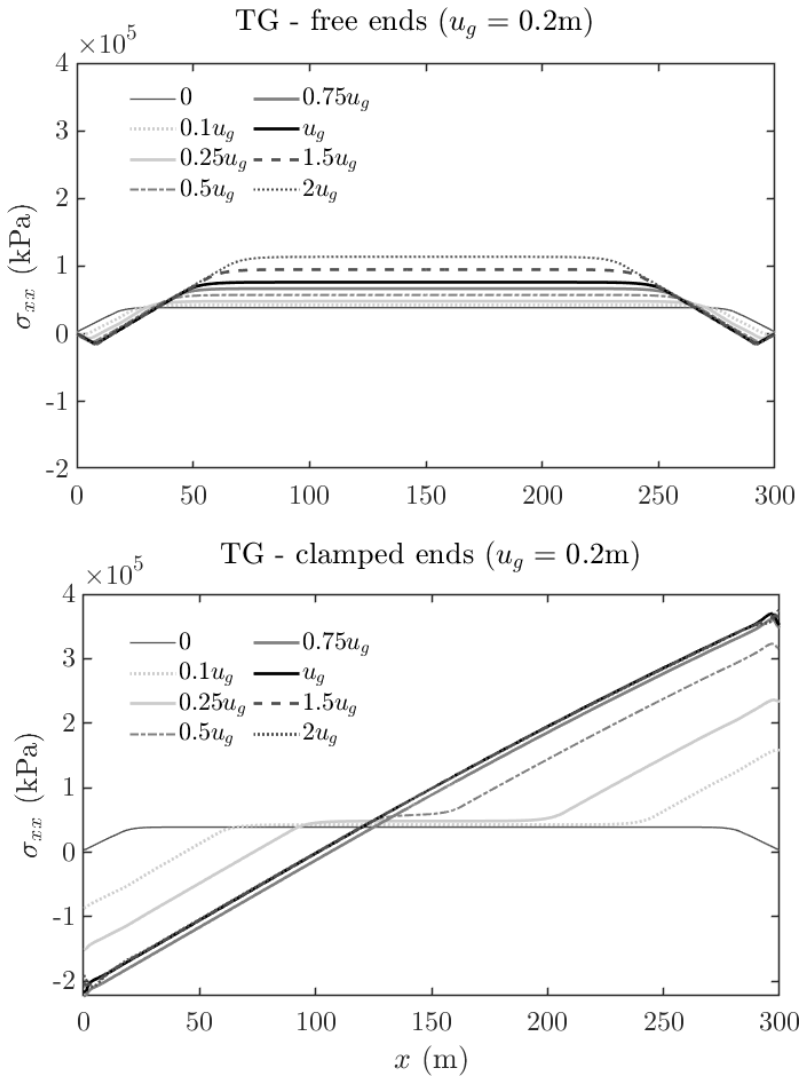

Figure 4-45. Axial stress profiles of TG baseline model due to different levels of along-the-pipe uniform displacement

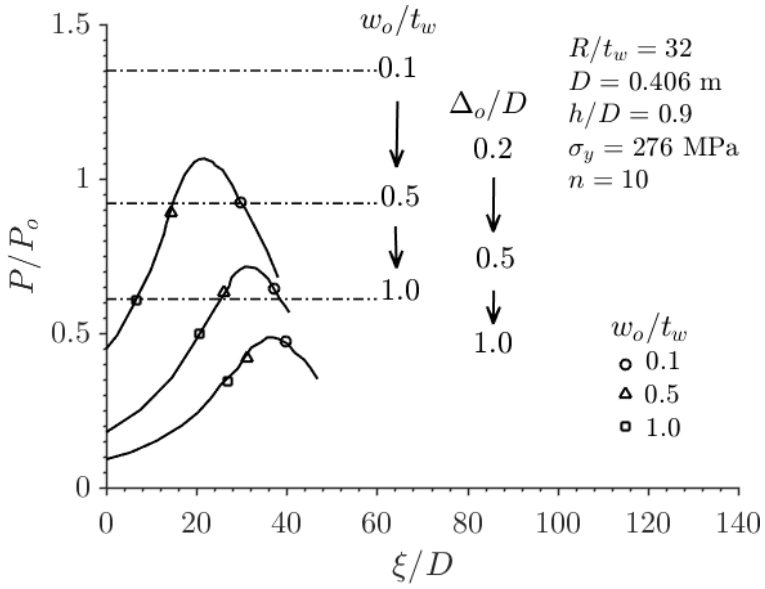

Figure 4-46. Predictions for local shell buckling loads under combined axial compression and bending by Yun (1988) (reproduced)

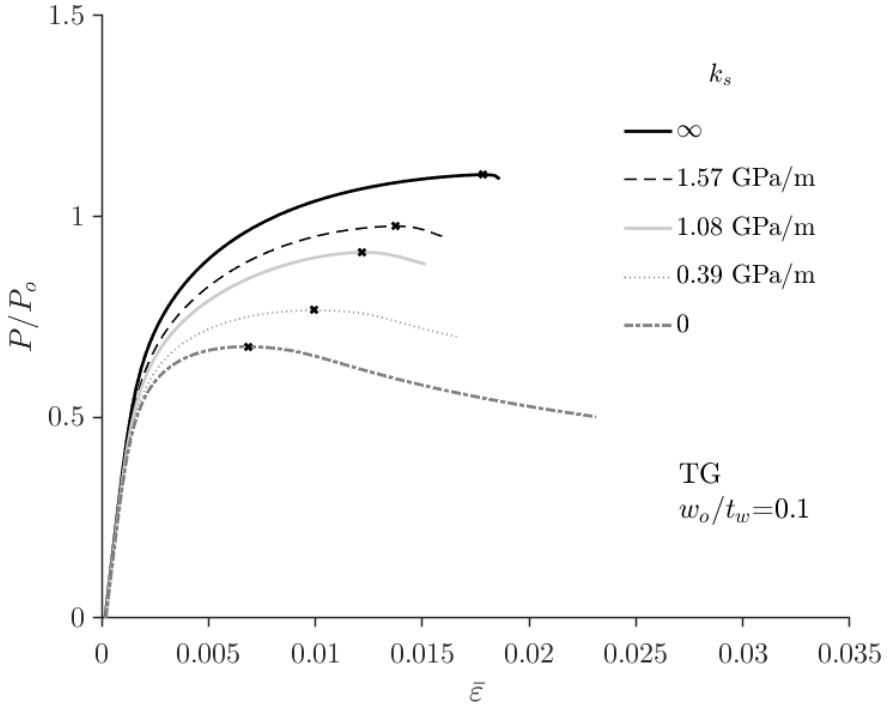

Figure 4-47. Axial load-deformation paths and limit loads of baseline TG pipeline with imperfection under pure axial compression and pressure, for different elastic soil stiffness

Chapter 5

Experimental Verification of Seismic Soil-Pipe Response

5.1 Introduction

Following the development and application in the previous two chapters of a numerical methodology for the seismic response analysis of gas pipelines buried in laterally inhomogeneous ground, this chapter presents the experimental component of this research programme. As noted in Chapter 2, the existing volume of experimental work on the problem at hand is insufficient; here, efforts are put to generate original test data from carefully executed experiments with the aim to substantiate the findings of Chapters 3 and 4 and to enhance the overall understanding of the coupled soil-pipe response to earthquake excitation.

Seven sections comprise the contents of this chapter. First, a brief overview of the test campaign is provided and the primary aims are outlined. Then, all aspects of the experimental setup and testing programme are described in detail. The test results are presented subsequently, followed by numerical validation. A discussion of various implications in relation to the test data obtained is supplied in the end prior to the summary of the chapter and the conclusions.

5.2 Overview

The fact that earthquake-induced pipeline strain concentrations in zones of lateral variation in soil properties and the consequences for the pipeline structural integrity have not been investigated experimentally to date can be understood in light of the spatially extended character of the problem and the difficulty in transforming it into manageable laboratory scales of acceptable fidelity. On the other hand, there have been a number of experimental studies recently on the response of buried pipes to permanent ground deformation from fault rupturing (Jalali *et al.*, 2016; Sarvanis *et al.*, 2017; Demirci *et al.*, 2018), either at full or reduced scale.

This experimental campaign is a contribution towards the lab-scale physical modelling of dynamic soil-pipeline interaction in the case of a gas transmission pipeline running through laterally non-homogeneous cohesionless soil and subject to vertically propagating shear waves. The project benefited from the long experience of the Earthquake and Large Structures (EQUALS) Laboratory at the University of Bristol in shake table testing of geotechnical and structural systems, yet testing buried pipelines was a new challenge. The test platform combined the 3-by-3 m shake table and the 5-m-long Equivalent Shear Beam soil chamber (ESB hereinafter). The specific objectives of the campaign were to

- physically model the actual dynamic soil-pipe interaction (SPI) effects in the presence of lateral gradients in soil properties;
- measure the magnitude and distribution of the induced axial and bending strains along the pipe;
- compare the experimental results with analytical predictions and gauge the adequacy of analytical tools;
- infer the possibility of plastic buckling failure at prototype scale;
- elucidate the role of the interface COF as a mitigating factor.

This chapter aims at consolidating a firm understanding of the mechanisms of SPI in laterally inhomogeneous soil and its effects on high-pressure gas pipelines in seismically active areas by presenting new experimental data. It does not aim strictly at validating numerical models through test data, rather on verifying the major loading mechanisms of the pipeline and its main response characteristics through a small-scale physical analogue.

5.3 The experimental setup

5.3.1 Laboratory equipment

The tests series used the earthquake simulator at the EQUALS Laboratory at University of Bristol (**Figure 5-1**a). The shake table comprises a 3-by-3m cast aluminium platform powered by 8 hydraulic actuators and is able to excite all 6 DOFs simultaneously. Each actuator has a dynamic capacity of 70 kN and a maximum stroke of 300 mm. The platform has a maximum payload of 15 Mg and is laid inside an isolated reinforced concrete block weighing 300 Mg. The table can attain maximum horizontal accelerations of 1.6 g at 10-tonne payload, with operational frequencies in the range 0-100 Hz, depending on the dead load.

To hold the test soil in place, the ESB developed by Crewe et al. (1995) was used. This apparatus is one of a series of similar devices built in the '90s at the University of Bristol to enable physical modelling of geotechnical systems under seismic shaking (**Figure 5-1**b and c). The ESB is made of eleven RHS aluminium rings, stacked alternately with soft rubber blocks to create a flexible hollow box measuring 4.8×1.2×1.0m (length×height×width). Its relatively large size makes it an ideal candidate for pipeline testing. Its floor is roughened with a thin sand layer to maximize shear wave transmission; the internal end walls (in the short direction) are similarly treated, while the internal side-walls (in the long direction) are lubricated to better approximate plane strain conditions. Rigid steel-restraining frames support the side walls on a system of bearings to prevent undesirable motion in the transverse direction.

Designed to provide minimum resistance to shearing, the ESB allows the test soil to drive the horizontal motion, while it offers minimum inertia thanks to its low weight, and sufficient soil confinement for geostatic conditions to develop. When empty, its natural frequency has been measured at 3.5 Hz.

5.3.2 Soil profiles and properties

To adequately reproduce the free field boundary conditions at the ESB ends, the same geomaterial should be used in the vicinity of both end-walls to ensure the best possible coupling between the compound soil mass and the ESB rings. To this end, it was preferred to employ a test soil with a geological structure utilizing reflection symmetry with respect to the mid transverse-vertical plane of the ESB. Common geological formations in nature exhibiting lateral inhomogeneities are often sediment-filled valleys of various shapes and aspect ratios; other possibilities include fault sites and cut-and-fill embankments. To simplify the test configuration while retaining the essential features of the problem, a profile consisting of three uniform equivoluminal blocks of sand in the long ESB direction was assembled, with a stiffness contrast between the central block and its adjacent blocks. This configuration guaranteed a degree of lateral stiffness gradation, symmetry and feasibility of construction.

Two dry sand grades were used to form the 3-block profile: Leighton Buzzard sand fraction B (LBB) and Silica Sand (SS). The first is an uncemented medium-coarse sand with rounded grains and well-documented properties (Stroud, 1971; Cavallaro, Maugeri and Mazzarella, 1992) and was readily available in the laboratory. The second consists of uniform fine particles and was procured for the purposes of the experiment. Index data for these sands obtained by sieve analysis are reported in **Table 5-1**. SS was on delivery found to contain 2.2% water by weight[2], but this was judged too low to affect the drainage conditions. The target was to prepare a dense-loose-dense configuration by filling the side blocks with LBB and the middle one with SS, as

[2] This test was not performed by the author himself

illustrated in **Figure 5-2**. By manipulating soil density and in light of the soil's stress-dependency, soil stiffness could be controlled indirectly. More details on sand deposition are provided in section 5.3.4.

5.3.3 Scaling laws

5.3.3.1 Basic principles and driving considerations

Following the line of reasoning developed in Wood et al. (2002), a set of first-order similarity laws were adopted to establish a valid connection between prototype and model, where not all physical quantities obey dimensional analysis principles simultaneously. Like in many 1-g geotechnical models, physical quantities chosen as independent were

- acceleration (by definition)
- length
- mass density and
- material stiffness.

Scaling was controlled on one hand by the reduction of the full-scale site length, which needed to be reasonably large to accommodate lateral variations in soil properties in a realistic way. Given the ESB length, a lower bound for the linear scale factor for length was enforced as $n \geq 30$ (amounting to a full-scale length not smaller than $30 \times 4.8 = 144$ m) to ensure that the spatial extent of the problem is well captured. On the other hand, the simultaneous reduction in the pipe dimensions imposed a further constraint being the limited market availability of very thin sections. Furthermore, for the convenience of having the same geomaterial in prototype and model, the scale factor for density was set equal to unity. To determine the model material stiffness, it was postulated that G_{max} is related to the mean effective confining stress, σ'_m, through a power law empirically expressed as $G_{max} \propto \sqrt{\sigma'_m}$ (Seed and Idriss, 1970; Hardin and Drnevich, 1972).

A modified version of the TG pipeline was selected as the prototype – the original is used in the numerical part of this thesis. Its section was redesigned for a lower operating pressure according to a typical safety factor (SF), keeping the same diameter and steel grade, in order to obtain a higher R/t_w ratio. The resulting pipe characteristics are $D = 900$ mm; $t_w = 8.7$ mm; $R/t_w = 51.5$; $h = 1.5$ m; $P/P_y = 0.57$; $SF = 1.75$; $E = 200$ GPa; $\sigma_y = 448$ MPa.

At its inception, the scope of the test was to reproduce the conditions required to trigger plastic buckling in a scale model pipe. To accomplish this in a controlled manner, the scaled pipe should simultaneously obey similitude laws for parameters governing the mode of buckling and the under-pressure collapse axial load, namely R/t_w ratio, h/D ratio, internal pressure and the plastic material properties, if one ignores the role of geometric imperfections.

An additional critical requirement at model scale would be to ensure a minimum pipe anchorage length for mobilization of the downscaled collapse load of the model pipe section from frictional stresses. This length is straightforward to determine analytically given the Coulomb friction per unit length, t_u, at the centreline and the target collapse axial load, $P_c = \sigma_c 2\pi R t_w$ (σ_c = the critical axial buckling stress), as

$$L_{an} = \frac{P_c}{t_u} = \frac{\sigma_c t_w}{\mu\gamma(H+R)\left(\frac{1+2K_o}{3}\right)} \tag{5.1}$$

For example, **Figure 5-4** plots the minimum required L_{an} against μ for the geometry of the modified TG pipe and for three levels of $\rho = \gamma/g$. The straight line intersecting the curves represents the provided L_{an} by the soil in the ESB for $n = 45$, when projected to full scale. The grey box identifies μ values for different γ that are compatible with a test at $n = 45$.

An iterative design process was undertaken to find a suitable pipe section in the market satisfying all or most of the above conditions. This approach proved troublesome though as it always led to extremely thin metal alloy tube sections ($t_w <$

0.2 mm) that no supplier contacted could manufacture. During this design process, an exploratory study carried out involved the development of a full dynamic 3-D finite-element replica of a candidate test setup with a super-thin tin model pipe, in order to evaluate the validity of the employed scaling laws. Information about this side undertaking are provided in Appendix D.

Under the foregoing circumstances, it was decided to restrict the model pipe deformation in the elastic range and use a section that approximately retains secant stiffness similarity to the prototype. **Figure 5-3** illustrates this idea: the nominal axial stress-axial deformation paths computed from nonlinear FE analysis of the prototype pipe are plotted for various levels of soil confinement and imperfection amplitudes, and the critical (limit) loads are identified. A secant elastic modulus $E_{sec}^{(p)}$ is calculated corresponding to the limit point at full scale, and the model scale analogue $E_{sec}^{(m)}$ is determined according to the adopted scaling rule – as long as the actual elastic modulus of the model material approximates $E_{sec}^{(m)}$, a reasonable similarity in material stiffness is preserved. Using $n = 45$, the scale factors for all variables relevant to the physical system were derived and are listed in **Table 5-2**. The order of derivation follows the listing order: from stress to strain to displacement to velocity to time (=displacement/velocity) and frequency. Derivation of the velocity scale factor was based on the consideration that the ratio of potential to kinetic energy from model to prototype must be preserved. It can be observed in **Figure 5-3** that the estimated scaled secant modulus $E_{sec}^{(m)}\Big|_{n=45} = 5.6$ MPa lies in the typical range of values for plastics. For this reason, unplasticized Polyvinyl Chloride (uPVC) with an elastic modulus of 2.1 GPa determined from tensile coupon tests was selected as the model pipe material.

5.3.3.2 Dimensionless ratios

Care was further taken to preserve dimensionless ratios controlling the soil-pipe system response as done in the experiment by Demirci *et al.* (2018). Because the expected predominant deformation mode of the pipe is alternating compression-

extension, the relative soil-pipe axial flexibility is a relevant dimensionless ratio and can be quantified using Eq. (2.5); its value for the adopted setup is 0.9. Another influencing parameter is the stiffness contrast between the different soil regimes, which may be correlated to the in-situ density contrast ρ_{LBB}/ρ_{SS} between the two sands; the latter ratio is preserved from model to prototype at any rate. The ratio h/D is handled by the length scaling factor, while a separate dimensionless ratio for internal pressure is superfluous since the effect of pressure is implicitly considered in $E_{sec}^{(m)}$. In evaluating grain size effects, the criterion $D/d_{50} \geq 50$ (d_{50} = median grain size) is tested for the two sands (Fioravante, 2002). Fine-grained SS passes the test by a margin ($D/d_{50} = 141$), with LBB failing closely ($D/d_{50} = 32$). Note that R/t_w is not preserved, but it is rendered irrelevant since the model pipe response is designed to be elastic, without elastic buckling being a possibility.

Model pipe properties are presented in **Table 5-3**. The interface COFs of the two sands with uPVC were determined from direct shear tests[3] using a Wykefam Farrance direct shear testing apparatus available at the Geotechnics laboratory of the University of Bristol. Samples of LBB and SS with $D_r = 70\%$ and 15% respectively were prepared, placed in the shear box and sheared against a uPVC plate sample (sourced from the pipe supplier) at three vertical stress levels, 10, 20 and 35 kPa. **Figure 5-5** presents aspects of the testing device and the samples; the acquired data are presented in **Figure 5-6** in the form of shear stress-displacement curves and stress ratios (i.e., interface COFs) against vertical stress. As one would intuitively expect, the interface COFs against uPVC are quite low due to the smooth surface of the material and are not normally representative of the interface COFs between steel and sand. Interestingly, the COF in the finer SS sand is somewhat higher than in LBB and is practically insensitive to the vertical stress level.

[3] These tests were not performed by the author.

5.3.4 Specimen preparation

The ESB was securely bolted on the shake table and shaken lengthways. Installation of falsework in the ESB was necessary to partition the three soil blocks throughout the pouring process. In order to maintain a level of density control on the sand blocks, an 'inverse' staged construction solution was opted for to facilitate independent compaction of the blocks. A small-scale earth retaining wall system consisting of steel sheets and timber studs was designed and built to temporarily retain the side LBB blocks and permit their compaction before SS was poured in the middle (**Figure 5-8**a).

The construction sequence is described in the following. The retaining structure was first placed in the ESB and restrained by timber guides; 208-liter drums filled with LBB were crane-lifted over the ESB top and LBB was poured in 10~15 cm layers in the side blocks, up to a target pipe bed elevation of 1005 mm (**Figure 5-8**b). After each layer pour, LBB was compacted by persistent low amplitude white noise table vibration, as well as by hand, using custom tamping tools, and the average density of the whole block was calculated from the soil mass poured and the volume occupied. For the 6 layers of LBB below backfill, the cumulative densities measured were 1.61, 1.67, 1.68, 1.62, 1.64 and 1.63 Mg/m3, showing good uniformity. Deposition of SS in the middle compartment followed again in layers, combined with gradual uplift of the retaining structure until its complete removal; SS layers were only slightly compacted and levelled (**Figure 5-8**c) – the average density of this block was calculated at the end of pouring, since it was intended to be loose. The pipeline specimen was then laid, the sensing instruments were installed and finally the backfill soil was poured, spread and gently levelled to avoid sensor damage or dislocation.

The final free surface elevation was 1085 mm, leaving an embedment depth to pipe crown of roughly 60 mm. This violated the prototype h/D ratio of 1.67 but was necessary to ensure a sufficient degree of confinement since the uppermost sand layers were unavoidably loose. For LBB, the achieved bulk mass density was calculated 1.63

Mg/m^3 for the bed layer and 1.49 Mg/m^3 for the backfill, while for SS it was 1.40 Mg/m^3 for the bed and 1.37 Mg/m^3 for the backfill. A reason why a higher density state for LBB was not achieved as in other tests (e.g., Taylor & Crewe 1996) may be that some local disturbances were induced in the soil while pulling up the retaining structure during preparation. On pulling up the retaining structure, lateral-downward sliding of soil grains was observed locally at the block interfaces to fill the narrow voids formed. These disturbances were brief in time and might have caused development of active lateral earth pressures. However, on pouring the overlying layers, the stress state gradually reverted to at-rest values and further densification occurred due to the surcharge.

It is to be noted that, partly on grounds of ease of installation, the pipe ends were left unrestrained. Under uniform ground excitation, this set of boundary conditions represents the most favorable of two extremes in terms of induced axial strain in the pipe, the other being clamping one or both pipe ends. The real condition lies between these two extremes, as the spatial continuation of the pipeline implies a finite axial stiffness (and force) at the ends of the truncated portion of the pipe. The theoretical argument behind this choice of boundary conditions is that, away from any lateral ground heterogeneities or man-made boundaries (e.g., compressor stations), a straight pipeline is expected to displace effectively as a rigid body in tandem with the soil mass under uniform ground excitation parallel to the pipe axis. This study did not investigate the effect of other pipe end restraints on the pipe response.

5.3.5 Instrumentation

Monitoring the deformation in the model pipe at multiple locations is an ideal application for the use of state-of-the-art fibre optic sensors. Two identical Draw Tower Grating (DTG®) chains were custom-ordered. These are spliceless, high-strength FBG cables of ultra-small diameter (125 μm) produced by drawing the optical fibre concurrently with inscribing the gratings. As shown in **Figure 5-9**b, cables C1 and C3 were attached to the crown and invert of the pipe, respectively, to monitor the total

longitudinal strains. Each one came with 25 strain sensors in a symmetrical configuration having a biased distribution towards the soil block borders. Bonding of the cables on uPVC was achieved using strong instant adhesive. The DTG cables were connected to a Micron Optics interrogator to acquire and process the data. Pictures of the DTG cables are given in **Figure 5-10**a and b.

Linear, high output acceleration transducers were also deployed to record accelerations in the shaking direction at free-field, table and ESB top. A total of 13 free-field accelerometers were encapsulated in miniature plastic boxes with artificially roughened external faces (via sand adhesion) to maximize friction; 11 of them were aligned parallel to the pipe centreline and two of them were embedded deeper to help extract estimates of the induced shear strains, as shown in **Figure 5-9**a. One of the instruments was secured to the shake table to measure the table motion and another at the third-from-the-top ring to help evaluate the soil-ESB coupling. Pictures of the accelerometers are presented in **Figure 5-10**c and d. All deployed transducers are summarized in **Table 5-4**.

5.3.6 Testing protocol

Gaussian white noise with RMS amplitude of 0.02 g was imposed as horizontal table excitation strategically throughout the core testing sequence in an attempt to identify the modal characteristics of the system. The seismic platform was first shaken with modulated harmonics ("sine dwells") at frequencies in the range 8.7-85.0 Hz, equivalent to a range of 0.5-5.0 Hz at full scale, and acceleration amplitudes from 0.01 g to 0.1 g in an increasing fashion. At each intensity level, motions were applied from the highest to the lowest frequency to delay unavoidable dilation and contraction effects (Crewe et al. 1998). The time histories of a typical white noise signal and a sine dwell are depicted in **Figure 5-11**.

The second phase of the shaking protocol comprised a set of broadband signals in the form of time-compressed versions of recorded strong ground motions, with PGA from 0.06 g to 0.49 g. Since time was to be compressed by a factor of 0.058, a significant

portion of the frequency content of these motions was unavoidably shifted substantially higher (>50 Hz). However, this had implications on the ability of the loaded table to reproduce these high-frequency motions, given that

i. it is a complex hydraulic-mechanical system whose response to input is determined by a nonlinear transfer function and

ii. exhibits a cut-off frequency that drops significantly with increasing payload.

Normally, an iterative approach involving shaking cycles is taken to match the realized table motion to the target one. Due to the risk of sample disturbance and stiffness deterioration under strong excitations, this was not done here, but rather a suite of pre-matched, de-convoluted motions from a previous testing program SERENA (Fiorentino *et al.*, 2019) were used along with a number of unmatched target motions, whose frequency spectrum was scaled up by a factor of 8.7 instead of the target 17.4. **Table 5-5** lists the properties of these ground motions; their time histories are displayed in **Figure 5-12**.

5.4 Test results

5.4.1 Data processing

The first operation performed on all raw signals acquired was removal of the mean; where a residual response was observable, only the initial ordinate offset of the signal was subtracted. To convert voltage fluctuations to time-histories of the desired physical parameters, the calibration factors listed in **Table 5-4** were used (λ here stands for light wavelength). For soil acceleration histories excluding the random noise response, de-noising was achieved using a wavelet transform scheme by soft-thresholding (Donoho 1995); the 'db8' (8th order) wavelet belonging to the Daubechies wavelets family was adopted as basis. This approach was found more effective in reducing noise in seismic signals than the standard band-pass filters requiring specification of cut-off frequencies (Chanerley and Alexander, 2007), and was

particularly suitable herein because displacement histories were to be derived by time-integration. Raw Fourier Amplitude Spectra (FAS) of acceleration histories were smoothed by passing them three times through a moving average filter with a 49-sample smoothing width; this ensured 'smooth ratios' of less than 0.2, sufficient to minimize distortion of the peak heights and bandwidths (O'Haver, 2018).

5.4.2 Modal identification

Frequency-Response Functions (FRF) were constructed by computing the FAS of free-field acceleration response histories to random noise input, and then dividing by the FAS of the table input (station A1). FRFs at recording stations A4 (LBB) and A11 (SS) are plotted in **Figure 5-13** for three cases: before the testing sequence begins, after shaking at 0.1g and in the end of the sequence. It is seen that the responses at both A4 and A11 are predominantly amplified at the same frequency (about 37 Hz for case 1); this confirms the coupled behaviour of the sand blocks. FRFs at A11 give a second higher peak amplification at about 56 Hz, which suggests a stiffer middle deposit despite its looser state. This may be explained by the sub-angular shape of SS grains, which results in more effective interlocking between grains. The resonant frequency of the system drops—moderately—with excitation level to 34.3 Hz, as does maximum amplification.

The half-power bandwidth method was used to extract soil internal damping estimates from the FRF low-end peaks. **Figure 5-14**a plots these estimates as a function of the maximum table PGA recorded in the sequence history. Evidently, there is a general but inconsistent upward trend across all recordings, from a minimum of 3.1% up to a maximum of 5.7%, with SS exhibiting higher dissipative action. However, it is acknowledged that the derived values might not be reliable due to the strongly spiked shape of the spectra and the associated dependence of the method on the employed smoothing operation. In contrast, Pitilakis et al. (2008) and Chidichimo et al. (2014) have measured damping ratios for LBB in excess of 10%.

It is not straightforward to obtain estimates of the shear wave velocities $V_s^{LBB}$and V_s^{SS} for the two sands using the expression $V_s = 4f_n h$ for horizontally layered deposits. Instead, an attempt was made to approximate these parameters in an average sense from the arrival times of the first incident wave in the recorded signals at surface, providing also statistical variance of the observations in terms of the standard error of the sample mean, expressed as

$$\sigma_{\bar{x}} = \frac{s}{\sqrt{n}} \tag{5.2}$$

where s is the sample standard deviation and n the sample size. These results are presented in **Figure 5-14**b, where one can identify an initial densification phase for both sands up to 0.05g, and a subsequent non-linear softening phase at higher table accelerations, which is more pronounced for the initially denser LBB. The reduction in mean V_s from the low-strain to the final state is 24% and 10% for LBB and SS, respectively, and the mean stiffness contrast $\overline{V_s^{SS}/V_s^{LBB}}$ achieved at final state is 1.3. Note that, for low table PGAs (< 0.05 g), no clear peaks were detectable in the acceleration signals, hence the large variability in derived V_s.

5.4.3 Response to harmonic excitation

Results for the first phase of single-frequency excitations are reported in this section. Primary outputs obtained are the soil accelerations and pipeline strains; derived output includes displacements, axial strains, shear strains and stresses of the soil, and axial strains of the pipeline. Where peak magnitudes are more of interest, unfiltered results are presented to retain the original character of the measurements.

Figure 5-15 plots filtered soil acceleration histories as recorded by sensors A1 (on table), A4 and A11 for different harmonic tests—a description of each test is supplied in **Table 5-6**. At a loading frequency close to the resonant frequency of ~ 36 Hz (Test H06), horizontal surface motion is amplified by both sands, more strongly by LBB, as shear waves propagate upwards through the soil mass. The degree of

amplification depends on ratios $\omega_f/\omega_{N,eq}$, where ω_f is the forcing frequency and $\omega_{N,eq}$ is a resonant frequency of a soil block determined by the FRFs of **Figure 5-13**, with zero or negative amplification being possible as recorded in Tests H08 and H11, respectively. It is noted that erratic behaviour is observed in SS in some cases in the form of double peaks (e.g., Test H10), possibly related to slipping of the instrument casing in the sand.

Instantaneous soil acceleration profiles along the recording array A15-A11 are illustrated in **Figure 5-16**. The profiles are extrapolated by reflection beyond the mid-point to compensate for the lack of accelerometers in the right half of the setup. For verification, output from sensor A12 is overlaid, showing a good match with the extrapolated value at the same location. Profiles are plotted for two time instants when a peak and a trough occur. In Test H06, the varying amplification levels in the two soils generate two fairly flat responses across each soil domain, in reasonable agreement with analytical soil amplification studies (Gelagoti *et al.*, 2010). This behaviour results in a relative horizontal motion at the block interfaces, which produces axial normal strain in the soil as shown in the following. On the other hand, surface accelerations are uniform across all blocks in Test H08, in consistency with **Figure 5-15**. Note that sensor A2 was found to be dysfunctional while A11 had undergone unwanted tilting after embedment and for this reason its output was discarded.

Figure 5-17a displays the total longitudinal pipeline strains as tracked by the crown and invert optic fibres. As anticipated, the shapes of the profiles are antisymmetric with respect to the mid-point, exhibiting alternating compression-extension at the soil interfaces, depending on the motion direction. Trends also agree very well qualitatively with the numerical predictions of Chapters 4 and 5. The strain distributions of the crown and invert are very similar, suggesting that bending in the pipe is generally not dominant. To obtain the axial strain profiles, the arithmetic mean of the total strains at the extreme fibres of the tube section $1/2\,(\varepsilon_C^t + \varepsilon_I^t)$ suffices (subscripts C and I here denote crown and invert respectively), as long as the pipe remains elastic and the neutral axis coincides with the centerline. The axial strains in

this first loading phase show mild deviation (<20%) from the total strains, indicating fairly small in-plane bending effects.

Moreover, to provide a picture of the axial strain transmissibility from soil to pipe, a crude calculation of horizontal normal soil strains ε_s at the recording stations was performed using a 2nd-order finite-difference approximation given by

$$\varepsilon_s(x_i) = \frac{(u_{i+1} - u_i)\frac{x_i - x_{i-1}}{x_{i+1} - x_i} + (u_i - u_{i-1})\frac{x_{i+1} - x_i}{x_i - x_{i-1}}}{x_{i+1} - x_{i-1}} \tag{5.3}$$

where u_i is the soil horizontal displacement at station i, computed by double integration of measured acceleration, and x_i is the horizontal coordinate of station i. **Figure 5-17**b shows the near-surface axial strain profiles for Test H06, taken at the same time instants as in **Figure 5-17**a. The distributions resemble the ones measured in the pipe, with magnitudes at the spike being significantly larger; about 50% of the soil strain is seen to be 'transferred' to the pipe in this case, an indication that some interface sliding has occurred.

To gain further insight into the hysteretic response of soil, shear stress-strain loops were produced according to the procedure outlined in Brennan et al. (2005), using the acceleration recordings from the two vertical arrays A4-A13 and A11-A14. According to **Figure 5-18**, LBB undergoes much larger shear strains (up to 0.06% in Test H10) than SS for the same excitation level. The loops are fairly stable, but nonlinearity is not pronounced; the slopes through the origin equating to secant shear moduli confirm that SS is a stiffer sand than LBB. Also, the deeper the station, the stiffer the sand as one would expect.

5.4.4 Response to broadband excitation

Along similar lines, select results obtained for broadband table input are presented in this subsection. In the top row of **Figure 5-19**, representative acceleration responses for the two sands as recorded by the mid-block instruments A4 and A11 are plotted for cases SM06 and SM08. Again, variable surface motion amplification is

understood to impose increased relative axial displacements on the pipeline. The bottom row of **Figure 5-19** shows the axial pipe strains calculated at stations falling on the block interfaces, for the same loading cases. By close inspection, it is seen that the peak strains are nearly in phase with the soil acceleration peaks. Axial strain histories at stations 6 and 20 are rough reflections of each other about the x-axis, which again confirms the alternating compressive-extensional deformation mode in the pipe close to the block interfaces. Moreover, in the cases shown, residual stresses and (elastic) strains are observed post-shaking due to residual ground deformations that alter the configuration of the pipe.

Critical tensile and compressive strain profiles for the same test cases are presented in **Figure 5-20**. The profiles in solid line refer to axial strain; dashed lines show actual recorded total strain at the extreme fibres. It is evident that absolute peaks are substantially increased compared to the harmonic tests, up to 66 με for axial strain and 140 με for total strain. Interestingly, bending strains are becoming significant as revealed by the disparity between total and axial strains; their proportion of total strains amounts to 51%, as can be seen in **Figure 5-21**. The reason for this is that higher dilatational modes are more strongly excited in the ground; these modes involve vertical components of motion, manifesting close to the block interfaces, that bend the pipeline. **Table 5-6** summarizes all directly measured and derived peak response parameters: soil acceleration, soil horizontal normal (axial) strain, soil shear strain, pipe total longitudinal strain, pipe axial tensile and compressive strain.

5.5 Numerical validation of test results

ABAQUS (Dassault Systèmes, 2014a) and Opensees (McKenna et al., 2010) were employed to simulate select experimental tests with the finite element method. Given the irregularity in geometry and inhomogeneity in material properties of the geotechnical specimen, 2-D continuum elements were used in the first place to verify the experimentally observed free-field response at the surface. Salient details of the

experimental assembly were included in the model, such as the lateral boundaries of the ESB and their contact response with the soil mass.

5.5.1 Eigenvalue analysis

The modal and material characteristics of the system as of Test WN4 were considered as reference to compare against. Only the soil and components of the ESB were included in the eigenvalue analysis. A structured mesh with plane-strain finite elements was created to discretize six distinct subdomains in the test soil (**Figure 5-22**), accounting for the difference in measured densities between pipe bed layer (ρ) and backfill (ρ') for both sands. Shear moduli were determined as $G = \rho V_s^2$ and a constant Poisson's ratio $\nu = 1/3$ was assumed across all subdomains. To couple the motion between the two ESB ends, tie constraints were enforced at all ring levels. The interaction of test soil and ESB at their interface was modelled using a finite-sliding, surface-to-surface contact discretization, assuming an interface COF equal to the as-measured internal COF of LBB, $\tan(32.6°) = 0.64$, in view of the sand-roughened internal ESB surfaces. Using mean observed V_s values from **Figure 5-14**b, the numerical model was found to be more flexible in its first mode, with the corresponding natural frequency underestimating the experimentally observed frequency of 35.8 Hz by ∼10%. **Figure 5-23** shows the first four eigenmodes; the lowest eigenfrequency is associated with a coupled shear-dilatational mode of vibration, as a result of the non-uniform shear stiffness of the soil. Higher modes involve more dominant flexural and vertical modes, both symmetric and antisymmetric ones. By comparison with **Figure 5-13**, it is seen that the numerical model captures well the second and fourth eigenfrequency as well.

5.5.2 Transient response analysis

To reproduce numerically the time-varying response of the soil and pipe to base excitation for Test H10, the two-step approach adopted in Papadopoulos et al. (2017) was tested. In the first step, the 2-D soil-ESB model in **Figure 5-22** was solved for

the realized table motion and the horizontal and vertical acceleration response histories were extracted at soil nodal points along the pipe centreline. The soil behaviour was assumed as linearly elastic and an effective stiffness was determined from the mean observed V_s for the two sands. Viscous damping of the Rayleigh type was introduced using target damping ratios as identified for the respective excitation level in **Figure 5-14**a.

Ignoring kinematic and inertial interaction effects, a separate, bi-directional, multi-support-excitation model of the pipeline idealized as an assembly of 2-D Euler-Bernoulli beams was developed in Opensees in the second step, where the frictional and transverse vertical SPI was represented by non-linear spring elements. A fine element mesh was created to match the spatial resolution of the strain sensors. Spring parameters were evaluated according to the standard ALA expressions (see **Table 2-3**), with the axial mobilizing relative displacement computed from separate FE pipe pull-out analysis as 2×10^{-5} m and 3×10^{-5} m for LB and SS, respectively. The ground spring nodes were subjected to the previously obtained horizontal and vertical free-field displacements at pipe bed level.

As illustrated in **Figure 5-24**a, the steady-state response of LBB sand compares favourably with the recorded response at A4, less a minor time lag. The average peak-to-peak discrepancy in the constant-amplitude window is ~5% and ~17% in the positive and negative direction, respectively, the difference being due to the lack of x-symmetry in the experimental response. Similarly, the match for SS is better in the negative than in the positive direction. Here, the effect of the double peaks, briefly discussed earlier, becomes obvious as it leads to a markedly larger discrepancy in the positive direction.

Shown in **Figure 5-25** are the axial strain histories at stations 6 and 20 as computed from analysis and as measured from test. For station 20, the results show differences in the strain magnitudes, though this is exaggerated by the fact that the experimental response is drifting away from the baseline. Ignoring the drift, the model under-predicts the pipe strains by an average 55%. The overall shapes are in good

agreement. For station 6, the match appears better, if one again ignores the drift. A more comprehensive picture of the level of agreement between test and numerical model is obtained by comparing the profiles of total longitudinal strains along the pipe at the time instant of the peak strain. This is presented in **Figure 5-26**, where it is apparent that the numerical model fails to capture the magnitudes of the strain peaks at the soil block interfaces by more than 100%

To trace the source of these discrepancies, an attempt was made to back-calculate the time-varying frictional force profile generated along the pipe specimen and compare against the frictional resistance used for the axial springs. The equation of motion of a continuous Euler-Bernoulli beam on dynamic non-linear Winkler foundation under axial excitation was used, given by

$$\rho_p A \frac{\partial^2 u_p}{\partial t^2} - E_p A \frac{\partial^2 u_p}{\partial x^2} = t_u \tag{5.4}$$

where $u_p = u_p(x,t)$ is the absolute axial pipe displacement and $t_u = t_u(x,t)$ is the friction per unit length. Using the recorded axial pipe strain profiles and safely assuming that the inertial term is negligible (if the recorded soil acceleration is used in place of pipe acceleration, this term is two orders of magnitude smaller than the restoring axial force), the t_u envelopes were calculated at each strain monitoring point for four different test outputs. **Figure 5-27** plots these envelopes normalized with respect to the Coulomb frictional resistance $t_{u,ALA} = \mu\gamma' h(\frac{1+K_o}{2})\pi D$. Where the envelopes are below the dotted horizontal line (=ALA), it means that $t_{u,ALA}$ captures reliably the friction response. It can be seen that, for the low-intensity test HM06, the envelopes lie below the ALA line almost everywhere. In stark contrast, the friction envelopes for test HM10 exceed the ALA resistance by a factor of 9.5 within the ground stiffness transition zones. This indicates that the soil stress state developing in these zones offer additional t_u to the pipe, allowing increased axial strains to develop, as measured. In particular, as shown in the previous, the soil in these zones undergoes compression-extension cycles; during compression, the confining stress in the soil

increases near the soil-pipe interface, leading to an increase in the contact stress, hence an increase in t_u locally. This increase in t_u is evident in the other two tests too, albeit not as sharp. The main reason why t_u is so much larger in HM10 is that the test soil in this case experiences near-resonance effects, which entails stronger amplification of the lateral displacements, thus more excessive compression.

Overall, the comparison for the soil response is judged acceptable, permitting to say that the computer model developed lends credence to the test results. For the prediction of the response of a pipe buried in a laterally inhomogeneous soil, more refined SPI models are thought to be essential to capture the cyclic variation in frictional resistance with the changing confining conditions at inhomogeneity features and the contribution of vertical/flexural site modes, bearing in mind that the ALA springs were developed solely for pipelines in laterally uniform soil.

5.6 Discussion

From the complete set of results presented in **Table 5-6**, two main trends in the pipe response are identified in **Figure 5-28**; on the left, plotted is the peak compressive axial strain of the pipe, $\max|\varepsilon_c|$, against the normalised site frequency as measured during the harmonic phase, while the right chart depicts the change in peak total pipe strain, $\max|\varepsilon_{tot}|$, with soil surface PGA as measured during the broadband phase. It is observed that, for a given laterally inhomogeneous site, $\max|\varepsilon_c|$ is maximised when the exciting frequency matches a resonant site frequency. There is also a consistent increasing trend of $\max|\varepsilon_{tot}|$ with increasing soil surface PGA; this however is largely illusory as it is known from sliding block theory that there is a yield ground acceleration that triggers slippage and limits shear stress transfer. It is the spatially non-uniform horizontal motions and the triggering of vertical/flexural site modes that modify the total pipe strain response.

When the peak pipe response obtained from the experiment is extrapolated to full-scale using the adopted similitude laws, the peak total strain becomes ~0.1% (after

division by the scale factor for strain, equal to 0.149), which is nearly half the yield strain of the prototype steel and nearly 1/6 of the limit strain corresponding to the plastic buckling load, shown in **Figure 5-3**. This result reveals a significant margin of safety for the prototype pipeline; however, it shows a non-negligible reduction of the margin of safety against buckling and it would be unwise to assume that, based on this result, local axial strain concentrations generated at soil boundaries would never result in shell buckling. If a more unfavourable combination of parameters were in place, such as a higher interface COF—as normally is the case for the steel-sand interface—and a larger soil stiffness contrast, the axial and bending strains developing in the pipe inside the transition zone would become substantially larger. Note that the ratio $\overline{V_s^{SS}/V_s^{LBB}}$ in this study varied from an initial 1.1 to 1.3 post-shaking, that is fairly low ratios.

From another standpoint, this series of tests demonstrates the benefit of a low interface COF as a means of reducing the dynamic axial loads transferred from ground to pipe during ground shaking. For comparison, using the simple SPI model presented above, the peak total strain in the pipe for the seismic input of Test HM10 and a uniform COF $\mu = 0.8$ across both sands is computed at 58 με, nearly three times larger than for $\mu = 0.23$. Given that the pipe is constructed along an engineered trench, this mitigating effect could be designed in a number of ways, such as by the use of smooth, low-friction pipe coatings, or the installation of layers of geosynthetic wrapping around the pipe to trigger axial slip at these interfaces (Honegger, 2002).

It is also worth noting that the testing sequence was performed in an uninterrupted fashion, assuming independent seismic events. However, the initially 'perfect' soil state and soil-pipe contact state was disturbed after the first strong table motions. This may have led to a gradual reduction of the in-situ COF, hence limiting the stress transfer to the pipe in subsequent tests. Unfortunately, there was no capability to measure the level of contact pressure at the pipe walls in this study. The implication is that, in the scenario of a single strong earthquake event where no loss of interface contact has previously occurred, the frictional stresses will likely induce larger axial strains in the pipeline than measured in the last tests here. Further

experimental work could shed more light on these aspects by deploying additional sensors, such as tactile pressure transducers and displacement transducers to measure settlements.

5.7 Summary of the chapter and conclusions

Results obtained from 1-g shake table tests of a 1:45 model of an onshore gas transmission pipeline embedded in a laterally non-homogeneous site are reported in this chapter. The experiments simulated the coupled dynamic response of the site and the pipeline under a set of uniaxial harmonic excitations and earthquake records applied in the pipeline direction. Three blocks made up from two types of dry sand were cast in a 4.8-m-long, 1.2-m-tall, 1.0-m-wide ESB chamber to form a symmetric test site with three zones of soil stiffness, i.e. soft-stiff-soft, and the pipeline specimen was laid in and covered. Pipeline strain measurements were acquired from two chains of fibre optic sensors bonded on the pipeline specimen. The test data were validated against finite element models. The main findings are summarized below:

- The state of deformation in the system is similar to this reported in other studies concerned with ground stiffness transitions, with the difference being that here the soil stiffness pattern was reversed. It was found that alternating compression-extension zones develop in the pipeline very close to the soil block boundaries, following the ground deformation pattern, while non-shear ground deformation remains negligible far from those interfaces. This anti-symmetric strain pattern is a result of the varying horizontal free-field motion amplification and vertical-flexural ground vibrations associated primarily with higher modes, which mobilize increased frictional stresses on the pipe walls.

- From the harmonic motion sequence, it was found that, for a given inhomogeneous site, pipeline strain magnitudes are governed by resonance effects on the site response. Peak strains were recorded for $\omega_f/\omega_{N,eq} \approx 1$ for two different table excitation levels 0.05g and 0.1g. Tests for stronger input motions showed that

the induced strains increased notably also with surface PGA, reaching values of 140 με for $PGA = 0.57$ g.

- Bending strains in the pipeline became considerable at stronger excitations, amounting to 50% of the total strains. This is an indication of vertical-flexural ground modes triggered at higher exciting frequencies, forcing the pipe to bend near the stiffness transition zones.

- A relatively simple plane-strain finite element model was successful in reproducing the recorded site surface response; however, using a beam-on-springs model with ALA spring parameters proved inadequate to predict well the pipe strain response, especially close to the stiffness transitions zones. This was attributed mainly to the inability of the axial springs to capture the increment in frictional resistance offered by the increased confinement in these zones, which permits transfer of additional contact shear stresses to the pipe.

- Results show that the prototype would accommodate the scaled-up strains of 0.1% without yielding. Nevertheless, the achieved test conditions do not reflect particularly unfavourable circumstances for the pipeline integrity from the complete set of realistically possible conditions; subtle variations in configuration, such as a higher soil stiffness ratio along with a higher interface COF, can potentially incur a more critical state of deformation in the pipeline. This remains to be investigated in future research.

The above conclusions are subject to the assumptions made in the employed test setup and the general limitations of 1-g shake table testing. Most prominently, the test model was adequate to first order and the extrapolation of the pipe response was performed with respect to the limit point of the prototype pipe. The pipe model ends were left unrestrained; this set of boundary conditions generally leads to reduced axial distress due to friction forces compared to a pipe model with clamped ends. Lastly, the test-to-test change of the soil-pipe contact conditions could not be monitored.

Figure 5-1. (a) The 6-DOF shaking table at the EQUALS research facility at University of Bristol; (b)-(c) aspects of the large ESB used

Table 5-1. Index properties for the sands used in the test

Grade	Void ratio		Grain size (mm)			C_u	Grain shape	Source
	Min	Max	d_{10}	d_{50}	d_{60}			
Leighton Buzzard B	0.49	0.78	0.450	0.620	0.70	1.56	Rounded	Lings and Dietz (2004)
Silica Sand	0.67	0.93	0.094	0.141	0.156	1.66	Sub-angular	Supplier; in-house testing

Note: $C_u = d_{60}/d_{10}$

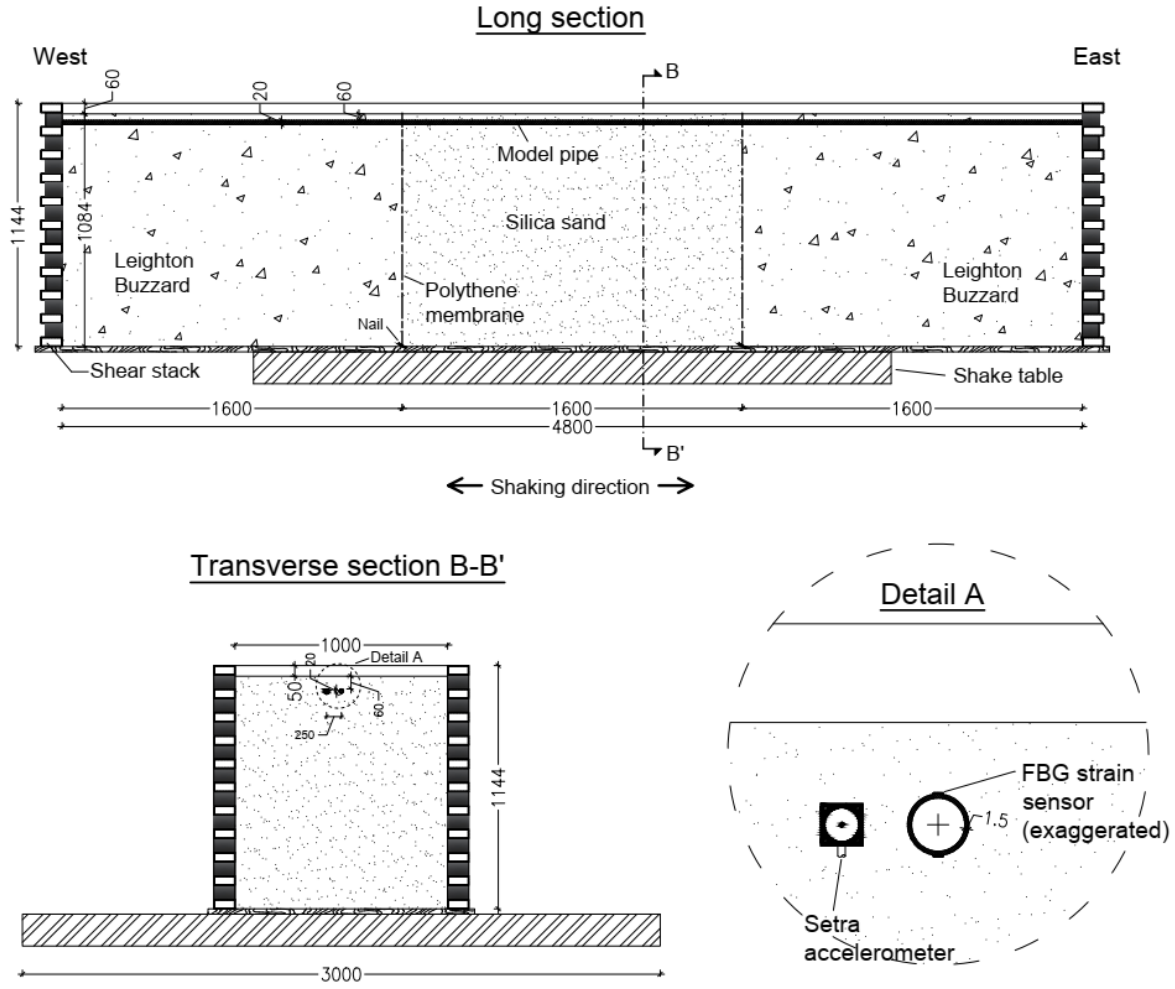

Figure 5-2. Long and transverse sections of the as-built test setup showing the geometry of the soil profile and the model pipe (all units in mm).

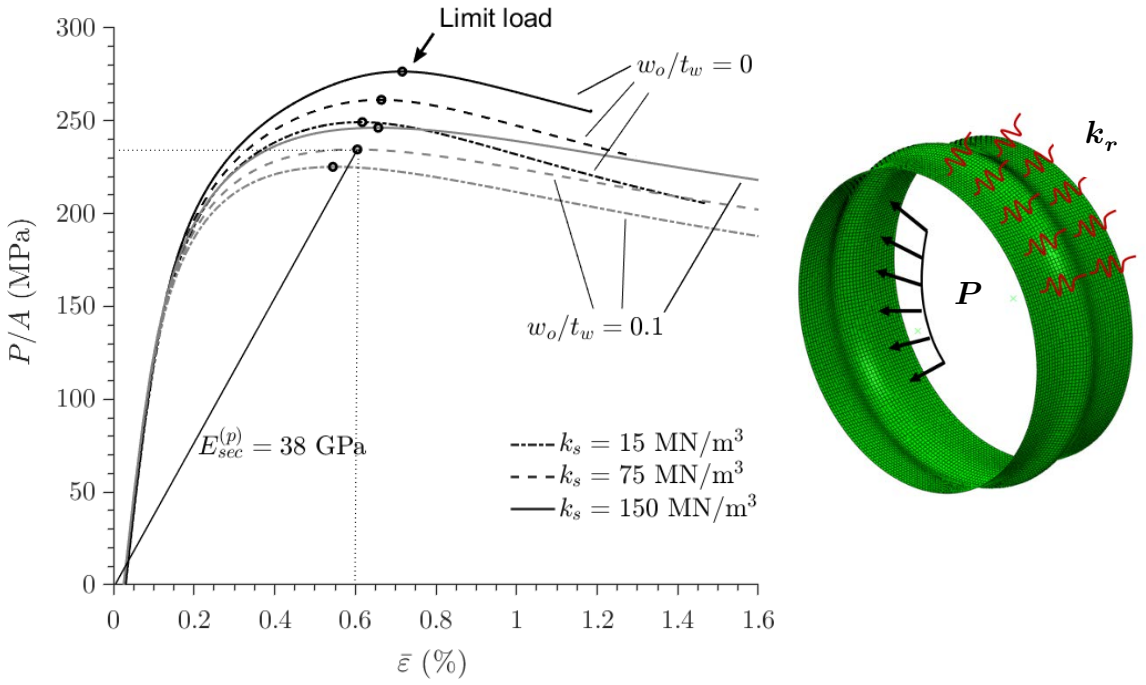

Figure 5-3. Shell axial load–axial shortening responses for the adopted prototype pipeline for various moduli of subgrade reaction, k_s, and w_o/t_w. In the FE model, deformation plasticity is employed for steel constitutive behaviour; the radial elastic soil springs k_r are calculated using k_s and nodal influence areas; the imperfection is axisymmetric with a sinusoidal shape and a half-wavelength estimated as $1.57\sqrt{Rt_w}$. Drawn is $E_{sec}^{(p)}$ for $k_s = 75$ MN/m^3 and $w_o/t_w = 0.1$.

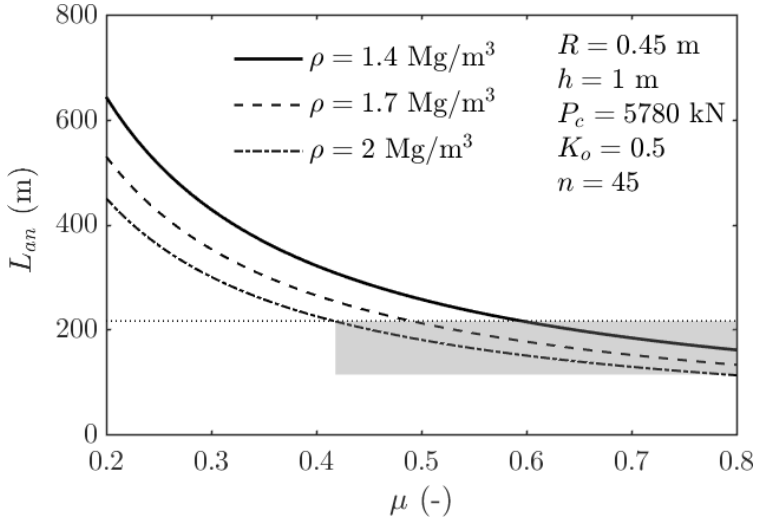

Figure 5-4. Minimum pipe anchorage length *required* for mobilization of the critical (limit) axial load of the modified TG pipeline as a function of interface COF for different sand densities; the straight dotted line denotes the scaled-up *provided* anchorage length in the available ESB for a length scale of 1:45; the grey area indicates the acceptable combinations of parameters for a scaled shake table test in the ESB

Table 5-2. 1-g scale factors employed in this study; variables in italics taken as independent

Variable	Scale factor (prototype-to-model)	Value for $n = 45$
Length	$1/n$	0.022
Density	1	1
Stiffness	$1/n^{0.5}$	0.149
Acceleration	1	1
Stress/Pressure	$1/n$	0.022
Strain	$1/n^{0.5}$	0.149
Displacement	$1/n^{1.5}$	0.003
Velocity	$1/n^{0.75}$	0.058
Time	$1/n^{0.75}$	0.058
Frequency	$n^{0.75}$	17.37
Wave propagation velocity	$1/n^{0.25}$	0.386
Force	$1/n^3$	0.000011

Table 5-3. Model pipe properties

Parameter	Unit	Value
Elastic modulus, E_p	MPa	2100
Poisson ratio, ν_p	-	0.4
Mass density, ρ_p	Mg/m^3	1.36
External diameter, D	mm	20
Wall thickness, t_w	mm	1.5
Axial rigidity, E_pA	kN	261.5
Interface COF against LBB*	-	0.23
Interface COF against SS†	-	0.27

*, † Measured at a normal stress of 10 kPa

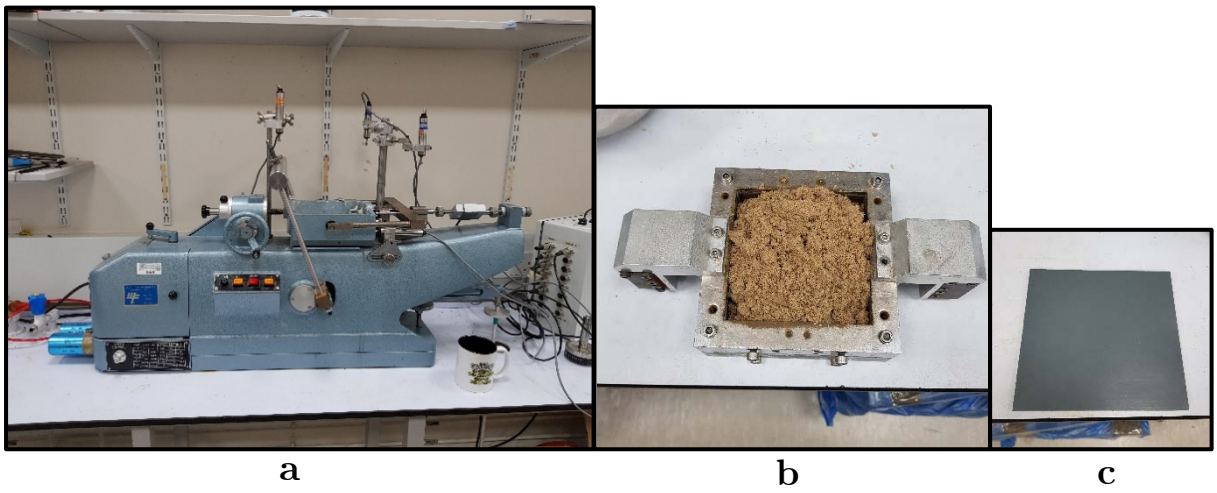

Figure 5-5. (a) The Wykefam Farrance direct shear apparatus used for the interface shear tests; (b) SS sample laid in the chamber; (c) uPVC sample

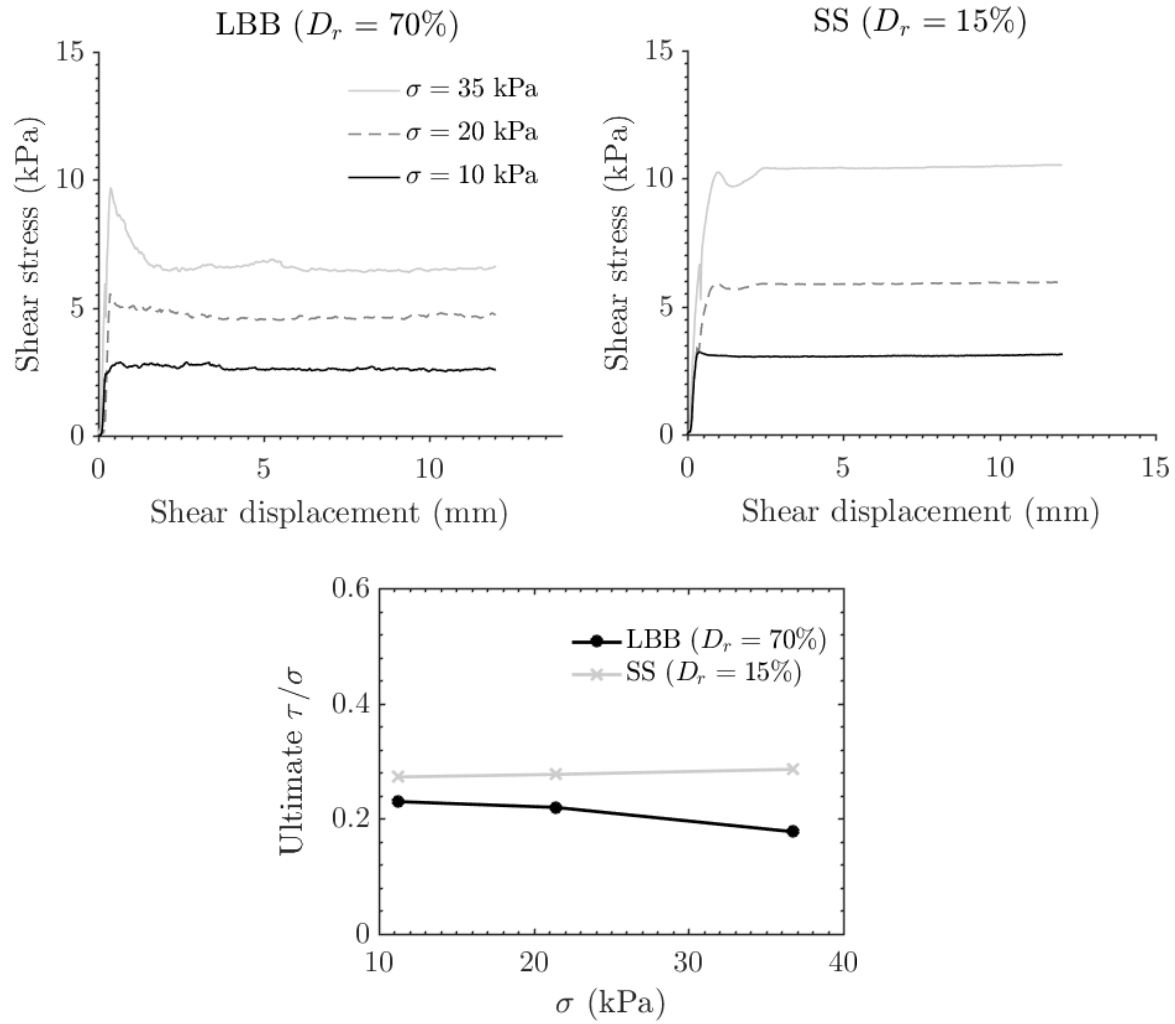

Figure 5-6. Top: Interface shear stress-displacement results between uPVC and the two sands for different normal stress; bottom: ultimate stress ratio (equivalent to the interface COF) at different normal stress

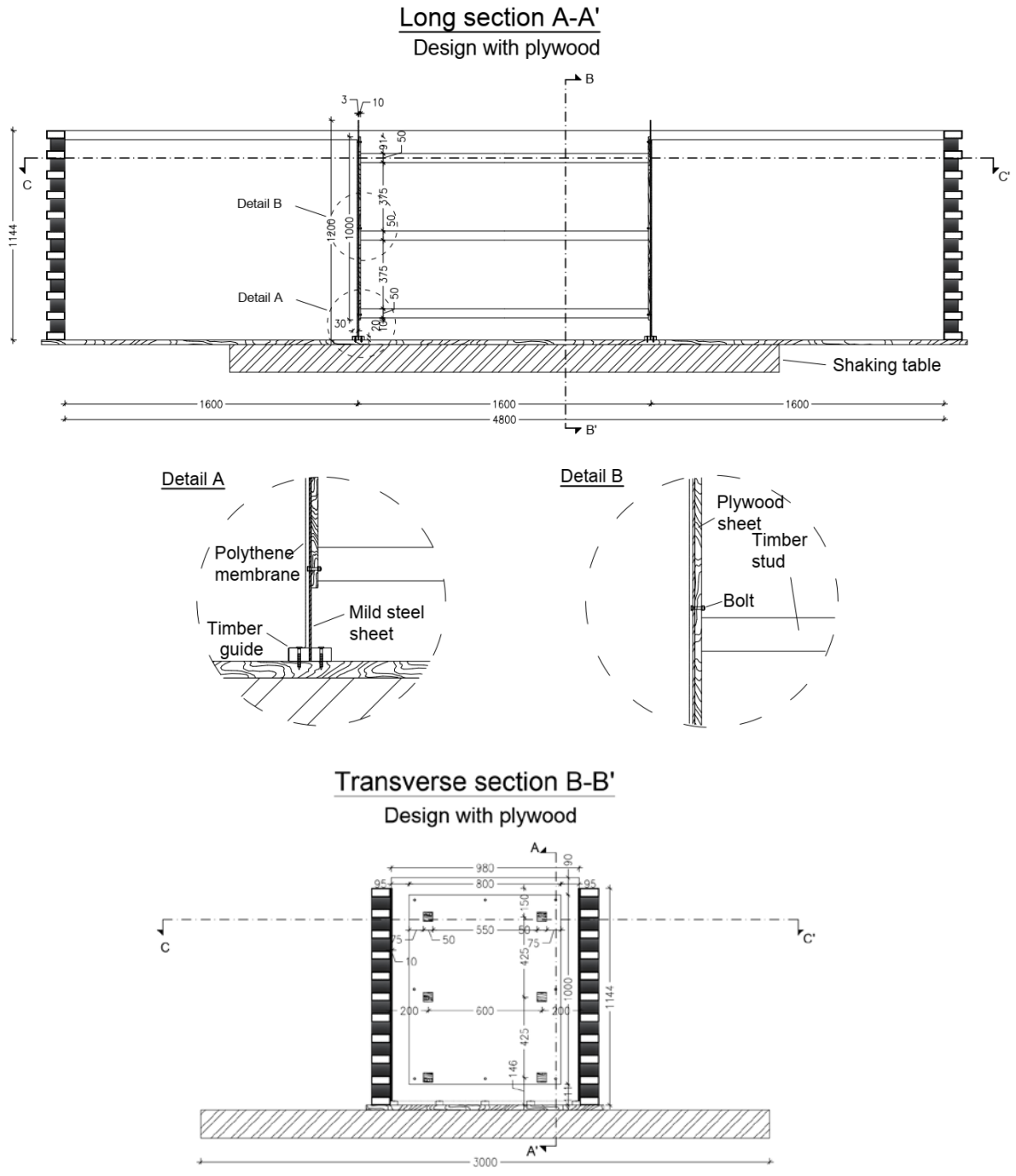

Figure 5-7. Design details of the auxiliary retaining wall system deployed in the ESB during specimen preparation

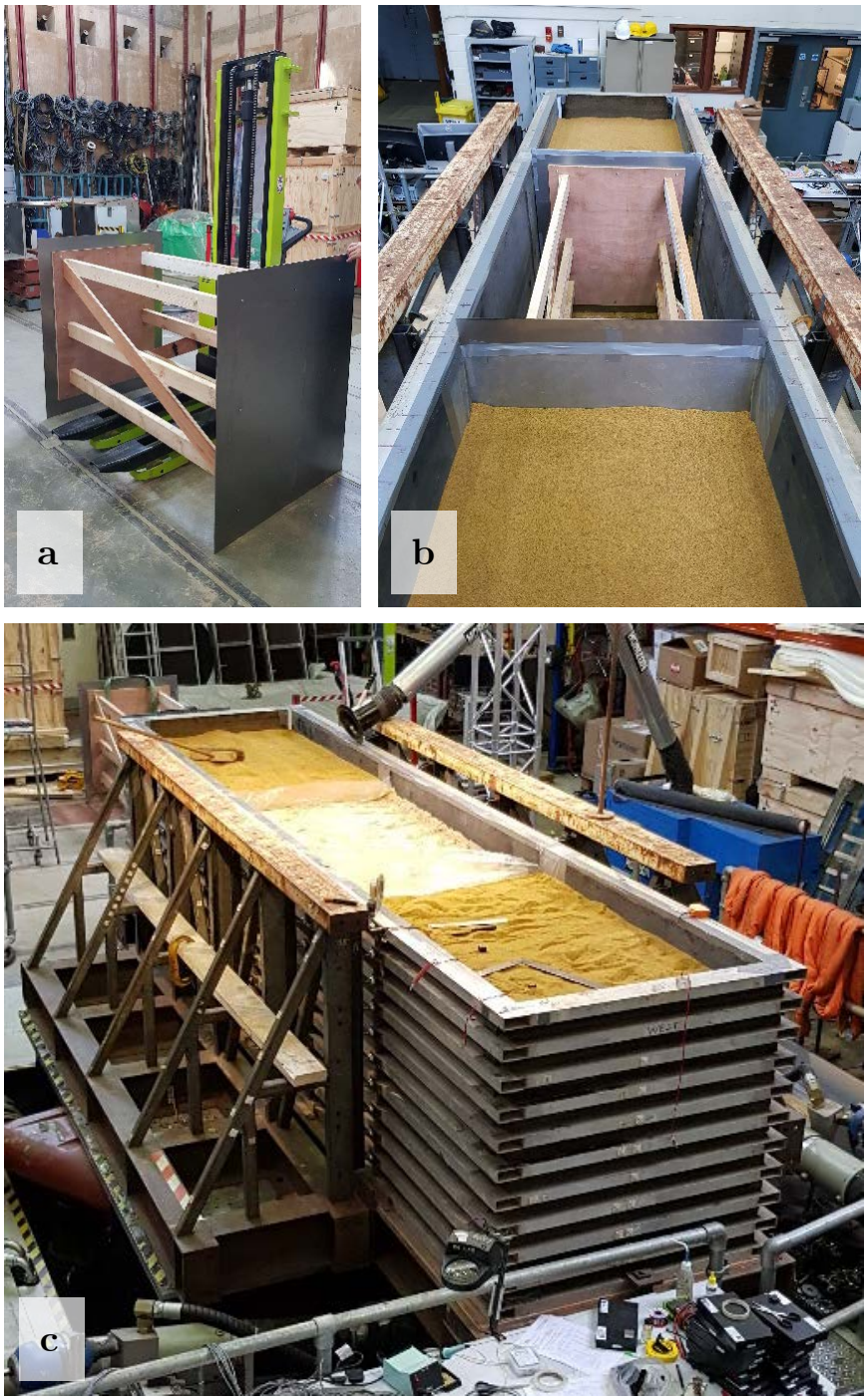

Figure 5-8. (a) Purpose-built auxiliary earth-retaining structure; (b) aspect of the filled with LBB sand side blocks during staged soil deposition; (c) the compound soil mass poured in to pipe bed level.

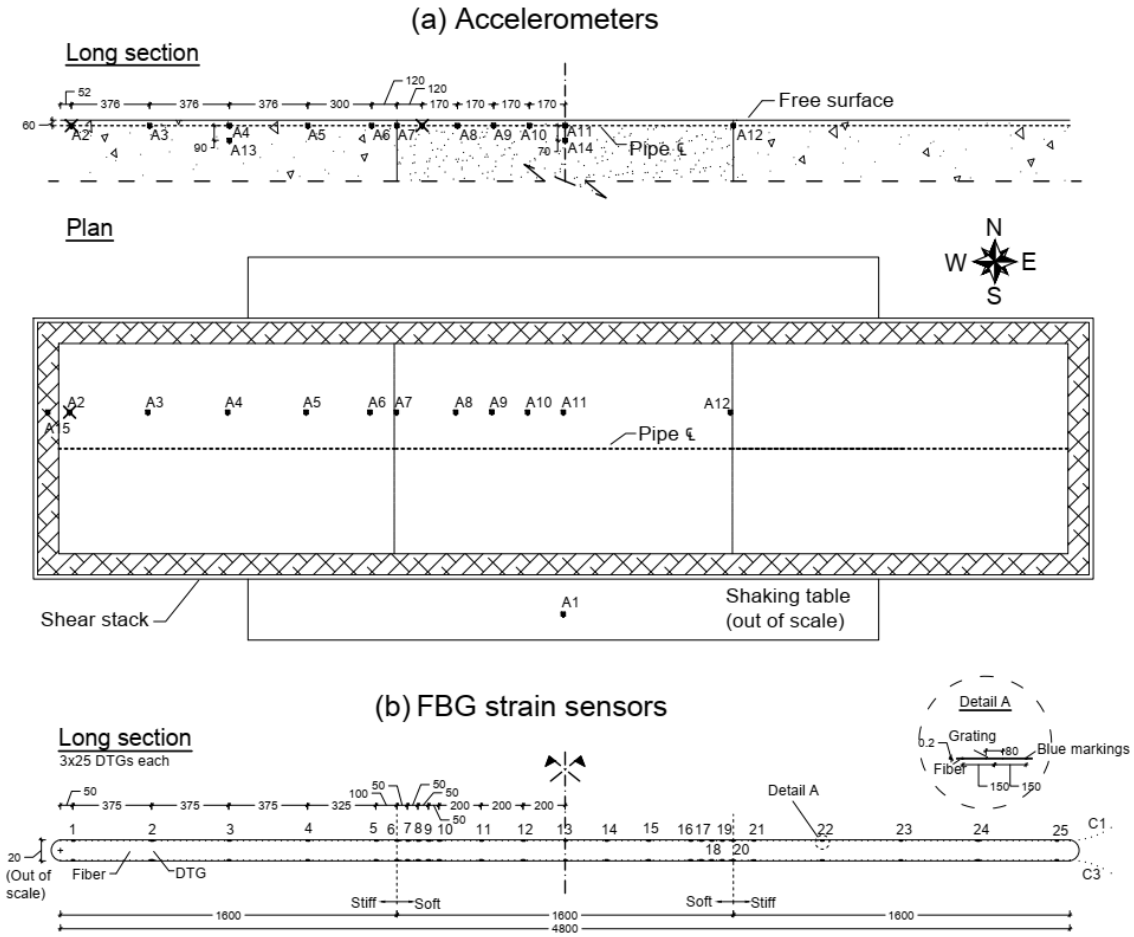

Figure 5-9. (a) Configuration of acceleration transducers in the soil mass and test rig; (b) configuration of fiber optic cables on the pipeline specimen to monitor axial and bending strains

a **b** **c** **d**

Figure 5-10. (a) A DTG cable rolled in its case; (b) DTG cable installed on the crown of the model pipe; (c) SETRA 141A accelerometer; (d) horizontal array of encased accelerometers laid in the test soil

Table 5-4. Details of transducers deployed in the test

Type	Number	Measured parameter	Characteristics	Calibration
Accelerometer SETRA 141A	14	Horizontal free-field and table acceleration	High output linear sensor Operating frequency: 0-3000 Hz Low transverse sensitivity 0.012g/g	1 g/V
Draw Tower Gratings (DTG®) by FBGS Technologies	2×25	Pipeline bending and axial strain	Bare FBG strain sensors in low bend loss fibre; reflectivity >15% Interrogator: Micron Optics si255 (f_{sample} = 1000 Hz)	$1.2/(\Delta\lambda/\lambda)$

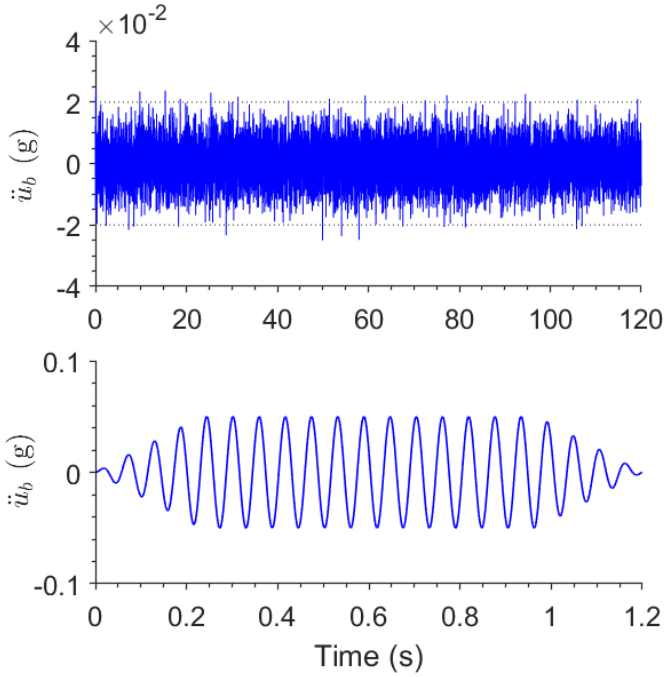

Figure 5-11. Typical Gaussian white noise with $PGA_{RMS} = 0.02$g (top) and sine dwell at $f = 17.4$ Hz (bottom) used as input motions

Table 5-5. Target ground motions used in this study and their properties

ID	Location and year	Station	Magnitude M_w	PGA (g)	Mean period at 1:1 (s)	Time scale factor
1	Italy 2017	AMT	5.4	0.09	0.40	0.2
2	Italy 2016	CSC	5.4	0.06	0.48	0.2
3	Italy 1998	SELE	5.0	0.09	0.36	0.2
4	Italy 2016	AMT	6.2	0.34	0.62	0.2
5	Italy 2016	AMT	6.5	0.44	0.48	0.2
6	Kocaeli 1999	Yarimca	7.6	0.35	1.34	0.1
7	Lefkada 2003	No. 1	6.2	0.42	0.48	0.1

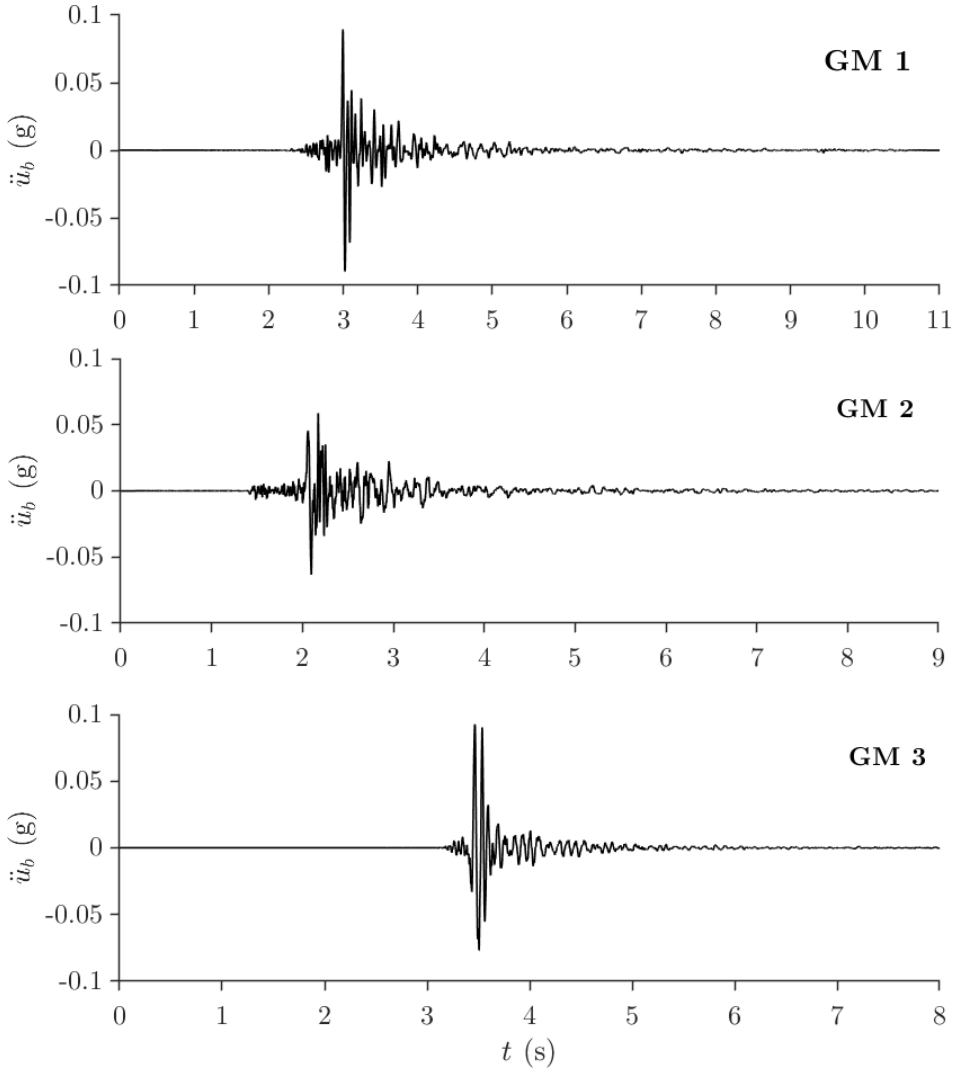

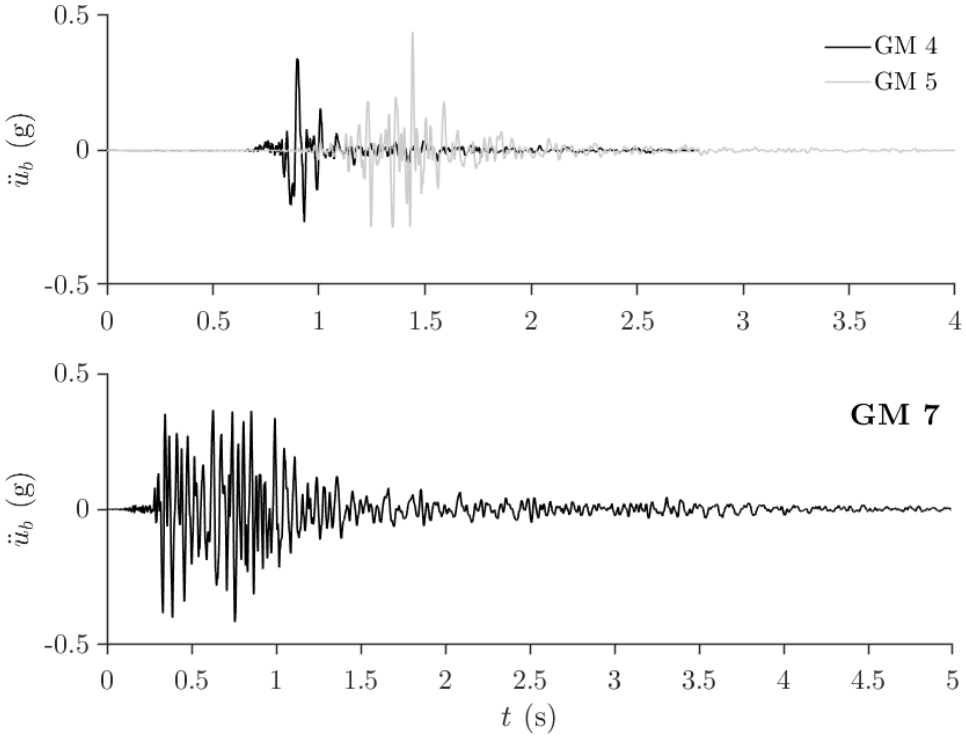

Figure 5-12. Time histories of the target ground motions used in this study

Table 5-6. Recorded and derived peak values of response parameters of interest for all tests

Test ID	Description	Target table PGA (g)	Peak soil $\ddot{u}_g$ (g)	Peak pipe ε_{tot} (με)	Max pipe ε_a (με)	Min pipe ε_a (με)	Peak soil ε_a (με)	Peak soil γ_{xy} (%)
WN1	White noise	0.02						
H01	SD* 85Hz	0.01	0.064	10	7	-8	11	0.003
H02	SD 34Hz	0.01	0.069	9.7	8	-8	20.6	0.01
H03	SD 17Hz	0.01	0.02	8	6	-6	10	0.01
H04	SD 8.7Hz	0.01	0.028	8	7	-6	27	0.05
WN2	White noise	0.02						
H05	SD 85Hz	0.05	0.23	48	25	-10	22	0.01
H06	SD 34Hz	0.05	0.23	26	23	-22	88	0.05
H07	SD 17Hz	0.05	0.05	8	8	-7	21	0.04
H08	SD 8.7Hz	0.05	0.07	9	8	-8	28	0.3
WN3	White noise	0.02						
H09	SD 85Hz	0.1	0.29	13	12	-10	40	0.02
H10	SD 34Hz	0.1	0.36	54	32	-25	155	0.08
H11	SD 17Hz	0.1	0.11	12	10	-9	45	0.08
H12	SD 8.7Hz	0.1	0.14	23	12	-14	80	0.8
WN4	White noise	0.02						
SM01	GM 1	0.068	0.14	13	11	-11	35	0.23
SM02	GM 2	0.063	0.19	19	16	-17	58	0.41
SM03	GM 3	0.0925	0.09	27	14	-7	31	0.24
WN5	White noise	0.02						
SM05	GM 4	0.34	0.42	62	37	-46	332	3
WN7	White noise	0.02						
SM06	GM 5	0.42	0.64	96	78	-72	930	2.3
WN8	White noise	0.02						
SM07	GM 6	0.35	0.44	68	39	-46	248	3.9
SM08	GM 7	0.49	0.57	140	73	-87	821	4.2
WN9	White noise	0.02						

H13	SD 34Hz	0.3	0.58	89	54	-46	407	0.16

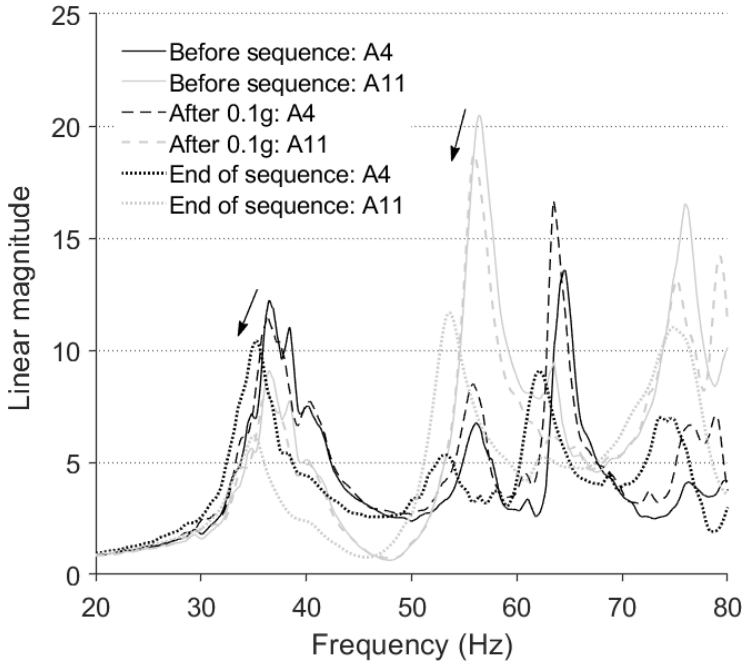

Figure 5-13. Smoothed FRFs, generated from white noise excitation, at surficial recording stations in the LBB and SS blocks, in different phases during the testing sequence; arrows indicate the gradual reduction of modal frequency with shaking intensity

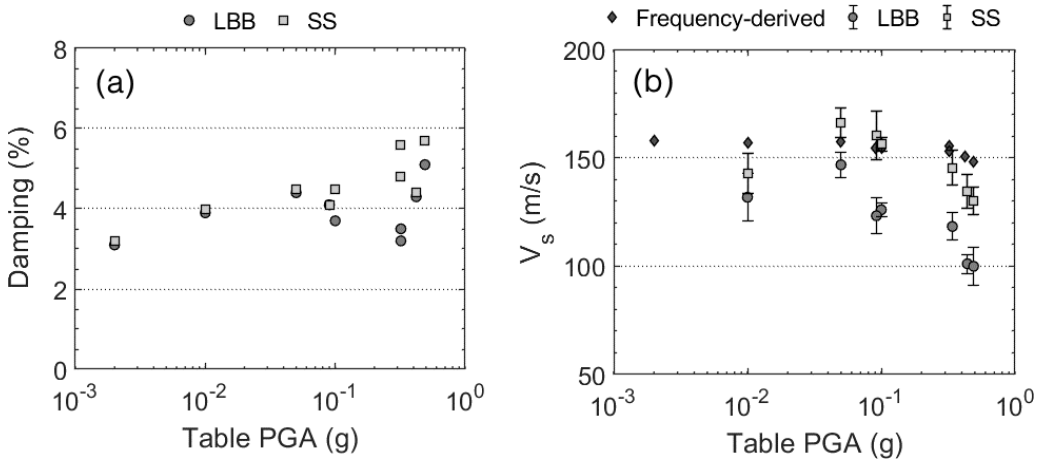

Figure 5-14. (a) Variation of damping ratios of LBB and SS with table excitation level; (b) Variation of mean shear wave velocities of LBB and SS with table excitation level along with standard mean errors; plotted also is the V_s variation of an equivalent laterally uniform 1-D soil column, determined from knowledge of the measured natural frequencies

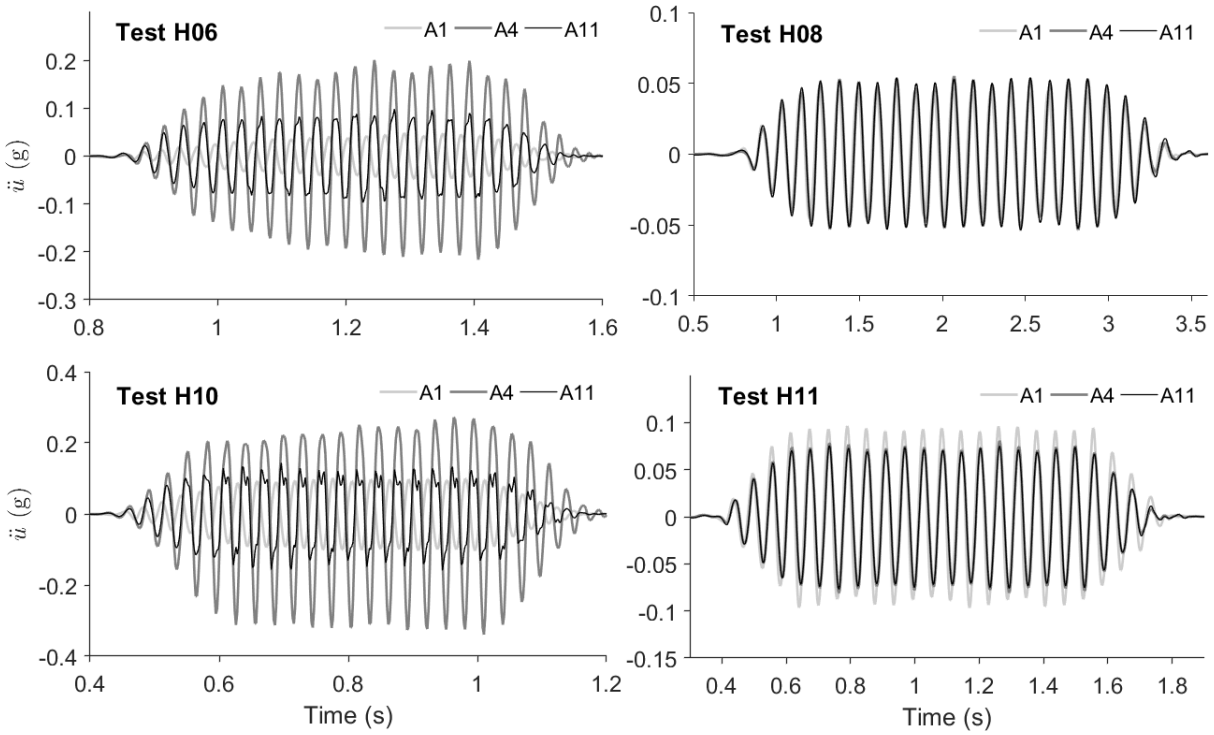

Figure 5-15. Recorded soil acceleration time-histories at surface stations A4 and A11 for different tests

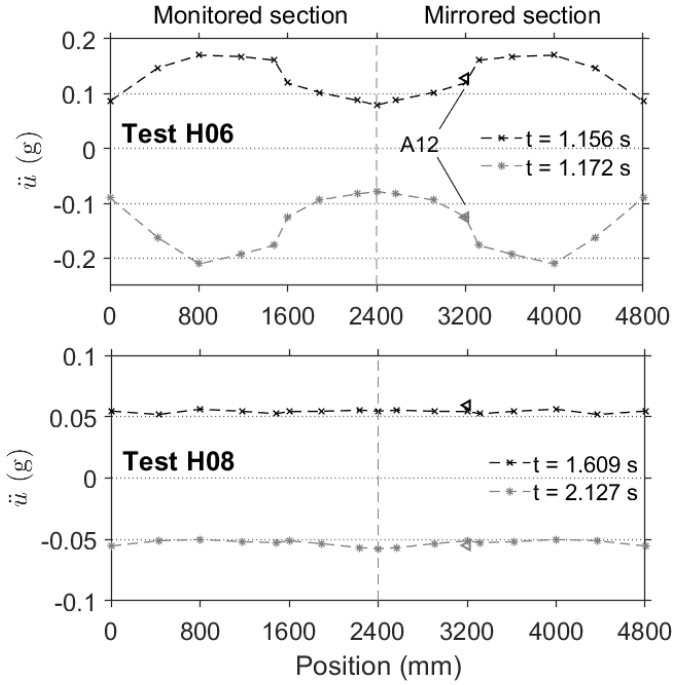

Figure 5-16. Soil acceleration profiles along the horizontal recording array

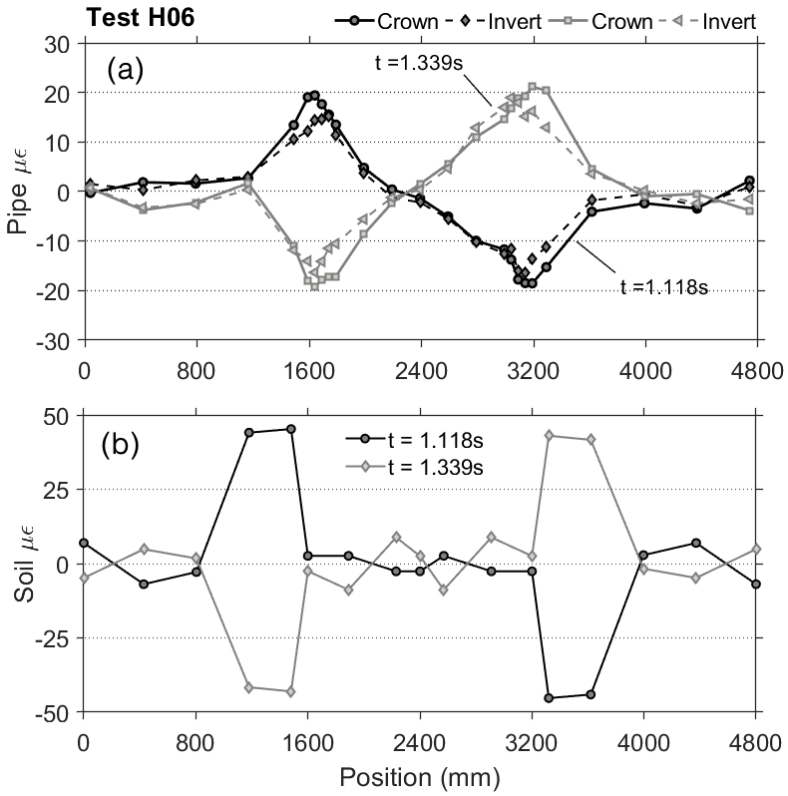

Figure 5-17. (a) Longitudinal profiles of total pipeline strains at extreme fibers; (b) longitudinal profiles of horizontal normal soil strain computed along the accelerometer array

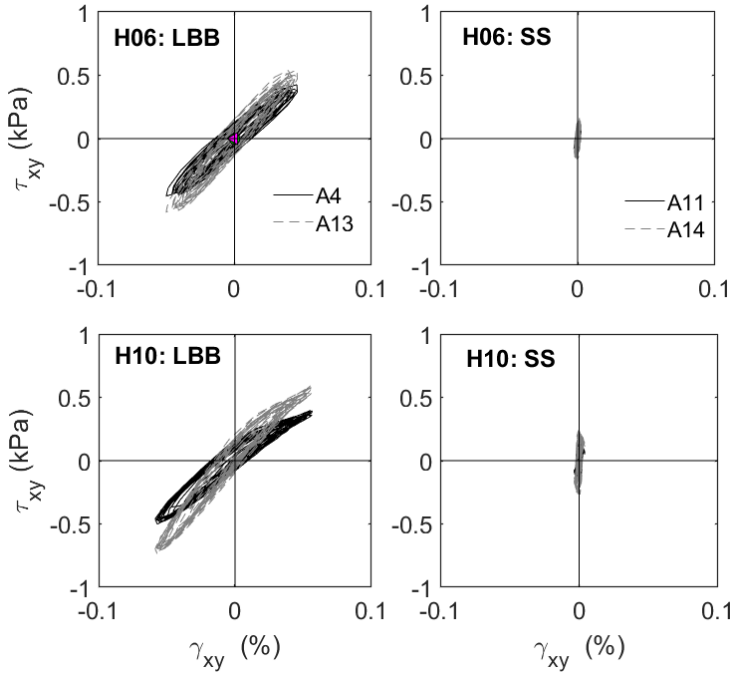

Figure 5-18. Shear stress-strain loops evaluated at stations A4, A13 (LBB) and A11, A14 (SS) for Tests H06 (0.05g) and H10 (0.1g); averaged measures of shear strain histories between the sensors were used (accurate to 1st order)

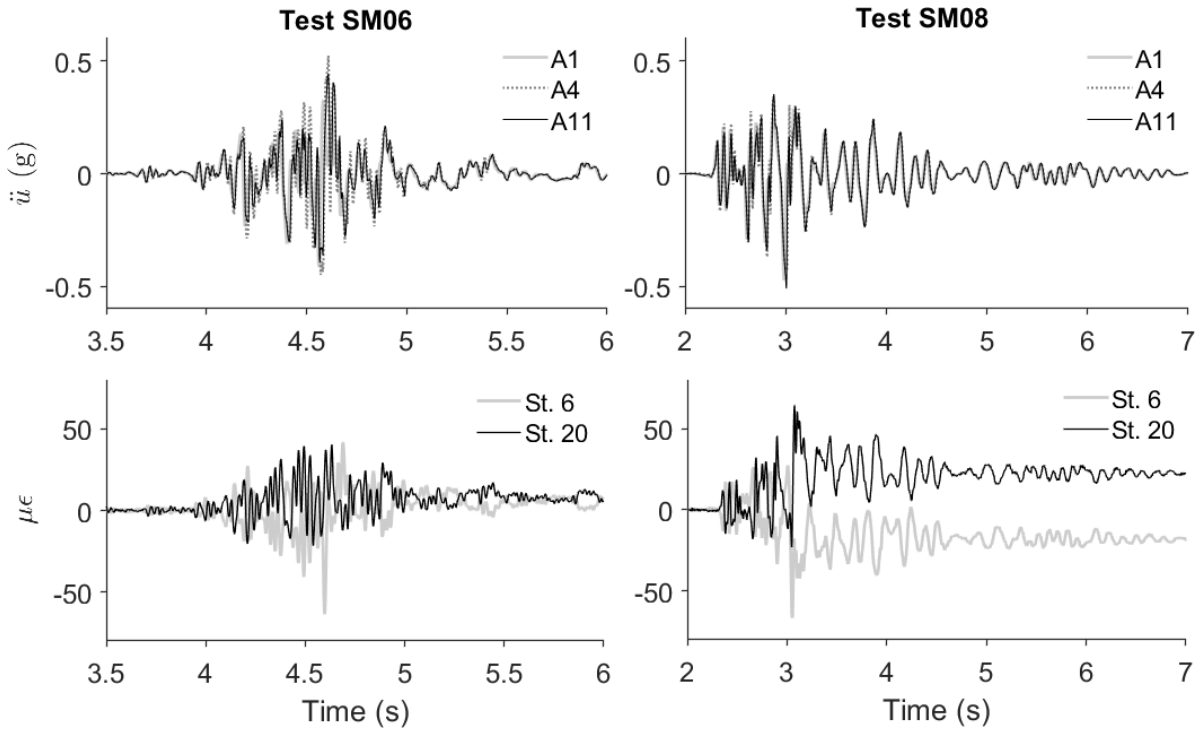

Figure 5-19. Time traces of recorded soil accelerations at surface stations A4, A13 and of axial pipe strains at interface stations 6 and 20, for different broadband table excitations

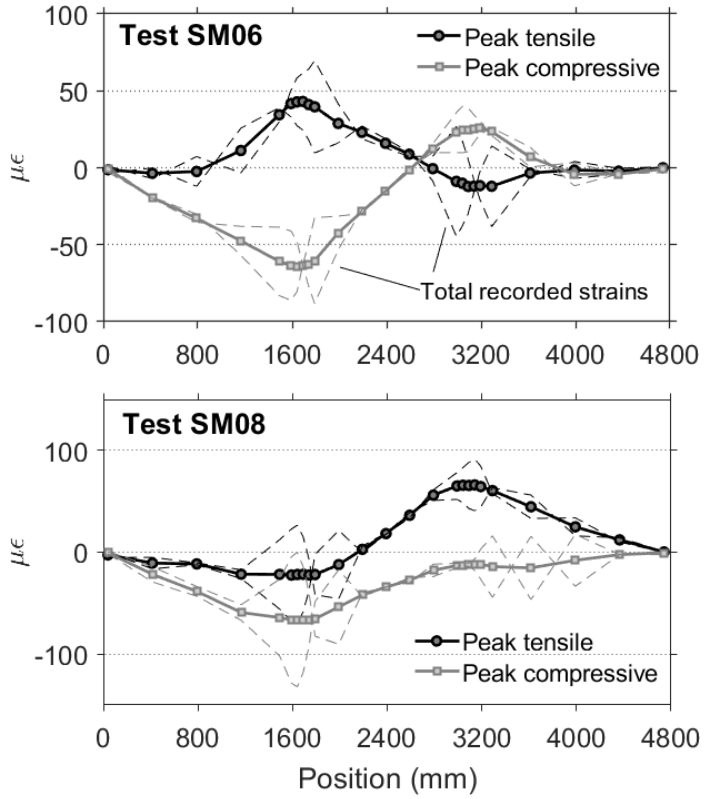

Figure 5-20. Critical tensile and compressive axial strain profiles along the pipeline for different broadband table excitations; shown in dashed lines are the recorded total strains at the crown and invert fibers

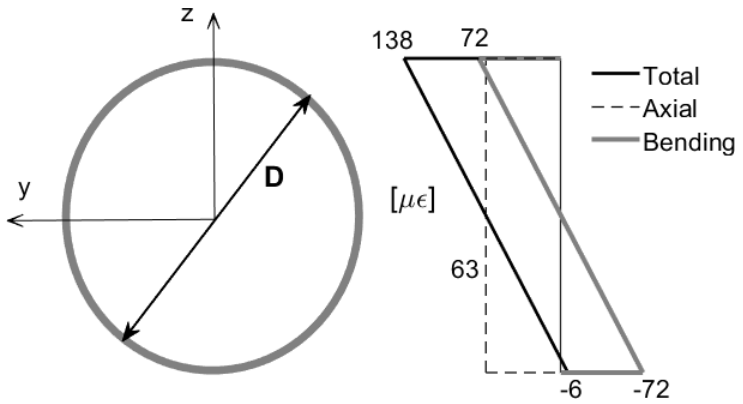

Figure 5-21. Section total, axial and bending pipe strains at St. 6, at the time of the critical compressive profile of Test SM08

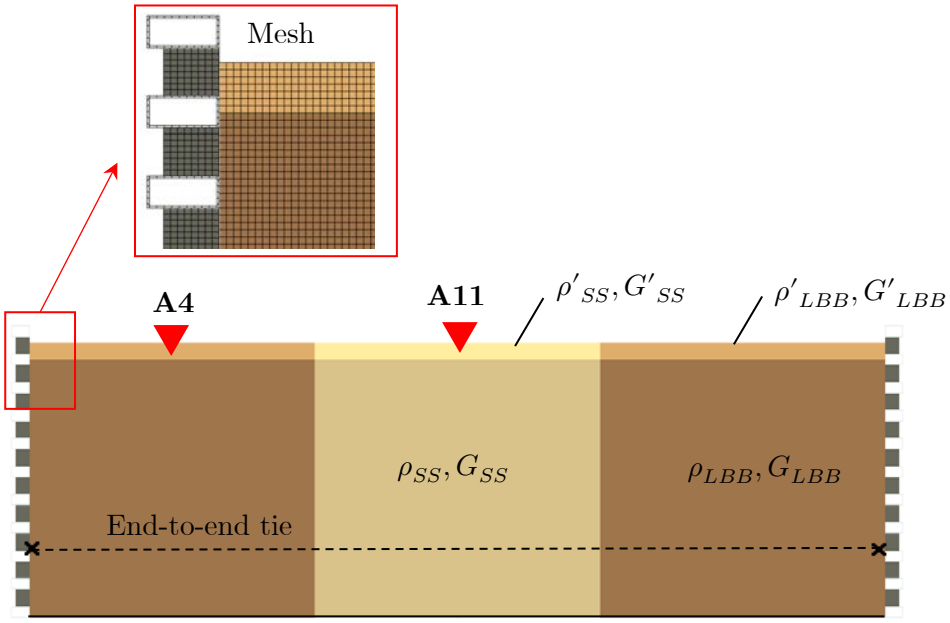

Figure 5-22. Plane strain finite element model of the ESB-soil system

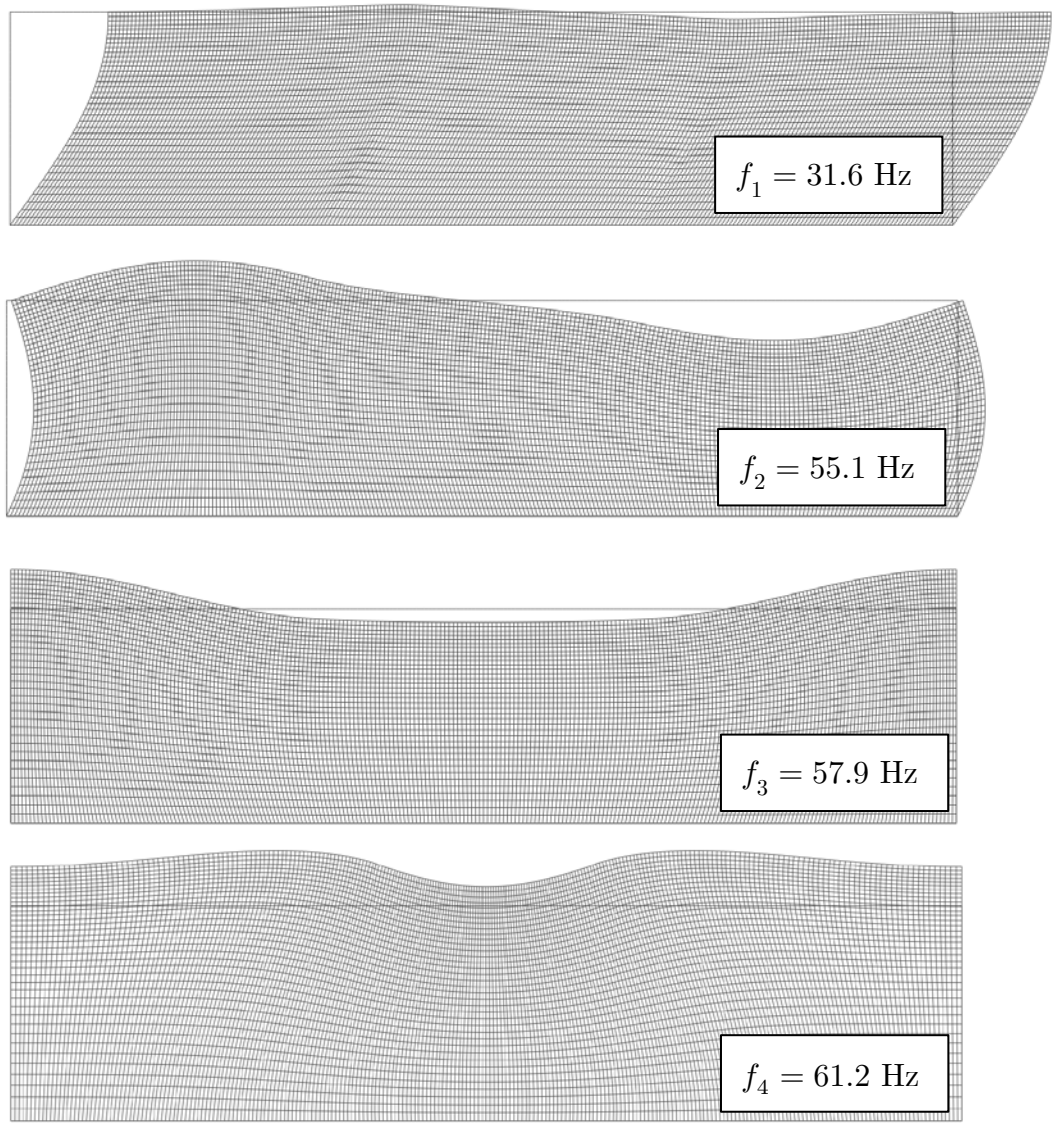

Figure 5-23. The first four computed eigenmodes of the ESB-soil system; scaling of deformation is not consistent across modes

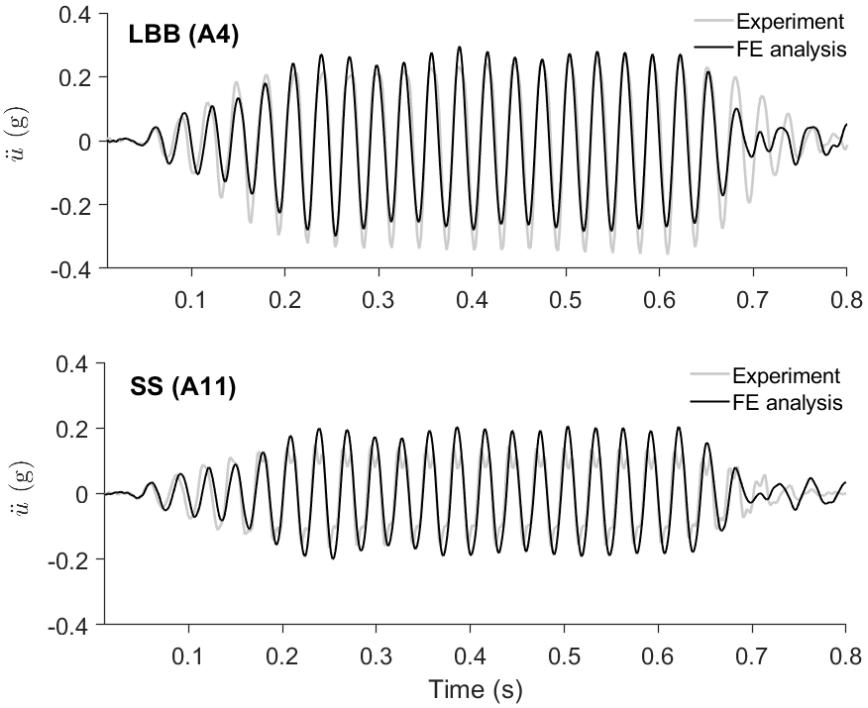

Figure 5-24. Comparison of acceleration response histories in LBB and SS between FE model and the experiment

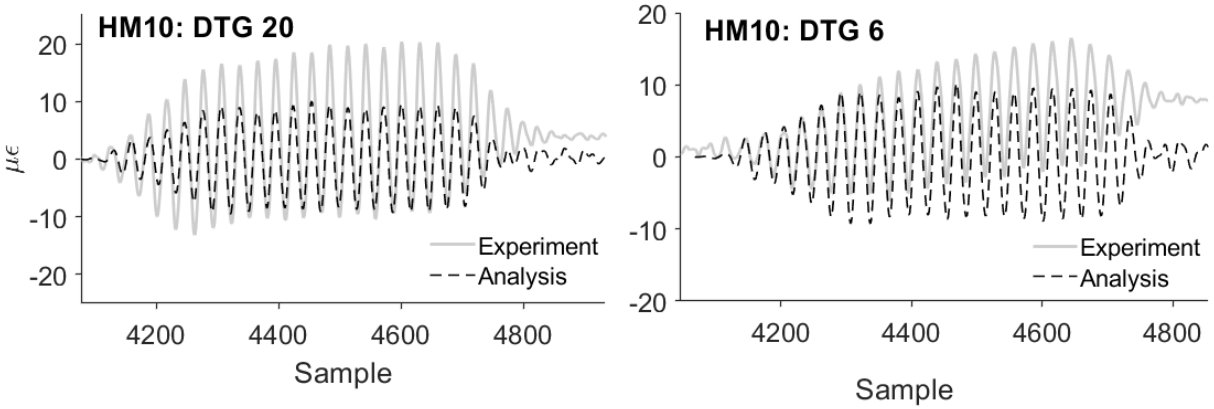

Figure 5-25. Comparison of pipe axial strain histories between FE model and the experiment at two monitoring points

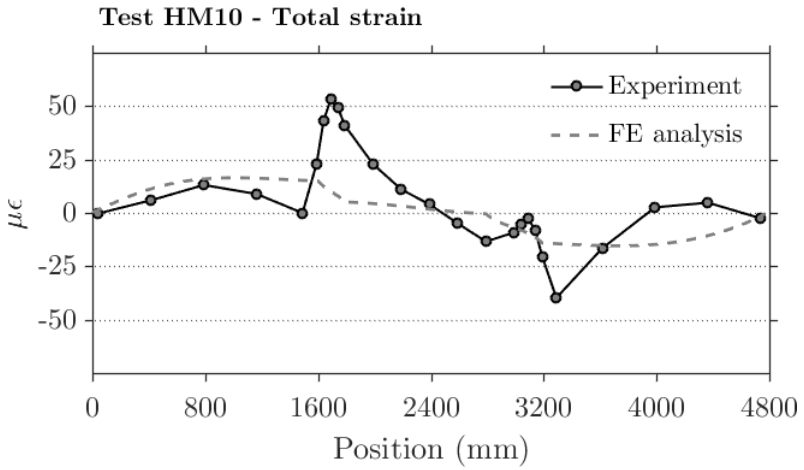

Figure 5-26. Total longitudinal strain profiles along the pipe from test HM10 and respective FE model, taken at the time of peak strain

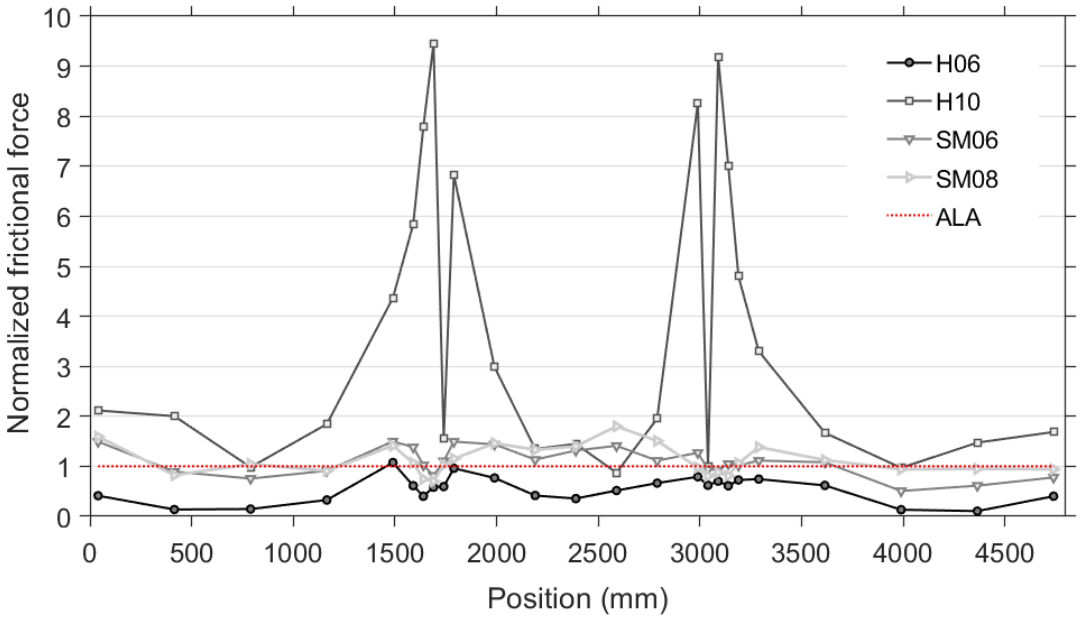

Figure 5-27. Variation of back-calculated frictional force per unit length along the pipeline from different tests, normalized with respect to the frictional resistance recommended by the ALA guideline

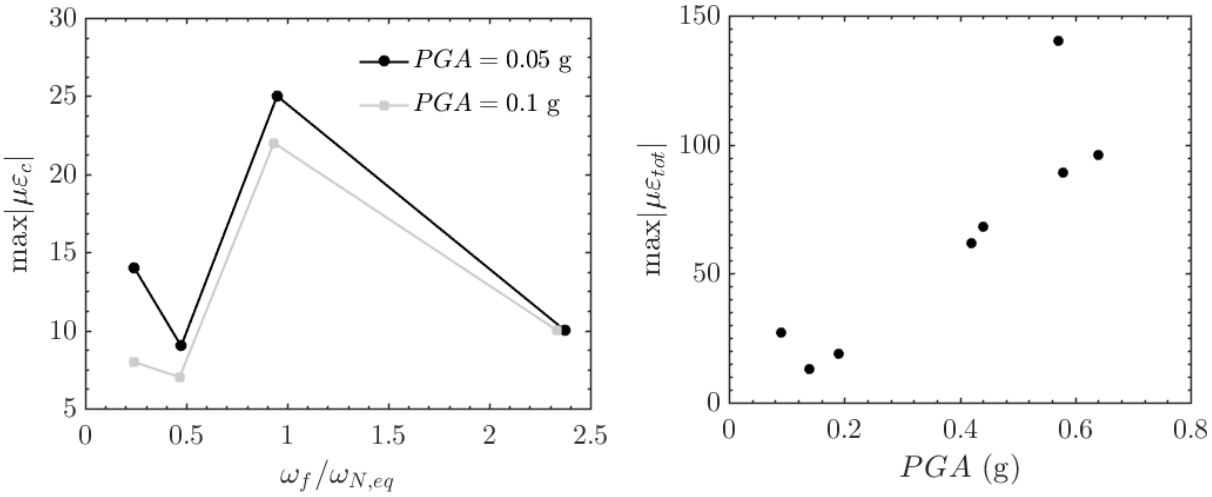

Figure 5-28. Left: variation of peak compressive axial pipe strain with normalised site frequency; right: variation of peak total pipe strain with soil surface *PGA*

Chapter 6

Conclusions

This thesis investigated the behaviour of buried gas pipelines in laterally inhomogeneous soil subjected to earthquake ground shaking. The dynamic SPI problem was approached through numerical simulation in Chapters 3 and 4 and experiment in Chapter 5. Emphasis was always placed on the identification of buckling failures. A rigorous FEM-based methodology was developed, suitable to determine the response of the soil-pipe system at three levels, the site level, the SPI level, and the pipeline level, accounting for salient aspects such as soil nonlinearity under strong shaking, nonlinear SPI effects, large deformation and material plasticity. The experimental campaign was designed to physically model at small scale the dynamic SPI in the case of a gas transmission pipeline cutting through a three-block configuration of cohesionless soil and subject to vertically propagating shear waves.

6.1 Key findings

- Lateral soil inhomogeneities along a pipeline alter significantly its response to seismic ground shaking compared to the case of uniform ground.

- In Site 1 soil structures, the maximum compressive strain develops very close to the separating interface, with values from as low as 0.01% to as high as 0.15%. Considerable vertical motions are also generated at the surface. The critical load pattern for a pipeline running through Site 1 is a combination of out-of-phase horizontal soil displacements in a step pattern and a localized uplift component inside the transition zone.

- In Site 2 valley-type scenarios, the axial strain field at the surface is antisymmetric and is dominated by local wave scattering inside the valley, predominantly Rayleigh waves trapped inside the valley. The absolute peaks occur above the wedge toes and range roughly from 0.01% to 0.11%. A pipeline buried in such a site would be subjected simultaneously to compression and tension along successive segments.

- The peak axial ground strains were found to depend mainly on (i) the impedance contrast of the soil deposits in contact and (ii) the resonant frequencies which greatly amplify oscillations. The absolute stiffness of the deposits is also a critical parameter, as the softer soils experience consistently larger deformations. The worst-case soil deformations are obtained for a combination of large impedance ratios, soft soil deposits and long-period input motions.

- When considering nonlinearity in the soil response under strong input motions, the induced axial ground strains were computed to be as much as two orders of magnitude larger (up to ~15%) than under weak input motions, a difference explained by the sharp decrease of the G-modulus with increasing cyclic shear strain. This level of strain is overestimated by the equivalent-linear soil model as is unlikely to occur in nature. This effect is more pronounced in Site 1, where the surface strain distribution peaks sharply at the boundary of the two soils.

- Neither of the two baseline pipeline models experienced failure on application of the critical soil displacement profiles from Site 1 and 2. Nevertheless, both responded in the inelastic regime and significant stress concentrations were computed near the soil block interface; considerable bending deformations were also present within the ground uplift zone, more so for the thinner TG pipeline. Section ovalisation was found to be appreciable, but within code-prescribed limits.

- The load-deformation analysis up to pipeline failure revealed profound differences between the responses of TG, an intermediate R/t_w buried steel pipe, and TAP, a thick one. Specifically, TG exhibited snap-through buckling at a load

23% larger than the nominal applied load, resulting to two sharp local buckles within the critical zone of loading. The interaction between axial load and bending moment at the worst affected section was strong in this case. TAP on the other hand experienced a sudden drop in axial load shortly after the first yield, and its response was dominated by bending, characterised by initially uniform and later localised ovalisation at a load too high to be met in reality.

- In terms of soil-pipe contact, a highly non-uniform contact state is anticipated. Soil and pipe slip against each other for the most part off the critical zone as the yield relative displacement is generally very small. Therefore, shear stresses are transferred from soil to pipe over a large surface and this contributes to the development of large internal axial force. Both pipelines were too stiff to conform to the soil uplift pattern, and for this reason gaps formed mainly over the top side.

- It was found that the Eurocode 8 no-buckling axial strain limit captures best the critical buckling condition of the examined (perfect) pipeline under combined P–M load when considering average pipe strains. The respective thresholds by ALA and JGA are judged perhaps overly conservative, with the latter being theoretically unfounded. However, further investigation is required for the case of pipelines with imperfections, where the critical buckling strain is expected to be lower than this for the perfect case.

- Generally, circumstances favouring the onset of instabilities in a buried gas pipeline crossing inhomogeneous soil are identified as the following:

  - relatively high R/t_w (≥ 30)
  - large initial shell imperfections
  - high interface COF (≥ 0.6)
  - spiked ground load profiles, especially those with a vertical component of the same order of magnitude with the axial (along the pipe) component
  - low pressures

- absence of any restraints along the pipeline

Buckling instabilities were found to occur at differential axial soil movements of 15 to 25 cm combined with local uplifts of 4 to 12 cm.

- When combinations of the above conditions are present for a buried gas pipeline crossing inhomogeneous soil, it is recommended that earthquake loads shall be a consideration for design. In such cases, mitigating measures can be in the form of either friction reduction, e.g., use of smooth coatings or geosynthetic wrapping around the pipe strategically, or pipe strengthening, e.g., increase of wall thickness or steel grade (Gantes and Melissianos, 2016).

- The state of deformation in the system as measured in the experiments was similar to that computed numerically for Site 2, the difference being that the stiffness patterns were reversed. Alternating compression-extension zones develop in the pipeline very close to the soil block boundaries, following the ground deformation pattern, while non-shear ground deformation remains negligible far from those interfaces. This anti-symmetric strain pattern is a result of the varying horizontal free-field motion amplification and vertical ground vibrations associated primarily with higher modes, which mobilize increased frictional stresses on the pipe walls.

- For a given inhomogeneous site, pipeline strain magnitudes are governed by resonance effects on the site response. Peak strains were recorded when the central excitation frequency approached a modal frequency of the soil in agreement with the conclusions of Chapter 3. The induced strains increased notably also with surface PGA.

- Bending strains in the pipeline became considerable at stronger excitations, amounting up to 50% of the total strains. This is an indication of vertical-flexural ground modes becoming active at higher exciting frequencies, forcing the pipe to bend near the stiffness transition zones.

- The recorded site surface response was sufficiently reproduced with a relatively simple plane-strain FE model; however, a beam-on-springs model with ALA springs was unable to predict well the pipe strain response, especially close to the stiffness transitions zones. This was attributed mainly to the inability of the axial springs to capture the large increment in frictional strength offered by the increased confinement in these zones, which allows transfer of additional contact shear stresses to the pipe.

- Extrapolation of the results to full scale confirms that the prototype would accommodate the scaled-up strains of 0.1% without yielding. However, the achieved test conditions did not reflect particularly unfavourable circumstances for the pipeline. Subtle variations in configuration, such as a higher soil stiffness ratio and a higher interface COF, can incur a more critical deformation regime in the pipeline as predicted from the numerical models.

- The additional value of the original test data presented here lies in their potential to be used for validation purposes of more advanced analytical or numerical models of seismic soil-pipe interaction.

6.2 Suggestions for future research

Although efforts were made to cover as many different aspects of the problem as possible, there is still room for further research in several domains, some of which are identified below.

- Only two generic site types were considered here. Examination of other possible types of soil inhomogeneity or even real sites mapped using data from ground investigations would greatly increase the value of this study. Also, it would be useful to investigate the effect of additional soil parameters on the seismic ground motion at pipe level, such as pore water pressure.

- The nonlinear behavior of the soil was considered in an approximate—yet acceptable—way. It is recommended to enhance the proposed numerical methodology by using elastoplastic soil constitutive models calibrated from field or test data. This could furnish a thorough comparison with the equivalent-linear model used exclusively here.

- Different pipe settings and configurations other than the straight case considered here can be studied in future research (e.g., connections to compressor stations, elbows etc).

- Although the numerical methodology presented is rigorous enough, it is far from practical to use in day-to-day practice or for rapid assessments. For this reason, future research could focus on developing a low-order mechanical model based on mass-spring-dashpot assemblies that can capture the nonlinear dynamic response of laterally inhomogeneous sites. This, when coupled with a suitable BDWF model or a more accurate shell model of the pipe, could capture the key features of the pipeline response.

- It would be interesting to obtain analytical failure envelopes of typical steel pipe sections under P–M interaction. This could be done either through detailed numerical simulations of shells under axial loads applied with varying eccentricity, or through quasi-static experiments. Then, given a pair of P–M values, one could determine if the pipeline buckles or not.

Bibliography

Abrahamson, N. A. *et al.* (1987) 'The SMART I Accelerograph Array (1980-1987): A Review', *Earthquake Spectra*, 3(2), pp. 263–287. doi: 10.1193/1.1585428.

Achenbach, J. D. (1973) *Wave Propagation in Elastic Solids*. North-Holland Publishing Company (Applied Mathematics and Mechanics Series). Available at: https://books.google.co.uk/books?id=jQFAAQAAIAAJ.

Akiyoshi, T. and Fuchida, K. (1988) 'Seismic Response of Pipeline Systems Buried in Dipping Soil Layers', in *Proc. 9th World Conference on Earthquake Engineering*. Tokyo-Kyoto, Japan.

American Society of Civil Engineers (2001) *Guideline for the Design of Buried Steel Pipe*.

American Society of Mechanical Engineers (2004) *ASME B31.8: Gas Transmission and Distribution Piping Systems*. doi: 10.1520/G0154-12A.

Anastasopoulos, I. *et al.* (2011) 'Simplified Constitutive Model for Simulation of Cyclic Response of Shallow Foundations: Validation against Laboratory Tests', *Journal of Geotechnical and Geoenvironmental Engineering*, 137(12), pp. 1154–1168. doi: 10.1061/(ASCE)GT.1943-5606.0000534.

Ando, H., Sato, S. and Takagi, N. (1992) 'Seismic Observation of a Pipeline Buried at the Heterogeneous Ground', *Proceedings of the Tenth World Conference on Earthquake Engineering*, pp. 5563–5567.

ArcelorMittal (2013) 'High yield SAW welded Pipe API 5L grade X65 PSL 2'. ArcelorMittal, pp. 5–6.

ASCE Technical Council on Lifeline Earthquake Engineering (1984) *Guidelines for the seismic design of oil and gas pipeline systems*. New York, N.Y.: American Society of Civil Engineers.

Assimaki, D., Kausel, E. and Gazetas, G. (2005) 'Wave propagation and soil-structure interaction on a cliff crest during the 1999 Athens Earthquake', *Soil Dynamics and Earthquake Engineering*, 25(7–10), pp. 513–527. doi: 10.1016/j.soildyn.2004.11.031.

Audibert, J. M. E. and Nyman, K. J. (1977) 'Soil Restraint Against Horizontal Motion Of Pipes', *ASCE J Geotech Eng Div*, 103(10), pp. 1119–1142.

Bard, P.-Y. and Bouchon, M. (1980) 'The seismic response of sediment-filled valleys. Part 2. The case of incident P and SV waves', *Bulletin of the Seismological Society of America*, 70(5), pp. 1921–1941. Available at: http://www.bssaonline.org/content/70/5/1921.abstract.

Bardi, F. C. and Kyriakides, S. (2006) 'Plastic buckling of circular tubes under axial compression—part II: Analysis', *International Journal of Mechanical Sciences*, 48(8), pp. 830–841. doi: 10.1016/j.ijmecsci.2006.03.005.

Bardi, F C and Kyriakides, S. A. (2006) 'Plastic buckling of circular tubes under axial compression — part I : Experiments', 48, pp. 830–841. doi: 10.1016/j.ijmecsci.2006.03.005.

Batterman, S. C. (1983) 'Plastic buckling of axially compressed circular cylindrical shells', *Thin-Walled Structures*, 1(2), pp. 139–163. doi: 10.1016/0263-8231(83)90018-6.

Bielak, J. *et al.* (2003) 'Domain Reduction Method for Three-Dimensional Earthquake Modeling in

Localized Regions, Part I: Theory', *Bulletin of the Seismological Society of America*, 93(2), pp. 817 LP – 824. Available at: http://www.bssaonline.org/content/93/2/817.abstract.

Brazier, L. G. (1927) 'On the Flexure of Thin Cylindrical Shells and Other "Thin" Sections', *Proceedings of the Royal Society of London. Series A*, 116(773), pp. 104 LP – 114. Available at: http://rspa.royalsocietypublishing.org/content/116/773/104.abstract.

Brennan, A. J., Thusyanthan, N. I. and Madabhushi, S. P. (2005) 'Evaluation of Shear Modulus and Damping in Dynamic Centrifuge Tests', *Journal of Geotechnical and Geoenvironmental Engineering*, 131(12), pp. 1488–1497. doi: 10.1061/(ASCE)1090-0241(2005)131:12(1488).

Brumund, W. and Leonards, G. (1973) 'Experimental Study of Static and Dynamic Friction Between Sand and Typical Constuction Materials'.

Bushnell, D. (1976) 'BOSOR5-PROGRAM FOR BUCKLING OF ELASTIC-PLASTIC COMPLEX SHELLS OF REVOLUTION INCLUDING LARGE DEFLECTIONS AND CREEP', *Computers & Structures*, 6(3), pp. 221–239.

Bushnell, D. (1982) 'Plastic Buckling', in Zamrik, S. Y. and Dietrich, D. (eds) *Pressure Vessels and Piping: Design Technology - A Decade of Progress*. New York, N.Y.: The American Society of Mechanical Engineers, pp. 47–117.

Castro, S. G. P. *et al.* (2014) 'Geometric imperfections and lower-bound methods used to calculate knock-down factors for axially compressed composite cylindrical shells', *Thin-Walled Structures*. Elsevier, 74, pp. 118–132. doi: 10.1016/j.tws.2013.08.011.

Cavallaro, A., Maugeri, M. and Mazzarella, R. (1992) 'Static and Dynamic Properties of Leighton Buzzard Sand From Laboratory Tests', (1), pp. 1–6. doi: 10.1007/BF01179416.

Chaloulos, Y. K. *et al.* (2015) 'Lateral soil-pipeline interaction in sand backfill: Effect of trench dimensions', *Computers and Geotechnics*, 69, pp. 442–451. doi: 10.1016/j.compgeo.2015.05.014.

Chaloulos, Y. K., Bouckovalas, G. D. and Karamitros, D. K. (2017) 'Trench effects on lateral p-y relations for pipelines embedded in stiff soils and rocks', *Computers and Geotechnics*. Elsevier Ltd, 83, pp. 52–63. doi: 10.1016/j.compgeo.2016.10.018.

Chanerley, A. A. and Alexander, N. A. (2007) 'Correcting data from an unknown accelerometer using recursive least squares and wavelet de-noising', *Computers and Structures*, 85(21–22), pp. 1679–1692. doi: 10.1016/j.compstruc.2007.02.025.

Chen, C. C., Ariman, T. and Lee, L. H. N. (1980) 'Buckling Analysis of Buried Pipelines Under Seismic Loads', in *Proc. 7th European Conf. Earthq. Engng*, pp. 249–256.

Chidichimo, A. *et al.* (2014) '1-g Experimental investigation of bi-layer soil response and kinematic pile bending', *Soil Dynamics and Earthquake Engineering*. Elsevier, 67, pp. 219–232. doi: 10.1016/j.soildyn.2014.07.008.

Corona, E. and Kyriakides, S. (1988) 'On the collapse of inelastic tubes under combined bending and pressure', *International Journal of Solids and Structures*. Pergamon Press Ltd., 24(5), pp. 505–535. doi: 10.1016/0020-7683(88)90005-4.

Crewe, A. J. *et al.* (1995) 'Development of a large flexible shear stack for testing dry sand and simple direct foundations on a shaking table', in Elnashai, A. S. (ed.) *European Seismic Design Practice, Research and Application: Proc. Fifth SECED Conference, Chester UK*. Balkema, pp. 163–168.

Crisfield, M. A. (1981) 'A fast incremental/iterative solution procedure that handles "snap-through"', *Computers & Structures*, 13, pp. 55–62.

Daiyan, N. *et al.* (2011) 'Investigating pipeline–soil interaction under axial–lateral relative movements

in sand', *Canadian Geotechnical Journal*, 48, pp. 1683–1695. doi: 10.1139/t11-061.

Darendeli, M. B. (2001) 'Development of a new family of normalized modulus reduction and material damping curves'. [Austin, Tex.]: [University of Texas]. Available at: https://repositories.lib.utexas.edu/bitstream/handle/2152/10396/darendelimb016.pdf.

Dassault Systèmes (2014a) 'ABAQUS'. Providence, RI: Dassault Systèmes, Inc.

Dassault Systèmes (2014b) 'ABAQUS 6.14 Analysis User's Guide', *ABAQUS 6.14 Analysis User's Guide*. Providence, RI: Dassault Systèmes, Inc., p. 946.

Demirci, H. E. *et al.* (2018) 'Experimental and numerical modelling of buried pipelines crossing reverse faults', *Soil Dynamics and Earthquake Engineering*. Elsevier Ltd, 114(June), pp. 198–214. doi: 10.1016/j.soildyn.2018.06.013.

Deodatis, G. and Shinozuka, M. (1989) 'Simulation of Seismic Ground Motion Using Stochastic Waves', *Journal of Engineering Mechanics*, 115(12), pp. 2723–2737.

Donnell, L. H. (1933) *Stability of Thin-Walled Tubes Under Torsion*, *NACA Technical Report 479*. Pasadena, CA. doi: 10.1097/00152192-198911000-00004.

European Committee for Standardization (2006) *EN 1998-4 Eurocode 8: Design of structures for earthquake resistance — Part 4: Silos, tanks and pipelines*. Brussels: CEN.

Fioravante, V. (2002) 'On the shaft friction modelling of non-displacement piles in sand', *Soils and Foundations*, 42(2), pp. 23–33. doi: 10.3208/sandf.42.2_23.

Fiorentino, G. *et al.* (2019) 'Shaking Table Tests on an Integral Abutment Bridge Model: Preliminary Results', in Papadrakakis, M. and Fragiadakis, M. (eds) *COMPDYN 2019, 7th International Conference on Computational Methods in Structural Dynamics and Earthquake Engineering*.

Folga, S. M. (2007) 'Natural Gas Pipeline Technology Overview', *Environmental Science Division*. doi: ANL/EVS/TM/08-5.

Galimov, K. Z. and Mushtari, K. M. (1961) *NON-LINEAR THEORY OF THIN ELASTIC SHELLS*.

Gantes, C. J. and Melissianos, V. E. (2016) 'Evaluation of Seismic Protection Methods for Buried Fuel Pipelines Subjected to Fault Rupture', *Frontiers in Built Environment*, 2(December). doi: 10.3389/fbuil.2016.00034.

Gelagoti, F. *et al.* (2010) 'Seismic wave propagation in a very soft alluvial valley: Sensitivity to ground-motion details and soil nonlinearity, and generation of a parasitic vertical component', *Bulletin of the Seismological Society of America*, 100(6), pp. 3035–3054. doi: 10.1785/0120100002.

Gresnigt, A. (1986) 'Plastic design of buried steel pipes in settelement areas', *HERON*. HERON, 4(31), pp. 1–113.

Hall, W. J. and Newmark, N. M. (1977) 'SEISMIC DESIGN CRITERIA FOR PIPELINES AND FACILITIES.', pp. 18–34.

Hamada, M., O'Rourke, T. and Yoshizaki, K. (2000) 'Large Deformation Behavior of Low-Angle Pipeline Elbows Subjected To In-Plane Bending', *Proc. 12th World Conference on Earthquake Engineering, Auckland, New Zealand*, Paper No., pp. 1–8.

Hardin, B. O. and Drnevich, V. P. (1972) 'Shear Modulus and Damping in Soils: Design Equations and Curves', *Soil Mechanics and Foundations Division*, (SM7), pp. 667–692. doi: 10.1017/S000748530002229X.

Hashash, Y. M. A. *et al.* (2016) 'DEEPSOIL 6.1, User Manual'.

Hatzigeorgiou, G. D. and Beskos, D. E. (2010) 'Soil–structure interaction effects on seismic inelastic analysis of 3-D tunnels', *Soil Dynamics and Earthquake Engineering*. Elsevier, 30(9), pp. 851–861. doi: 10.1016/j.soildyn.2010.03.010.

Hindy, A. and Novak, M. (1979) 'Earthquake response of underground pipelines', *Earthquake Engineering & Structural Dynamics*, 7, pp. 451–476.

El Hmadi, K. and O'Rourke, M. (1988) 'Soil Springs for Buried Pipeline Axial Motion', *Journal of Geotechnical Engineering*, 114(11), pp. 1335–1339.

Housner, G. W. and Jennings, P. C. (1972) 'The San Fernando California Earthquake', *Earthquake Engineeirng and Structural Dynamics*, 1(August 1971), pp. 5–31. doi: 10.1002/eqe.4290010103.

Hsu, T., Chen, Y. and Wu, C. (2001) 'Soil Friction Restraint of Oblique Pipelines in Loose Sand', *Journal of Transportation Engineering*. American Society of Civil Engineers, 127(1), pp. 82–87. doi: 10.1061/(ASCE)0733-947X(2001)127:1(82).

Hudson, M., Idriss, I. and Beikae, M. (1994) 'QUAD4M: a computer program to evaluate the seismic response of soil structures using finite element procedures and incorporating a compliant base', *Center for Geotechnical Modeling, Department of Civil and Environmental Engineering, University of California, Davis, CA*, (January). Available at: http://nisee.berkeley.edu/elibrary/Text/200606152.

Hutchinson, J. W. (1973) 'Post-bifurcation behavior in the plastic range', *Journal of the Mechanics and Physics of Solids*, 21(3), pp. 163–190. doi: 10.1016/0022-5096(73)90017-3.

Hutchinson, J. W. and Budiansky, B (1976) 'Analytical and Numerical Study of the Effects of Initial Imperfections on the Inelastic Buckling of a Cruciform Column', in Budiansky, Bernard (ed.) *Buckling of Structures*. Berlin, Heidelberg: Springer Berlin Heidelberg, pp. 98–105.

International Energy Agency (2015) *World energy outlook 2015*.

Jalali, H. H. *et al.* (2016) 'Experimental and finite element study of the reverse faulting effects on buried continuous steel gas pipelines', *Soil Dynamics and Earthquake Engineering*. Elsevier, 86, pp. 1–14. doi: 10.1016/j.soildyn.2016.04.006.

Japan Gas Association (2000) 'Seismic Design for Gas Pipelines', pp. 91–100.

Jennings, P. C. and Housner, G. W. (1971) *Engineering features of the San Fernando Earthquake of February 9, 1971*. Pasadena, Calif.: California Institute of Technology, Earthquake Engineering Research Laboratory.

Kaklamanos, J. *et al.* (2015) 'Comparison of 1D linear, equivalent-linear, and nonlinear site response models at six KiK-net validation sites', *Soil Dynamics and Earthquake Engineering*. Elsevier, 69(February), pp. 207–219. doi: 10.1016/j.soildyn.2014.10.016.

Karamanos, S. A. and Tassoulas, J. L. (1996) 'Tubular Members. I: Stability Analysis and Preliminary Results', 122(Needleman 1982), pp. 64–71.

Karamitros, D. K., Bouckovalas, G. D. and Kouretzis, G. P. (2007) 'Stress analysis of buried steel pipelines at strike-slip fault crossings', *Soil Dynamics and Earthquake Engineering*, 27(3), pp. 200–211. doi: 10.1016/j.soildyn.2006.08.001.

Karimian, S. A. (2006) 'Response of buried steel pipeline subjected to longitudinal and transverse ground movement', *The University of British Columbia*, (September).

Von Karman, T. and Tsien, H.-C. (1941) 'The Buckling of Thin Cylindrical Shells Under Axial Compression', *Journal of the Aeronautical Sciences*, 8(8), pp. 303–312. doi: 10.2514/8.10722.

Kouretzis, G. P., Bouckovalas, G. D. and Gantes, C. J. (2006) '3-D shell analysis of cylindrical underground structures under seismic shear (S) wave action', *Soil Dynamics and Earthquake Engineering*, 26(10), pp. 909–921. doi: 10.1016/j.soildyn.2006.02.002.

Kouretzis, G. P., Bouckovalas, G. D. and Karamitros, D. K. (2011) 'Seismic verification of long cylindrical underground structures considering Rayleigh wave effects', *Tunnelling and Underground Space Technology*. Elsevier Ltd, 26(6), pp. 789–794. doi: 10.1016/j.tust.2011.05.001.

Kouretzis, G. P., Sheng, D. and Sloan, S. W. (2013) 'Sand-pipeline-trench lateral interaction effects for shallow buried pipelines', *Computers and Geotechnics*, 54, pp. 53–59. doi: 10.1016/j.compgeo.2013.05.008.

Kramer, S. L. (1996) *Geotechnical earthquake engineering*. Upper Saddle River: Upper Saddle River. : Prentice Hall.

Kubo, K. (1975) 'Fundamental Concept Of Aseismic Design Of Underground Piping Systems', in *Proc. 5th European Conf. Earthq. Engng*. Istanbul, Turkey.

Kuesel, T. R. (1969) 'Earthquake Design Criteria for Subways', *J Struct Div ASCE*.

Kuhlemeyer, R. and Lysmer, J. (1973) 'Finite Element Method Accuracy for Wave Propagation Problems', *Journal of the Soil Mechanics and Foundations Division*, 99(5), pp. 421–427.

Kyriakides, S. and Corona, E. (2007) 'Plastic Buckling and Collapse Under Axial Compression', in *Mechanics of Offshore Pipelines: Buckling and Collapse, Vol. I*, pp. 280–318. doi: http://dx.doi.org/10.1016/B978-008046732-0/50011-8.

Lee, L. N. H., Ariman, T. and Chen, C. C. (1984) 'Elastic-plastic buckling of buried pipelines by seismic excitation', *International Journal of Soil Dynamics and Earthquake Engineering*, 3(4), pp. 168–173. doi: 10.1016/0261-7277(84)90032-9.

Liang, J. (1995a) '3-D Seismic Response of Pipelines Through Multiple Soil Media', in *PVP-Vol. 312*, pp. 101–107.

Liang, J. (1995b) 'Dynamic Response of Pipelines Laid Through Riverbeds', in *PVP-Vol. 312*, pp. 147–152.

Lings, M. L. and Dietz, M. S. (2004) 'An improved direct shear apparatus for sand', *Géotechnique*, 54(4), pp. 245–256. doi: 10.1680/geot.54.4.245.36353.

Loh, C. H., Penzien, J. and Tsai, Y. B. (1982) 'Engineering analyses of smart 1 array accelerograms', *Earthquake Engineering & Structural Dynamics*, 10(4), pp. 575–591. doi: 10.1002/eqe.4290100407.

Lysmer, J. and Kuhlemeyer, R. (1969) 'Finite dynamic model for infinite media', *J. Eng. Mech. Div.*, 95(EM4), pp. 859–877.

Makra, K. and Chavez-Garcia, F. J. (2016) 'Site effects in 3D basins using 1D and 2D models: an evaluation of the differences based on simulations of the seismic response of Euroseistest', *Bulletin of Earthquake Engineering*, 14(4), pp. 1177–1194. doi: 10.1007/s10518-015-9862-7.

Manolis, G. D., Shaw, R. P. and Pavlou, S. (1999) 'Elastic waves in nonhomogeneous media under 2D conditions: I. Numerical implementation', *Soil Dynamics and Earthquake Engineering*, 18(1), pp. 19–30. doi: 10.1016/S0267-7261(98)00038-4.

Matheson, I. *et al.* (2008) 'An Upheaval Buckling Limit State Function for Onshore Natural Gas Pipelines', *2008 7th International Pipeline Conference, Volume 3*, pp. 781–791. doi: 10.1115/IPC2008-64687.

Matsubara, K. and Masaru, H. (2000) 'Soil Spring Constants of Buried Pipelines for Seismic Design',

Journal of Engineering Mechanics. American Society of Civil Engineers, 126(1), pp. 76–83. doi: 10.1061/(ASCE)0733-9399(2000)126:1(76).

Mavridis G. A and Pitilakis, K. D. (1996) 'Axial and transverse seismic analysis of buried pipelines', in *Eleventh World Conference on Earthquake Engineering*.

McKenna, F., Scott, M. H. and Fenves, G. L. (2010) 'Nonlinear Finite-Element Analysis Software Architecture Using Object Composition', *Journal of Computing in Civil Engineering*. American Society of Civil Engineers, 24(1), pp. 95–107. doi: 10.1061/(ASCE)CP.1943-5487.0000002.

McNorgan, J. D. (1989) 'Relieving Seismic Stresses Locked in Gas Pipelines', in *Proceedings of the Second U.S.-Japan Workshop on Liquefaction, Large Ground Deformation and Their Effects on Lifelines*. Buffalo, New York: Technical Report NCEER-89-0032, Multidisciplinary Center for Earthquake Engineering Research, pp. 363–369.

Meyersohn, W. D. and O'Rourke, T. D. (1991) 'Pipeline Buckling Caused by Compressive Ground Failure During Earthquakes', in *Proceedings of the third Japan-U.S. Workshop on Earthquake Resistant Design of Lifeline Facilities and Countermeasures for Soil Liquefaction*. Buffalo, NY: Technical Report NCEER-91-0001, NCEER, pp. 489–496.

Mindlin, R. D. (1936) 'Force at a point in the interior of a semi-infinite solid', *Journal of Applied Physics*, 7(5), pp. 195–202. doi: 10.1063/1.1745385.

Mitsuya, M., Sakanoue, T. and Motohashi, H. (2013) 'Beam-Mode Buckling of Buried Pipeline Subjected to Seismic Ground Motion', *Journal of Pressure Vessel Technology*, 135(2), pp. 1–10. doi: 10.1115/PVP2012-78559.

National Academies of Sciences, E. and M. (2008) *Seismic Analysis and Design of Retaining Walls, Buried Structures, Slopes, and Embankments*. Washington, DC: The National Academies Press. doi: 10.17226/14189.

Needleman, A. and Tvergaard, V. (1976) 'An analysis of the imperfection sensitivity of square elastic-plastic plates under axial compression', *International Journal of Solids and Structures*, 12(3), pp. 185–201. doi: https://doi.org/10.1016/0020-7683(76)90062-7.

Newmark, N. M. (1968) 'Problems in wave propagation in soil and rock', in *Proceedings of the international symposium on wave propagation and dynamic propertiesof earth materials*. Albuquerque: University of New Mexico Press, pp. 7–26.

Nishio, N., Ishita, O. and Tsukamoto, K. (1983) 'Model experiments on the behavior of buried pipelines during earthquakes', in *Am. Soc. Mech. Eng., Pressure Vessels Piping Div., (Tech. Rep.) PVP; (United States)*.

Nishio, N., Ukaji, T. and Tsukamoto, K. (1980) 'Experimental Studies and Observation of Pipeline Behavior During Earthquakes', in *PVP-Vol. 43*, pp. 67–76.

Norman, J. A. P. *et al.* (2006) 'Physical modelling of bridges subject to multiple support excitation', pp. 5111–5120.

O'Haver, T. (2018) *A Pragmatic Introduction to Signal Processing with applications in scientific measurement*, *University of Maryland at College Park*. doi: ISBN: 9781533372857.

O'Rourke, M. J. and Hmadi, K. El (1988) 'Analysis of continuous buried pipelines for seismic wave effects', *Earthquake Engineering & Structural Dynamics*, 16(6), pp. 917–929. doi: 10.1002/eqe.4290160611.

O'Rourke, M. J. and Liu, X. (1999) *Response of Buried Pipelines Subject to Earthquake Effects*.

O'Rourke, M. and Wang, L. R. L. (1978) 'Earthquake response of buried pipelines', in *Special Conf. on*

Earthquake Engineering and Soil Dynamics. Pasadena, CA: ASCE, pp. 720–731.

Papadopoulos, S. P. *et al.* (2017) 'Impact of spatial variability of earthquake ground motion on seismic demand to natural gas transmission pipelines', in *16th World Conference on Earthquake Engineering, Santiago, Chile, 9-13 January*.

Papanikolaou, V. . *et al.* (2017) 'GiD+OpenSees Interface : An Integrated Finite Element Analysis Platform'. Thessaloniki, Greece: Lab of R/C and Masonry Structures, Aristotle University of Thessaloniki. Available at: http://gidopensees.rclab.civil.auth.gr/.

Paquette, J. A. and Kyriakides, S. (2006) 'Plastic buckling of tubes under axial compression and internal pressure', *International Journal of Mechanical Sciences*, 48(8), pp. 855–867. doi: 10.1016/j.ijmecsci.2006.03.003.

Parmelee, R. A. and Ludtke, C. A. (1975) 'Seismic soilstructure interaction of buried pipelines', in *U.S. National Conference on Earthquake Engineering*. Ann Arbor, pp. 406–415.

Peck, R. B., Hendron, A. J. and Mohraz, B. (1972) 'State of the Art of Soft-Ground Tunneling', in *International Proceedings of the North American Rapid Excavation and Tunneling Conference*. New York: American Institute of Mining, Metallurgical, and Petroleum Engineers, pp. 259–286.

Pitilakis, D. *et al.* (2008) 'Numerical simulation of dynamic soil-structure interaction in shaking table testing', *Soil Dynamics and Earthquake Engineering*, 28(6), pp. 453–467. doi: 10.1016/j.soildyn.2007.07.011.

Psarropoulos, P. N. *et al.* (2007) 'Linear and Nonlinear Valley Amplification Effects of Seismic Ground Motion', *Soils and Foundations, Japanese Geotechnical Society*, 47(5), pp. 857–871.

Rajani, B. B. and Tesfamariam, S. (2004) 'Uncoupled axial, flexural, and circumferential pipe-soil interaction analyses of partially supported jointed water mains', *Canadian Geotechnical Journal*, 41(6), pp. 997–1010.

Rathje, E. M., Abrahamson, N. A. and Bray, J. D. (1998) 'Simplified frequency content estimates of earthquake ground motions', *Journal of Geotechnical and Geoenvironmental Engineering*, 124(2), pp. 150–158. doi: 10.1061/(ASCE)1090-0241(1998)124:2(150).

Rayleigh, Lord (1885) 'On Waves Propagated along the Plane Surface of an Elastic Solid', *Proceedings of the London Mathematical Society*, s1-17(1), pp. 4–11. doi: 10.1112/plms/s1-17.1.4.

Saberi, M., Behnamfar, F. and Vafaeian, M. (2013) 'A semi-analytical model for estimating seismic behavior of buried steel pipes at bend point under propagating waves', *Bulletin of Earthquake Engineering*, 11(5), pp. 1373–1402. doi: 10.1007/s10518-013-9430-y.

Saiidi, M. S., Vosooghi, A. and Nelson, R. B. (2013) 'Shake-Table Studies of a Four-Span Reinforced Concrete Bridge', *ASCE Journal of Structural Engineering*, 139(August), pp. 1352–1361. doi: 10.1061/(ASCE)ST.1943-541X.0000790.

Sakurai, A. and Takanashi, T. (1969) 'Dynamic Stresses of Underground Pipelines During Earthquakes', in *Proceed. of 4th World Conf. on Earthq. Engng.* Santiago, Chile, p. 81.

Sanders, J. L. (1959) *An Improved First-Approximation Theory for Thin Shells*, *NASA Technical Report R-24*. Langley Field, VA. doi: TR R-24.

Sanders, L. J. J. (1963) 'Nonlinear Theories for Thin Shells', *Quarterly of Applied Mathematics*, XXI(1), pp. 21–36. Available at: http://www.ams.org/journals/qam/1963-21-01/S0033-569X-1963-0147023-4/S0033-569X-1963-0147023-4.pdf.

Sarvanis, G. C. *et al.* (2017) 'Permanent earthquake-induced actions in buried pipelines: Numerical modeling and experimental verification', *Earthquake Engineering & Structural Dynamics*, (May),

pp. 1–22. doi: 10.1002/eqe.3001.

Scandella, L. and Paolucci, R. (2010) 'Earthquake induced ground strains in the presence of strong lateral soil heterogeneities', *Bulletin of Earthquake Engineering*, 8(6), pp. 1527–1546. doi: 10.1007/s10518-010-9186-6.

Seed, H. B. and Idriss, I. M. (1970) *Soil moduli and damping factors for dynamic response analyses*. Berkeley, Calif. : College of Engineering, University of California.

Selvadurai, A. P. S. (1985) 'Soil-pipeline interaction during ground movement', in *Civil engineering in the Arctic offshore, ARCTIC `85*. New York, N.Y.: American Society of Civil Engineers, pp. 763–773.

Sextos, A. *et al.* (2015) 'Multiple support seismic excitation of the Evripos bridge based on free-field and on-structure recordings', *Structure and Infrastructure Engineering*, 11(11), pp. 1510–1523. doi: 10.1080/15732479.2014.977302.

Sextos, A. G., Pitilakis, K. D. and Kappos, A. J. (2003) 'Inelastic dynamic analysis of RC bridges accounting for spatial variability of ground motion, site effects and soil-structure interaction phenomena. Part 1: Methodology and analytical tools', *Earthquake Engineering & Structural Dynamics*, 32(4), pp. 607–627. doi: 10.1002/eqe.241.

Sextos, A. and Kappos, A. (2009) 'Evaluation of seismic response of bridges under asynchronous excitation and comparisons with Eurocode 8-2 provisions', *Bulletin of Earthquake Engineering*. Dordrecht, 7(2), pp. 519–545. doi: 10.1007/s10518-008-9090-5.

Shamass, R., Alfano, G. and Guarracino, F. (2014) 'A numerical investigation into the plastic buckling paradox for circular cylindrical shells under axial compression', *Engineering Structures*. Elsevier Ltd, 75, pp. 429–447. doi: 10.1016/j.engstruct.2014.05.050.

Sheil, B. B. *et al.* (2018) 'Full-scale laboratory testing of a buried pipeline in sand subjected to cyclic axial displacements', *Géotechnique*, 68(8), pp. 684–698. doi: 10.1680/jgeot.16.P.275.

Shinozuka, B. M., Kameda, H. and Koike, T. (1983) 'Ground strain estimation for seismic risk analysis', 109(1), pp. 175–191.

Shinozuka, M. and Koike, T. (1979) *Estimation of Structural Strains in Underground Lifeline Pipes*.

St John, C. M. and Zahrah, T. F. (1987) 'Aseismic design of underground structures', *Tunnelling and Underground Space Technology*, 2(2), pp. 165–197. doi: 10.1016/0886-7798(87)90011-3.

Stroud, M. . (1971) *The behaviour of sand at low stress levels in the simple-shear apparatus (Doctoral thesis)*. University of Cambridge. doi: https://doi.org/10.17863/CAM.11446.

Taylor, C. and Crewe, A. (1996) 'Shaking Table Tests of Simple Direct Foundations', in Sísmica, S. M. de I. (ed.) *11th World Conference of Earthquake Engineering (WCEE)*. Acapulco, Mexico: Pergamon.

The European Union (2010) 'REGULATION (EU) No 994/2010 OF THE EUROPEAN PARLIAMENT AND OF THE COUNCIL of 20 October 2010 concerning measures to safeguard security of gas supply and repealing Council Directive 2004/67/EC', *Official Journal of the European Union*, (L 295/1), pp. 1–22.

The U.S. Energy Information Administration (EIA) (2017) *U.S. Energy Facts*. Available at: https://www.eia.gov/energyexplained/?page=us_energy_home (Accessed: 10 March 2019).

Timoshenko, S. P. and Gere, J. M. (1961) *Theory of Elastic Stability*. McGraw-Hill (Engineering Series).

Trautmann, C. H. and O'Rourke, T. D. (1985) 'Lateral force-displacement response of buried pipe',

Journal of Geotechnical Engineering, 111(9), pp. 1077–1092.

Trifonov, O. V. and Cherniy, V. P. (2012) 'Elastoplastic stress-strain analysis of buried steel pipelines subjected to fault displacements with account for service loads', *Soil Dynamics and Earthquake Engineering*. Elsevier, 33(1), pp. 54–62. doi: 10.1016/j.soildyn.2011.10.001.

Tsatsis, A., Gelagoti, F. and Gazetas, G. (2018) 'Performance of a buried pipeline along the dip of a slope experiencing accidental sliding', *Géotechnique*, 68(11), pp. 968–988. doi: 10.1680/jgeot.17.P.029.

Vazinram, F. and Rasti, R. (2006) 'Seismic Hazards for Lifelines', in *Geohazards, Engineering Conferences International*. New York: Engineering Conferences International, p. 9.

Vazouras, P., Dakoulas, P. and Karamanos, S. A. (2015) 'Pipe-soil interaction and pipeline performance under strike-slip fault movements', *Soil Dynamics and Earthquake Engineering*. Elsevier, 72, pp. 48–65. doi: 10.1016/j.soildyn.2015.01.014.

Vazouras, P. and Karamanos, S. A. (2017) 'Structural behavior of buried pipe bends and their effect on pipeline response in fault crossing areas', *Bulletin of Earthquake Engineering*. Springer Netherlands. doi: 10.1007/s10518-017-0148-0.

Vazouras, P., Karamanos, S. A. and Dakoulas, P. (2012) 'Mechanical behavior of buried steel pipes crossing active strike-slip faults', *Soil Dynamics and Earthquake Engineering*. Elsevier, 41, pp. 164–180. doi: 10.1016/j.soildyn.2012.05.012.

Vazouras, P., Karamanos, S. and Dakoulas, P. (2010) 'Finite element analysis of buried steel pipelines under strike-slip fault displacements', *Soil Dynamics and Earthquake Engineering*. Elsevier, 30(11), pp. 1361–1376. doi: 10.1016/j.soildyn.2010.06.011.

Vucetic, M. (1994) 'Cyclic Threshold Shear Strains in Soils', *Journal of Geotechnical Engineering*. American Society of Civil Engineers, 120(12), pp. 2208–2228. doi: 10.1061/(ASCE)0733-9410(1994)120:12(2208).

Vucetic, M. and Dobry, R. (1991) 'Effect of Soil Plasticity on Cyclic Response', *Journal of Geotechnical Engineering*. American Society of Civil Engineers, 117(1), pp. 89–107. doi: 10.1061/(ASCE)0733-9410(1991)117:1(89).

Wang, J. *et al.* (2011) 'Mobilization distance for upheaval buckling of shallowly buried pipelines', *Journal of Pipeline Systems Engineering and Practice*, 3(4), pp. 106–114. doi: 10.1061/(ASCE)PS.1949-1204.0000099.

Weingarten, V. I., Seide, P. and Peterson, J. P. (1968) *Bucking of Thin-Walled Circular Cylinders*. Washington. doi: 19690013955.

Wong, B. K. C. *et al.* (1987) 'Three-dimensional motion of buried pipeline. i: Analysis', 112(12), pp. 1319–1337.

Wood, D. M., Crewe, A. and Taylor, C. (2002) 'Shaking table testing of geotechnical models', *International Journal of Physical Modelling in Geotechnics*, 2(1), pp. 1–13. doi: 10.1680/ijpmg.2002.020101.

Yu, H. *et al.* (2018) 'Analytical solution for longitudinal seismic response of tunnel liners with sharp sti ff ness transition', *Tunnelling and Underground Space Technology*. Elsevier, 77(March), pp. 103–114. doi: 10.1016/j.tust.2018.04.001.

Yun, H. (1988) *On the Beam and Shell Modes of Buckling of Buried Pipelines*. The University of Texas at Austin. doi: 10.1016/j.jaci.2012.05.050.

Yun, H. and Kyriakides, S. (1990) 'On the beam and shell modes of buckling of buried pipelines', *Soil*

Dynamics and Earthquake Engineering, 9(4), pp. 179–193. doi: 10.1016/S0267-7261(05)80009-0.

Zerva, A. (1993) 'Pipeline Response to Directionally and Spatially Correlated Seismic Ground Motions', *Journal of Pressure Vessel Technology*, 115(February 1993), pp. 53–58.

Zerva, A. (1994) 'On the spatial variation of seismic ground motions and its effects on lifelines', *Engineering Structures*, 16(7), pp. 534–546. doi: 10.1016/0141-0296(94)90089-2.

Zerva, A. (2009) *Spatial Variation of Seismic Ground Motions: Modeling and Engineering Applications*. Boca Raton, Fla.: CRC Press, Taylor & Francis Group.

Zerva, A., Ang, A. .-S. and Wen, Y. K. (1985) 'A Study of Seismic Ground Motion for Lifeline Response Analysis', *Civil Engineering Studies, Structural Research Series (University of Illinois at Urbana-Champaign, Department of Civil Engineering)*, (521).

Zervos, A., Papanastasiou, P. and Vardoulakis, I. (2001) 'A finite element displacement formulation for gradient elastoplasticity', *International Journal for Numerical Methods in Engineering*, 50(6), pp. 1369–1388. doi: 10.1002/1097-0207(20010228)50:6<1369::AID-NME72>3.0.CO;2-K.

Zhang, B. and Papageorgiou, A. S. (1996) 'Simulation of the response of the marina district Basin, San Francisco, California, to the 1989 Loma Prieta earthquake', *Bulletin of the Seismological Society of America*, 86(5), pp. 1382–1400.

Zhang, J. (2009) *Elastic/Plastic Buckling of Cylindrical Shells with Elastic Core under Axial Compression*. McGill University.

Appendix A

A.1 Investigation of the effect of soil-pipe kinematic interaction

In this appendix, a comprehensive effort is made to study the influence of the kinematic soil-structure interaction on a range of possible soil-pipe systems. For this purpose, the steady-state harmonic response of these different systems to unilateral unit shear excitation at their base is analysed using finite-element procedures. The influence of kinematic interaction on the free-field motion below pipe bed (i.e., the foundation input motion according to SSI terminology) is evaluated by comparing in the frequency space the horizontal motion amplifications between 2-D plane-strain soil-pipe models and the equivalent soil-only models analysed in ABAQUS.

A.1.1 Description of the model

A 20-m-deep uniform soil deposit overlying rigid rock is considered, with a circular inclusion to accommodate a buried steel pipe section of variable R and t_w. The rest of the geometry is as illustrated in **Figure A-1**. Both the soil and the pipe material are assumed linearly elastic since the problem is treated in the frequency domain, with properties as listed in **Figure A-1**. The two bodies are assumed perfectly bonded ('weld' contact); to this end, the 'rough' friction model combined with the no-separation relationship are used to define the surface interaction in ABAQUS, precluding any relative motion once the two bodies are in contact. The lateral edges of the soil are constrained to move together in pairs of nodes located at the same depth, in a shear-beam mode. Four-node, bilinear isoparametric plane-strain elements, with enhanced hourglass control to suppress zero-energy bending modes, are used to discretise both the soil and the pipe.

A.1.2 Theoretical background

To isolate the effect of the pipe stiffness on the foundation input motion, the pipe is considered massless in the analysis. Linear rate-independent (or structural or hysteretic) damping is assumed for the soil, which is conveniently incorporated in a frequency-domain formulation of the problem. For a single-DOF spring-mass-dashpot system, the equation describing the response of its mass to harmonic external force $P(t) = P_o e^{i\omega t}$ is

$$m\ddot{u} + c\dot{u} + ku = P_o e^{i\omega t} \tag{A.1}$$

in which P_o is the complex force amplitude; $i = \sqrt{-1}$; $\omega = 2\pi f$ is the loading frequency. If it is assumed that the system will, at steady state, undergo harmonic motion at frequency ω, the displacement response can be expressed as

$$u(t) = H_u(\omega) e^{i\omega t} \tag{A.2}$$

Substituting this expression into Eq. (A.1), one can solve for the function $H_u(\omega)$ as

$$H_u(\omega) = \frac{P_o}{k - \omega^2 m + i\omega c} \tag{A.3}$$

In the unit force case, the function $H_u(\omega)$ is called the complex frequency-response function of the system and fully describes its response to unit sinusoidal load.

In Eq. (A.3), the spring stiffness and the dashpot coefficient are conventionally embodied into a single entity known as the complex stiffness $k^* = k + i\omega c$, so that the total response of the system is given by

$$u(t) = \frac{P_o}{k^* - \omega^2 m} e^{i\omega t} \tag{A.4}$$

In the case of linear rate-independent damping, the damping force is proportional to the stiffness and is described by

$$f_D = \frac{\eta k}{\omega} \dot{u}$$

where $\eta =$ the structural damping ratio taken to be twice the equivalent viscous damping ratio, ξ_{eq}, at resonant loading frequencies. Therefore, the complex stiffness becomes

$$k^* = k + i\eta k = k(1 + i\eta) \tag{A.5}$$

In the problem at hand, harmonic excitation is applied as a unit harmonic horizontal displacement of the base $u_b(t) = 1e^{i\omega t}$. Thus, neglecting for simplicity at the moment the additional unknown contact forces, the dynamic equilibrium now takes the matrix form

$$\mathbf{M}\ddot{\mathbf{u}} + \mathbf{C}\dot{\mathbf{u}} + \mathbf{K}\mathbf{u} = -\mathbf{M}\boldsymbol{\mathcal{I}}\ddot{u}_b(t) \tag{A.6}$$

where $\mathbf{u}, \dot{\mathbf{u}}, \ddot{\mathbf{u}} =$ nodal displacement, velocity, acceleration vectors relative to the base; $\boldsymbol{\mathcal{I}} =$ a vector consisting of ones at horizontal translation DOFs and zeros at vertical translation DOFs; the system matrices can be partitioned as

$$\mathbf{M} = \begin{bmatrix} \mathbf{M}_{\mathrm{s}} & \mathbf{0} \\ \mathbf{0} & \mathbf{0} \end{bmatrix}$$

$$\mathbf{C} = \begin{bmatrix} \mathbf{C}_{\mathrm{s}} & \mathbf{0} \\ \mathbf{0} & \mathbf{0} \end{bmatrix}; \quad \mathbf{C}_{\mathrm{s}} = \frac{\eta}{\omega}\mathbf{K}_{\mathrm{s}}$$

$$\mathbf{K} = \begin{bmatrix} \mathbf{K}_{\mathrm{s}} & \mathbf{K}_{\mathrm{sp}} \\ -\mathbf{K}_{\mathrm{sp}} & \mathbf{K}_{\mathrm{p}} \end{bmatrix}$$

In analogy to the single-DOF system, if the vector of unknown displacements is expressed as $\mathbf{u} = \mathbf{H}_{\mathrm{u}}(\omega)e^{i\omega t}$, where $\mathbf{H}_{\mathrm{u}}(\omega)$ represents a vector of complex transfer functions, Eq. (A.6) yields

$$-\omega^2\mathbf{M}\mathbf{H}_{\mathrm{u}}(\omega)e^{i\omega t} + i\omega\mathbf{C}\mathbf{H}_{\mathrm{u}}(\omega)e^{i\omega t} + \mathbf{K}\mathbf{H}_{\mathrm{u}}(\omega)e^{i\omega t} = \omega^2\mathbf{M}\boldsymbol{\mathcal{I}}e^{i\omega t} \tag{A.7}$$

and eliminating the common factor and rearranging gives

$$\mathbf{H}_{\mathrm{u}}(\omega)(-\omega^2\mathbf{M} + \mathbf{K}^*) = \omega^2\mathbf{M}\boldsymbol{\mathcal{I}} \tag{A.8}$$

where

$$\mathbf{K}^* = \begin{bmatrix} \mathbf{K}_{\mathrm{s}} & \mathbf{K}_{\mathrm{sp}} \\ -\mathbf{K}_{\mathrm{sp}} & \mathbf{K}_{\mathrm{p}} \end{bmatrix} + i\omega \begin{bmatrix} \mathbf{C}_{\mathrm{s}} & \mathbf{0} \\ \mathbf{0} & \mathbf{0} \end{bmatrix} = \begin{bmatrix} \mathbf{K}_{\mathrm{s}}(1 + i\eta) & \mathbf{K}_{\mathrm{sp}} \\ -\mathbf{K}_{\mathrm{sp}} & \mathbf{K}_{\mathrm{p}} \end{bmatrix}$$

A.1.3 Analysis results

The solution to Eq. (A.8) is obtained using the direct steady-state dynamics procedure encompassed in ABAQUS. A set of discrete loading frequencies with $f_{min} =$ 0.1 Hz and $f_{max} = 15$ Hz are specified for which results are to be obtained; the frequency space is divided into subintervals by the computed natural frequencies of the system and 13 frequency points are defined in each one, with spacing biased towards the natural frequencies. A set of different soil-pipe systems is generated by considering combinations of values for the following parameters: V_s, R, and t_w. The values assigned to these parameters are given in **Table A-1** and **Table A-2.** To characterise the different systems in a consistent dimensionless way, the relative lateral pipe-to-soil flexibility is used (Eq. (2.4)), reiterated here:

$$F_\ell = \frac{2E(1-\nu_p^2)R^3}{E_p(1+\nu){t_w}^3}$$

The built-in facility for parametric modelling in ABAQUS is utilised to analyse a total of 36 models; this requires the development of parametrized input files and Python scripts that contain instructions on how to generate the parametric variations to the base models.

The ratio of the displacement magnitude at soil node B located directly below the pipe bed to the base displacement magnitude (unity) is defined as the modulus of the complex transfer function of this node, $\left|H_{u,B}(\omega)\right|$, and is evaluated in the decibel scale for the frequency range examined. The results for all cases are presented in **Figure A-1** and **Figure A-2** for models $R = 400$ mm and **Figure A-3** for models $R = 600$ mm, alongside the amplification for the corresponding soil-only models.

The comparison of the curves in nearly all plots reveals a remarkable match between the soil-only model and soil-pipe models with various F_ℓ. Not only that, but it is shown that free-field motion below pipe bed appears insensitive to the stiffness of the pipe, as curves in any given plot corresponding to different F_ℓ coincide almost perfectly. The only exception to these behaviours is identified in the plots for the softest

soil with $V_s = 100$ m/s, where deviations of the FIM motion from the free-field motion is observed for loading frequencies above approximately 9 Hz. This is in line with common sense: a more flexible soil cannot impose its motion to an embedded structure in the way a stiffer soil can. However, it is seen that parameter F_ℓ alone cannot determine the degree of kinematic interaction; the frequency content of the excitation needs to be additionally considered.

In conclusion, this parametric numerical study demonstrates that the effects of kinematic interaction for typical steel gas pipelines embedded in soils of various rigidities are negligible at least for excitation frequencies up to 10 Hz, which is a reasonable upper limit for the frequency content of the majority of recorded earthquake motions. Therefore, the modelling choice to ignore kinematic interaction in this study appears justified.

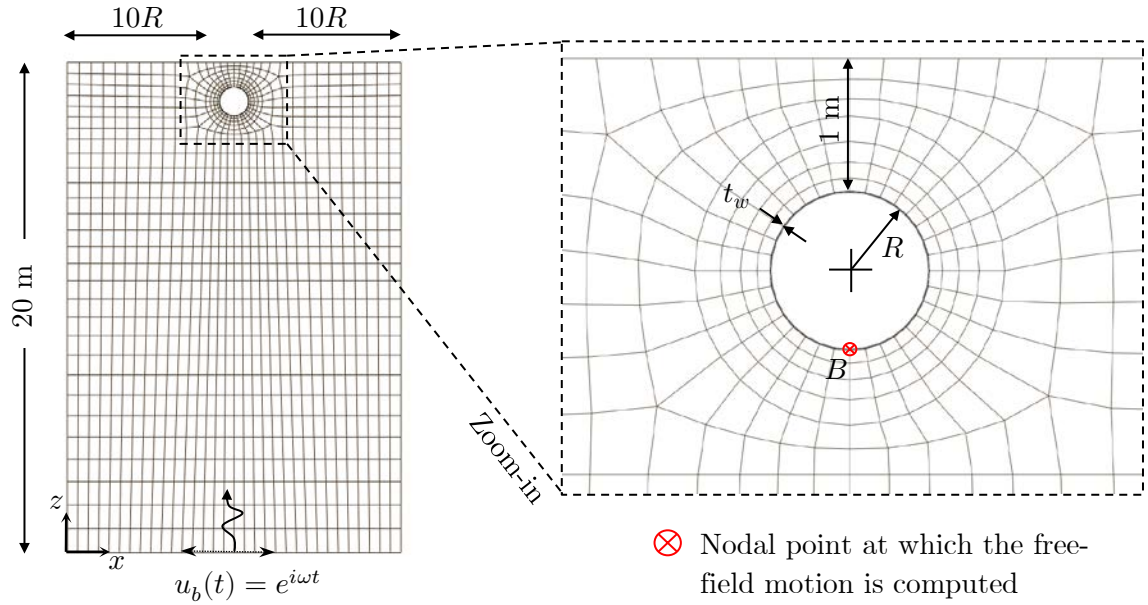

Soil	**Pipe**
V_s $\nu = 1/3$ $\rho = 1.8$ Mg/m^3 $\xi = 5\%$	$E_p = 200$ GPa $\nu_p = 0.3$ $\rho = 0$

Figure A-1. Overview of the geometry, input excitation, and material properties of the reference 2-D finite-element model of the dynamic soil-pipe system developed in ABAQUS

Table A-1. Relative lateral pipe-to-soil flexibility ratio (F_ℓ) for all different soil-pipe systems with $R = 400$ mm

$R = 400$ mm		t_w (mm)			
		8	16	24	32
V_s(m/s)	100	41	5.1	1.5	0.5
	200	164	20	6	2.5
	300	370	46	14	6
	400	655	82	24	10

Table A-2. Relative lateral pipe-to-soil flexibility ratio (F_ℓ) for all different soil-pipe systems with $R = 600$ mm

$R = 600$ mm		t_w (mm)			
		8	16	24	32
V_s(m/s)	100	138	17	5	2
	200	550	70	20	8.5
	300	1245	156	46	20
	400	2210	276	82	35

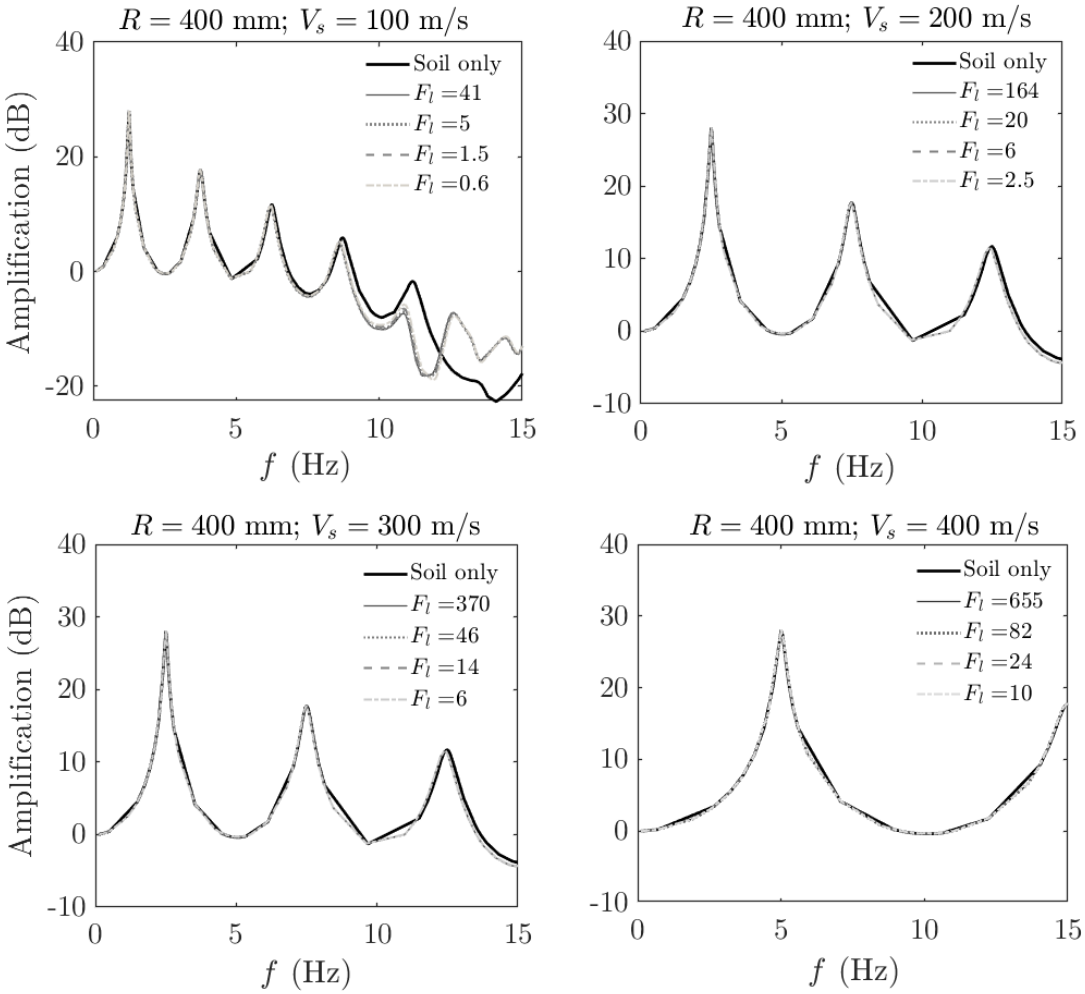

Figure A-2. Frequency spectra of the amplification of the steady-state horizontal free-field motion below pipe bed level for variations of soil-pipe systems with $R = 400$ mm

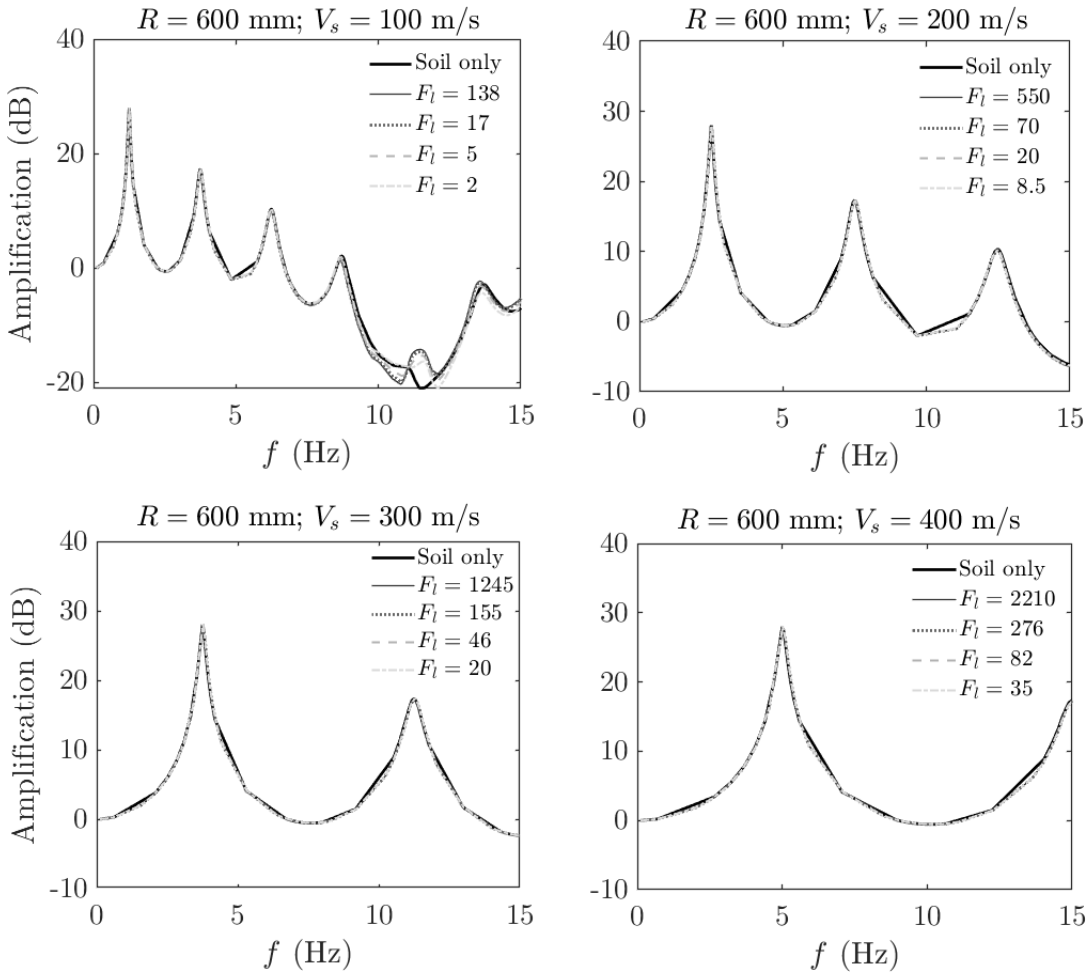

Figure A-3. Frequency spectra of the amplification of the steady-state horizontal free-field motion below pipe bed level for variations of soil-pipe systems with $R = 600$ mm

B Appendix B

B.1 Position-dependent soil moduli in ABAQUS site response models

B.1.1 Fortran USDFLD user-subroutine

```
      subroutine USDFLD(field,statev,pnewdt,direct,t,celent,time,
     1 dtime,cmname,orname,nfield,nstatv,noel,npt,layer,kspt,
     2 kstep,kinc,ndi,nshr,coord,jmac,jmtyp,matlayo,laccflg)
C
      include 'aba_param.inc'
C
      character*80 cmname,orname
      character*8  flgray(15)
      dimension field(nfield),statev(nstatv),direct(3,3),t(3,3),time(2),
     & coord(*),jmac(*),jmtyp(*)
      dimension array(15),jarray(15)
C      Implementation:
       x = coord(1)
       FIELD(1) = x
      return
      end
```

B.1.2 ABAQUS input file

```
...
*Material, name="Variable sand"
*Damping, alpha=_ALPHA, beta=_BETA
*Density
_DENS,
*Elastic, dependencies=1
_E1, _nu1, ,   0.
_E1, _nu1, , _LTx
_E2, _nu2, , _RTx
_E2, _nu2, , 500.
*User Defined Field
...
```

B.2 GiD-QUAD4M interface

This section lists scripts that enable the use of GiD, a commercial pre- and post-processor for numerical simulation applications, to automate the meshing process and the input file generation in accord with the requirements of the CLI (i.e., lacking any GUI) finite-element code QUAD4M.

When the following script files are reposited in the designated installation directory of GiD, a new problem type with the name 'QUAD4M' appears in the GiD environment, allowing GiD to act as a pre-processing tool for QUAD4M. This level of integration is incomplete, as one needs to manually run the QUAD4M command window and specify the input file name generated by GiD. Post-processing capabilities are not provided.

These scripts are based on an open-source add-on developed to interface GiD with Opensees (Papanikolaou *et al.*, 2017), hence its inclusion is required for trouble-free functionality. This add-on is freely available from https://github.com/rclab-auth/gidopensees/releases under the GNU General Public License.

For reference purposes, an example QUAD4M input file and a Matlab function that generates QUAD4M-compatible files for the definition of equivalent-linear properties are listed in subsections B.2.5 and B.2.6, respectively.

B.2.1 QUAD4M.bas file

```
GiD + QUAD4M Interface: *GenData(Project_Name)
Site Response Analysis
S
       DRF        PRM     ROCKVP     ROCKVS    ROCKRHO
*format "%9.0f%9.0f%9.0f"
         1      0.65 *GenData(P-Wave_Velocity,real) *GenData(S-
Wave_Velocity,real) *GenData(Unit_Weight,real)
 NELM NDPT NSLP   ! # of elements # of points, #surfaces for seismic coeff
anal.
*# Number of Elements and Nodes
*format "%5d%4d"
*nelem *npoin    0
KGMAX KGEQ N1EQ N2EQ N3EQ NUMB   KV KSAV
*format "%5d%5d%5d"
```

```
*GenData(Number_of_Steps,int)*GenData(Number_of_Steps,int)    1
1*GenData(Number_of_Steps,int)   20    1    1
      DTEQ    EQMUL1    EQMUL2    UGMAX1    UGMAX2 HDRX HDRY NPLX NPLY
PRINPUT
*format "%9.3f%9.2f%5d%5d%9.2f"
 *GenData(Time_Increment_Size,real) *GenData(Scaling_Factor,real)
0          *GenData(Number_of_Header_Lines_in_File,int)
*GenData(Number_of_Time_Points_per_Line,int)
*GenData(Predominant_Period,real)
Earthquake Input File , Names and Formats (asterisk for free format)
*GenData(Earthquake_Input_File_Name_\n(with_suffix))
(8F9.6)
 SOUT AOUT KOUT
    0    1    0
ACCELERATION OUTPUT FORMAT (M or C)
COMBINED
*GenData(Project_Name)
acc
SYSTEM STATE OUTPUT FILE
*GenData(Project_Name).Q4R
    N  NP1  NP2  NP3  NP4 TYPE      DENS        PO       GMX         G
XL LSTR
*# QuadElements
*include bas\Elements\Quadrilateral\QuadElements.bas
*# Tri31 Elements
*include bas\Elements\Triangular\Tri31Elements.bas
*# Nodes
    N      XORD      YORD   BC  OUT X2IV      X1IV       XIV
(I5,2F10.0,2I5,6F10.0)
*include bas\Nodes.bas
```

B.2.2 QuadElements.bas file

```
*#--------------------------------------------------------------------
*#                        Quad Elements
*#--------------------------------------------------------------------
*set var LSTR=0
*loop elems
*if(strcmp(elemsMatProp(1),"Quad")==0)
*loop materials *NotUsed
*if(strcmp(elemsMatProp(4),MatProp(0))==0)
*format "%5d%5d%5d%5d%5d%4d%9.0f%9.2f%9.0f%9.0f%9.2f"
*ElemsNum*ElemsConec *MatProp(Reduction_Curve_Type,int)
*MatProp(Specific_Weight,real) *MatProp(Poisson_Ratio)
*MatProp(SmallStrain_Shear_Modulus) *MatProp(Initial_Shear_Modulus)
*MatProp(Initial_Critical_Damping_Ratio)    *LSTR
*endif
*end materials
*endif
*end elems
```

B.2.3 Tri31Elements.bas file

```
*#-----------------------------------------------------------------
*#                      Tri31 Elements
*#-----------------------------------------------------------------
*set var LSTR=0
*loop elems
*if(strcmp(elemsMatProp(1),"Tri31")==0)
*loop materials *NotUsed
*if(strcmp(elemsMatProp(4),MatProp(0))==0)
*format "%5d%4d%5d%5d%4d%4d%9.0f%9.2f%9.0f%9.0f%9.2f"
*ElemsNum *ElemsConec *elemsconec(3) *MatProp(Reduction_Curve_Type,int)
*MatProp(Specific_Weight,real) *MatProp(Poisson_Ratio)
*MatProp(SmallStrain_Shear_Modulus) *MatProp(Initial_Shear_Modulus)
*MatProp(Initial_Critical_Damping_Ratio)    *LSTR
*endif
*end materials
*endif
*end elems
```

B.2.4 Nodes.bas file

```
*if(GenData(Dimensions,int)==2)
*# node $NodeTag $XCoord $Ycoord $BC $OUT $AXin $VXin $UXin $AYin $VYin
$UYin
*set Cond Boundary_conditions *nodes
*loop nodes *OnlyInCond
*format "%5d%9.2f%9.2f%4d%4d"
*NodesNum *nodescoord(1) *nodescoord(2) *Cond(1,int) *Cond(2,int)         0
0         0         0         0         0
*end nodes
*endif

function formatRedCurves(varargin)
% Creates the soil curve data file for QUAD4M input with the proper format.
%% Input
% Arbitrary number of matrices each one representing a set of curves.
% Each matrix must have 3 columns (1: strain (%), 2: G/Gmax, 3: Damping(%))
% OR a cell array containing n 3-column matrices
%% Input check
nVarargs = length(varargin);
cellFlag = 0;                                % Check if cell array
if nargin == 1
if iscell(varargin{1})
    nVarargs = size(varargin{1},2);
    cell = varargin{1};
    cellFlag = 1;
end
end
```

```
%% Implementation
% Locate user profile path
if ispc
home = [getenv('HOMEDRIVE') getenv('HOMEPATH')];
else
home = getenv('HOME');
end

cd([home '\Documents\QUAD4M']);

prompt = 'Please give a name to the file to be created: ';
fName = input(prompt,'s');
fName = [fName '.txt'];
prompt = 'What is the soil type? ';
soil = input(prompt,'s');
fileID = fopen(fName,'w');
fprintf(fileID, '%5d \n', nVarargs);
for k = 1:nVarargs

if cellFlag == 1
    data = cell{k};
else
    data = varargin{k};
end

strain = data(:,1);
Gratio = data(:,2);
damp = data(:,3);
numPoints = length(strain);
numCols = 8;
for i=1:numPoints
    if strain(i)<1
        strain(i) = round(strain(i),4);
    else
        strain(i) = round(strain(i),2);
    end
    if Gratio(i)<1
        Gratio(i) = round(Gratio(i),4);
    else
        Gratio(i) = round(Gratio(i),2);
    end
    if damp(i)<1
        damp(i) = round(damp(i),4);
    else
        damp(i) = round(damp(i),2);
    end
end
```

B.2.5 Example QUAD4M input file

```
GiD + QUAD4M Interface - An Integrated FEA Platform: Scenario 2
Site Response Analysis
S
       DRF        PRM    ROCKVP    ROCKVS   ROCKRHO
         1       0.65      2200      1000     23544
 NELM NDPT NSLP
 8982 7214    0
KGMAX KGEQ N1EQ N2EQ N3EQ NUMB   KV KSAV
 3949 3949    1    1 3949   15    1    1
DTEQ  EQMUL1 EQMUL2 UGMAX1 UGMAX2 HDRX HDRY NPLX NPLY  PRINPUT
0.010 1.00               0           2         1          0.13
Earthquake Input File , Names and Formats (asterisk for free format)
Imp_Valley2.dat
(8F9.6)
 SOUT AOUT KOUT
    0    1    0
ACCELERATION OUTPUT FORMAT (M or C)
COMBINED
S2C2d8
acc
SYSTEM STATE OUTPUT FILE
S2C2d8.Q4R
N  NP1  NP2  NP3  NP4 TYPE   DENS    PO     GMX      G     XL  LSTR
1    1    2    4    3   11  14715  0.33   98813  98813  0.02      0
2    2    5    6    4   12  14715  0.33   75200  75200  0.02      0
...




N    XORD   YORD  BC  OUT  X2IV  X1IV  XIV   (I5,2F10.0,2I5,6F10.0)
1  500.00   0.00   4    0     0     0    0    0    0      0
2  499.00   0.00   4    0     0     0    0    0    0      0
...
```

B.2.6 MATLAB function for $G-\gamma-D$ curves

This is a Matlab function that writes the data of a family of G–γ–D curves to a text file of specific format to be used as input to QUAD4M.

```
function formatRedCurves(varargin)
% Creates the soil curve data file for QUAD4M input with the proper format.
%% Input
% Arbitrary number of matrices each one representing a set of curves.
% Each matrix must have 3 columns (1: strain (%), 2: G/Gmax, 3: Damping(%))
% OR a cell array containing n 3-column matrices
```

```
%% Input check
nVarargs = length(varargin);
cellFlag = 0;                                % Check if is cell
if nargin == 1
if iscell(varargin{1})
    nVarargs = size(varargin{1},2);
    cell = varargin{1};
    cellFlag = 1;
end
end
%% Implementation
% Locate user profile path
if ispc
home = [getenv('HOMEDRIVE') getenv('HOMEPATH')];
else
home = getenv('HOME');
end

cd([home '\Documents\QUAD4M']);

prompt = 'Please give a name to the file to be created: ';
fName = input(prompt,'s');
fName = [fName '.txt'];
prompt = 'What is the soil type? ';
soil = input(prompt,'s');
fileID = fopen(fName,'w');
fprintf(fileID, '%5d \n', nVarargs);
for k = 1:nVarargs

if cellFlag == 1
    data = cell{k};
else
    data = varargin{k};
end

strain = data(:,1);
Gratio = data(:,2);
damp = data(:,3);
numPoints = length(strain);
numCols = 8;
for i=1:numPoints
    if strain(i)<1
        strain(i) = round(strain(i),4);
    else
        strain(i) = round(strain(i),2);
    end
    if Gratio(i)<1
        Gratio(i) = round(Gratio(i),4);
```

```
    else
        Gratio(i) = round(Gratio(i),2);
    end
    if damp(i)<1
        damp(i) = round(damp(i),4);
    else
        damp(i) = round(damp(i),2);
    end
end

fprintf(fileID, '%5d%s \n', numPoints, ['    ' soil num2str(k) ' -- Shear
Modulus']);
%   Reshape strain, Gratio & damp arrays to [x,8] matrices with a remainder
%   array to comply with QUAD4M format specifications

remainder = mod(numPoints,numCols);
if remainder == 0
    strainM = reshape(strain,numCols, []);
    strainM = strainM';
    GratioM = reshape(Gratio,numCols, []);
    GratioM = GratioM';
    dampM = reshape(damp,numCols, []);
    dampM = dampM';
else
    strainM = strain(1:(end - remainder));
    strainM = reshape(strainM, numCols, []);
    strainM = strainM';
    strainR = strain((end - remainder + 1):end);
    GratioM = Gratio(1:(end - remainder));
    GratioM = reshape(GratioM, numCols, []);
    GratioM = GratioM';
    GratioR = Gratio((end - remainder + 1):end);
    dampM = damp(1:(end - remainder));
    dampM = reshape(dampM, numCols, []);
    dampM = dampM';
    dampR = damp((end - remainder + 1):end);
end

%   Gmax reduction data
for i=1:size(strainM,1)
    for j=1:size(strainM,2)
        fprintf(fileID, '%10s', num2str(strainM(i,j)));
    end
fprintf(fileID, '\n');
end
if ~isempty(strainR)
    for j=1:numel(strainR)
        fprintf(fileID, '%10s', num2str(strainR(j)));
```

```
    end
end
fprintf(fileID, '\n');

for i=1:size(GratioM,1)
    for j=1:size(GratioM,2)
        fprintf(fileID, '%10s', num2str(GratioM(i,j)));
    end
fprintf(fileID, '\n');
end
if ~isempty(strainR)
    for j=1:numel(GratioR)
        fprintf(fileID, '%10s', num2str(GratioR(j)));
    end
end
fprintf(fileID, '\n');
fprintf(fileID, '%5d%s \n', numPoints, ['    ' soil num2str(k) ' --
Damping']);

%   Damping reduction data
for i=1:size(strainM,1)
    for j=1:size(strainM,2)
        fprintf(fileID, '%10s', num2str(strainM(i,j)));
    end
fprintf(fileID, '\n');
end
if ~isempty(strainR)
    for j=1:numel(strainR)
        fprintf(fileID, '%10s', num2str(strainR(j)));
    end
end
fprintf(fileID, '\n');

for i=1:size(dampM,1)
    for j=1:size(dampM,2)
        fprintf(fileID, '%10s', num2str(dampM(i,j)));
    end
fprintf(fileID, '\n');
end
if ~isempty(strainR)
    for j=1:numel(dampR)
        fprintf(fileID, '%10s', num2str(dampR(j)));
    end
end
fprintf(fileID, '\n');
end
fclose(fileID);
cd([home '\Documents\MATLAB']);
```

```
end
```

B.3 Python script for introducing pipe geometric imperfections in ABAQUS

```
import meshEdit, assembly
from numpy import  pi, sqrt, cos, arcsin

# defining shell characteristic dimensions (lc=axial half-wavelength from
buckling eigenvalue analysis)
R = 0.45; L = 0.378; t = 0.012; lc = 0.12;
# defining the imperfection amplitude
w0 = 0.1;

modelName = 'TG- Pipe-shell-springs'
setName = 'Pipe'
part = mdb.models[modelName].parts['Pipe']
a = mdb.models[modelName].rootAssembly
setNodes = a.sets['All']

#Axisymmetric sinusoidal imperfection function
def calc_dr (z) :
      dr = (w0*t)*cos(pi*z/lc)
      return dr

# Create local cylindrical CSYS datum (with axis 1 coinciding with pipe
centerline) and assign it to following variable
local_csys = a.datums[1]
for node in setNodes.nodes:
      z = node.coordinates[2]  # 2=longitudinal axis
      dr = calc_dr(z=z)
      if dr <> 0. :
            a.editNode( localCsys = local_csys,
            nodes = (node,), offset1 =dr )

print "--- Geometric imperfection introduced successfully ---"
```

ℂ Appendix C

C.1 Strain-displacement relationships for circular cylindrical shells

C.1.1 Second-order relationships – small strains and small finite out-of-plane rotations

Sanders's strain-displacement relationships for small strains and moderately large rotations (ABAQUS uses by default the more general set for finite strains)

$$E_{11} = u_{,1} + \frac{1}{2}\varphi_1^2 + \frac{1}{2}\varphi^2 \tag{C.1}$$

$$E_{22} = u_{,2} + \frac{1}{R}w + \frac{1}{2}\varphi_2^2 + \frac{1}{2}\varphi^2$$

$$E_{12} = \frac{1}{2}(u_{,2} + v_{,1}) + \frac{1}{2}\varphi_1\varphi_2$$

$$K_{11} = \varphi_{1,1}$$

$$K_{22} = \varphi_{2,2}$$

$$K_{12} = \frac{1}{2}\left(\varphi_{1,2} + \varphi_{2,1} + \frac{1}{R}\varphi\right)$$

where

$$\varphi_1 = -w_{,1}$$

$$\varphi_2 = -w_{,2} + \frac{1}{R}v$$

$$\varphi = \frac{1}{2}(v_{,1} - u_{,2})$$

$$(*)_{,1} \equiv \frac{\partial(*)}{\partial x}; \quad (*)_{,2} \equiv \frac{1}{R}\frac{\partial(*)}{\partial\theta}$$

The total strains at a material point located at any distance $0 \leq |z| \leq t_w/2$ from the middle surface are given by

$$\varepsilon_{\alpha\beta} = (A_\alpha A_\beta)^{-1/2}(E_{\alpha\beta} + zK_{\alpha\beta}) \tag{C.2}$$

in which

$$A_1 \cong 1; \qquad A_2 \cong 1 + z/R$$

C.1.2 First-order relationships

The 'best' first-order strain-displacement relationships for general thin shells were presented by Sanders (1959). The difference with respect to the second-order set is identified only on the membrane strains, which are simplified to the following forms:

$$E_{11} = u_{,1} \tag{C.3}$$

$$E_{22} = u_{,2} + \frac{1}{R}w$$

$$E_{12} = \frac{1}{2}(u_{,2} + v_{,1})$$

𝔻 Appendix D

D.1 Development and analysis of a full 3-D dynamic SPI FE model of a candidate experimental setup

This Appendix presents supplementary information about an exploratory numerical study carried out during the design phase of the shaking table tests. The study involved the development of a 3-D dynamic FE model of an envisaged 1-g test setup and was aimed to provide insights into the validity of the similarity rules employed and serve as a benchmark to evaluate the computational efficiency of this modelling approach.

D.1.1 Background

As highlighted in Section 5.3.3, the early goal of the experimental campaign was to observe plastic buckling in a pipeline laid through different soil layers and study the characteristics of this failure mode. Since such an approach would require a metal pipe specimen with similar material characteristics to those of the prototype steel, an opportunity investigated was to use a tin pipe specimen with the same set of scaling laws and a scale factor for length $n = 40$.

A setup with a tin pipe would result in crucial non-dimensional ratios being preserved from prototype to model, thus allowing the underlying mechanisms to act in order to trigger buckling instability in the model pipe under the mobilising loads. These ratios include R/t_w and h/D; it is also particularly convenient that the tin elastic modulus and yield stress scale very well with prototype steel. The scale factors considered for each physical quantity are listed in **Table D-1**, while the mechanical and geometrical properties of the tin pipe specimen are given in **Table D-2**. The prototype pipe is the same as the one considered in Chapter 5.

D.1.2 The numerical model

Some key aspects of the numerical model representing the testing regime at hand are illustrated in the following.

The soil structure is the one displayed in **Figure D-1**. In terms of geometry, it differs from the final version in that the side blocks are shorter in the along the pipe direction (1.15m). The stiffness and density selected for the three blocks and shown in **Figure D-1** represent an impedance contrast of 2; the values for stiffness were uniform with depth. For the rubber blocks, an elastic modulus of 1 MPa, a density of 1.25 Mg/m^3 and a small-strain damping of 20% were used; these values were found to yield natural frequencies of the empty ESB that match the experimentally measured ones. To model the soil-pipe contact, the strategy outlined in Section 4.4.4 was adopted, with an interface COF of 0.5. The contact between the soil and the ESB surfaces was duly modelled as well. The constitutive laws for all model components were assumed linear elastic, therefore the only source of nonlinearity in the model was the soil-pipe and soil-ESB contact.

The mesh design was based on similar principles as in the numerical part of this thesis. C3D8H brick elements were used for the soil, with a maximum size of 25mm to resolve wave frequencies up to 15 Hz, with the same element type used for the aluminium rings and rubber blocks of the ESB. S4R shell elements were chosen for the tin pipeline, with progressive mesh refinement towards the soil block interfaces. This mesh strategy resulted in a staggering 815,000 elements, equivalent to 19.5 million DOFs.

To excite the table base, the Imperial Valley acceleration record was used scaled to 0.05g in amplitude and appropriately transformed in time according to the adopted similarity laws. The default implicit time-integration scheme in Abaqus was chosen to solve the equations of motion in time, with a time step of 0.0006s.

D.1.3 Key Findings

The solution cost was immense: it took the BlueCrystal HPC nearly 8.5 days to solve 1671 steps. This cost is even more pronounced considering the high computer performance of the system, which was equivalent to 100 TFlops/iteration, with parallel execution activated (64 cores and 256GB of RAM utilized). Apparently, computational efficiencies can be gained on a more optimized system, but the general conclusion from this is that a 3-D dynamic FE model involving nonlinear contact is not a practical approach, perhaps not even for specialized research purposes. When contrasted with the typical solution performance of the proposed sub-structuring methodology (about 3.5 hours) on the same system, it comes to demonstrate the benefit of using the latter for scenarios similar to those treated in this thesis, where the full 3-D response of the pipeline is not of interest.

Indicative results of the pipe response are illustrated in **Figure D-3**. The pipe response was constrained to the elastic regime, but the observed trends in the strains are similar to both the numerical predictions of Chapter 4 and the experimental results of Chapter 5. Strain peaks occur right at the soil discontinuities, with peak magnitudes of 185 με, comparable to those measured in the experiments with the uPVC pipe. Undeniably, we cannot establish a straight relationship between this model and the real experiment performed as they have different geometries and material characteristics; however, the similarity in the general response characteristics is obvious. When extrapolated to full-scale the peak pipe strain is equivalent to 0.06%, a result also close to the 0.1% strain estimated from the experiment.

Table D-1. 1-g scale factors employed in test setup with tin pipe

Variable	Scale factor (prototype-to-model)	Value for $n = 40$
Length	$1/n$	0.025
Density	1	1
Stiffness	$1/n^{0.5}$	0.158
Acceleration	1	1
Stress/Pressure	$1/n$	0.025
Strain	$1/n^{0.5}$	0.158
Displacement	$1/n^{1.5}$	0.004
Velocity	$1/n^{0.75}$	0.063
Time	$1/n^{0.75}$	0.063
Frequency	$n^{0.75}$	15.905
Wave propagation velocity	$1/n^{0.25}$	0.398
Force	$1/n^3$	0.000016

Table D-2. Mechanical and geometrical properties of tin pipe

Parameter	Unit	Value
Elastic modulus, E_p	MPa	45
Poisson ratio, ν_p	-	0.33
Yield stress, σ_y	MPa	9~12
Mass density, ρ_p	Mg/m^3	7.3
External diameter, D	mm	22.5
Wall thickness, t_w	mm	0.24

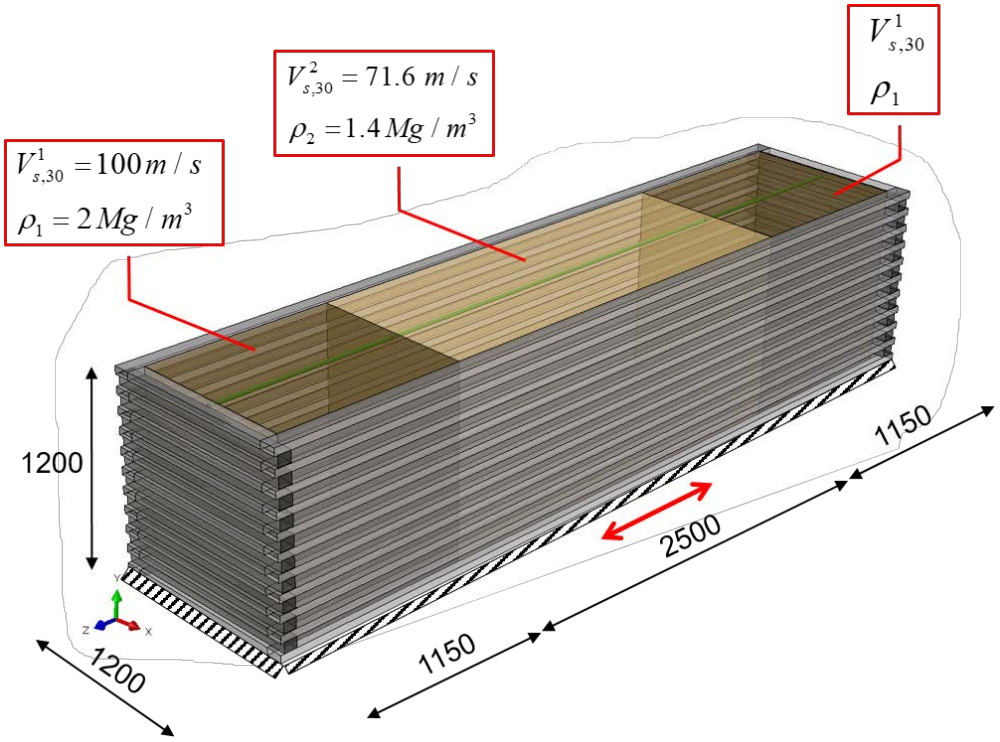

Figure D-1. Perspective view of the 3-D FE model of the shaking table setup developed, with soil properties of the sand blocks noted; dimensions in mm

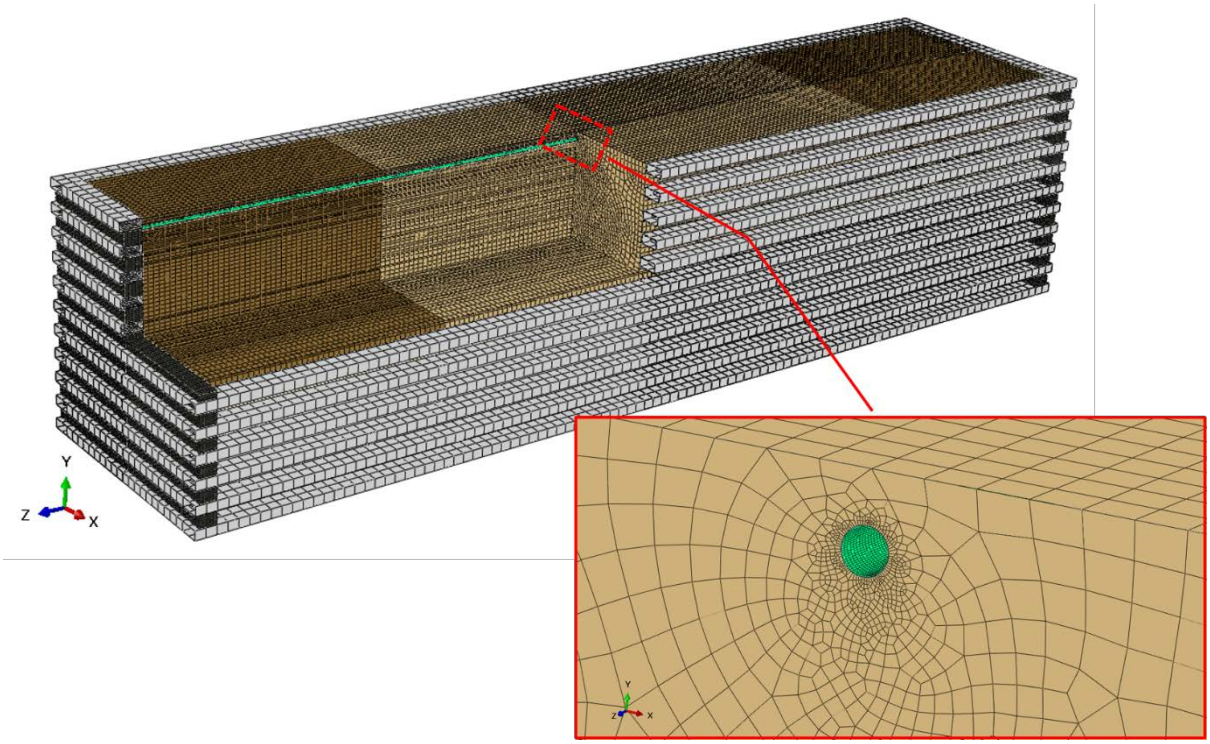

Figure D-2. Aspects of the finite-element mesh used

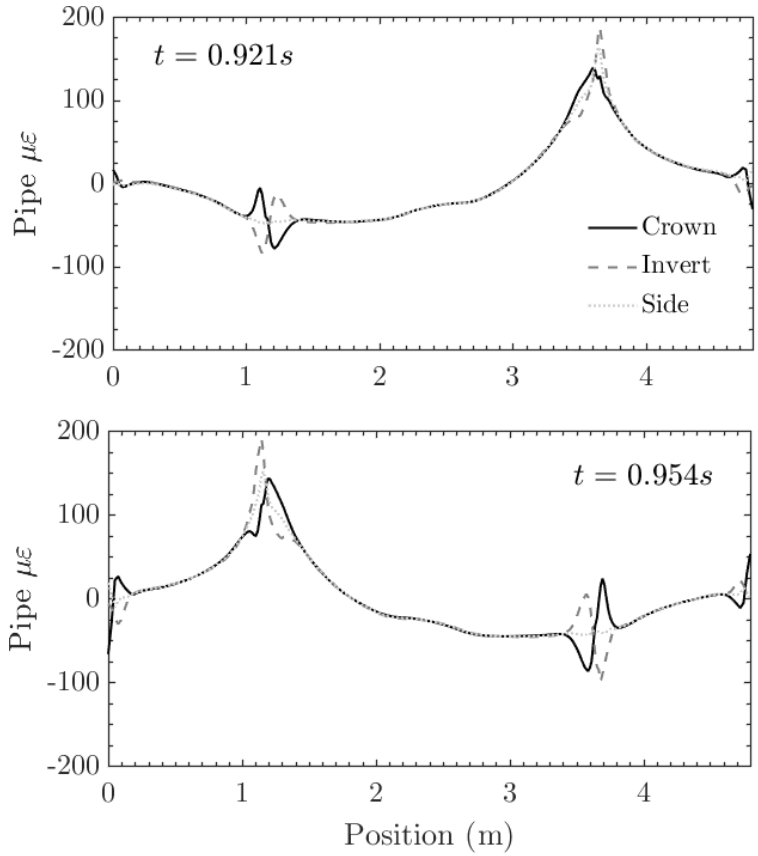

Figure D-3. Longitudinal (elastic) strain profiles along the pipe specimen at three positions over the section: crown, invert and side (at 90deg), at two time instants giving the largest stain magnitudes